

NUMERICAL STUDY OF TWO-PHASE PHENOMENA USING OPENFOAM



Atheel Shuker Jameel

School of Engineering
Cardiff University

A thesis submitted for the degree of
Doctor of Philosophy

March 2017

Table of Contents

TABLE OF CONTENTS	II
ABSTRACT	VI
DECLARATION.....	VII
DEDICATION	VIII
ACKNOWLEDGEMENT	IX
LIST OF FIGURES.....	X
LIST OF TABLES.....	XX
NOMENCLATURE	XXII
ABBREVIATIONS	XXVI
CHAPTER 1 INTRODUCTION.....	1
1.1 MULTI-PHASE FLOWS AND THEIR SIGNIFICANCE	1
1.2 MULTI-PHASE FLOWS AND NUMERICAL SIMULATION	4
1.3 AIM AND OBJECTIVES.....	11
1.4 THESIS STRUCTURE	12
CHAPTER 2 LITERATURE REVIEW	13
2.1 INTRODUCTION.....	13
2.2 DEVELOPMENT OF NUMERICAL MODELS FOR FREE-SURFACE FLOWS.....	13
2.2.1 Surface Methods.....	14
2.2.2 Volume Methods	16
2.3 IMPACT OF TWO DROPLETS ON SUBSTRATE	19
2.4 LIQUID JET BREAKUP AND BURST PHENOMENA	21
2.4.1 Overview of Liquid Jet Breakup Regimes and Relevant Literature	24

2.4.2 Previous Numerical Studies of Liquid Jet Breakup	29
2.4.3 Liquid Burst Phenomena	33
2.5 SUMMARY	37
CHAPTER 3 VALIDATION OF OPENFOAM SOLVERS FOR FREE BOUNDARY	
TWO-PHASE PROBLEMS	
3.1 INTRODUCTION.....	39
3.2 GENERAL OPENFOAM CASES STRUCTURE	39
3.3 CHOOSING AN OPENFOAM SOLVER	39
3.3.1 interFoam Solver.....	40
3.3.2 sclsVOFFoam Solver.....	40
3.3.3 Governing Equations and Numerical Algorithm Used in OpenFOAM	42
3.4 SOLVER VERIFICATION AND VALIDATION.....	45
3.4.1 Rising Bubble	46
3.4.2 Contracting and Disintegration of Liquid Filament.	49
3.4.3 Splashing Droplet.....	54
CHAPTER 4 TWO DROPLET INTERACTION ON A SUBSTRATE	
4.1 INTRODUCTION.....	
4.2 VALIDATION OF THE NUMERICAL SETTING USED FOR TWO DROPLETS PROBLEM.....	
4.3 RESULTS AND DISCUSSION.....	
4.3.1 Influence of Lateral Separation on Final Steady State Composite Location for Various Impact Speeds.....	60
4.3.2 Effect of Surface Tension on Droplets Centre-of-Mass	76
4.3.3 Effect of Viscosity on Droplets Centre-of-Mass.....	79

4.3.4 Effect of Surface Tension, Viscosity and Impact Velocity on Final Composite Centre of Mass Location	82
4.4 SUMMARY AND CONCLUSIONS.....	99
CHAPTER 5 HIGH SPEED LAMINAR JET BURST PHENOMENA.....	101
5.1 INTRODUCTION.....	101
5.2 VALIDATION OF THE NUMERICAL SETTING USED FOR LIQUID JET PROBLEM.....	101
5.3 RESULTS AND DISCUSSION	108
5.3.1 Fully Developed (Parabolic) Laminar Jet	108
5.3.2 Inflow Velocity Profile Effect on Burst Phenomena.....	130
5.3.3 Effect of the Gas Ambient Conditions on the Liquid Jet Burst.....	153
5.3.4 Effect of Low Viscous Liquid on Laminar Burst Jet.....	172
5.4 SUMMARY AND CONCLUSIONS.....	181
CHAPTER 6 CONCLUSIONS AND FUTURE WORK	185
6.1 CONCLUSIONS	185
6.1.1 Two Droplets Interaction on Substrate	185
6.1.2 Liquid Jet Burst Phenomena	186
6.2 RECOMMENDATIONS FOR FUTURE RESEARCH.....	188
6.2.1 Two Droplets Interaction on Substrate	188
6.2.2 Liquid Jet Burst Phenomena	188
APPENDIX A.1 MULTI-PHASE SOLVER VERIFICATION	190
A.1.1 SWIRLING LIQUID JET	190
A.1.2 SWIRL-INDUCED SPRAY	193
APPENDIX A.2 NUMERICAL SETTING USED FOR TWO DROPLETS PROBLEM.	196

A.2.1 Two Droplets Case Pre-processing	196
A.2.2 Two Droplets Case Processing	199
A.2.3 Two Droplets Case Post-processing.....	201
APPENDIX A.3 NUMERICAL SETTING USED FOR LIQUID JET PROBLEM	202
A.3.1 Liquid Jet Burst Phenomena Case Pre-processing.....	202
A.3.2 Liquid Jet Burst Phenomena Case Processing	210
A.3.3 Liquid Jet Burst Phenomena Case Post-processing	210
A.4 RESULTS OF LAMINAR LIQUID JET BURST PHENOMENA	211
A.5 RESULTS OF TURBULENT JET (TOP-HAT) INFLOW VELOCITY PROFILE	211
A.6 RESULTS OF SEMI-TURBULENT INFLOW VELOCITY PROFILE	211
A.7 RESULTS OF LAMINAR JET BURST RELEASED AT HIGHER AMBIENT GAS VISCOSITY	211
A.8 RESULTS OF LAMINAR JET BURST RELEASED AT LOWER AMBIENT GAS VISCOSITY	211
A.9 LAMINAR JET RESULTS AT $Re=2200$ AND LOW VISCOUS LIQUID	211
REFERENCES.....	212

Abstract

An Open source “OpenFOAM” CFD modelling tool and multi-phase solvers are used to solve two-phase flow problems of relevance a variety of engineering applications. Validation of several benchmark two-phase model predictions is presented and discussed. For the different cases considered, the comparison showed that this CFD simulation tool is suitable for modelling multi-phase problems. Furthermore, the comparison revealed that the sclsVOFFoam (LS+VOF) solver is more accurate than interFoam (VOF) and showed better agreement with previous studies. Hence, it is concluded that OpenFOAM with the sclsVOFFoam (VOF+LS) solver is suitable for simulation of multi-phase problems, and so is chosen for implementation in this research study. Numerical studies of two multi-phase problems of practical significance are studied in detail, namely: (i) the coalescence of two droplets and (ii) the jet-burst phenomena of a high speed laminar jet. The numerical framework (geometrical, computational and physical settings) for the two problems are constructed and validated against relevant studies from literature. For the interaction of two droplets problem, numerical results are obtained for the flow phenomena to investigate the final composite droplet location at different lateral separation, impact speed and liquid properties (viscosity and surface tension). It is found that the composite droplet location (centre-of-mass) relative to the initial condition (initial centre-of-mass) is influenced significantly by the impacting droplet velocity and liquid properties, but showed the same non-intuitive final location displacement for the three overlap ratios (lateral separation) studied in this research. For the high speed laminar jet problem, at $Re_L=2200$, results are obtained for different inflow velocity profile, ambient gas viscosity and reduced liquid viscosity. From the results for the high speed laminar liquid jet, it is concluded that this is predominantly a laminar phenomenon, where the inlet velocity profile plays a critical role in determining burst onset. Secondary flow due to the axial velocity relaxation is found to be influential in determining the onset of the jet burst. Also, the results demonstrate that aerodynamic effects play a minimal role in influencing liquid jet burst characteristics. These results are useful in informing estimates of jet breakup length in practical problems, such as (explosive) area classification for accidental releases of high-flashpoint fuels.

Declaration

This work has not previously been accepted in substance for any degree and is not concurrently submitted in candidature for any degree.

Signed.....(Candidate) Date.....

This thesis is being submitted in partial fulfilment of the requirements for the degree of PhD.

Signed.....(Candidate) Date.....

This thesis is the result of my own independent work/investigation, except where otherwise stated. Other sources are acknowledged by explicit references.

Signed.....(Candidate) Date.....

I hereby give consent for my thesis, if accepted, to be available for photocopying and for inter-library loan, and for the title and summary to be made available to outside organisations.

Signed.....(Candidate) Date.....

Dedication

- ❖ *I dedicate this work to my wife, Rafad, who has been a persistent source of support and encouragement during the challenges of study and life. I am really blessed for having you in my life.*
- ❖ *I dedicate this work also to my parents, Shuker and Salma, who have always loved me unconditionally and whose good examples have taught me to work tenaciously for the things that I plan to accomplish.*
- ❖ *I also dedicate this dissertation to my sister, Ghada, my brother, Ghaith, to my few friends and my church family in Mosul who have supported me during the study.*
- ❖ *Last but not the least, those unforgettable innocent eyes of my children, Sandy and Salam who their smiley faces kept pushing me, giving me the hope, the desire to carry on and overcome all the difficulties I had, therefore, this success was attributed to them.*

Acknowledgement

After more than four years, I would like to say that it has been a period of intense learning for me, not only in the engineering field but also on a personal level. Doing this work and writing this thesis has had a great influence on me, therefore, I would like to pay gratitude to the people and organizations who have supported and helped me throughout this study.

Foremost, I would like to express my sincere gratitude to my supervisor, Professor Phil Bowen, for the continuous support of my Ph.D. study and research, for his patience, motivation, enthusiasm, and wide knowledge. His guidance helped me in all the time of research and writing of this thesis. I could not have imagined having a better advisor and counsellor for my Ph.D. study. In addition, I would like to thank my second supervisor, Dr. Kensuke Yokoi, for his guidance.

Finally, this research would not have been possible without the financial assistance, therefore I must express my very profound gratitude to Cardiff University, school of Engineering, energy department for their tuition fees contribution.

List of Figures

Figure 1.1 Classification of multi-phase flow sorts. (adopted from [2]).....	1
Figure 1.2 Classification of gas-liquid two-phase flows. (adapted from [1])	2
Figure 1.3 Different interfacial flow solution methodologies: (a) interface fitting, (b) interface capturing, and (c) interface tracking. (adopted from [6])	8
Figure 1.4 A schematic representation of a gas-liquid-solid turbulent flow. (adapted from [1]).....	10
Figure 2.1 Different methods of representing the interface (adapted from O. Ubbink [9])	14
Figure 2.2 Particles on the interface surface method. (adapted from O. Ubbink [9])	15
Figure 2.3 Schematic representation of height functions for (a) open interfaces	15
Figure 2.4 Two droplets contours of the level set function: (a) initial configuration, (b) just before merging with no corrections (c) just before merging with corrections. (adapted from Sussman et al. [11])	16
Figure 2.5 Volume methods to treat the interface. (adapted from O. Ubbink [9])	17
Figure 2.6 The various fashions of jet disintegration.....	24
Figure 2.7 Breakup regimes dependence on liquid Reynolds number (Re_L) and Ohnesorge number (Oh).....	25
Figure 2.8 Stability curve. (adapted from M. Birouk and N. Lekic [26])	27
Figure 3.1 OpenFOAM case directory structure.....	41
Figure 3.2 3-D geometrical setting for rising bubble validation case	46
Figure 3.3 Snapshots of a comparison between the of 3-D numerical result of a single rising bubble by the OpenFOAM model (b) and the Yokoi's simulation (a) [68] .	47

Figure 3.4 Snapshots of a 3-D numerical simulation results of single rising bubble by the OpenFOAM model	48
Figure 3.5 3-D geometrical setting for filament contraction validation case	49
Figure 3.6 2-D geometrical setting for filament breakup validation case	50
Figure 3.7 3-D evolution of a contract liquid filament simulation results: (a) VOF; (b) VOF+LS, compared with: (c) simulation results [70] and (d) experiment results [69]	52
Figure 3.8 2-D evolution of a breakup liquid filament simulation results: (a) VOF; (b) VOF+LS, compared with: (c) simulation results [70]	53
Figure 3.9 3-D geometrical setting for droplet splashing validation case	54
Figure 3.10 Snapshots of a comparison between the numerical results of 3-D simulation of single droplet splashing by the OpenFOAM model (b) and the experimental data (a). (adapted from [71])	55
Figure 3.11 Snapshots of results of three dimensional numerical simulation of single droplet splashing by the OpenFOAM model	56
Figure 4.1 Time-resolved results of a comparison between the experimental [24] (top) and 3-D numerical simulation (bottom) of a two droplets interaction on substrate at five different centre displacements Using OpenFOAM model	59
Figure 4.2 (a) Deposition of two droplets on a solid surface; (b) intermediate spread length - D_y ; (c) maximum spread length - $D_{y,max}$; (d) minimum spread length - $D_{y,min}$	61
Figure 4.3 Top and side view contour of impact and coalescence droplets at different impact speed of case $\lambda=0.5$. Early stage of impact on top, steady state condition on bottom	63
Figure 4.4 Top and side view contour of impact and coalescence droplets at different impact speed of case $\lambda=0.34$. Early stage of impact on top, steady state condition on bottom	64

Figure 4.5 Top and side view contour of impact and coalescence droplets at different impact speed of case $\lambda=0.18$. Early stage of impact on top, steady state condition on bottom.....	65
Figure 4.6 Composite droplet location details and mass centre compared with initial mass centre at different impact speed for $\lambda=0.5$	66
Figure 4.7 Composite droplet location details and mass centre compared with initial mass centre at different impact speed for $\lambda=0.34$	67
Figure 4.8 Composite droplet location details and mass centre compared with initial mass centre at different impact speed for $\lambda=0.18$	67
Figure 4.9 Side view contour of the two droplet composite at steady state for three different overlap ratios (λ) and different impact speeds.....	68
Figure 4.10 Displacement of the right and left edges of composite droplets for $U=0$ m/s.....	71
Figure 4.11 Displacement of the right and left edges of composite droplets for $U=0.2$ m/s.....	71
Figure 4.12 Displacement of the right and left edges of composite droplets for $U=0.4$ m/s.....	72
Figure 4.13 Displacement of the right and left edges of composite droplets for $U=0.5$ m/s.....	72
Figure 4.14 Displacement of the right and left edges of composite droplets for $U=0.6$ m/s.....	73
Figure 4.15 Displacement of the right and left edges of composite droplets for $U=0.8$ m/s.....	73
Figure 4.16 Displacement of the right and left edges of composite droplets for $U=1$ m/s.....	74
Figure 4.17 Displacement of the right and left edges of composite droplets for $U=1.5$ m/s.....	74

Figure 4.18 Displacement of the right and left edges of composite droplets for $U=2$ m/s	75
Figure 4.19 Displacement of the right and left edges of composite droplets for $U=3$ m/s	75
Figure 4.20 Effect of liquid surface tension on the Final Centre of Mass Location for different impact velocities	78
Figure 4.21 Effect of liquid viscosity property on the Final Centre of Mass Location for different impact velocities	81
Figure 4.22 Threshold splitting between right and left composite mass centre location relative to the initial mass centre for $U=0$ m/s at different surface tension and viscosity	83
Figure 4.23 Threshold splitting between right and left composite centre-of-mass location relative to the initial centre-of-mass for $U=0.2$ m/s at different surface tension and viscosity	85
Figure 4.24 Threshold splitting between right and left non-dimensional composite mass centre location relative to the initial mass centre for $U=0.2$ m/s at different Re and We	86
Figure 4.25 Threshold splitting between right and left composite centre-of-mass location relative to the initial centre-of-mass for $U=0.5$ m/s at different surface tension and viscosity	87
Figure 4.26 Threshold splitting between right and left non-dimensional composite mass centre location relative to the initial mass centre for $U=0.5$ m/s at different Re and We	89
Figure 4.27 Enlarged picture showing the top and side view of local free surfaces for coalescence of two different surface tension droplets at constant viscosity. (a), (b), (c), (d), (e), (f), (g), (h), (i), (j), (k), (l) at time= 0, 5, 10, 15, 20, 25, 30, 35, 50, 100,1100 and 5100 ms respectively	91
Figure 4.28 Threshold splitting between right and left composite centre-of-mass location relative to the initial centre-of-mass for $U=0.8$ m/s at different surface tension and viscosity	98

Figure 4.29 Threshold splitting between right and left composite centre-of-mass location relative to the initial centre-of-mass for U=1 m/s at different surface tension and viscosity	98
Figure 4.30 Threshold splitting between right and left composite centre-of-mass location relative to the initial centre-of-mass for U=1.2 m/s for different surface tension and viscosity	99
Figure 5.1 Snapshots of a 3-D liquid jet numerical simulation at Re=480, We=3.1, Oh=3.7 10 ⁻³ , Bo=0.23 by the interFoam (VOF) in OpenFOAM model compared to the experimental value [80] as presented in the bars next to each time step. Time (T) in milliseconds	103
Figure 5.2 Snapshots of a 3-D liquid jet numerical simulation at Re=480, We=3.1, Oh=3.7 10 ⁻³ , Bo=0.23 by the sclsVOFFoam (LS+VOF) in OpenFOAM model compared to the experimental value [80] as presented in the bars next to each time step. Time (T) in milliseconds	104
Figure 5.3 Snapshots of a 3-D liquid jet numerical simulation at Re=480, We=7.45_ Oh=5.7*10 ⁻³ , Bo=0.55 by the sclsVOFFoam (LS+VOF) in OpenFOAM model compared to the experimental value [80] as presented in the bars next to each time step. Time (T) in milliseconds	105
Figure 5.4 Snapshots of a 3-D liquid jet numerical simulation of water jet into air at Re=480, We=3.1, Oh=3.7*10 ⁻³ . (adapted from [58]).....	106
Figure 5.5 Snapshots of a 3-D liquid jet numerical simulation of water jet into air at Re=480, We=7.45, Oh=5.7*10 ⁻³ . (adapted from [58]).....	106
Figure 5.6 Comparison of Current results for breakup length of laminar jets at different Weber numbers studied compared with previous data [80] and [58]. (adapted from [58])	107
Figure 5.7 Liquid jet results for present work compared with experimental [39] and numerical [58] studies. The number next to each image indicates the dimensional physical time elapsed in milliseconds	109
Figure 5.8 Current study physical conditions located on Ohnesorge chart and present study regime	110

Figure 5.9 Liquid column (1 st row), domain velocity profile (2 nd row), domain velocity field (3 rd row), liquid velocity stream lines (4 th row) and gas velocity stream lines (5 th row)	117
Figure 5.10 Liquid jet core velocity components (U_x U_y and U_z at the early time (Time =0.195.5 seconds) of liquid jet burst phenomena	118
Figure 5.11 Distribution of instantaneous liquid velocity vectors projected onto longitudinal and cross-sectional planes at different axis locations. The vector length is scaled appropriately in each cross-section to show the radial motion in the liquid core	119
Figure 5.12 Longitudinal and lateral velocity (1 st and 2 nd rows) and vorticity (3 rd and 4 th rows) field's distribution at the onset of liquid jet burst phenomena	120
Figure 5.13 Longitudinal and lateral velocity (1 st and 2 nd rows) and vorticity (3 rd and 4 th rows) field's distribution of liquid jet burst phenomena	121
Figure 5.14 Distribution of instantaneous vorticity fields in an axis plan at the onset of the liquid jet burst phenomena. 1 st row in the gas phase, 2 nd row in the liquid phase, 3 rd row vorticity-x distribution in the liquid phase, 4 th row vorticity-y distribution in the liquid phase and 5 th row vorticity-z component distribution in the liquid phase	122
Figure 5.15 Distribution of instantaneous vorticity fields in an axis plain of the liquid jet burst phenomena. 1st row in the gas phase, 2nd row in the liquid phase, 3rd row vorticity-x distribution in the liquid phase, 4th row vorticity-y distribution in the liquid phase and 5 th row vorticity-z component distribution in the liquid phase.....	123
Figure 5.16 Liquid different vortex structures at time 194.6 ms. 1st row: axial vorticity vector (ω_z) in the liquid side, 2nd row: Helicity vortex structure in the liquid side, 3 rd row: normalized helicity structure sliced longitudinally across the customized domain, 4 th row: vorticity stream lines in the liquid side	128
Figure 5.17 Liquid different vortex structures at time 198 ms. 1st row: axial vorticity vector (ω_z) in the liquid side, 2nd row: Helicity vortex structure in the liquid side, 3rd row: normalized helicity structure sliced longitudinally across the customized domain, 4th row: vorticity stream lines in the liquid side	129
Figure 5.18 Laminar (blue), top hat turbulent (green) and typical turbulent (black) velocity profile produced by the current modelling benchmark.....	131

Figure 5.19 Schematic diagram for laminar and turbulent velocity profile	132
Figure 5.20 Power-law velocity profiles for turbulent flow in a pipe for different exponents, and its comparison with the laminar velocity profile. (adapted from [88]).	132
Figure 5.21 Liquid jet column ejected with an inflow condition of the top hat (turbulent) velocity profile. The number next to each image indicates the dimensional physical time elapsed in milliseconds	133
Figure 5.22 Top hat turbulent case results show the liquid column (1 st row), domain velocity profile (2 nd row), domain velocity field (3 rd row), liquid velocity stream lines (4 th row) and gas velocity stream lines (5 th row)	136
Figure 5.23 Liquid jet core velocity components (U _x , U _y and U _z) at time 198 ms of liquid jet top hat (flat) inflow turbulent condition	137
Figure 5.24 Distribution of instantaneous liquid velocity vectors projected onto longitudinal and cross-sectional planes at different axis locations for top (flat) inflow turbulent condition	138
Figure 5.25 Longitudinal and lateral velocity (1 st and 2 nd rows) and vorticity (3 rd and 4 th rows) field's distribution of turbulent liquid jet problem	139
Figure 5.26 Distribution of instantaneous vorticity fields in an axis plain of the turbulent liquid case. 1 st row in the gas phase, 2 nd row in the liquid phase, 3 rd row vorticity-x distribution in the liquid phase, 4 th row vorticity-y distribution in the liquid phase and 5 th row vorticity-z component distribution in the liquid phase	140
Figure 5.27 Different vortex structures for top flat turbulent liquid jet case at time 198 ms. 1 st row: axial vorticity vector (ω_z) in the liquid side, 2 nd row: Helicity vortex structure in the liquid side, 3 rd row: normalized helicity structure sliced longitudinally across the customized domain, 4 th row: vorticity stream lines in the liquid side	141
Figure 5.28 Laminar (blue), top hat turbulent (green), typical turbulent $n=7$ (black) and semi-turbulent $n=3$ (red) velocity profile produced by the current modelling benchmark	142
Figure 5.29 Liquid jet column ejected with an inflow condition of semi-turbulent velocity profile. The number next to each image indicates the dimensional physical time elapsed in milliseconds	144

Figure 5.30 Semi-turbulent case results show the liquid column (1 st row), domain velocity profile (2 nd row), domain velocity field (3 rd row), liquid velocity stream lines (4 th row) and gas velocity stream lines (5 th row)	147
Figure 5.31 Liquid jet core velocity components (Ux Uy and Uz) at time 198 ms of liquid jet semi-turbulent inflow condition	148
Figure 5.32 Distribution of instantaneous liquid velocity vectors projected onto longitudinal and cross-sectional planes at different axis locations for the semi-turbulent inflow condition.....	149
Figure 5.33 Longitudinal and lateral velocity (1 st and 2 nd rows) and vorticity (3 rd and 4 th rows) field's distribution of semi-turbulent liquid jet case	150
Figure 5.34 Distribution of instantaneous vorticity fields in an axis plain of the semi-turbulent liquid case. 1 st row in the gas phase, 2 nd row in the liquid phase, 3 rd row vorticity-x distribution in the liquid phase, 4 th row vorticity-y distribution in the liquid phase and 5 th row vorticity-z component distribution in the liquid phase.....	151
Figure 5.35 Different vortex structures for top semi-turbulent liquid jet case at time 198 ms. 1 st row: axial vorticity vector (ω_z) in the liquid side, 2 nd row: Helicity vortex structure in the liquid side, 3 rd row: normalized of helicity structure sliced longitudinally across the customized domain, 4 th row: vorticity stream lines in the liquid side.....	152
Figure 5.36 Liquid jet column ejected with laminar (parabolic velocity profile) inflow condition to a high viscous ambient (10 times higher than air viscosity). The number next to each image indicates the dimensional physical time elapsed in milliseconds.....	155
Figure 5.37 Laminar burst jet at high ambient gas viscosity; results show the liquid column (1 st row), domain velocity profile (2 nd row), domain velocity field (3 rd row), liquid velocity stream lines (4 th row) and gas velocity stream lines (5 th row)	157
Figure 5.38 Liquid jet core velocity components (Ux Uy and Uz) at time 181.5 ms of a laminar burst jet at high ambient gas viscosity.....	158
Figure 5.39 Distribution of instantaneous liquid velocity vectors projected onto longitudinal and cross-sectional planes at different axis locations for a laminar burst jet at high ambient gas viscosity	159

Figure 5.40 Longitudinal and lateral velocity (1st and 2nd rows) and vorticity (3rd and 4th rows) field's distribution for a laminar burst jet at high ambient gas viscosity .160

Figure 5.41 Distribution of instantaneous vorticity fields in an axis plain for a laminar burst jet at high ambient gas viscosity at time 181.5 ms. 1st row in the gas phase, 2nd row in the liquid phase, 3rd row vorticity-x distribution in the liquid phase, 4th row vorticity-y distribution in the liquid phase and 5th row vorticity-z component distribution in the liquid phase 161

Figure 5.42 Different vortex structures for a laminar burst jet at higher ambient gas viscosity at time 181.5 ms. 1st row: axial vorticity vector (ω_z) in the liquid side, 2nd row: Helicity vortex structure in the liquid side, 3rd row: normalized of helicity structure sliced longitudinally across the customized domain, 4th row: vorticity stream lines in the liquid side 162

Figure 5.43 Liquid jet column ejected with laminar (parabolic velocity profile) inflow condition to a low viscous ambient (10 times less than air viscosity). The number next to each image indicates the dimensional physical time elapsed in milliseconds.164

Figure 5.44 Laminar burst jet at low ambient gas viscosity case results show the liquid column (1st row), domain velocity profile (2nd row), domain velocity field (3rd row), liquid velocity stream lines (4th row) and gas velocity stream lines (5th row) 166

Figure 5.45 Liquid jet core velocity components (U_x U_y and U_z) at time 257 ms of a laminar burst jet at low ambient gas viscosity 167

Figure 5.46 Distribution of instantaneous liquid velocity vectors projected onto longitudinal and cross-sectional planes at different axis locations for a laminar burst jet at low ambient gas viscosity 168

Figure 5.47 Longitudinal and lateral velocity (1st and 2nd rows) and vorticity (3rd and 4th rows) field's distribution for a laminar burst jet at low ambient gas viscosity... 169

Figure 5.48 Distribution of instantaneous vorticity fields in an axis plain for a laminar burst jet at low ambient gas viscosity at time 257 ms. 1st row in the gas phase, 2nd row in the liquid phase, 3rd row vorticity-x distribution in the liquid phase, 4th row vorticity-y distribution in the liquid phase and 5th row vorticity-z component distribution in the liquid phase 170

Figure 5.49 Different vortex structures for a laminar burst jet at higher ambient gas viscosity at time 257 ms. 1 st row: axial vorticity vector (ω_z) in the liquid side, 2 nd row: Helicity vortex structure in the liquid side, 3 rd row: normalized of helicity structure sliced longitudinally across the customized domain, 4 th row: vorticity stream lines in the liquid side	171
Figure 5.50 Low viscous liquid physical conditions located on Ohnesorge chart and the present investigation regime	173
Figure 5.51 Low viscosity liquid jet column ejected with inflow condition of laminar (parabolic velocity profile). The number next to each image indicates the dimensional physical time elapsed in milliseconds	174
Figure 5.52 Low viscosity laminar liquid jet case results show the liquid column (1 st row), domain velocity profile (2 nd row), domain velocity field (3 rd row), liquid velocity stream lines (4 th row) and gas velocity stream lines (5 th row)	177
Figure 5.53 Liquid jet core velocity components (U_x U_y and U_z) at time 227 ms of a low viscosity laminar liquid jet case results	178
Figure 5.54 Distribution of instantaneous liquid velocity vectors projected onto longitudinal and cross-sectional planes at different axis locations of a low viscosity laminar liquid jet case results	179
Figure 5.55 Longitudinal and lateral velocity (1 st and 2 nd rows) and vorticity (3 rd and 4 th rows) field's distribution for a low viscosity laminar liquid jet case results	180
Figure A.2.1 3-D geometrical setting for two droplets validation case	196
Figure A.3.1 Geometrical domain used for Liquid Jet Case	203

List of Tables

Table 2.1 Ohnesorge’s classification based on values of liquid and ambient properties. (adapted from M. Birouk and N. Lekic [26])	26
Table 3.1 Geometrical and mesh details for rising bubble case	47
Table 3.2 Physical parameters conducted for rising bubble. (adapted from [67])	47
Table 3.3 Geometrical and mesh details of liquid filament contraction and breakup validation cases	50
Table 3.4 Physical parameters conducted for filament contraction. (adapted from [70])	50
Table 3.5 Physical parameters conducted for filament breakup. (adapted from [70])	50
Table 3.6 Geometrical and mesh details for droplet splashing case	54
Table 3.7 Physical parameters conducted for droplet splashing. (adapted from [71])	55
Table 4.1 Droplets geometrical conditions explored in this work	60
Table 4.2 Three sets of overlap ratios λ used in our research	62
Table 5.1 Geometrical and mesh details of $We=3.1$ and $We=7.45$ laminar jets	102
Table 5.2 Physical parameters conducted for $We=3.1$ liquid jet case	102
Table 5.3 Physical parameters conducted for $We=7.4$ liquid jet case	102
Table 5.4 physical properties and non-dimensional parameters used for high and low liquid to gas viscosity ratio	154
Table 5.5 Properties and non-dimensional parameters used for low viscous liquid case	172
Table A.2.1 Geometrical and mesh details for two droplets case	197

Table A.2.2 Physical parameters conducted for two droplets case. (adapted from [24]) 197

Nomenclature

Roman Characters

<i>Symbol</i>	<i>Unit</i>	<i>Definition</i>
C_o	-	Courant number
C_α	-	Interface phase compression factor
D	m	Jet, nozzle and/or droplet diameter
D_o	m	Impacting droplet diameter
D_s	m	Sessile droplet diameter
D_y	m	Droplets spread length
$D_{y,max}$	m	Maximum droplets spread length
$D_{y,min}$	m	Minimum droplets spread length
d_L	m	Droplet's left edge displacement
d_R	m	Droplet's right edge displacement
\vec{F}_σ	N	Volumetric surface tension force
G	m/s^2	Gravity acceleration
H	-	Heaviside function
H_d	m/s^2	Helicity density
H_n	-	Normalized helicity
H	m	Liquid height
L	m	spacing between two droplets centres
L_B	m	Breakup length

N	-	Constant number for power-law velocity profile
\hat{n}	-	Normal vector of the interface
Oh	-	Ohnesorge number
P	N/m^2	Total pressure
P_{rgh}	N/m^2	Dynamic pressure
Re	-	Reynolds number
R	m	Radius of Jet, nozzle and/or droplet
R	m	Any radius value less than the whole radius (R)
S	$1/m\ s$	Viscous stress tensor
t	s	Time
U	m/s	Jet and/or droplet velocity
U_x	m/s	Velocity component in x-axis
U_y	m/s	Velocity component in y-axis
U_z	m/s	Velocity component in z-axis
u	m/s	Any jet velocity value ranged between the mean and maximum velocities
u_{mean}	m/s	Mean velocity
u_{max}	m/s	maximum velocity
\vec{u}	m/s	Velocity vector
\vec{u}_r	m/s	liquid–gas relative velocity
We	-	Weber number
X_L	-	non-dimensional droplet's left edge displacement

X_R	-	non-dimensional droplet's right edge displacement
z	m	Any distance measured from jet exit

Greek Characters

<i>Symbol</i>	<i>Unit</i>	<i>Definition</i>
α	-	volume of fluid fraction
Γ	-	depends on the mesh step size (Δx)
δ	$1/m$	Dirac delta function
Δt	s	time step
Δx	m	mesh increment
ε	m	interface thickness
κ	$1/m$	interface curvature
λ	-	overlap ratio between the two droplets
μ	$Pa.s$	viscosity coefficient
ρ	Kg/m^3	density coefficient
σ	N/m	surface tension coefficient
ψ	m	level set function
ω	$1/s$	Vorticity
ω_x	$1/s$	vorticity component in x-axis
ω_y	$1/s$	vorticity component in y-axis
ω_z	$1/s$	vorticity component in z-axis

Subscripts

<i>Symbol</i>	<i>Unit</i>	<i>Definition</i>
<i>g</i>	-	gas
<i>l</i>	-	liquid

Abbreviations

BI	Boundary integral
CAD	Computer-aided design
CFD	Computational fluid dynamics
CPU	Central processing unit
CSF	Continuum surface force
CFL	Courant number
C++	Programming language
DNS	Direct numerical simulation
FD	Finite difference
FE	Finite element
FS3D	Free surface three dimensional
FV	Finite volume
HPC	High performance computing
LES	Large eddy simulation
LS	Level Set
MAC	Marker-And-Cell
MPI	Message Passing Interface
MULES	Multidimensional Universal Limiter for Explicit Solution
PDEs	Partial differential equations
PIMPLE	Pressure Implicit Method for Pressure Linked Equations
PISO	Pressure Implicit with Splitting of Operator
RAM	Random-access memory
RAS	Reynolds-averaged stress

S-CLSVOF	Simple coupled level set volume of fluid
SIMPLE	Semi-Implicit Method for Pressure Linked Equations
SSH	Secure Socket Shell
STL	Standard Triangle Language
VOF	Volume fraction or volume of fluid
2-D	Two dimensional
3-D	Three dimensional

Chapter 1 Introduction

This chapter introduces the importance of multiphase flows, development in numerical modelling, and the different applications and relevance of the problems dealt with in this research programme. Against this background, the aim and objectives of the current research project adopted as well as the thesis structure are presented at the end of the Chapter.

1.1 Multi-phase Flows and their Significance

Many applications in engineering and chemical processing give rise to multiphase flows. With the addition of chemical reactions in the case of chemical processing for example, it may be appreciated that understanding and predicting the behaviour of multiphase flows is hugely beneficial to enable development of more efficient designs and for safe operation for a wide range of engineering applications. Multiphase flows exist in many different forms and can be described more generally as a branch of fluid dynamics. Multi-phase flows comprise two or more distinct phases which flow concurrently [1].

Multi-phase flows can be categorised according to the condition of the various phases present in the system: Gas-solid flows, liquid-solid flows, or gas-liquid flows as shown in Figure 1.1.

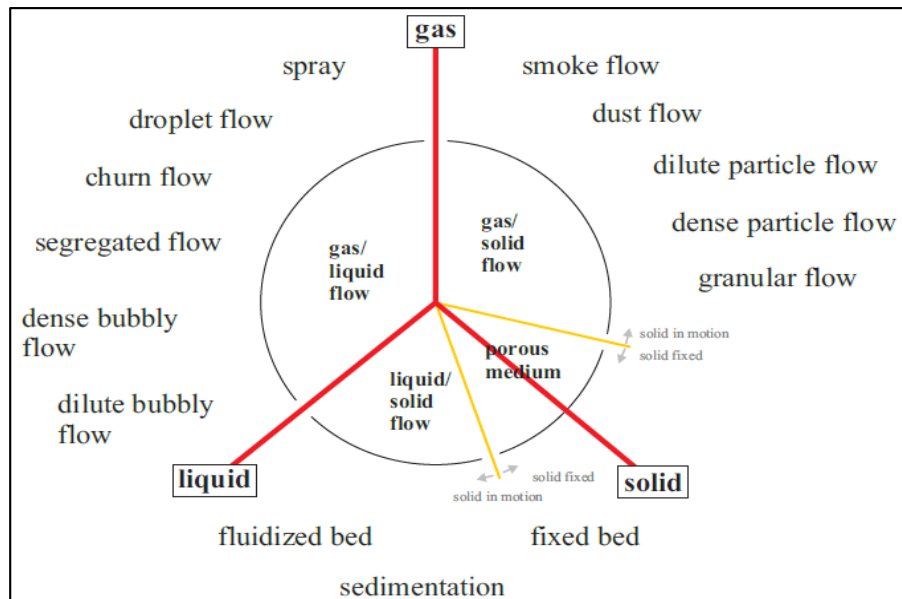


Figure 1.1 Classification of multi-phase flow sorts. (adopted from [2])

Gas-liquid flows can appear in various configurations. The motion of bubbles in a liquid flow is one example, whilst the motion of liquid droplets in a gas stream is another. Further classification such as dispersed (or scattered) flows can be applied to the two previous examples. For the motion of bubbles in a liquid flow example, the liquid is classed as continuous phase, whereas the bubbles are taken as the discrete element of the dispersed phase. Similarly, for the motion of liquid droplets in a gas stream example, the gas is considered the continuous phase and the droplets are the dispersed phase. Typically, bubbles or droplets distort naturally within the continuous phase. They may appear in various geometrical shapes such as spherical, elliptical, distorted, toroidal, cap, and so on. In addition to dispersed flows, gas-liquid flows often exhibit other complex interfacial structures called separated flows and mixed or transitional flows [2].

For a more sophisticated and comprehensive understanding of gas-liquid classification, Figure 1.2 presents different formations that can exist for multi-phase flows [1]. The transformation between the dispersed flows and separated flows includes the presence of both of these flows to a degree, as indicated in the schematics in Figure 1.2. Coalescence, breakup and interaction between discrete phase elements (droplets or bubbles) means that dynamic changes in interfacial structural phenomena can often take place.

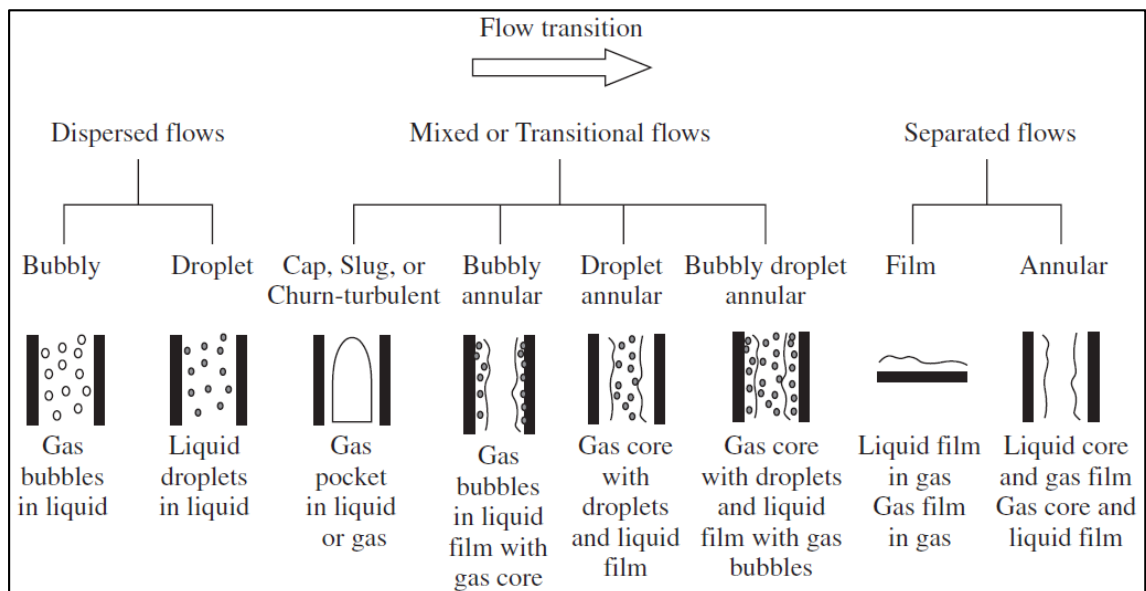


Figure 1.2 Classification of gas-liquid two-phase flows. (adapted from [1])

For immiscible liquid flows, existence of the identified interfaces complicate the free surface flows. In fact, immiscible liquid flows do not classified into the category of

two-phase flows, but, they can be addressed as two-phase mixtures for functional intent. With regard to the categorization of two-phase flows, gas and liquid flows that fundamentally encompass the free surface flows are commonly considered with both phases treated as continuous. Likewise, the operation of solidification or freezing could also be treated as a different distinctive state of a two-phase mixture, where the solid regions and the liquid could be considered individually and later grouped together during suitable dynamic and kinematic situations at the interface [1].

Liquid-gas-solid as in the three-phase flows are also experienced in some engineering problems and applications of technical relevance. For this specific category of three phase flows, the gas bubbles and the solid particles can be considered as the separated ingredient of the dispersed (scattered) phases, co-flowing with the continuous liquid phase. The simultaneous existence of three phases considerably complicates the problem due to the various potential phenomena associated with bubble-bubble, particle-particle, particle-bubble, particle-fluid, and bubble-fluid interactions changing the physics of the flow [1].

Many practical applications comprising multi-phase flows exist not just in cutting edge technological industries, but also naturally in the global environment. Examples of multi-phase flow systems include:

- Gas-particle Flows
 - Natural sand storms, volcanoes, avalanches.
 - Biological aerosols, dust particles, smoke (fine soot particles), rain droplets, mist formation.
 - Industrial pneumatic conveyers, dust collectors, fluidized beds, solid propellant rockets, pulverized solid particles, spray drying, spray casting, granular beds, interior ballistics.
- Liquid-Solid Flows
 - Natural sediment transport of sand in rivers and sea, soil erosion, mud slides, debris flows, iceberg formation.
 - Biological blood flow.
 - Industrial slurry transportation, flotation, fluidized beds, water jet cutting, sewage treatment plants.
- Gas-Liquid Flows
 - Natural ocean waves.
 - Biological blood flow.

- Industrial boiling water and pressurized water nuclear reactors, chemical reactor desalination systems, boilers, heat exchangers, internal combustion engines, liquid propellant rockets, fire sprinkler suppression systems.
- Liquid-Liquid Flows
 - Industrial emulsifiers, fuel-cell systems, micro channel applications, extraction systems.
- Gas-Liquid-Solid Flows
 - Industrial air lift pumps, fluidized beds, oil transportation.

In the systems listed above, by contrast to single-phase systems, multi-phase is considered systematically more complicated due to the presence of dynamically changing interfaces, where considerable discontinuities of the fluid properties, and complicated flow fields near the interface can be observed. An additional complicated phenomena could be introduced when one or both phases become turbulent, where an exchange between the separate phases occurs as a result of the interaction between the turbulent eddies and the interfacial structures. It is worth noting that multi-phase flow is physically a multi-scale phenomena in nature, and so it is important to consider the consequent effects of the physics at different scales [1].

1.2 Multi-phase Flows and Numerical Simulation

As already illustrated, the different sorts of multi-phase structures include continuous series of systems of temporal and spatial scales often changing over orders of magnitude (multi-scale) and multiple coupled phenomena (multi-physics). Hence, numerical simulation of such systems is extremely complicated, and so no generic methodology or technique application to all categories of multi-phase flow has been developed to date consequently. In general, any approach adopted strictly relies on the specific phenomena of the multi-phase flow that is to be investigated.

Computational fluid dynamics (CFD) is the system analysis consisting of a potential combination of fluid flow, heat transfer and chemical reactions with the help of a computer simulation [3]. CFD has become an integral part of engineering design and analysis. Prior to CFD, fluid dynamics was studied either through empirical analysis involving carefully designed experimental programmes and monitoring or analytical numerical techniques such as perturbation analysis.

Due to the huge potential advantage of CFD, many engineering problems are now able to be considered, such as multiphase modelling, turbo-machinery, aerodynamics, gas turbines, ship hydrodynamics, etc. Many of these engineering

problems would require experimental results which are often very difficult to realize or economically not viable. These are essentially the reasons why CFD is in such high demand when dealing with fluid flow problems; it is potentially cheaper and less time consuming than empirical design, though there are still significant challenges in obtaining reliable CFD results. In real experiments, some physical parameters (pressure, velocity, temperature, etc.) which are difficult to measure can be considered within a CFD framework. In order to predict the outcome of real fluid flow problems, it has become common in recent years to use CFD analysis both in industrial and academic contexts, due to its capability to obtain results much faster and potentially more accurate. However, validation and verification of predictions is still essential because CFD can present very impressive post-processed visualisation of results which may be very persuasive but undermine their accuracy. Through careful validation and verification, CFD predictions can be made considerably more reliable [3].

In fluid dynamics, the motion of fluids is described by systems of partial differential equations (PDEs); however, these equations do not have exact analytical solutions in their general form [4]. Through discretization of the partial differential equation system across a definite group of increments or cells represented by grid points organized or distributed throughout the computational domain or the physical geometry of interest, an approximate solution for the physical problem can be obtained.

Generally, all 'solutions' predicted by CFD contain a degree of error due to the approximations utilised. The modelling errors are defined as the difference between actual flow behaviour and the solution of the numerical model used to approximate the flow behaviour. It is essential to understand that even with low discretization error, the precise solution of the mathematical model may be physically not accurate if the actual flow performance deviates from the modelling assumptions [5]. Engineering knowhow must be utilized to decide which models are the most suitable for any chosen case in terms of accuracy and computational speed. Hence, efficient use of CFD as an engineering tool requires determining the balance between the solution precision and computational cost. Approximate solutions obtained by numerical methods inherently contain both discretization and modelling errors.

Discretization errors are defined as the difference between the exact solution of the system of PDEs and the exact solution of the set of algebraic equations obtained by discretizing the PDEs over a domain. Enhancing the discretization precision of a CFD simulation often demands the usage of higher order methods (which could be unstable numerically), or an increase in the number of grid-cells within the computational domain. The effect of increasing the number of cells and grid refinement results in improving the

approximation solution of the PDE system, interpreted as reducing the discretization error to the minimum range depending on the order of precision required by the user. Increasing the number of grid cells, however, usually incurs appreciable computational cost concerning the time needed to resolve the discretized equations, and often demands considerable computational facilities. For complex engineering problems, this increase in cost may be infeasible due to budget constraints.

Use of computational fluid dynamics (CFD) as an integral part of engineering design and analysis has emerged as a powerful simulation tool for understanding the different types of flow in two-phase applications. Therefore, over the last two decades different approaches have developed and have been continuously improved for the numerical modelling of multi-phase fluid systems. Generally, for multi-phase problems such as liquid jet breakup, droplet formation and spray formation, accurate simulation of the complex deforming liquid–gas interfaces and atomization processes are highly desirable. Therefore, particular categories of numerical techniques are required for flows such as these with high dynamic and deforming interfaces. Since the location of the interface between the two phases is not known but rather, is part of the solution, these categories of problems are particularly complicated. Moreover, the physical phenomena often include multi-phase flow with high value of velocity, viscosity and density ratios. Therefore, deriving a solution of the governing partial differential equations (PDEs) is considered very complex.

Various numerical techniques are modified to overcome the multi-phase complication in fluid flow. Those techniques can be classified based on the type of the flow modelling (Lagrangian, Eulerian, or mixed), the type of interface modelling (tracking or capturing), flow interface coupling (segregated or integrated), or the type of spatial discretization (meshless, finite difference, finite volume, finite element [FE], or others) [6]. In general, normal numerical techniques such as the finite element (FE), finite volume (FV), and finite difference (FD) methods utilized for standard flows can also be utilized to simulate interface flows. However, non-traditional techniques are required to treat the unknown location of the fluid interfaces.

For the interface solvers, there are two major classifications. The first class belongs to methods encompassing mesh deformation and mesh movement, whereas the second class utilizes a uniform fixed grid. The cell points change position according to the local flow features for the former method involving the moving mesh. When all the cells shift and change position as in most problems, the method is considered “Lagrangian”, in other respects, it is considered “Lagrangian–Eulerian” approximation.

Generally, the Eulerian approach represents an overall picture of the flow field compared to the Lagrangian approach where particles are tracked in the solution. Eulerian techniques can be subdivided into mixed- and separated-fluid approaches. The mixed-fluid approach assumes that the continuous and the dispersed phases are in local kinetic and thermal equilibrium, i.e. the relative velocities and temperatures between the two phases are small in comparison to predicted variations in the overall flow field [7]. The mixed-fluid approximation identifies only the volume/mass portions of the dispersed and continuous phases in a mixed volume. For the reason that the velocities and temperatures of both phases are now considered to be demonstrated by single values, the mixed-fluid approximation has also been named “locally homogeneous flow”, “single-fluid scalar transport approach” and “modified-density approach” [7]. A single set of momentum equations for the flow mixture will be used as a result of a mixed-fluid treatment. The mixed-fluid set of equations is substantially a two-way coupled system. Thus the gas-phase physics depends on the liquid-phase physics and vice versa.

Both of the continuous and dispersed phases include two separate, but intermixed, continua as proposed in the separated-fluid approximation. Consequently, two sets of momentum equations are required, one for the continuous phase and one for the dispersed phase. As two sets of partial differential equations are required, this approximation is also known as the “two-fluid” method. The two sets of equations is also applied to the energy equation. Therefore, compared to the mixed-fluid treatment, the relative temperatures and velocities of the two phases are not necessarily zero. Finally, it should be stated that the separated-fluid approach significantly increases the overall computational cost as a result of solving two sets of governing equations [7].

The Lagrangian or Eulerian description encompasses methods such as: (i) finite element, or FE-based Lagrangian, (ii) interface fitting (or boundary-fitted coordinates), and (iii) boundary integral (BI) methods. The cell points close to the interface basically work as marker points in the aforementioned methods. Therefore, these techniques tackle those problems with accompanying complexities related to high surface distortions, interface surface breaking, and merging. The grids are adapted and adjusted on the interface line and moved in time, utilizing some iterative methods for the convergence of the conservation equations as shown in Figure 1.3(a) for the interface fitting methods. These methods are generally serviceable for interface lines with low distortions, and are considered complicated if utilized in flows with high interface distortions. To avoid computational failures, grid recreations are important when grid points and elements are meant to be highly deformed. This can make the interface fitting scheme and other moving mesh techniques very complex and ineffectual.

The fixed grid methods are the most generally utilized schemes because they have been the more successful systems in flows with high interface distortion. Either Eulerian or the combined Lagrangian–Eulerian framework can be involved in fixed grid methods. A supplementary indicator is proposed in order to mark the interface as required for the fixed grid method. The fixed grid methods are featured based on the kind of indicator utilized and are split into three major classifications: interface capturing as shown in Figure. 1.3(b), interface tracking as shown in Figure. 1.3(c), and compound interface capturing–interface tracking techniques [6]. Types, examples of the classifications, and details about the interface capturing and tracking methods are discussed in Chapter Two.

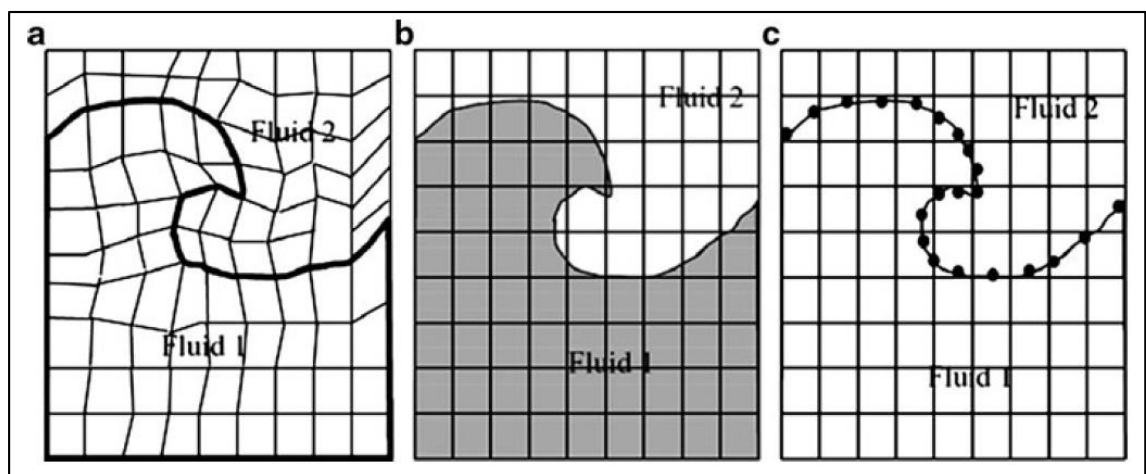


Figure 1.3 Different interfacial flow solution methodologies: (a) interface fitting, (b) interface capturing, and (c) interface tracking. (adopted from [6])

Generally, corresponding to its Lagrangian nature, the interface tracking methods show a higher and more precise depiction of the free surface, whereas the interface capturing methods can deal with complicated interfacial domains more easily. The location of the interface line in the interface tracking methods is delineated in a direct way, either by presenting a height function which explicitly defines the interface line location, or by assigning a group of marker points placed on the interface line. Nevertheless, as the location and curvature of the free surface is specified, enforcement of the surface tension force is direct and simple in the interface tracking schemes. The restriction of these methods, in contrast to interface capturing methods, is their inability to transact naturally with foldable or breaking up interfaces [6].

In computational fluid dynamics (CFD) and for turbulence in two-phase systems, it is not necessary or desirable to resolve all details pertaining to turbulent fluctuations.

This can be resolved as in direct numerical simulation (DNS) and large eddy simulation (LES) approaches with the micro level evolution of the interfaces separating the multiple phases that coexist simultaneously in the fluid flow.

Currently, greater attention is focused on promoting and advancing towards the next step of the numerical models' application and improving the resolution of turbulent multiphase flows by direct numerical simulation (DNS). Usage of DNS involves solving multiphase flows at sufficiently high spatial and temporal resolutions, which is controlled by the accessibility of the computational resources. Through usage appropriate tracking methods (tracking methods defined in Chapter 2), and involving high adequate resolution in the computational domain, it is possible in DNS to present the exact location of the interfaces separating different phases that coexist within the flow, between the smallest and the largest turbulent eddies [1].

On the other hand, when using the large eddy simulation (LES) based approach, the structure of the turbulent flow is viewed as the distinguished transmit of large and small scale movements, as represented in Figure 1.4. On the basis LES the small-scale movement is modelled, while the scale of the fundamental computational mesh will consequently allow direct simulation of the large-scale movement. Since the large-scale movement is mostly much more dynamic and by far the most efficient means of transmission of the conserved properties than the small-scale ones, such an LES approach handles the large eddies accurately but estimates the smaller scales, which is a convenient approach for turbulent modelling [1]. Large computational resources are required for DNS in comparison to the multi-fluid model. On the other hand, the computational requirement for LES are intensive but still not as costly when compared to DNS.

It is worth commenting that the multiphase DNS approach used in this research within OpenFOAM utilizes the one-fluid formalism, comparable to the principle of the mixed-fluid approximation, where the methods are based on resolving a single set of transport equations (Navier-Stokes equations) for the entire computational domain, and the various phases are addressed as a single fluid with inconstant material and physical properties. Differences in the material and physical properties across the interface line are addressed by advecting a phase indicator function so that the heat and mass transfer between multiple phases can be accounted for.

The physics of gas-liquid two-phase flows generally is important in liquid jet disintegration and spray processes which have not been well understood due to the multiple time and length scales involved and the coupling between the two phases, which

is always difficult to investigate using simple experimental and/or computational approaches. To enhance our understanding of the jet disintegration, a particular high speed laminar jet burst phenomena is investigated numerically under different inflow velocity profile conditions and different liquid and ambient viscosity. Although high speed laminar jet burst phenomena has been investigated previously, the mechanisms behind disintegration of a laminar jet in a violent fashion are still not fully understood or certain. It is of interest to ascertain the influence of the liquid jet burst phenomena on the flammability of accidental releases of high-flashpoint liquids, a topic of considerable interest for hazardous area classification [8]. This is one motivation for the current research study.

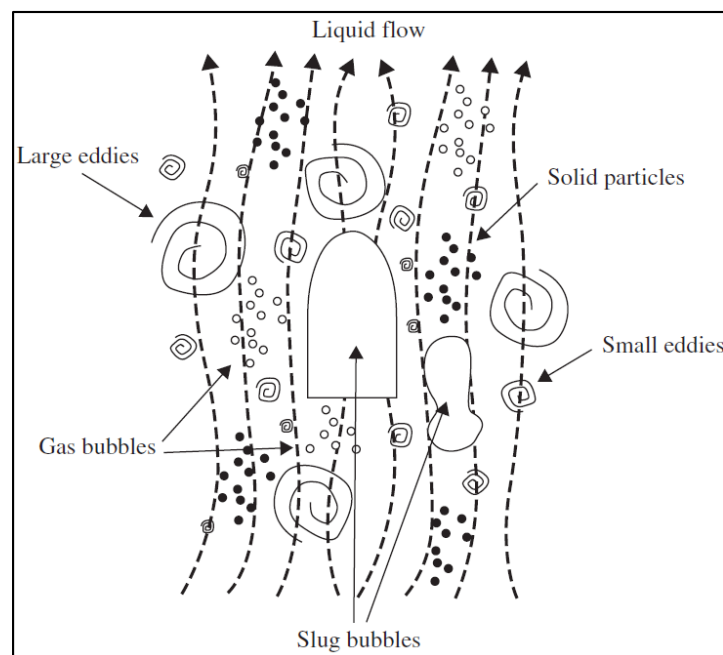


Figure 1.4 A schematic representation of a gas-liquid-solid turbulent flow. (adapted from [1])

Accurate and controlled deposition of droplets on solid surfaces or a solid surface with another pre-located sessile droplet is a principle in many industrial processes or applications such as solid inkjet printing, micro-fabrication, rapid prototyping, and electronic packaging. Although considerable progress has been made in recent coalescence studies on non-porous substrates, there are still a few issues to be addressed in the context of its wider applications. There is no information in literature on the trend of final footprint location between two consecutively deposited drops which is limited in the variety of impact speed at different lateral displacement and liquid physical

properties. Different impact speeds can generate very different results depending on the wettability and the contact angle hysteresis of the substrate system and liquid parameters. Furthermore, the trend of coalescence of two droplets to the final footprint location at variant speed has not been explored. Nevertheless, the effect of liquid physical properties such as viscosity and surface tension at any impact speed can affect the coalescence mechanism and subsequent final footprint. This provided the motivation to undertake the study on the second research problem, which is to provide an insight into the influence of the relevant parameters on the final composite footprint location. Better understanding this process would help designers in relevant applications to avoid any undesirable breakup which could happen in printing, for example by predicting the exact or final composite footprint at equilibrium condition.

1.3 Aim and Objectives

Hence, the aim of this research is using an appropriate numerical solver, to develop numerical models for and analyse the influence of initial conditions on the numerical solution of two complex, two-phase problems, namely the impact of a falling droplet on an initially stationary droplet resting on a solid surface and secondly the so-called jet-burst phenomena associated with the breakup of a laminar liquid jet exiting from a circular orifice.

This aim is achieved by delivering the following objectives:

- 1/ Appraise the efficacy of three-dimensional, parallel-computing Navier-Stokes solvers using the OpenFOAM computational framework for solving complex 2-phase fluid dynamic problems.
- 2/ Using OpenFOAM, develop a numerical model for solving the two-droplet problem of a falling droplet impacting upon an initially stationary droplet resting upon a solid surface (referred to in this thesis as the 'two-droplet' problem).
- 3/ Utilise the two-droplet computational model to assess the influence of various initial conditions upon the characteristics of the droplets final stationary state.
- 4/ Using OpenFOAM, develop a numerical model capable of identifying the 'jet burst' phenomena associated with a laminar jet release from a simple orifice.
- 5/ Using the 'jet burst' model, undertake parametric numerical experiments to determine the sensitivity of the phenomena to various initial conditions including inlet conditions and fluid properties.

1.4 Thesis Structure

In Chapter 2, an overview of the state of the art concerning numerical models used to approximate solutions to multi-phase engineering problems is provided. Then an overview of the current physical background concerning interaction of two droplets on solid substrate. This is followed by the liquid jet breakup and its categorization from the relevant specific literature is provided. In Chapter 3, first, the OpenFoam tutorial structure including case files and different dictionaries is comprehensively introduced. Then, several multi-phase test cases with validation where possible are presented and discussed; finally the two aforementioned problems of industrial relevance are selected for more thorough analysis as the focus of the thesis.

In Chapter 4, the dynamics of two droplets' interactions on a horizontal substrate (falling droplet impact on a sessile or stationary droplet) and the final footprint composite location are investigated numerically using the OpenFOAM and sclsVOFFoam solver. From numerical investigations, the results are discussed in terms of the effect of impact speed, the droplets' lateral separation, and different liquid viscosity and surface tension. Non-dimensional reduction is discussed. In Chapter 5, the mechanisms giving rise to the bursting of a liquid jet under laminar jet flow conditions are investigated. The analysis includes the influence of different inlet boundary condition velocity profiles ranging from fully parabolic to semi-turbulent to completely flat (top hat) profile on the jet-burst phenomena. Finally, at a constant liquid jet Reynolds number $Re=2200$, the influence of liquid viscosity and different ambient physical properties have been implemented to investigate their effect on laminar jet burst phenomena. The results are compared with the default burst jet throughout discussion of the parametric numerical studies undertaken. Conclusions and priorities for further work are presented in Chapter 6.

Chapter 2 Literature Review

2.1 Introduction

The main purpose of this chapter is to provide an overview of the current status of numerical models used in solving multi-phase fluid dynamic problems posed in this thesis, and also to review corresponding experimental benchmark studies. First, the problem of two droplets impacting upon solid substrate is considered. Secondly, the process of unobstructed liquid jet breakup and its categorization is appraised. A summary of the factors that are currently known to have an influence on these two problems is provided at the end of this chapter, providing a basis on which to build the later research studies.

2.2 Development of Numerical Models for Free-surface Flows

In the majority of multi-phase cases, the free boundary is approximated due to the computational resource required to obtain the full solution of the three dimensional Navier-Stokes equations. Within the categorisation of static meshes, where the interface is captured at a static grid, or dynamic meshes, where the grid moves or is generated wherever interface exists, various methods to estimate the free-boundary can be distinguished. The existed techniques for the calculation or prediction of free boundaries or fluid interfaces can be categorized into two groups or different methodologies [9], specifically:

- Surface methods (surface fitting).
- Volume methods (surface capturing).

Figure 2.1 presents these two methods schematically. For surface methods, the interface is predicted and tracked explicitly either by identifying it with special indicator points or by connecting (supplementing) it to the mesh surface which is forced to move with the free boundary. For volume methods, the fluids on both sides of the boundary line are indicated by either mass less particles or an 'indicator' function. Further details describing both methods are now presented.

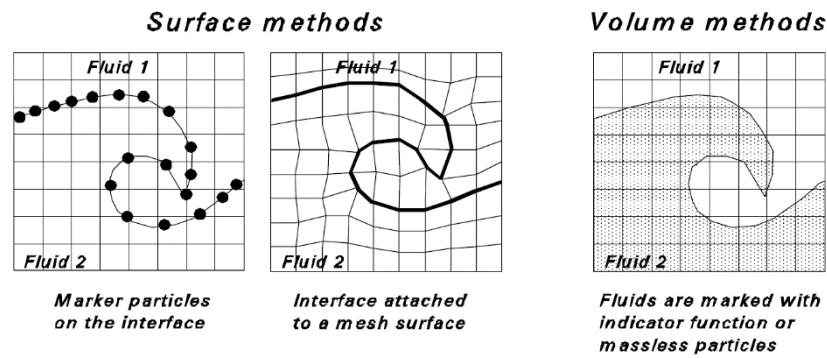


Figure 2.1 Different methods of representing the interface (adapted from O. Ubbink [9])

2.2.1 Surface Methods

In this method, the free boundary may be tracked by identifying it with particular locations, known as marker points, enabling the boundary surface to be traced by a polynomial function interpolating between these marker points. Also, the free boundary could be tracked by following its position as known by a sharp interface [9]. The stability and accuracy of the interpolation method are crucial factors affecting the precision of the surface tracking methods. There are several methods of marking the interface:

- (a) Particles on interface method: Daly 1969 (as reported by O. Ubbink [9]) presented this method to track the free boundary explicitly using a group of mass fewer particles as attached marker points on a static grid, as illustrated in Figure 2.2. As the distance between particle and points increases, the boundary interface becomes less well represented.
- (b) Height function method: A 'height function' that reduces the space between the point on the boundary interface for a certain reference plane or line has been introduced by Nichols et.al. (as reported by O. Ubbink [9]) illustrated schematically in Figure 2.3(a). In the case of closed boundaries, such as bubbles or droplets, a representative point should be defined within the enclosed body. In this case, the distance function would be represented by the radius at different angular positions, as shown in Figure 2.3(b). The main problem with this method is that each coordinate of the reference plane is associated with only one interface value. Hence, for some physical processes such as droplet breakup or overturning and breaking of liquid jets, the reference coordinates is multi-valued and cannot be predicted as shown in Figure 2.3.

(c) Level Set method (LS): Osher and Sethian [10] proposed this method which introduces a continuous function over the entire computational domain. According to Sussman et al. [11], the level set function value at each point is presented as the minimum space between that point and the boundary line. The level set function is negative in one fluid phase and positive in the other. The zero level represents the exact position of the free boundary surface. The level set function propagates with the fluids as a scalar property, which is resolved by solving a scalar convection equation.

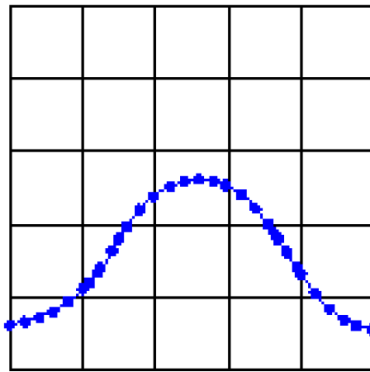


Figure 2.2 Particles on the interface surface method. (adapted from O. Ubbink [9])

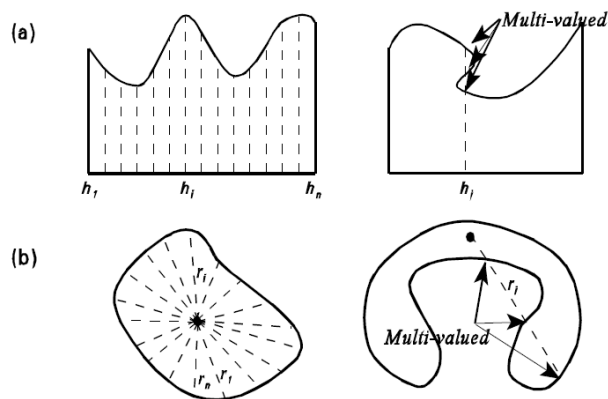


Figure 2.3 Schematic representation of height functions for (a) open interfaces (b) closed interfaces. (adapted from Sussman et al. [11])

It has been found that the interface remains at the zero level [9]. However, the initial distance function does not remain fixed. This is because the level set function keeps its initial minimum and maximum values, and remains the same throughout the calculation, causing a steep gradient in the level set function when the free boundary

surface changes its location and shape in time. This is seen as a disadvantage of the level set method. Figure 2.4(a) shows two droplets moving towards each other, represented by the level set contours. Figure 2.4(b) shows the two droplets just before merging, as represented by level set contours. The initial maximum level set value between the two boundaries still prevails and forms a sheet preventing any penetration or natural merging between the two interfaces. Therefore, Sussman et al. [11] recommended reinitializing the distance function after each time step, as shown in Figure 2.4(c).

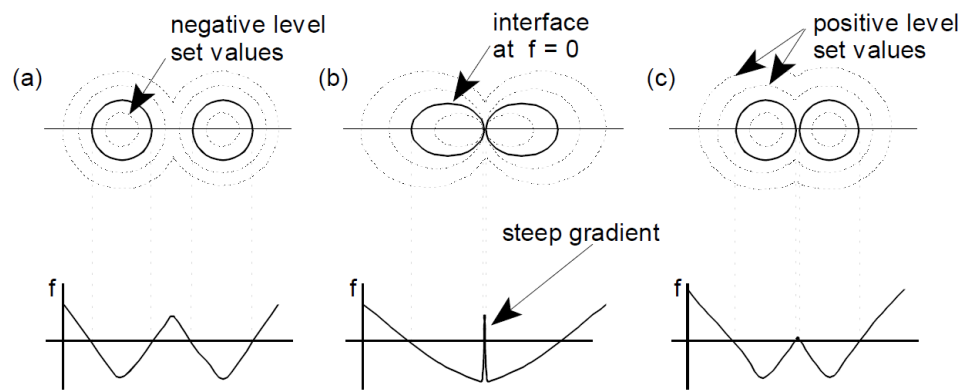


Figure 2.4 Two droplets contours of the level set function: (a) initial configuration, (b) just before merging with no corrections (c) just before merging with corrections. (adapted from Sussman et al. [11])

2.2.2 Volume Methods

In this method, the interface between two fluids is defined by the boundary of volume by assigning the whole computational domain using an indicator function or marking it by mass-less particles. The surface tension force calculation has historically been problematic in volume methods. Brackbill et al. [12] have partially overcome this by proposing the continuum surface force (CSF) model. The continuum surface force (CSF) model has been executed successfully in different volume based methods. Nevertheless, in contrast with the surface method, the volume method does not provide an accurate estimate of the location of the interface boundary. Therefore, the solution algorithm needs to be modified to include special treatment to capture a reasonable definition of the interface [9]. In this regard, two important techniques have been developed:

(a) Particles on fluid method: In this method, which is also well known as the Marker-And-Cell (MAC) method of Harlow and Welch [13], mass-less marker particles moving with the fluid are used to determine the location of the fluid within a fixed mesh. The marker particles (wherever existed on the mesh) are considered to occupy fluid. Whilst the rest of the grid cells with no marker particles is considered empty. Consequently, the interface boundary will be indicated by those grids cells with a marker particles neighbouring at least one empty grid, as shown in Figure 2.5(a). This method is considered successful because the fluid volumes have been tracked as indicated by the markers, instead of tracking the surface directly and hence, the surfaces are simply the boundaries of the volumes.

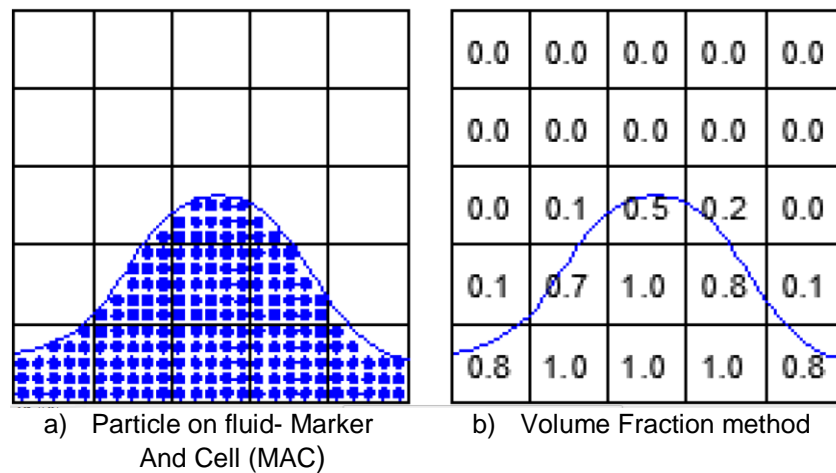


Figure 2.5 Volume methods to treat the interface. (adapted from O. Ubbink [9])

(b) Volume fraction methods or volume of fluid (VOF): Volume fraction methods are one of the most popular methods to handle free fluid interfaces. Volume fraction methods are well known by the volume fraction function, use a scalar indicator function confined between one (all liquid) to zero (no liquid, all gas) to characterize the existence of fluid phase, as illustrated in Figure 2.5(b). Compared to the MAC method, volume fraction methods have some advantageous features in terms of computational cost and variable storage. In volume fraction methods, just one value is saved (the value of the fraction of volume), instead of the coordinates of the marked particles method.

The best advantage of the VOF method is that the volume owned by one fluid will not be owned by the other, and so this method always maintains continuity. Regarding the fluid properties (i.e. density, viscosity), they are a weighted (averaged) for both phases properties across the interface. The surface tension property is calculated in the VOF using the continuum surface force (CSF) proposed by Brackbill et al. [12]. Numerical simulation with large cell sizes was considered the major drawback of the VOF technique. This is crucial in applications such as formation of small bubbles or droplets, smaller than the minimum grid size. Consequently, missing capturing some parts of the fluid could result in artificial outcomes hence limiting the method. Numerous techniques have been developed to improve the accuracy of VOF models over the years, all falling into the classification of line techniques, the donor-acceptor formulation and higher order differencing schemes [9]. Comprehensive theoretical and technical details could be found in the abundant literature discussing these approaches but not in this review because they are not in the scope of the current work.

The VOF model was deployed in OpenFOAM™ by O. Ubbink [9] within the *interFoam* solver. There are many numerical applications of *interFoam* concerning air/water and air with other types of liquid interactions in the literature. As an example, an experimental and numerical studies of horizontal jets below a free surface were performed by Trujillo et al. [14]. The *interFoam* solver has been evaluated in self-aeration regions of stepped spillways in a study conducted by Lobosco et al. [15]. In these two previous studies, the researchers accurately produced predictions of air entrapped inside the liquid enabling comparison with experimental studies. However, the researchers have discovered some problems with the air-entrainment simulations. Another study conducted by Deshpande et al. [16] evaluated the *interFoam* solver by investigating horizontal jets submerging into a pool and compared it with experimental data. The average vertical velocity profile was compared with experiments and compared satisfactorily. Regarding the surface curvature, the solver showed accuracy even in modest grid resolution; excellent mass conservation; and acceptable advection errors. On the other hand, as expected the numerical simulations did not produce the smallest elements of droplets or bubbles due to mesh limitations.

2.3 Impact of Two Droplets on Substrate

Accurate and controlled deposition of droplets on solid surfaces or solid surface with another pre-located sessile droplet is a principle in many of industrial processes or applications such as inkjet printing (Snyder et al. cited in Li [17]), micro-fabrication [18], rapid prototyping [19], and electronic packaging [20]. These applications demand highly accurate placement of molten wax, polymer or metal droplets on substrates to construct images, three-dimensional parts or electrically conductive lines. It is desirable that droplets in touch meant to overlap and coalesce during the impact process to bypass disconnects in the fashions being structured. However, surface tension-driven phenomena that take place when contacted droplets touch can shift droplets location after they have been placed on the substrate and such unexpected movements may make lines disconnect or vary in their thickness.

An important issue in understanding the effects of coalescence on the aforementioned applications is understanding coalescence between two drops on a solid substrate. For a falling drop coalescing with a stationary sessile drop, Li et al. [17] studied experimentally the evolution of the spread length of the two coalesced drops along their original centres. Two coalescing water droplets and two coalescing ethylene glycol droplets on a smooth steel substrate were conducted in their experiments. The volume of the two drops was kept equal whilst their centre-to-centre spacing was varied in both experiments. From their results and observations, researchers established correlations to define the deposition conditions for forming continuous or discontinuous lines.

Using experiments and numerical simulations, Casterjón-Pita et al. [21] investigated a falling drop coalescing with a stagnant sessile drop. Two coalescing glycerol/water drops deposited with TiO_2 particles distributed on a polymethyl methacrylate (Perspex, Lucite) substrate have been considered in their investigation. A parameter such as drop spacing was varied through the study, whereas the drop volume was kept invariant in all experiments. In order to characterize the internal flows and the development of the spread length throughout the coalescence process, the lattice Boltzmann method was used, including a model for contact angle hysteresis. Technically, a high speed camera, particle image velocimetry, and image processing algorithms have been applied to generate the experimental results.

Comparison of experimental and numerical results showed qualitative agreement but quantitative discrepancies. Therefore, in order to validate computational methods, good experimental visualization and quantification of flows both internally and externally

have been recommended. Nevertheless, fluid velocities predicted numerically explained some of the issues in modifying experimental systems capable of illustrating comprehensively the internal dynamics of droplets in the early stages of impact and coalescence. They have remarked that pinning of the contact line (droplet edges where the liquid, the solid and the gas are all intersecting at one point) has a considerable influence on the format of the final footprint of the composite droplet. It is recommended that the issue of contact line pinning requires further investigation for more than one model of contact angle hysteresis (The difference between the advancing (maximal contact angle) and receding (minimal contact angle) while droplet moving or sliding on an inclined surface).

An experimental investigation was undertaken by Yang et al. [22] to study the coalescence between two consecutively printed drops of a colloidal mixture of carboxylate-modified polystyrene fluorescent beads in deionized (DI) water on cleaned glass substrates. The formation process of the composite drop was studied by changing the droplets' centres lateral separation and the deposition time difference between the two drops. Time difference of deposition was changed from 0.2 s (well after the first drop had equilibrated on the surface) until 0.9 s (about 60% of the time for the initial drop to evaporate). Measurement of particle density in the dried composite drop was gained experimentally by utilizing a fluorescent microscope. During their experiments, the initial volumes of the two coalescing drops were kept constant and the drop spacing were varied. During the whole evaporation and coalescence process, their results showed that the contact line of the original drop stayed pinned during the entire evaporation and coalescence operation. For the water-air interface of the merged drop, smaller relaxation time was achieved than that of a single drop on a dry surface, and circularity of the composite drop reduces with increased drop spacing for all jetting delays. Furthermore, they identified that the pendent particles in the second drop flow toward the first drop due to inertia and capillary action, which results in more fluid deposited on the first drop side, a phenomenon referred to as a drawback.

Boley et al. [23] examined how coalescence affects the uniformity of printed pairs of drops and printed lines as well as the functional performance of printed lines of a Pd (Pd ink) based ink on Silicon and oxidized Silicon substrates. The ink used in their study has a relatively high vapour pressure (high liquid evaporation rate) at room temperature and the ink/substrate used exhibits small contact angle hysteresis. The deposition time of the second drop varied throughout the entire life time of the first drop. The Ink migration

after the coalescence process for two consecutively adjacent drops was tracked experimentally. Optical uniformity and functional performance of the printed lines was compared based on the two-drop experiments at different drop spacing and time of deposition. The most important factors of the liquid migration between the two droplets are considered to be variations in surface energy and de-pinning the contact line. To enable characterisation of solute mass between two adjacently printed drops, image analysis measurements provided results for validation. In order to boost the film consistency and modify functional performance, their results recommended that the ink migration resulting from 'Marangoni flow' (mass transfer between two fluids due to surface tension gradient) should be minimized by avoiding coalescence of adjacently deposited drops.

Casterjón-Pita et al. [24] investigated experimentally and numerically the coalescence and mixing of a sessile and an impacting liquid droplet on a solid surface in terms of lateral separation and droplet speed. They used two droplet generators to produce differently coloured droplets. Two high-speed imaging systems are utilized to investigate the impact and coalescence of the droplets in colour from a side view with a simultaneous gray-scale view from below. Experimental measurements were employed to calibrate a contact angle hysteresis model within a lattice Boltzmann framework. Their results showed that no detectable mixing occurs during impact and coalescence of similar-sized droplets, but when the sessile droplet is sufficiently larger than the impacting droplet, vortex ring generation can be observed. They showed how a gradient of wettability on the substrate can potentially enhance mixing.

2.4 Liquid Jet Breakup and Burst Phenomena

The generation of liquid jets or liquid particles has been used in many processes we use in everyday life or utilise in industry. These include applications such as using shower heads to produce coarse jets and sprays to generating very fine fuel sprays for power generation in the automotive or aerospace industries. Because of the importance of liquid jet and their wide applications, liquid jet has received considerable research attention over the past century or more. Despite this considerable body of work, liquid jet disintegration is still not fully understood.

Early attempts used to describe jet breakup adopted surface wave instability (Kelvin-Helmholtz instability that occurs when there is velocity shear in a single continuous fluid, or where there is a velocity difference across the interface between two

fluids) theories which approximate the surface of the jet as a sinusoidal wave. However, experimental observations of irregular surface waves invalidated wave instabilities approximations as noticed in the laminar jet [25]. Based on those early studies, researchers built up aerodynamic-based theories for the problem. It was concluded that the short waves generated at the liquid's surface as the jet leaves the nozzle grow because the gaseous ambience amplifies the growth of such waves. This is confirmed in many experimental studies published in the literature which supported this mechanism of jet breakup. However, because of the large number of variables that affect a jet's behaviour, and due to the added complexity of interaction of these variables with each other, any theories adopted may fail to explain the phenomenon of jet breakup successfully. Jet breakup and associated features are controlled by aerodynamic effects, liquid and gas fluid properties, and the condition of the flow at the nozzle exit, including turbulence and the velocity profiles [25]. Many of these factors were ignored in early studies which is likely to have resulted in limitations of many early published results.

The jet breakup mechanism may be explained in relatively simple terms; liquid emerges from the nozzle, aerodynamic forces and turbulence forces effects on the jet, leading to break the jet up at some location downstream from the nozzle exit due to the disturbances and instabilities generated from the liquid gas interaction. The ambient gaseous atmosphere gradually infiltrates the jet core as the distance downstream from the nozzle exit increases, transforming the jet into a mixture of liquid and air. In some cases, liquid jets may not fully breakup or disintegrate and in these situations, the jet is said to have a large breakup length L_B . To add further complication, if the free jet impacts upon a solid surface, then this is termed an impinging jet, which again is utilised in various industrial processes usually to improve breakup of liquid jets. Remarkably, notwithstanding the considerable literature concerning liquid jet formation and breakup, relatively few numerical studies have been undertaken. Based on previous studies concerning the various liquid jet phenomena, one can summarise that the jet disintegration is affected by the following parameters [26]:

- Aerodynamic forces.
- Hydrodynamic forces (i.e., viscous and capillary forces).
- External mechanical disturbances (such as supply line pressure vibration, electromechanical disturbances).
- Nozzle internal flow (e.g., flow separation, cavitation).
- Jet nozzle profile at the nozzle exit.

- Turbulence at the nozzle exit.
- Thermodynamic and physical states of both the liquid and the ambient gas.
- Superheating, electrostatic charge, acoustical excitation, and chemical reaction [27].

The influence of some of these processes upon liquid jet breakup were investigated in the early study by Lee and Spencer [28]. Using photomicrography, Lee and Spencer summarised that if the disintegration forces do not dominate over the liquid's physical forces (viscosity and capillary), breakup length increases with increasing distance outward from nozzle exit. Increasing ambient density enhanced the degree of liquid jet disintegration. The degree of disintegration increases with increasing jet velocity and turbulence, and decreases with increasing liquid physical properties of viscosity and surface tension. The degree of disintegration decreases with increasing nozzle exit diameter.

Many other researchers tried to investigate the effect of different parameters on liquid jet disintegration. The earliest study was undertaken by Lord Rayleigh in 1878 [29] who focused only on breakup of a low-speed inviscid jet. Lord Rayleigh hypothesized that the surface tension presented in the capillary forces related to the breakup length of the liquid jet. Rayleigh explained that the hydrodynamic instabilities induced led to breakup of the liquid jet. However, he did not take into consideration viscous, high speed, and turbulent liquid jets which may be influenced by aerodynamic forces.

In a later study, Schweitzer [30] concluded that Rayleigh's analysis did not appear to be valid for pressure-injection flows. Many authors extended the work of Rayleigh most notably, Weber [31] and Haenlein [32]. They used different designs of nozzles in terms different aspect ratios and different types of liquid's viscosities. Weber expanded Rayleigh's work to consider the influence of air resistance on the breakup of jets into drops, and found that air friction shortens the optimum wavelength for drop formation. For zero relative velocity, he showed that the value of λ_{opt} is 4.44 D, which is close to the value of 4.51 D anticipated by Rayleigh for this case. For a relative velocity of 15 m/s, Weber showed that λ_{opt} decreases to 2.8D and the drop diameter becomes 1.6 D. Therefore, the effect of relative velocity between the liquid jet and the ambient air is to shorten the optimum wavelength for jet disintegration, which in turn results in a smaller drop size. Weber also studied the influence of liquid viscosity on jet breakup, noting that the influence of an increase in liquid viscosity is to increase the optimum wavelength for jet breakup.

From these and many other investigations, researchers found that at higher jet velocities, disintegration occurs by corrugating of the jet as shown in Figure 2.6(b). This manner of generating drops is generally associated with a reduction of the effect of surface tension and increase in the influence of aerodynamic forces. The expression “sinuous” is predominating utilized to represent the jet in this mode. At higher velocities, the disintegration procedure is promoted by the influence of proportional movement between the surface of the jet and the surrounding ambient gas. This aerodynamic interaction gives rise to non-uniformity in the formerly smooth liquid surface. Consequently, the ruffled jet surface becomes more disturbed by amplifying instabilities which ultimately disconnect themselves from the liquid surface, as illustrated in Figure 2.6(c). Ligaments are established which thereafter disintegrate into drops. The diameter of the ligaments reduce as the jet velocity increases, and when they breakdown, smaller droplets are established, in agreement with Rayleigh’s theory [26].

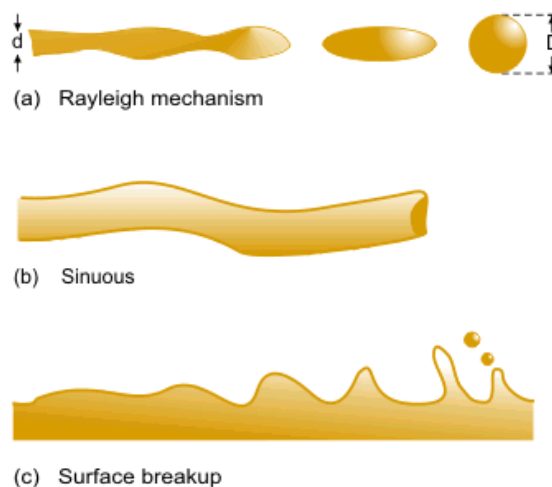


Figure 2.6 The various fashions of jet disintegration

2.4.1 Overview of Liquid Jet Breakup Regimes and Relevant Literature

The aforementioned observations suggest that a liquid jet possibly disintegrates in different breakup modes or regimes. The forces that govern jet disintegration throughout a specified set of circumstances, illustrate these regimes of disintegration. From the considerable literature concerning liquid jet breakup, two main methods are identified to categorize liquid jet breakup. They are the jet stability curve and the Ohnesorge’s categorization. The best way to differentiate between laminar and turbulent jets is by using the jet stability criterion, which will be discussed later in this Chapter.

Many researchers have utilised the Ohnesorge number ($Oh = \mu/\sqrt{\rho\sigma D}$) as a non-dimensional parameter to enable classification. Using the Ohnesorge number (Oh), the disintegration modes distinguishing between regimes are: Rayleigh's regime, the first wind-induced regime, the second wind-induced regime and the atomization regime (for example, see [25], [33], [34]). Different disintegration regimes are presented graphically on the log-log graph of the Ohnesorge number (Oh) versus Reynolds number (Re) as shown in Figure 2.7.

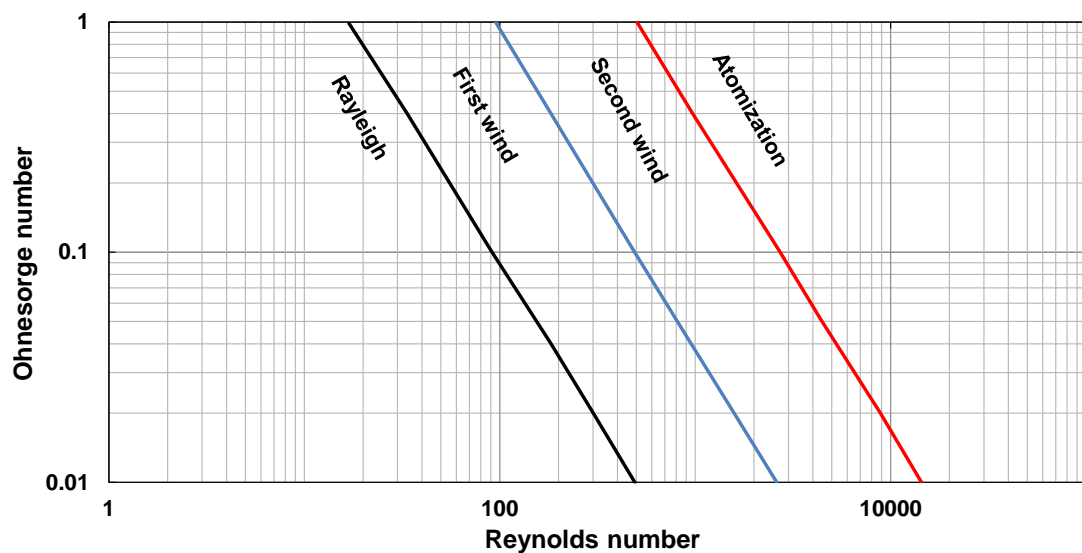


Figure 2.7 Breakup regimes dependence on liquid Reynolds number (Re_L) and Ohnesorge number (Oh)

The main features that characterize Rayleigh breakup (also called varicose regime) are low injection speed or low jet velocity, small liquid jet surface disruption and aerodynamic effect as shown in Figure 2.6(a). In this regime, surface tension forces induce axisymmetric disturbances along the jet surface which considered the main reason for jet breakup. Furthermore, the liquid jet disintegration occurs when the wavelength of the disturbed liquid surface approaches the magnitude of the jet radius [26]. When velocities increase beyond those associated with Rayleigh breakup, the liquid jet disturbances change from being varicose to sinuous. This an indication of the start of the first wind-induced breakup regime (which is also called the sinuous regime) as represented in Figure 2.6(b). For a moderate Reynolds number ($Re = \rho DU/\mu$), the jet assumes a wavy shape due to sinusoidal oscillation about its axis. Due to the aerodynamic forces, these oscillations magnify leading to disintegration of the jet into

drops relative to the size of the jet diameter (according to Rietz and Bracco as cited in [26]).

With a further increase in liquid jet velocity, the liquid-ambient interaction become considerably strongly, as noticed in the second wind-induced breakup regime presented in Figure 2.6(c). Here, the liquid jet surface becomes more disrupted and ruffled comparing to the first wind regime due to the aerodynamic effects. These strong disturbances are translated into breaking up the jet just a few diameters downstream from the nozzle exit, with drops smaller than the jet diameter in size [26]. The atomization regime is associated with a very sharp increase in the dynamic nature of the liquid jet disintegration. The main feature of atomization is that (i) jet disintegration occurs almost immediately after leaving the nozzle exit and (ii) the droplets diameter's much smaller than the nozzle or jet orifice diameter. There is a considerable body of research focused on atomization in literature, with many studies investigating the effect of influential factors on atomization quality, such as cavitation generated inside nozzle as observed by Tamaki [35], [36]. One can utilise Ohnesorge's classification to determine the influence properties of both the liquid and ambient gas. The Weber number for liquid We_L and gas We_G , respectively has also been utilised to generalise the influence of fluid properties. Table 2.1 represented by M. Birouk and N. Lekic [26] summarise from the literature the criteria for evaluating the mode of liquid jet breakup based on Weber number ($We = \rho DU^2 / \sigma$).

Table 2.1 Ohnesorge's classification based on values of liquid and ambient properties. (adapted from M. Birouk and N. Lekic [26])

Regime	Range
Rayleigh's Regime	$We_L > 8$
First wind-Induced regime	$0.4 < We_G < 13$
Second wind-Induced regime	$13 < We_G < 40$
Atomization regime	$We_G \sim > 40$

Another non-dimensional method used for categorizing jet disintegration mechanisms is based on the graph of the breakup length L_B versus jet velocity U ; this graph is well known as the jet stability curve. Similarly to Ohnesorge's classification illustrated earlier, the curve shown in Figure 2.8 categorizes different liquid jet

disintegration mechanisms based on the dominant forces acting on the jet during the breakup under a given set of conditions. The jet stability curve is divided into the following five regions [37].

- Dripping region
- Laminar region
- Transition region
- Turbulent region
- Fully developed spray region

In the first two regimes, dripping and laminar, flow is featured by surface forces and inertial forces. The dripping region is not discussed thoroughly here because it takes place at low flow rates where liquid simply drips out of the tube without any noticeable 'jet' length [38], as the process is dominated by inertia. Linear increase of breakup length (L_B) is associated with increasing velocity (U) of the jet incorporated in the laminar region. In the transient region, it is generally well known that aerodynamic forces become more dominant, changing the breakup characteristics from dilational (varicose) to sinuous, although those forces are not considered to be the main reason behind the breakup in this mode. Many researchers remark that liquid turbulence is an essential parameter causing the jet breakup. As we can notice from Figure 2.8, in the transition region where the flow changes from laminar to turbulent, the jet breakup length (L_B) decreases with jet velocity (U).

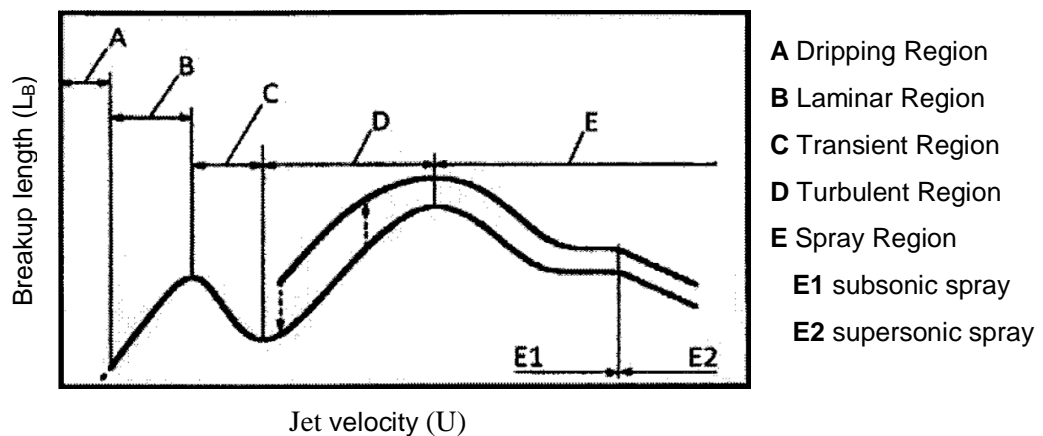


Figure 2.8 Stability curve. (adapted from M. Birouk and N. Lekic [26])

The aerodynamic forces represented in the shear forces at the jet surface become more considerable than liquid turbulence in the fully turbulent region, which

interpreted as an increase in the breakup length (L_B) and the liquid turbulence with the jet velocity [26]. Another issue worth noting is that the transition from semi-turbulent to the turbulent region corresponds to a discontinuous increase in the breakup length [38]. R. P. Grant and S. Middleman [38] debated that under such conditions, the flow has been stabilized at the fully turbulent case. As another example of this, Rupe [39] in his experimental study observed that high speed laminar liquids jet tend to breakup faster than fully developed turbulent ones. Rupe attributes this observation to the regression of the fully developed laminar profile.

Because of the many contradictions reported from data within the atomization region, some aspects concerning characteristic features have been the subject of much debate and dispute. The early studies declared that the breakup length decreases until it vanishes when the liquid jet velocity increases. However, this has not always been the case, as for example McCarthy and Molloy (as cited in [26]) revealed that a small coherent length of the jet exists after the nozzle exit, regardless of further increase in jet velocity. These observations were also recognised by Hiroyasu et al. and Arai et al. (as cited in [26]). Nevertheless, Wu et al. [40] found the appearance of a turbulent regime near the nozzle exit within the atomization regime. In general, from the aforementioned studies, researchers appear to converge to a consensus that the jet always retains a finite breakup length that is the jet never seems to breakup precisely at the nozzle exit.

According to Weber's theory (illustrated the laminar regime thoroughly), for any given liquid and nozzle, based on what is called the capillary phenomena, jet instabilities appear naturally from the liquid's surface tension, and the breakup length is a function of jet velocity. In his theory, Weber integrated parameters such as the liquid's physical properties (viscosity, surface tension, and density) and nozzle exit diameter. But he did not, however, take into consideration other factors affecting the breakup phenomena, such as cavitation, general turbulence, and velocity profile relaxation. At the peak of the instability curve between B and C regimes as in Figure 2.8, Weber's theory no longer holds, because of the transition from a fully laminar jet to semi-turbulent flow jet. This is related to the fact that the transition region is distinguished by supplementary factors that contribute to the jet breakup such as the ambient parameters. Decay in taking ambient forces in consideration was one of the factors considered the cause of ineligibility of Weber's theory.

Several attempts have been made by Weber and other researchers to incorporate the influence of atmospheric parameters. These improved theories were

unable to predict the configuration of the local maximum and the laminar to the semi-turbulent transition of stability curve [38], [41]. No study has to date proposed an exact Reynolds number (Re) or even jet velocity (U) at which transition happens from laminar to turbulent jet breakup. McCarthy and Molloy (as cited in [26]) supported their experimental study with an empirical correlation to predict a critical Reynolds number as:

$$Re = 3.25(Oh)^{-0.28} \quad \text{Equation 2.1}$$

This correlation applied to a fully developed laminar liquid jet only.

2.4.2 Previous Numerical Studies of Liquid Jet Breakup

To date there has been very few numerical studies considering jet disintegration and breakup. The most important problem is that there is still no solid theoretical framework to support a numerical model [42]. However, there are a few studies in the last decade which do undertake numerical analyses of the liquid jet breakup problem.

In 2003, Pan and Suga [43] undertook a numerical investigation using a Navier-Stokes solver for incompressible flow of the ejection of a water jet into air. The level set method (LS) and (CSF) model of surface tension was applied using sufficiently high mesh resolution to capture the interface between the liquid and the surrounding gas during the evolution of the jet. Cavitation was not considered in their study for water jet exit Reynolds number (Re) = 1000-15000, with Weber number (We) = 44 - 4994 and a liquid/gas density ratio equal to 816. The Rayleigh instabilities observed develop naturally from a smoothly injected jet and breakup at low Reynolds number where the dynamic features and breakup length agreed well with experimental validation data. Their 2-D simulation obviously presented the transition from laminar instability to turbulent breakup leading to spray formation. They also investigated the effect of surface tension and the initial fluctuation at the jet exit. The characteristics of the spray and the breakup modes are correlated with the disturbance introduced at the jet exit.

In 2006, Wolfgang et al. [44] solved the Navier-Stokes equations for incompressible flows with free surfaces using a 3-D (CFD) free surface program (FS3D) to simulate the physical phenomena leading to the breakup of liquid jets. No turbulence model was required as direct numerical simulation (DNS) was employed. The presence of the liquid and the gaseous phase was represented by the Volume-of-Fluid (VOF) method. The size of the computational domain adopted depends on the specific spreading rate of the jet. The domain is decomposed using the communication library

(MPI) of parallelization to run it on multi-processor systems. Inflow boundary conditions are set at constant velocity at inlet, while slip used for the velocity at all other sides (walls) to avoid the influence of solid walls on the jet.

Their liquid jet breakup numerical results were validated with pre-existing experimental results for a 3-D simulation of an n-pentane liquid jet ejected into air at atmospheric pressure. Good qualitative agreement for Rayleigh breakup and jet characteristics for a low speed jet and a higher velocity jet were found between the numerical and experimental results. A comparison between 2-D and 3-D liquid jet simulations conducted in this study concluded that breakup phenomena of circular liquid jets can only be simulated with full 3-D simulation models which require higher computational resources. It is concluded that direct numerical simulation (DNS) is able to provide the basic results of the breakup process of the liquid jets with high reliability when compared with experimental data.

In 2007, Ishimoto et al. [45] used a new type of integrated simulation technique to investigate numerically the 3-D structure of liquid atomization behaviour through and beyond the exit of a cylindrical nozzle. Two immiscible fluids and unsteady flow with fixed value of viscosity and surface tension represented the flow within their numerical framework. The Navier–Stokes and continuity equations govern the flow which is assumed to be a Newtonian, incompressible, laminar and isothermal. The fluid flow equations for the high-speed atomizing nozzle are solved using a LES-VOF model in conjunction with the CSF model coded within the OpenFOAM finite volume CFD framework. The integrated model is used to obtain atomization process details such as atomization length, liquid core shape, droplet distribution sizes, and spray angle and droplet velocity profiles which are difficult to perform experimentally. Throughout analysis, they concentrated on the successive disintegration of a liquid column, liquid film formation, and droplets generation of the jet in downstream of the nozzle exit.

From their results, they conclude that a combination of nozzle-generated turbulence and relaxation of the velocity profile as the liquid exits from the orifice, characterizes the initial wave growth and disturbances of the liquid column surface. The author's comment that as the velocity at the centre of the liquid column is greater than the speed at the jet circumference, the vortices tend to approach the liquid-gas interface. They also found that the hydrodynamic shear stress between the jet core and the circumference region of the liquid column increases because of a sharp increase in the velocity gradient in those regions. The combined effect of both these vortices and shear

stress initiates a Kelvin-Helmholtz instability at the interface. Due to the Kelvin-Helmholtz instability, rapid growth and development is exhibited by waves initiated on the surface of the liquid column jet. This is translated progressively into the atomization process which leads to its breakup into liquid ligaments, liquid film and droplets until it completely disintegrates. From analysing the atomized droplet diameter distribution, it was found that the atomization of relatively large size homogeneous droplets is promoted as droplets reached the area of the domain exit whereas coalescence of small droplets occurs with the homogeneous atomization downstream of the nozzle throat.

Lebas et al. [46] in 2009 conducted numerical simulations for liquid atomization and primary breakup modelling of a high Weber and Reynolds liquid jet using direct numerical simulation (DNS). This study included coupling (LS/VOF/ghost) fluid methods to capture the free surface with validation against the primary break-up of a liquid jet. Combining these methods was intended to take advantage of the benefits each strategy, i.e. keep a fine description of interface properties with the LS method and to minimize the mass loss by using the VOF. Ghost cells are determined on each side of the interface and appropriate schemes are applied for variable (density and viscosity) jumps in the Ghost fluid method. The model is tested on experimental data, and liquid and vapour penetrations show good agreement when they are compared to experiments in diesel atomization.

In 2010, Shinjo and Umemura [47] undertook a direct numerical simulation (DNS) study with fine grid resolution, and reported on the physical processes occurring in high-speed sprays, focusing on the dynamics of the primary atomization of liquid injection. Their study focussed on the physical mechanisms of liquid jet injection to droplet formation. Liquid jet injection into a quiescent high-pressure air ambient environment is considered. The injection nozzle is a round and straight (non-converging) nozzle with diameter of 0.1 mm. Three injection velocities of 30 m/s, 50 m/s, and 100 m/s are appraised, thus the liquid Weber number based on the nozzle radius ranges from 1270 to 14100. The initial jet shape is set as a liquid cylinder of the length of the nozzle diameter.

Nozzle disturbances were not considered in this study. The velocity profile of the injected liquid is set flat so that, instability should be naturally excited by air-liquid interaction. The computational domain is a rectangular region and an equidistant Cartesian grid system is used for each case in this simulation. As the bulk Weber number increases, the number of grid points required increases because the local structures are

likely to become smaller. The computation was parallelized on the JSS (JAXA Supercomputer System, (Japan) to accelerate the calculation process. They concluded that ligament formation occurs both from the 'mushroom-tip' edge and the liquid core surface of the jet. They noticed that the formation phenomenon is very complicated, but that shear from local vortices plays an important part. Shear from vortices affects the dynamics and multiple ligaments are usually created at one time.

In 2011, Srinivasan et al. [48] investigated numerically the effect of various finite velocity modulations imposed on an undisturbed cylindrical liquid jet ejected into a static ambience. Sinusoidal velocity fluctuations of finite frequency and amplitude are imposed at the liquid jet inlet and the resulting liquid jet surface deformation is captured using a volume of fluid (VOF) based interface tracking method for computing liquid jet behaviour. Throughout the numerical computations performed, variation of several simulation parameters are investigated, including of the mean liquid jet velocity, modulation amplitude and frequency grouped together using a set of non-dimensional parameters. Incompressible, multiphase solvers which employ the finite volume method to present the governing equation and VOF methodology is implemented within the framework of OpenFoam (C++) libraries. Parallel computations of the standard message passing interface (MPI) are used. The simulation domain extends 2.4×1.6 mm in the axial and radial directions respectively. A mesh (200,000 cells in total) is employed, appropriately refined in flow regions of importance such as just downstream of the nozzle exit and the core regions of the primary flow. The default value of the inlet velocity (uniform velocity profile distribution) is set to 20 m/s. The liquid used in the study is ethanol and water, while the ambience is assumed to be filled with air. The Reynolds number (Re) of the issuing jets with ethanol and water lie close to the laminar/turbulent threshold value and hence no turbulence modelling has been included.

Their computations results efficiently captured the different flow structures generated by the evolving modulated liquid jet including of several non-linear dynamics such as the growth of surface waves, ligament interaction with shear vortices and its subsequent thinning process. Their simulations identified the deterministic behaviour of modulated liquid jets which predicted the liquid disintegration modes under given set of non-dimensional parameters.

In 2011, Delteil et al. [49] studied the growth of a capillary instability and of the breakup of a jet using a one-fluid model to describe the two-phase flow motion using 3-D simulations and a VOF approach to capture the interface, and the Continuum Surface

Force (CSF) or as known by Brackbill surface tension model. Through simulating the growth of a capillary instability, and comparing results to those predicted by the Rayleigh theory for capillary instabilities, the numerical methods were validated. Based on the experimental work, the jet breakup in the three-dimensional simulations of two immiscible fluids, water as an injected liquid and carbon dioxide as an ambient gas. A Poiseuille velocity profile is imposed at the inlet boundary with a mean velocity (U) with a Reynolds number of (Re) = 321 for the laminar regime prevalent in the experimental injection device. From their results, it was shown that the simulation predicted the breakup length accurately and the droplet size evidenced experimentally in literature.

In 2016, Grosshans et al. [50], studied numerically the characteristics of the primary disintegration of a liquid jet at Diesel injection conditions and different fluid properties (liquid-gas viscosity and density ratio). The turbulent flow field is simulated by performing a LES, the VOF method is used and Continuum Surface Force (CSF) model used to solve the surface forces at the interface. Cuboid domains utilized to solve the liquid jet flow with a Dirichlet condition was applied to the inlet. The velocity components and scalars at the outlet correspond to a zero-gradient condition. At the walls, no-slip and zero-gradient were imposed for the velocity components and the scalars, respectively. The inlet nozzle was assumed to have a diameter of (D) = 10^{-4} m. A uniform velocity profile considered at the nozzle orifice of (U) = 500 m/s. To assess the sensitivity of the atomization on the fluid properties, simulations with liquid-gas density ratios of 10, 20 and 30 were performed. Other conditions are namely $Re = 15000$, $We = 10000$ and $\mu_l / \mu_g = 3.42$. Liquid jets with the properties $\mu_l / \mu_g = 1, 2$ and 7 were simulated, while ρ_l / ρ_g was set to 10.

Their modelling predicted the features of the droplet size distributions, indicating that the disintegration of the liquid core into ligaments and droplets due to aerodynamic instabilities has been captured sufficiently well. The influence of varying the liquid-gas density ratio between 10 and 30 on the aerodynamic breakup was proved to be low. On the other hand, the reduction of the liquid-gas viscosity ratio from 7 to 1 resulted in smaller droplets and consequently larger dispersion.

2.4.3 Liquid Burst Phenomena

An understanding of the stability of liquid jets is of importance in many industrial applications like fuel combustion chambers, liquid extraction columns and for hazard quantification of accidental liquid fuel releases. In practice, such applications usually involve relatively complex flow geometries and liquids exhibiting shear and or time

dependent rheological properties. An understanding of such complicated systems can be best achieved by obtaining information under conditions more amenable to quantitative analysis. The stability of the jet column appears to be influenced by the liquid properties, the flow evolution within the nozzle, and the ambient conditions of the medium into which the jet is injected. Varying these parameters can lead to transitions between several instabilities that radically change the characteristics and evolution of the jet. Although jet stability has been the object of numerous experimental and theoretical studies, it should be recognised that the problem of jet disintegration is by no means complete. It is true to say that some details of the overall stability process have been resolved to a reasonable degree of completion. However, there are many missing links in the description of the series of events commencing in a liquid reservoir and terminating with the complete breakup of a free jet and spray formation.

At complete understanding of all the liquid jet processes leading to breakup has yet to be achieved. For example, no well-defined breakup length data may be found in the literature, nor full explanation of a liquid jet in the transient laminar-to-turbulent region. Here we introduce a specific, rarely reported phenomenon where liquid jet suddenly bursts in a very violent fashion. Hooper (as cited by R. P. Grant and S. Middleman [38]) describes a bursting breakup as “a form of breakup hitherto unknown”. In this case, the jet consisted of a smooth glassy section followed by a region of complete and sudden atomization. He believed that the decay of the laminar parabolic profile to a flat profile supplied kinetic energy which was converted into an internal pressure to burst the jet. To substantiate the theory, the breakup length of the bursting jet was reported to be independent of ambient pressures between 1 and 0.031 atm. Rupe [39] commented that the decay of the parabolic velocity profile results in the creation of a radial pressure gradient which produces a radial velocity component. He believed that this radial velocity was primarily responsible for the disintegration of the jet.

Rupe [39] observed that high velocity laminar jets may actually be more unstable and break up in an extremely violent fashion, indeed much sooner than fully developed turbulent jets. This is totally contrary to previous information in the literature. Rupe [39] believed this behaviour to be related to the decay of the fully developed laminar profile. As in the preceding cases, except for the work of Hooper (as cited by R. P. Grant and S. Middleman [38]) no breakup length data is available in the literature to either support or refute these hypotheses regarding the role of velocity profile development. Focusing on the role of the inlet velocity profile on the jet instability and liquid jet burst phenomena,

some researchers have explored using different types of liquid and jet configurations. Rupe [39] suggested that the jet instability may be affected by the relaxation of the velocity profile that takes place once the liquid exits the nozzle and is no longer constrained by its wall.

Ritz and Bracco [51] conducted an experimental study to evaluate several proposed mechanisms as possible catalysts of jet atomization and concluded that rearrangement of the velocity profile (velocity relaxation) from parabolic to uniform upon the emergence of the jet from the nozzle. They concluded that relaxation could be, at least in part, a contributing factor or a probable reason for instability and atomization. In their theoretical study, Leib and Goldstein [52] were the first researchers to present a theoretical analysis of the instability of an inviscid liquid jet with a velocity profile that could be varied from parabolic to uniform. Their results showed that the instability of an inviscid liquid jet issued into a vacuum is more pronounced for a uniform profile than a parabolic one and concluded that the uniform profile is the most unstable. Debler and Yu [53] followed with an experimental study and generated results which agreed with the data of Leib and Goldstein [42] considering only a liquid jet injected into a vacuum.

Ibrahim [54] developed a mathematical solution for the problem of instability of an inviscid liquid sheet with a parabolic velocity profile ejected from a nozzle into an inviscid gas. A comparison of the instability of a sheet of a parabolic velocity profile to one of a uniform velocity profile is performed in order to deduce the effects of velocity profile relaxation on instability. Ibrahim claims that the more the velocity profile was parabolic (higher difference between the maximum velocity along the centreline of the sheet and a lower velocity at the liquid-gas interface for a constant mean flow), the lower aerodynamic instability produced for a parabolic velocity profile case showing more stability due to the reduction in the liquid-gas relative velocity across the interface. On the other hand, uniform velocity profile produces the maximum relative velocity at the liquid-gas interface for the same mean flow, and is the most unstable. Therefore, any non-uniformity of the velocity profile (e.g., parabolic) would lead to a reduction in instability, and his results were in agreement with the findings of Leib and Goldstein [52] for the instability of a liquid jet injected into a vacuum. However, Leib and Goldstein [52] found the instability of the liquid jet to persist throughout the variation from homogeneous to fully developed parabolic profile (Hagen-Poiseuille profile). Ibrahim [54] found that instability of the liquid sheet becomes unpredictable as the velocity profile approaches Poiseuille profile.

Physically, it is well understood from the work of Squire [55] that, unlike a liquid jet, a liquid sheet can't be destabilized without the aerodynamic interaction with the surrounding fluid. Therefore, we should take notice that liquid jets and sheets develop different fluid mechanics or instability, and extrapolation of results obtained for liquid jets to predict the behaviour of liquid sheets is inappropriate. Ibrahim and Marshall [56] used a theoretical study to investigate the instability of an inviscid liquid jet emanated into an inviscid gas. The effect of velocity relaxation on the jet instability and breakup was considered because it affects the location of the resultant liquid drops and subsequently combustion performance in combustion systems. Their results showed that the most unstable jet occurred when the inlet velocity was uniform and closer to flat profile. Increasing aerodynamic instability produces an unstable jet because of higher relative velocity at the liquid-gas interface as a consequence of a uniform velocity profile. In the same study [56], the effect of a surrounding gaseous environment was investigated on the jet in the atomization regime, by changing Weber number and gas-to-liquid density ratio. They found that increasing Weber number results increased instability, since in this regime the aerodynamic forces are dominant. It was also found that increasing gas-to-liquid density ratio promoted jet instability, findings that agree very well with Lin and Ibrahim [57], who concluded that the higher gas density boosts the destabilization of the jet by increased aerodynamic forces [53].

Pan and Suga [58] utilised a Navier-Stokes solver for an incompressible fluid coupled with the level set method and the (CSF) surface tension force model, to simulate the breakup phenomena of laminar liquid jets at Rayleigh, first wind and second wind regimes into still air and liquid/gas density ratios are in the order of 10^3 . 3-D simulation using a DNS model was able to capture the dynamic process of primary breakup and the simulated breakup length which was validated against an experimental correlation. Their numerical results suggested that the conventional classification of the jet breakup regimes using Weber numbers is not always successful, particularly for low Weber numbers, whereas the classification by the Ohnesorge chart is generally reasonable. Nevertheless, in their study, Pan and Suga [58] replicated the high laminar liquid jet burst phenomena, observed experimentally by Rupe [39]. For such characteristics of a jet with a high liquid viscosity and a high Weber number, and which is usually represented by a relatively high Ohnesorge number, Pan and Suga [58] confirmed that rearrangement of the axial velocity profile and surface shear induce initial large-scale vortex structures inside the liquid core. They conclude that such a large-scale vortex motion is amplified

by surface instability, and when its energy is accumulated enough to overcome inertial and surface tension forces, the jet starts to break up from the inside in a violent fashion.

2.5 Summary

This chapter discussed the relevant literature (experimentally and numerically) to impact and coalescence of two droplets on a solid substrate and the liquid jet under different conditions. For each subject, a summary has been drawn as followed:

- (a) Two droplets interaction on a substrate: Although some recent progress has been made concerning coalescence studies of two droplets on solid substrates, there are still many issues to be addressed in the context of its broad range of applications. One notable omission from the literature is the investigation location of the final footprint trends between two consecutively deposited drops which depend upon the variety of impact speed at different lateral displacement. Different impact speed can generate very different results depending on the wettability and the contact angle hysteresis of the substrate system and liquid parameters. Hence, this study studies and analyses the composite trend location for different impact velocities, centre-to-centre displacements and different physical liquid parameters.
- (b) Breakup of the liquid jet: Investigation the principles of the liquid jet breakup have received a lot of attention and research mostly focused either theoretically or experimentally. Notwithstanding the considerable literature concerning aspects of liquid jet breakup, not many relevant numerical studies have been devoted to the subject. Based on previous, one can summarise that jet disintegration is affected by many parameters, and hence, the understanding of liquid jet disintegration is still is not complete. The high speed laminar burst jet is considered an interesting jet breakup phenomena because of its violent burst at a laminar Reynolds number ($Re=2200$), and its applicability to some practical industrial problems. For example, despite the fact that its Reynolds number (Re) =2200 is not within the range utilized in the combustion industry for propulsion or power generation, such phenomena are potentially crucial in developing understanding and quantitative techniques for accidental releases of high-flashpoint liquid fuels and the subsequent combustion hazard. Moreover, the effect of different parameters and the inflow inlet condition on the high speed laminar burst jet has not been

studied previously. Therefore, developing upon the previous research of Pan and Suga [58], a 3-D (DNS) numerical study will be conducted to improve understanding of the mechanism and controlling parameters for liquid jet bursts. Given the findings of previous work, different velocity profile ranging from fully developed laminar to turbulent has been implemented in this study to investigate the effect of inlet conditions on the burst phenomena. Furthermore, physical fluid properties such as the ambient gas viscosity as well as liquid viscosity have been varied a part of the current investigation for the fully developed laminar jet to explore the conditions pertaining to the jet burst phenomena.

Chapter 3 Validation of OpenFOAM Solvers for Free Boundary Two-phase Problems

3.1 Introduction

In this chapter, an overview of the OpenFOAM 2.1.1 tutorial structure is presented briefly with reference to cases files and different dictionaries. The rationale for choosing a specific solver over others is discussed. Validation of several benchmark two-phase model predictions is presented and discussed. The selected solver is utilised throughout the remainder of the thesis without further justification. Two of the seven two-phase research problems studied are prioritised for research investigations through the remainder of this thesis.

3.2 General OpenFOAM Cases Structure

OpenFOAM 2.1.1 is provided with a set of example cases for different types of physical problems, for example, multi-phase, heat transfer, incompressible flow, etc. These are located in `$FOAM_TUTORIALS` and are divided into folders depending on the particular solver used in the example. Usually, when a user wishes to run a case, the user will copy the source case most suitable for the case the user wants to run and subsequently will make the modifications that are needed. An OpenFOAM simulation is defined by a specific file structure which holds the setup information, mesh definition and solution files. The standard OpenFOAM file structure for a serial (single processor) case is shown in Figure 3.1. Each simulation directory holds three sub-directories: the system, constant, and 'time' directories (named using the physical time step or iteration step identifier). All the details regarding the main directory of OpenFOAM case including the sub-directories and the different dictionaries definitions and its functions can be thoroughly illustrated in OpenFOAM user guide [59].

3.3 Choosing an OpenFOAM Solver

The OpenFOAM library is a comprehensive combination of code, written in the (C++) programming language. It is designed to run on UNIX or UNIX-like systems such as Linux. A large number of CFD solvers are provided with this library solving for a broad range of parameters using a wide selection of methods. As they are all based on the same fundamental code, they have many features in common. All use a three-

dimensional unstructured finite-volume mesh and have the same selection of matrix solvers and discretisation schemes. Different solvers and discretisation schemes can be selected on a per-operation basis at run-time. Additionally, all of the models can take advantage of message passing interface (MPI) parallelism, allowing single models to be run over multiple cores, processors and machines without modification [60].

The simulations considered within this thesis consider two-phase problems. Thus, the chosen solver has to be capable of addressing these kinds of problems. Of several modelling methods and algorithms that are devoted to simulating multiphase flows, the *interFoam* solver as named and based within OpenFOAM as a free and open source has received more credit in dealing with multi-phase applications and physical cases as reported in recent research publications [14], [16], [61].

3.3.1 *interFoam* Solver

InterFoam (formerly known as *rasinterFoam* in early versions of OpenFOAM) is a two-phase solver for incompressible, isothermal and immiscible fluids using a VOF (volume-of-fluid) based interface capturing approach. The *interFoam* solver has previously been used for problems similar to those which are attempted in this thesis. The *interFoam* solver was used for some validation cases of the work of this thesis as will be explained later in this chapter. The *interFoam* solver has not been used for the results in cases of two droplets interactions on substrate and liquid jet burst phenomena described later in this and subsequent chapters.

The “*interFoam*” solver has several additional features in common with other multi-phase and OpenFOAM solvers in general. (OpenCFD Ltd. 2008):

- The solvers use the Volume-of-Fluid (VOF) method for calculating interfacial flows, taking into account surface tension.
- They are dynamic, solving for unsteady, time-varying flows.
- They use the PISO algorithm for solving the Navier-Stokes equations.
- Either Reynolds-Averaged Stress (RAS) or Large Eddy Simulation (LES) turbulence formulation may be used, or turbulent flow may be omitted and direct numerical simulation (DNS) used for either laminar or turbulent problems.

3.3.2 *sclsVOFFoam* Solver

As discussed earlier in Section 2.1 (Chapter two), the volume of fluid (VOF) method conserves mass. However, as discussed above, maintaining a sharp and

accurate interface with VOF methods is far from trivial. Level set methods (LS) offer a more accurate representation of the interfacial quantities such as interfacial normal and curvature. This is desirable especially in two-phase flows involving surface tension effects. In order to use the advantages of both VOF and LS, coupling both methods to be implemented within *interFoam* in OpenFOAM was highly desirable.

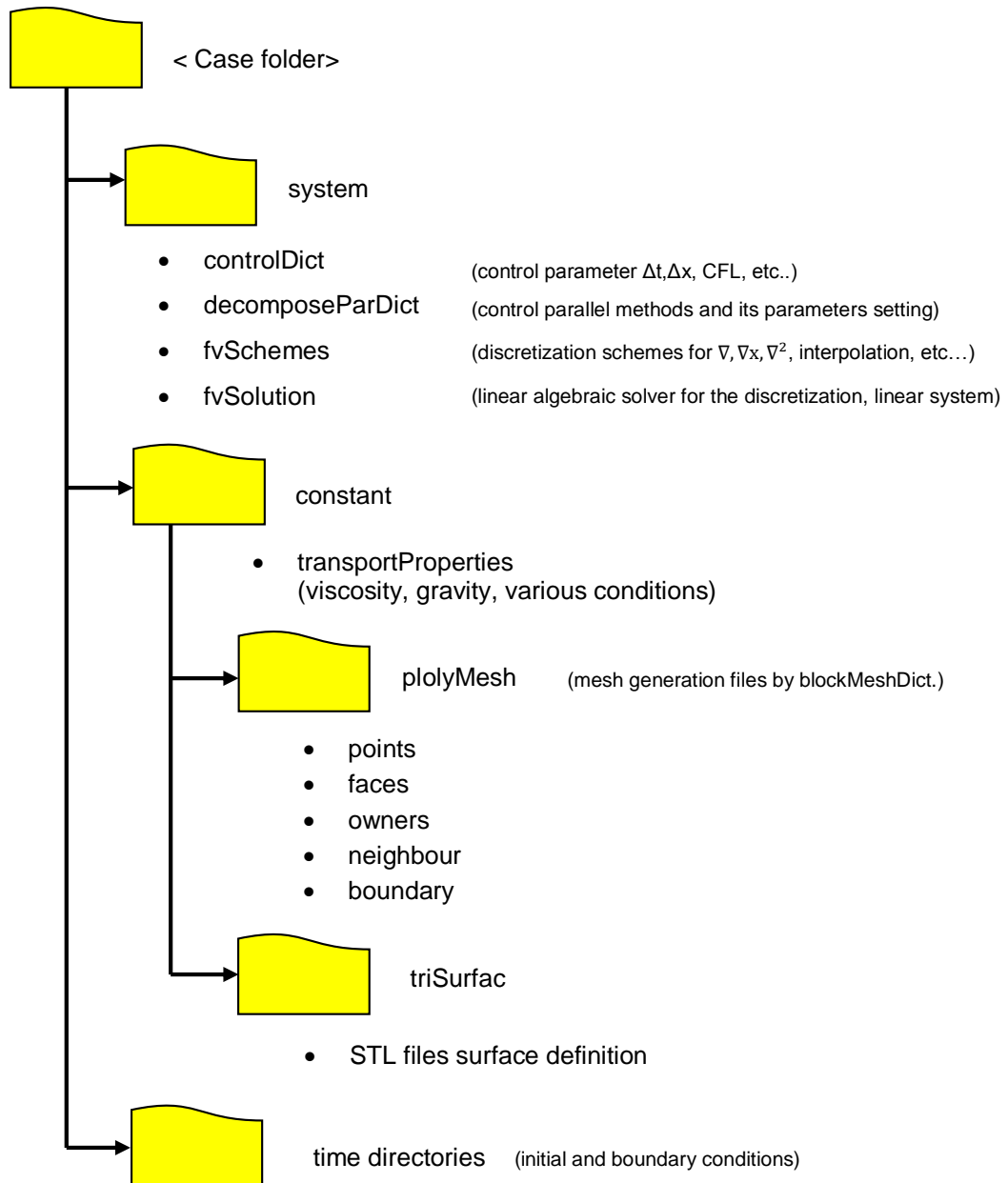


Figure 3.1 OpenFOAM case directory structure

Amongst the different methods of coupling VOF and LS, a simple coupled Volume of Fluid (VOF) with Level Set (LS) method (S-CLSVOF) for improved surface tension implementation, proposed and utilised by Albadawi et al. [62], was used in this study. The Albadawi et al. [62] coupling method was implemented and appraised by Yamamoto [63] within the *interFoam* solver in OpenFOAM, and named *sclsVOFFoam*, which stands for simple coupling level set volume of fluid foam. The Yamamoto solver *sclsVOFFoam* is published online.

After compiling the solver, several additions need to be applied to enable its effective use:

1. Edit constant directory inside the case and open transportProperties dictionary file.
2. Add the following comments in transportProperties:

```
deltaX    deltaX [ 0 0 0 0 0 0 ] 0.00010;
```

where the *deltaX* value (number in bold in the above syntax line) is the cell width near the interface position and depends on mesh resolution or the grid spacing used in any case.

3. Access to 0 folder (initial condition) inside the case directory and add the psi (Level-Set function) file. This file should be generated based on the alpha1 file for the VOF initial condition and can be simply copied from alpha file by using the command:

```
cp -r 0/alpha1 0/psi
```

After undertaking all of the steps above correctly, *sclsVOFFoam* will be ready for execution.

3.3.3 Governing Equations and Numerical Algorithm Used in OpenFOAM

The governing equations for the two isothermal, incompressible, and immiscible fluids include the continuity, momentum, and interface capturing advection equations based on the VOF method:

$$\nabla \cdot \vec{u} = 0 \quad \text{Equation 3.1}$$

$$\rho \left(\frac{\partial \vec{u}}{\partial t} + \vec{u} \cdot \nabla \vec{u} \right) = -\nabla p + \nabla \cdot (2\mu S) + \vec{F}_\sigma \quad \text{Equation 3.2}$$

$$\frac{\partial \alpha}{\partial t} + \nabla \cdot (\vec{u} \alpha) + \nabla \cdot [\vec{u}_r \alpha (1 - \alpha)] = 0 \quad \text{Equation 3.3}$$

where ρ is the fluid density, \vec{u} the fluid velocity vector, S the viscous stress tensor defined as: $S_{ij} = (\partial_i u_j + \partial_j u_i)/2$, μ is the dynamic viscosity, p is the scalar pressure, and \vec{F}_σ is the volumetric surface tension force. The volume fraction function α is used to represent a space mesh cell whether it is occupied by the dispersed phase or the continuous phase. When the cells are full of the dispersed phase, the value of α is unity; the continuous phase corresponds to zero; when the mesh cells contain both the dispersed phase and the continuous phase, the value of α is between 0 and 1, which denotes an interface between the two phases. \vec{u}_r is the liquid–gas relative velocity, compressing the interface to improve its resolution [64]. The term $\alpha(1-\alpha)$ limits the effect of \vec{u}_r to the interface region. Moreover, \vec{u}_r can be calculated as follows:

$$\vec{u}_r = \min(C_\alpha |\vec{u}|, \max(|\vec{u}|)) \frac{\nabla \alpha}{|\nabla \alpha|} \quad \text{Equation 3.4}$$

where the default value of unity for C_α is used; however, a larger value of C_α can enhance the compression of the interface. The boundedness of α function is guaranteed by a special solver named Multidimensional Universal Limiter for Explicit Solution (MULES) [65].

A new level set field is introduced to provide a more precise interface reconstruction. The LS field is estimated from the VOF field in each time step by $\psi = (2\alpha - 1)\Gamma$, where Γ is a small non-dimensional number whose value depends on the mesh step size (Δx) at the interface of the two fluids, and is defined as $\Gamma = 0.75\Delta x$ [62]. The LS field is corrected by solving the re-initialization equation:

$$\frac{\partial \psi}{\partial t} = \text{sign}(\psi)(1 - |\nabla \psi|) \quad \text{Equation 3.5}$$

where ψ should satisfy $|\nabla \psi| = 1$ by its definition. The normal vector of the interface $\hat{n} = \nabla \psi / |\nabla \psi|$ can be accurately determined due to the continuity of the LS function. Thus, more precise and smoother interface curvature $\kappa = \nabla \cdot \hat{n}$ can be obtained. Based on the Continuum Surface Force (CSF) model [12], the volumetric surface tension force can be calculated as:

$$\vec{F}_\sigma = \sigma \kappa(\psi) \delta(\psi) \nabla \psi \quad \text{Equation 3.6}$$

where σ is the surface tension coefficient, and δ is the Dirac function used to limit the influence of the surface tension to a narrow region around the interface. The function of δ is centred at the interface and takes a zero value in both fluids:

$$\delta(\psi) = \begin{cases} 0 & |\psi| > \varepsilon \\ \frac{1}{2\varepsilon} \left(1 + \cos\left(\frac{\pi\psi}{\varepsilon}\right) \right) & |\psi| \leq \varepsilon \end{cases} \quad \text{Equation 3.7}$$

where ε is the interface thickness which is chosen as $\varepsilon = 1.5\Delta x$. The physical properties and the fluxes across the cell faces can be defined using a smoothed Heaviside function:

$$H(\psi) = \begin{cases} 0 & \psi < -\varepsilon \\ \frac{1}{2} \left[1 + \frac{\psi}{\varepsilon} + \frac{1}{\pi} \sin\left(\frac{\pi\psi}{\varepsilon}\right) \right] & |\psi| \leq \varepsilon \\ 1 & \psi > \varepsilon \end{cases} \quad \text{Equation 3.8}$$

The physical properties of the two immiscible fluids are discontinuous at the interphase and calculated below using a weighted average, so that the volume fluid fraction α has a significant effect on determining these properties in each cell.

$$\rho = \rho_g \alpha + (\rho_l - \rho_g) \alpha \quad \text{Equation 3.9}$$

$$\mu = \mu_g \alpha + (\mu_l - \mu_g) \alpha \quad \text{Equation 3.10}$$

Alternatively, the physical properties also can be defined based on the Heaviside function rather than VOF.

$$\rho = \rho_g H + (\rho_l - \rho_g) H \quad \text{Equation 3.11}$$

$$\mu = \mu_g H + (\mu_l - \mu_g) H \quad \text{Equation 3.12}$$

Although the latter method (Equations (3.11) and (3.12)) gives smoother transition of the properties across the interface compared with Equations (3.9) and (3.10), Albadawi [62] found that both approaches gave similar results for his test problems. Equations 3.9 and 3.10 are also adopted in the *sclsVOFFoam* solver used in our study. The governing equations are discretized based on a Finite Volume formulation. The discretization is performed in this study on a fixed Cartesian uniform structured grid for the two droplets study (in Chapter 4) and Cartesian non-uniform adaptive grid for liquid jet burst problem (in Chapter 5).

The S-CLSVOF solver can be described in eight main steps:

1. Define vector and scalar fields for the multiphase flow problem including u , p , ρ , μ , H , δ , α , and ψ . The pressure used in the OpenFOAM and VOF solver is

the dynamic pressure P_{rgh} where $P_{rgh} = P - \rho gh$ where h is the liquid height. The reason behind using dynamic pressure (P_{rgh}) in OpenFOAM is to avoid any sudden changes in the pressure at the boundaries for hydrostatic problems [66].

2. Initialize the numerical fields, reinitialize the Level Set function and calculate the initial values of the Dirac functions and Heaviside function.
3. Start the time loop by correcting the interface and the volume fraction.
4. Solve the volume fraction advection equation (Equation 3.3), and correct the new values of α . Interface normal vector involved in the curvature calculation is calculated from the gradient of the volume fraction in each cell at the interface. Interface normal vector involved in the curvature calculation which is updated in each cell at the interface to be used and fed in Equation 3.6. Then, calculate the new LS function as in $\psi = (2\alpha - 1)\Gamma$ using the results of the advection equation.
5. Re-initialize the LS function using Equation 3.5 in order to obtain the signed (ψ) distance function and correct the interface at the boundaries. Then, calculate the new values of the Dirac functions, the Heaviside function and the interface curvature.
6. Update the fluid physical properties and the fluxes using the volume fraction function α (Equations (3.9) and (3.10)).
7. Solve the Navier Stokes equations of both fluids (Equations (3.1) and (3.2)) for velocity and pressure using the PIMPLE algorithm. PIMPLE algorithm is an assembly of SIMPLE and PISO algorithms. The PIMPLE algorithm consists of inner and outer loops. In the inner loop only the continuity equation is solved while in the outer loop all equations are solved. The PIMPLE structure is based on the original PISO algorithm, but allows equation under-relaxation to secure the convergence of equations with the required number of iterations within a single time step, as in SIMPLE.
8. Move to the next time step (starting from 3).

3.4 Solver Verification and Validation

In this study, a thorough investigation of the performance of the solver described in Section 3.3, is undertaken using a variety of verification and validation test cases, which include (1) validation tests for rising bubble due to buoyancy effects, (2) the dynamic of liquid filament contraction and breakup, (3) dynamics of a splashing droplet,

(4) two droplets dynamic after impact on substrate (presented in Chapter 4), (5) low Weber (We) breakup jet in Rayleigh regime (presented in Chapter 5), then finally (6) and, (7) show swirling jet and spray verification cases (Illustrated in Appendices A.1.1 and A.1.2). These problems are now studied to enable a recommendation and assessment for the technique and solvers proposed in this study.

3.4.1 Rising Bubble

To validate the multi-phase solver implemented in the OpenFoam framework modelling software, a three dimensional numerical simulation is conducted for the single rising bubble problem studied experimentally at $Re = 9.8$ by Hnat and Buckmaster (case A of Table 1 in [67]), and compared with the rising bubble case simulated numerically by Yokoi [68]. Geometrical and mesh details are presented in Table 3.1. The initial condition is given zero for velocity and pressure. The No-slip boundary condition is used for velocity and Neumann for pressure at all the geometrical boundaries. The physical parameters which have been presented in [67] are used as shown in Table 3.2. The results presented in Figure 3.3 show good agreement with a numerical study [68] as evidenced in Figure 3.3 indicating the capability of OpenFoam to handle multiphase problems more generally. Figure 3.4 shows snapshots of the numerical result from the OpenFoam model for over double the time duration.

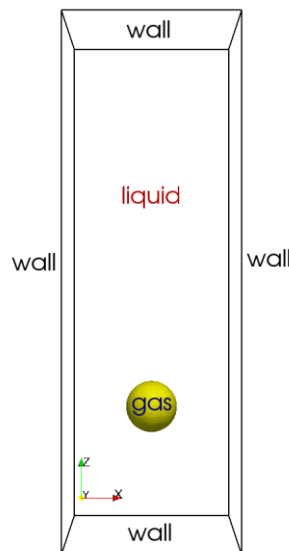


Figure 3.2 3-D geometrical setting for rising bubble validation case

Table 3.1 Geometrical and mesh details for rising bubble case

<i>Geometrical and mesh details</i>	
Computational domain (m)	$0.04 \times 0.04 \times 0.12$
Bubble diameter (m)	0.01214
Mesh resolution	$64 \times 64 \times 256$
Mesh size (m)	6.25×10^{-4}

Table 3.2 Physical parameters conducted for rising bubble. (adapted from [67])

<i>Medium</i>	<i>Density</i> ρ (kg/m ³)	<i>Dynamic viscosity</i> μ (Pa.s)	<i>Surface tension</i> σ (N/m)
Gas	1	1.48×10^{-5}	
Liquid	875.5	0.118	0.0322

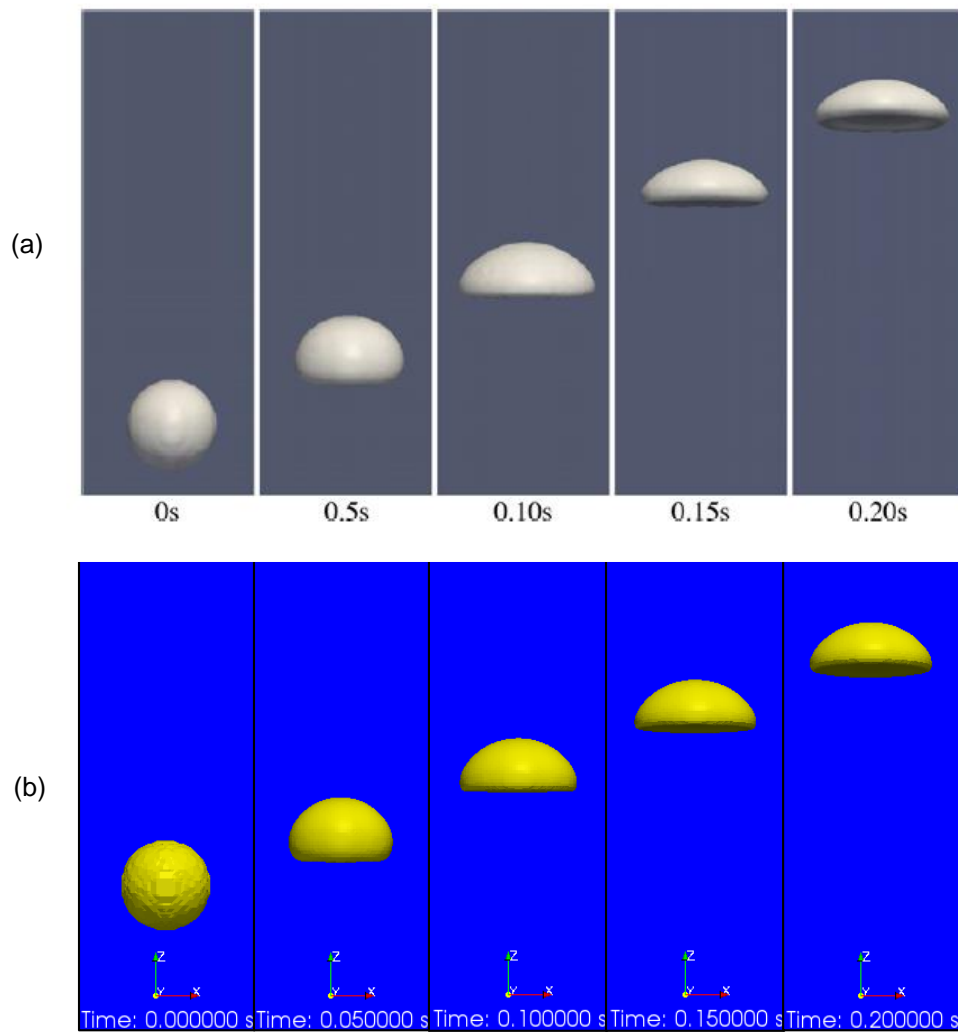


Figure 3.3 Snapshots of a comparison between the of 3-D numerical result of a single rising bubble by the OpenFOAM model (b) and the Yokoi's simulation (a) [68]

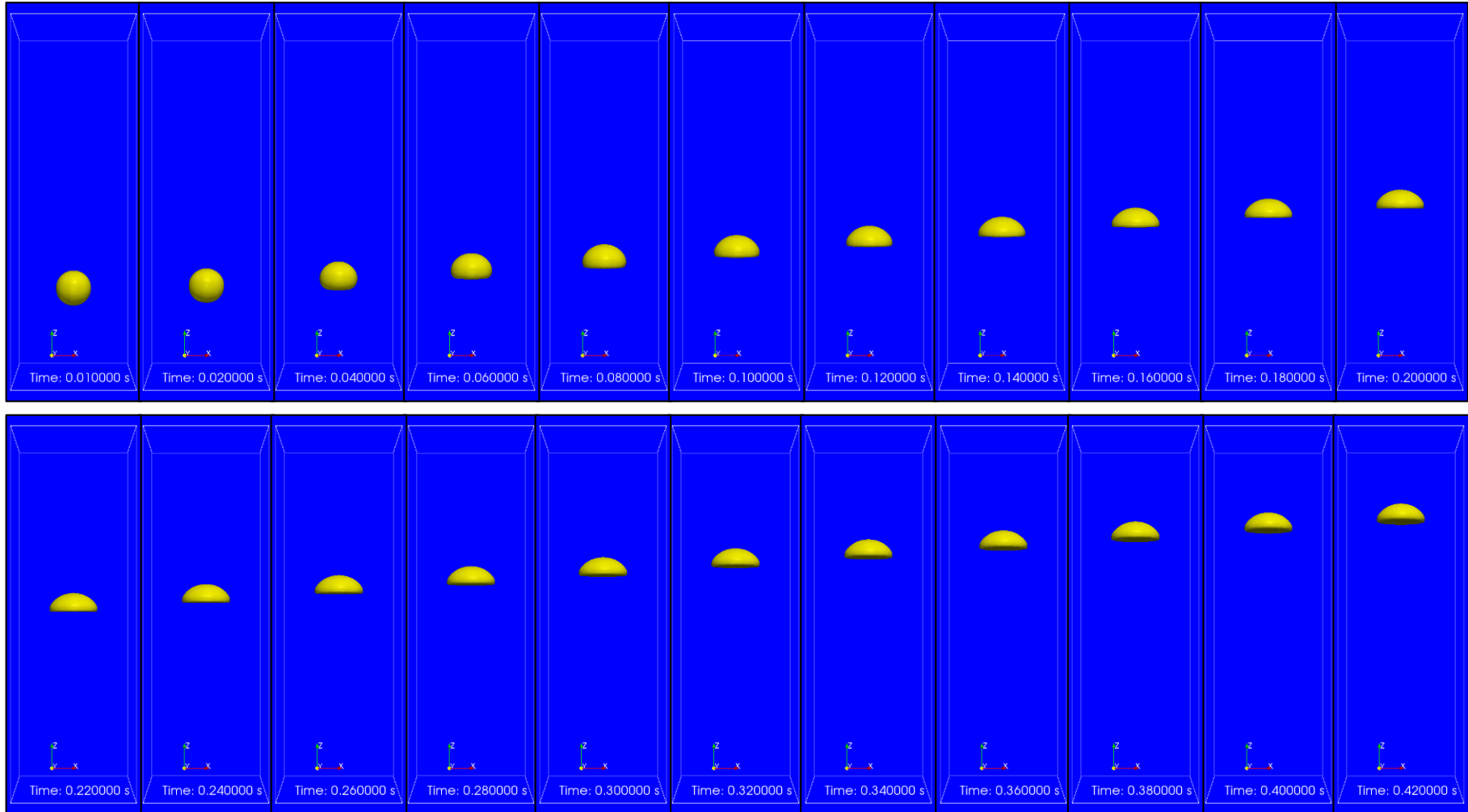


Figure 3.4 Snapshots of a 3-D numerical simulation results of single rising bubble by the OpenFOAM model

3.4.2 Contracting and Disintegration of Liquid Filament.

To validate *interFoam* (VOF) and *sclsVOFFoam* (VOF+LS) solvers, the following simulations are conducted:

- (i) 3-D contracting of a liquid filament (reported experimentally by Alfonso et al. [69] and numerically by Xiangyu Hu et al. [70])
- (ii) 2-D breakup of the liquid filament (reported numerically [70])

The geometrical setting for both filaments contracting and disintegration is shown in Figure 3.5 and Figure 3.6, respectively. The initial condition is given zero for the velocity and the pressure. Neumann boundary condition is used for velocity and fixed atmospheric for pressure at all the geometrical boundaries. Geometrical and mesh details of both cases are presented in Table 3.3. The physical parameters for both problems are presented in Table 3.4 and Table 3.5. Both simulation results presented in Figure 3.7 and Figure 3.8 showed reasonable agreement with previous studies [69] and [70]. As shown from results, *sclsVOFFoam* (VOF+LS) showed better agreement for both cases over *interFoam* (VOF) comparing with previous studies.

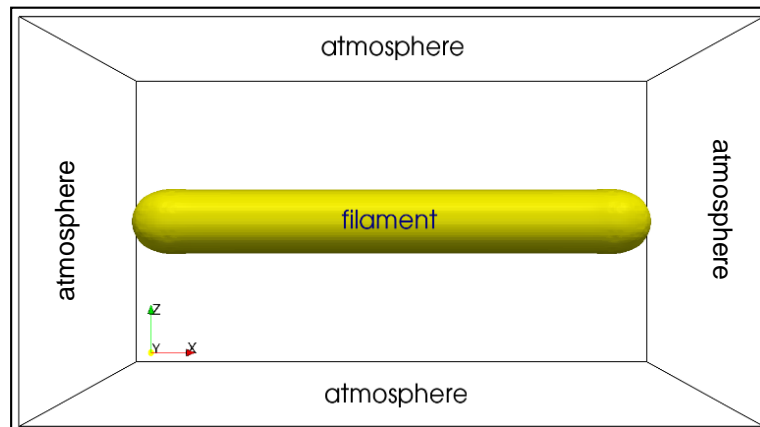


Figure 3.5 3-D geometrical setting for filament contraction validation case

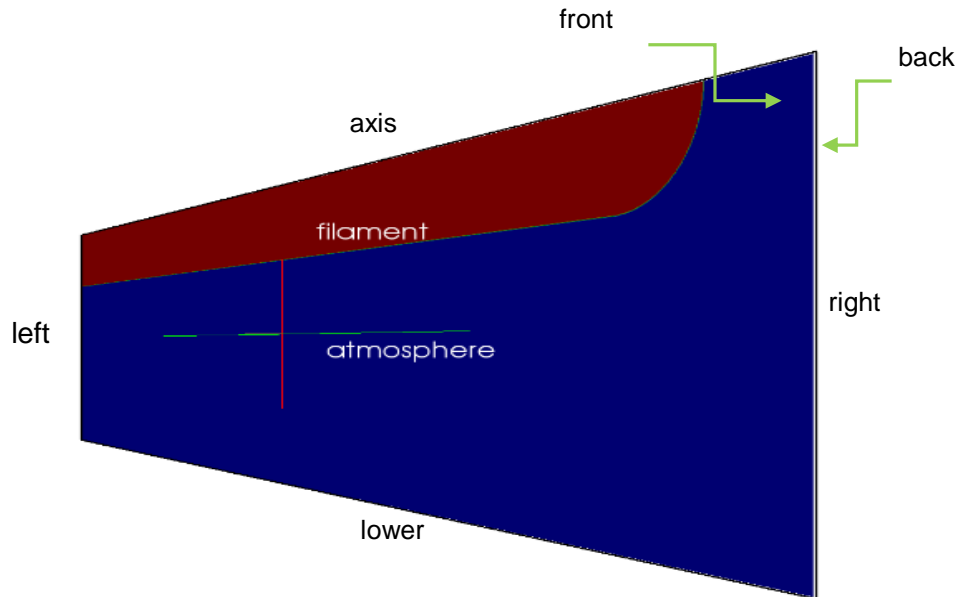


Figure 3.6 2-D geometrical setting for filament breakup validation case

Table 3.3 Geometrical and mesh details of liquid filament contraction and breakup validation cases

	<i>Filament contraction problem</i>	<i>Filament breakup problem</i>
Computational domain (m)	0.004 × 0.002 × 0.002	0.0004 × 0.0 × 0.0016
Filament diameter and length (m)	Diameter (D) = 0.00038 Length (L) = 0.00304	Diameter (D) = 0.0002 Length (L) = 0.0014
Mesh resolution	256 × 128 × 128	512 × 1 × 2048
Mesh size (m)	1.58 × 10 ⁻⁵	7.81 × 10 ⁻⁶

Table 3.4 Physical parameters conducted for filament contraction. (adapted from [70])

<i>Medium</i>	<i>Density</i> ρ (kg/m ³)	<i>Dynamic viscosity</i> μ (Pa.s)	<i>Surface tension</i> σ (N/m)	<i>Oh</i>
Gas (air)	1.226	1.6 × 10 ⁻⁵		
Liquid (water+ glycerol)	1000	0.005	0.073	0.04

Table 3.5 Physical parameters conducted for filament breakup. (adapted from [70])

<i>Medium</i>	<i>Density</i> ρ (kg/m ³)	<i>Dynamic viscosity</i> μ (Pa.s)	<i>Surface tension</i> σ (N/m)	<i>Oh</i>
Gas (air)	1.226	1.6 × 10 ⁻⁵		
Liquid (water+ glycerol)	1000	0.001	0.1	0.01

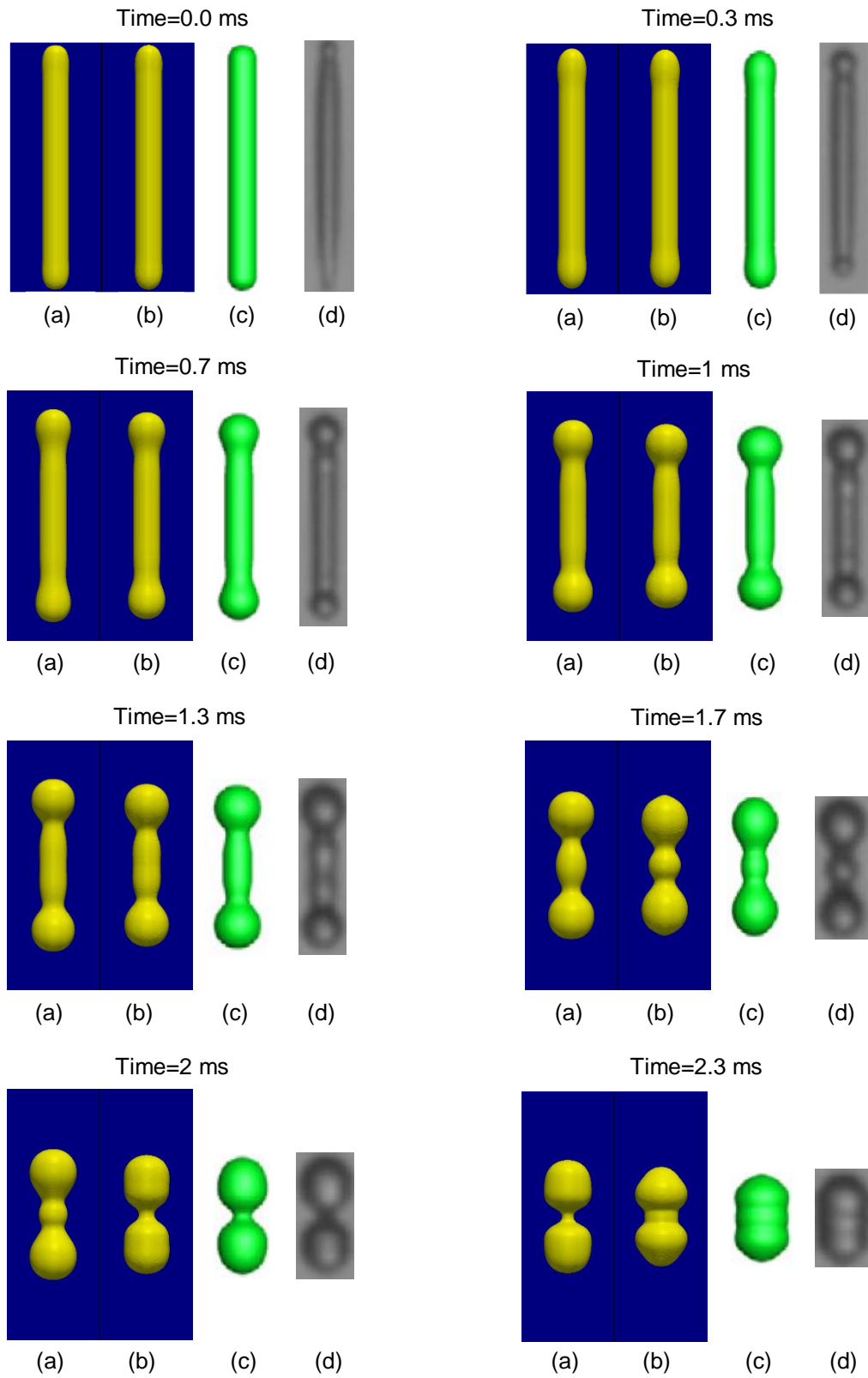


Figure 3.7 (a). For legend see next page.

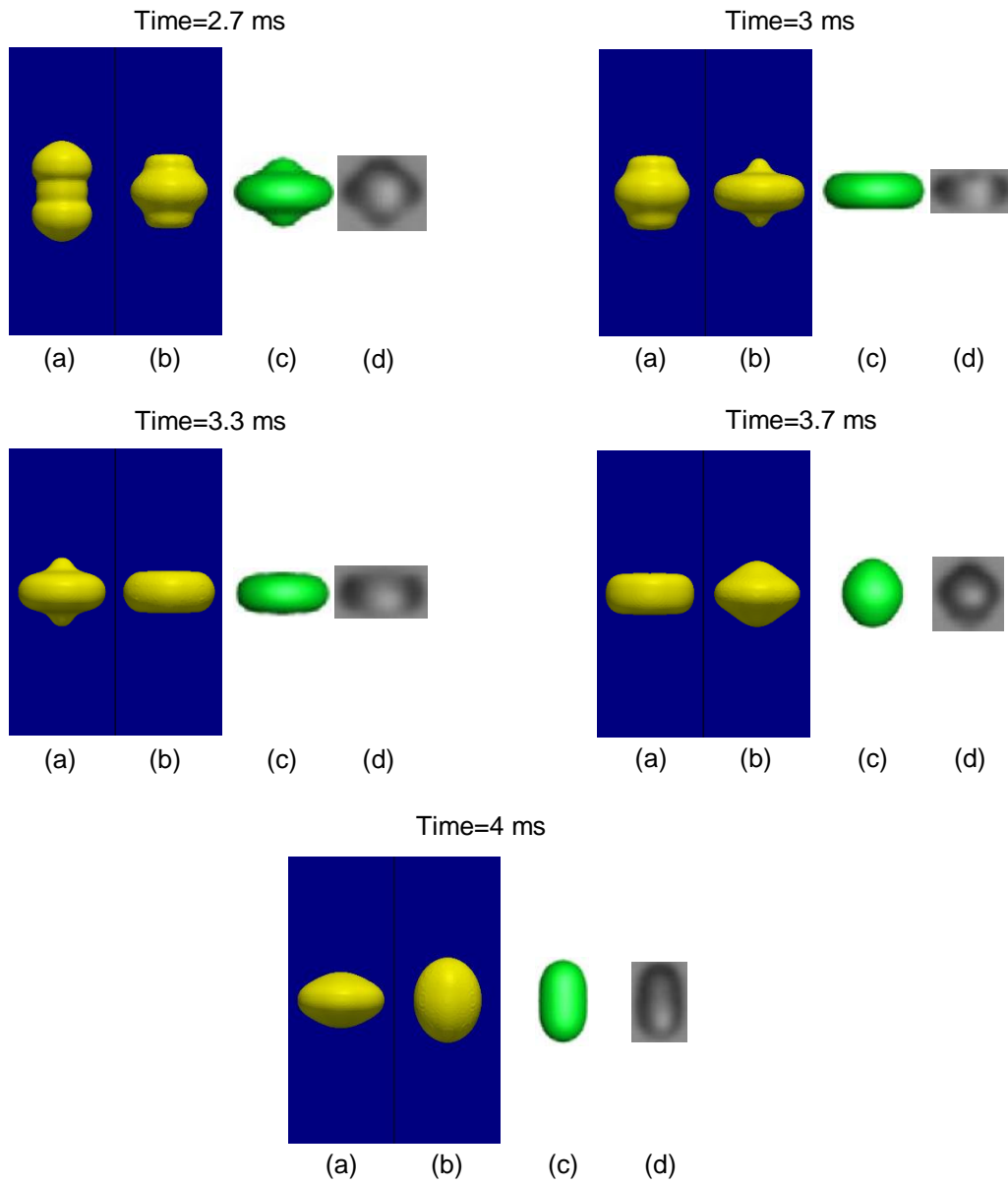


Figure 3.7 3-D evolution of a contract liquid filament simulation results: (a) VOF; (b) VOF+LS, compared with: (c) simulation results [70] and (d) experiment results [69]

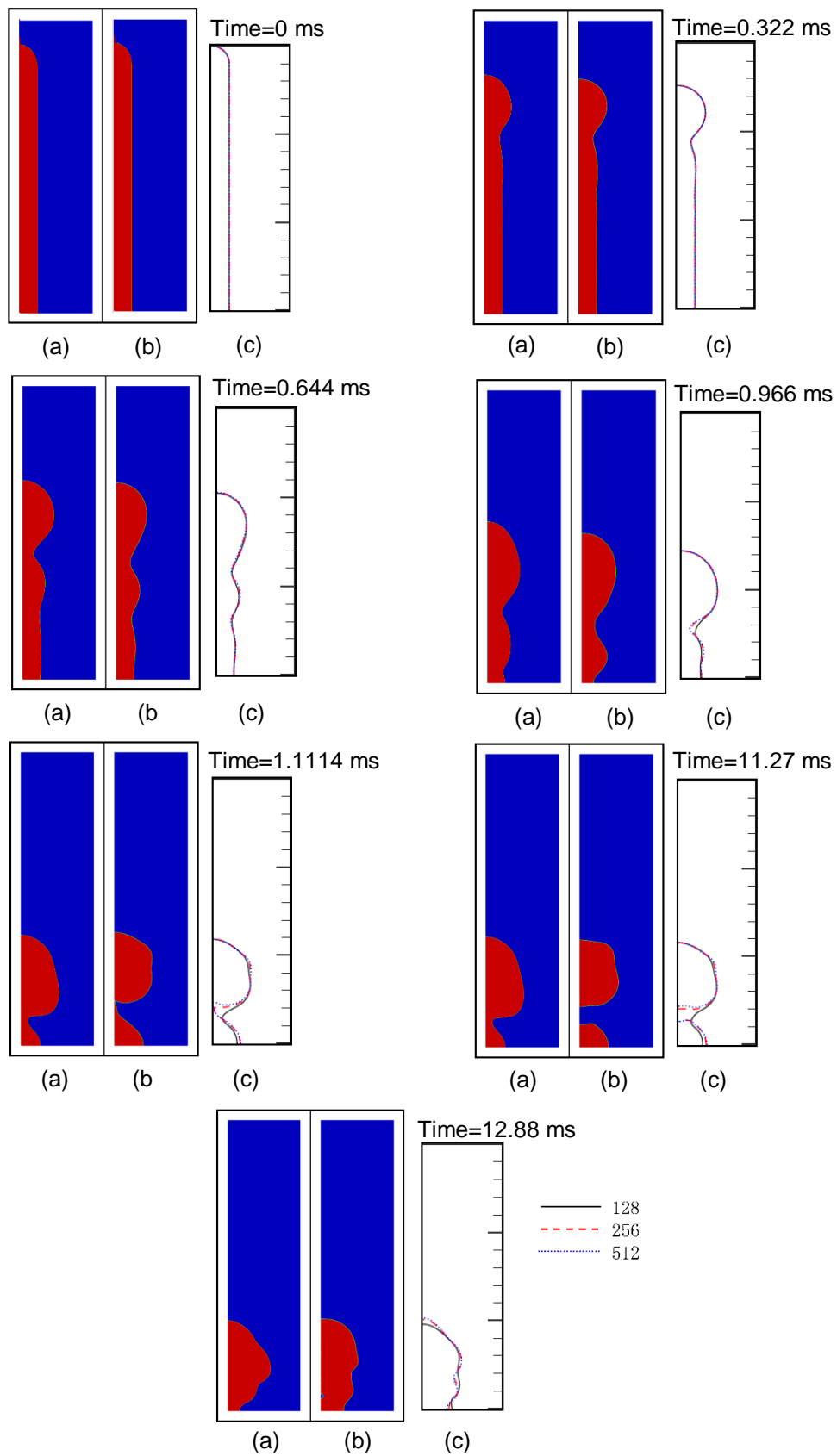


Figure 3.8 2-D evolution of a breakup liquid filament simulation results: (a) VOF; (b) VOF+LS, compared with: (c) simulation results [70]

3.4.3 Splashing Droplet

Next, a comparison is made between the OpenFOAM simulation and experiment [71], in which a water droplet impacts onto a super hydrophobic substrate (static contact angle =163°) with a velocity $U=2.98$ m/s. The geometrical setting for the problem is presented in Figure 3.9. Excluding the impact droplet, the initial condition is given zero for the velocity and the pressure. For the substrate (wall), the no-slip ($U=0$) is used, while Neumann boundary condition is used for the velocity to all other boundaries (atmospheric). For the substrate, Neumann boundary condition was utilized for pressure, while fixed atmospheric pressure to all other boundaries (atmospheric). Geometrical and mesh details are presented in Table 3.6. The physical parameters which have been specified in [71] are presented in Table 3.7.

Figure 3.10 shows the result of the comparison between the experiment [71] and the current numerical simulation. Results show the top view for longer time duration are presented in Figure 3.11.

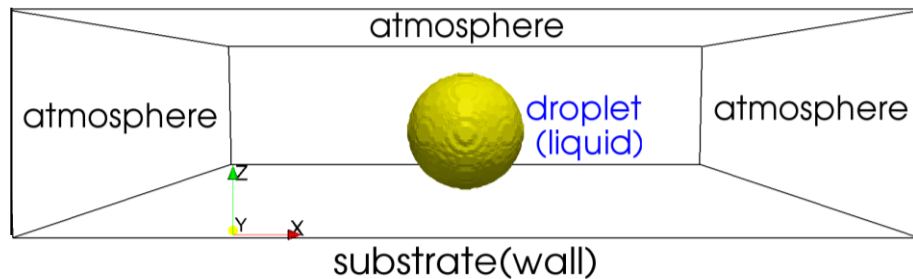


Figure 3.9 3-D geometrical setting for droplet splashing validation case

Table 3.6 Geometrical and mesh details for droplet splashing case

Geometrical and mesh details	
Computational domain (m)	$0.01 \times 0.01 \times 0.0025$
Droplet initial diameter (m)	0.00186
Mesh resolution	$256 \times 256 \times 64$
Mesh size (m)	3.9×10^{-5}

Table 3.7 Physical parameters conducted for droplet splashing. (adapted from [71])

<i>Medium</i>	<i>Density</i> ρ (kg/m ³)	<i>Dynamic viscosity</i> μ (Pa.s)	<i>Surface tension</i> σ (N/m)
Gas (air)	1.25	$1.82 \cdot 10^{-5}$	
Liquid (water)	1000	0.001	0.072

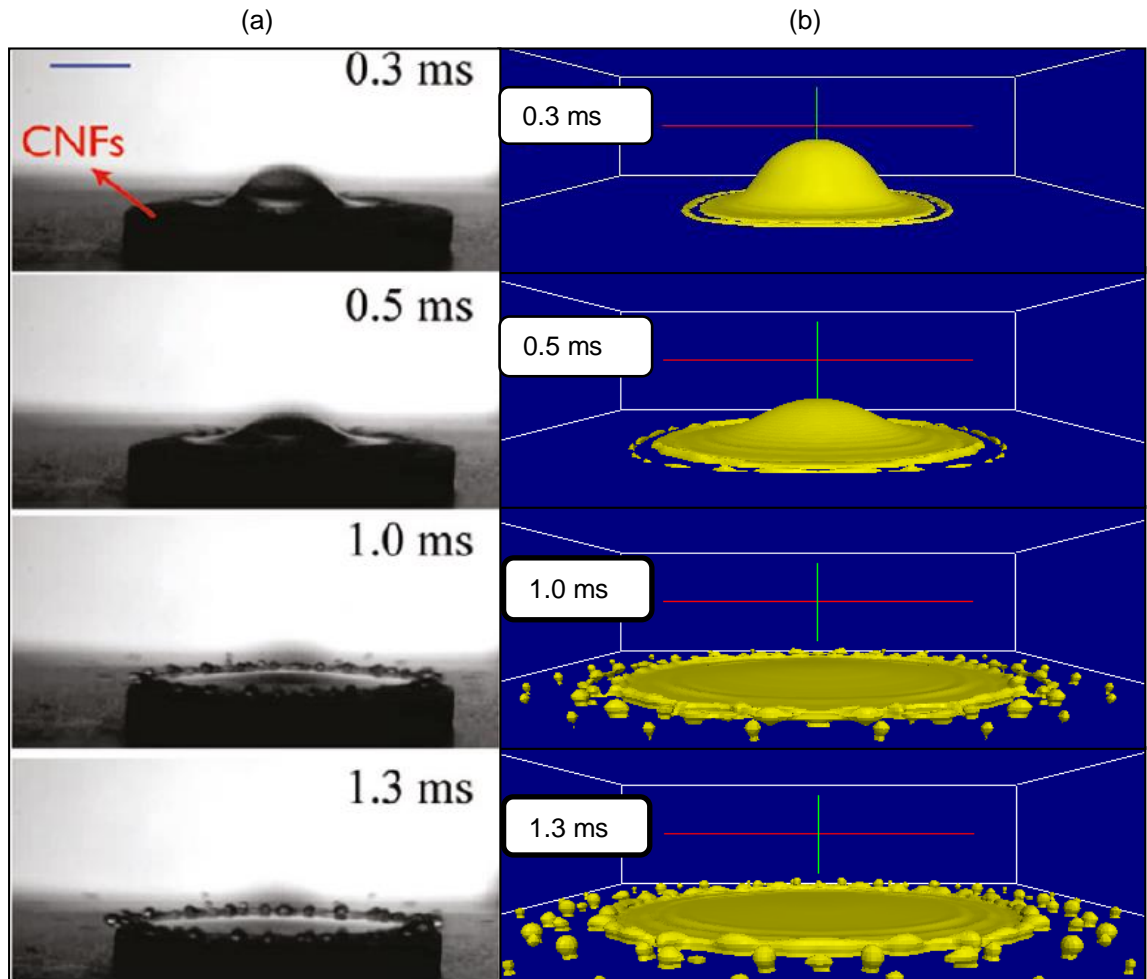


Figure 3.10 Snapshots of a comparison between the numerical results of 3-D simulation of single droplet splashing by the OpenFOAM model (b) and the experimental data (a). (adapted from [71])

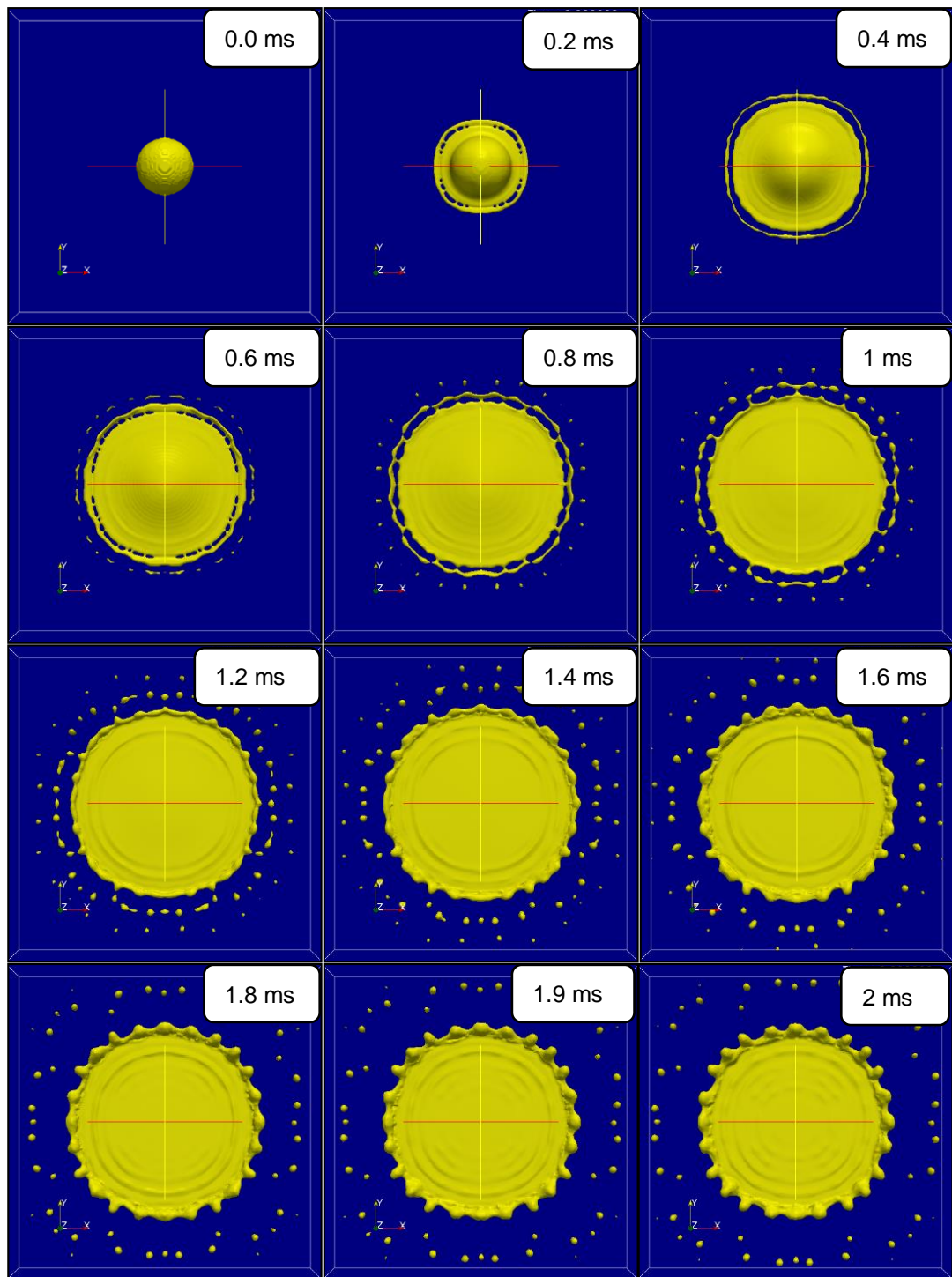


Figure 3.11 Snapshots of results of three dimensional numerical simulation of single droplet splashing by the OpenFOAM model

3.5 Summary and Conclusions

In this chapter, OpenFOAM software case structure, has been presented. OpenFOAM's solver was tested with different multiphase cases, its performance was evaluated, and the most accurate multi-phase solver was chosen. For the different cases tested, the comparison showed that OpenFOAM CFD tool can model multi-phase problems. Also, the comparison revealed that *sclsVOFFoam* (LS+VOF) solver was more accurate and showed better agreement with previous studies (whereas the surface forces were the dominate force in that phenomenon) for the variety of applications tested in this Chapter over *interFoam* (VOF) solver.

Therefore, it was concluded that OpenFOAM is reliable to handle multi-phase cases and can be used for liquid jet and two droplets study cases very confidently. It is concluded that using the LS method alongside with VOF by coupling them in *sclsVOFFoam* (VOF+LS) solver increased the accuracy of surface forces in the calculation (considered essential to capture and represent the real phenomena for low Weber number liquid jet and filament breakup as represented in Chapter 5). A decision was made to use *sclsVOFFoam* (VOF+LS) solver to produce the results for two droplets interactions on the substrate and liquid jet burst phenomena as will be explained in Chapters 4 and 5, respectively.

Chapter 4 Two Droplet Interaction on a Substrate

4.1 Introduction

The aim of this research is to investigate the effect of various initial conditions upon the characteristics of the droplets final stationary state. In this chapter, the numerical setting (illustrated in Appendix A.2) used to study the interaction of two droplets problem was validated. The impact velocity conducted in this study ranged between 0 - 4 m/s. The results are presented for different surface tension values ranging from 4.47 to 1667.5 mN/m, and viscosities ranging from 8.58 to 300.3 mPa.s, hence, representing a wide range of liquids. The centre-of-mass of the composite droplet at its final location is utilised to explore the trend of final footprint location, which signifies whether the impacting droplet results in final translation to the right or to the left. Parameters such as impact speed, viscosity and surface tension effect on the final composite droplet location are investigated and the final composite centre-of-mass was compared in location with the initial centre-of-mass before impact.

4.2 Validation of the Numerical Setting Used for Two Droplets

Problem

A comparison is made between the OpenFOAM simulations and experiments [24] in which a liquid droplet (glycerol-water) impacts onto a sessile droplet. A droplet with a velocity $U=1.12$ m/s impacts on a stationary sessile droplet (static contact angle = 63°) at five different centre-to-centre spacing. The geometrical setting, initial and boundary conditions, and the physical properties) are illustrated in Table A.2.1 (Appendix A.2, section A.2.1.1) and Table A.2.2 (Appendix A.2, section A.2.1.2) respectively. Figure 4.1 shows the result of the comparison between the experiment (Figure 3, [24]) and the current numerical simulation. From comparison, the numerical model showed good agreement with previous experimental study [24].

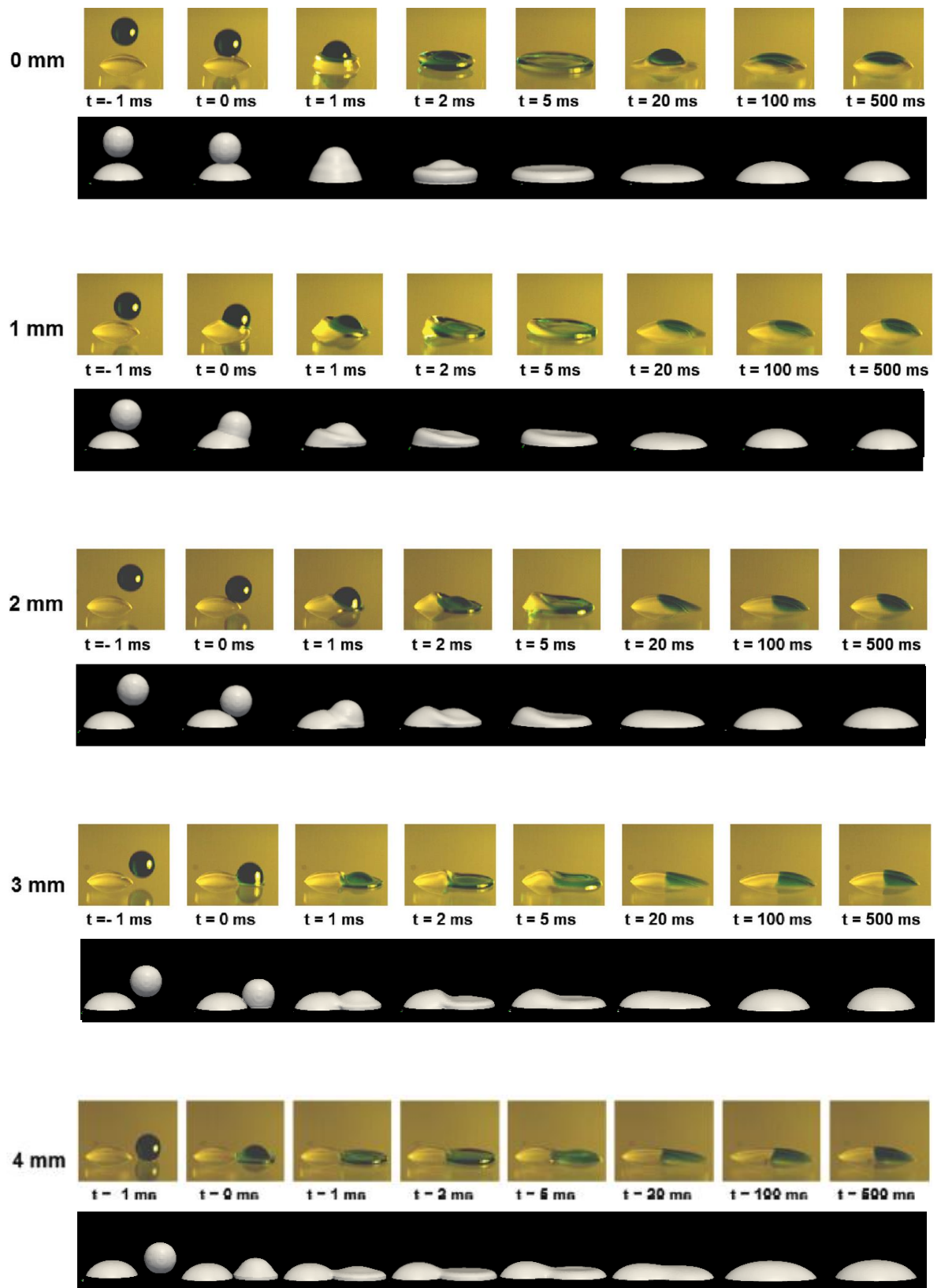


Figure 4.1 Time-resolved results of a comparison between the experimental [24] (top) and 3-D numerical simulation (bottom) of a two droplets interaction on substrate at five different centre displacements Using OpenFOAM model

4.3 Results and discussion

4.3.1 Influence of Lateral Separation on Final Steady State Composite Location for Various Impact Speeds

The physical and geometrical conditions studied in this research programme are adapted from [24] and detailed previously in Table A.2.1, Table A.2.2 (Appendix A.2) and Table 4.1 below. Both droplets were identical in size and have the same liquid properties. Initially, a glycerol-water mixture was used, then the physical properties of both droplets changed as specified in the following. According to R. Li [17], the droplet impacting on a solid surface will coalesce with the sessile droplet if the spacing between their centres (L), is less than the spread diameter of sessile droplet (D_s) as shown in Figure 4.2(a). The overlap between the two droplets has been quantified as a ratio; overlap ration (λ) and defined in Equation 4.1 [17].

Table 4.1 Droplets geometrical conditions explored in this work

<i>Droplets geometrical condition</i>	<i>value</i>
Impacting droplet diameter D_o (mm)	2.8
Initial diameter of sessile droplet D_o (mm)	2.8
Final steady state diameter of sessile droplet after deposition in D_s (mm)	4.4
Final height of sessile droplet after deposition in steady state h (mm)	1.34
Impacting droplet speed U (m/s)	0 - 4

$$\lambda = 1 - \frac{L}{D_s}$$

Equation 4.1

According to Equation 4.1, if $L=0$, $\lambda=1$, which signifies complete overlap and axial co-centric impact of two droplets. Whilst if $L=D_s$, $\lambda=0$, and the droplets edges are just touching each other upon impact. Between these two limiting cases, a set of three overlapping ratios λ were proposed subjectively to explore the final footprint location as a function of several initial displacements and impact speeds. The three sets of the overlap ratios λ values adopted in the current research are presented in Table 4.2.

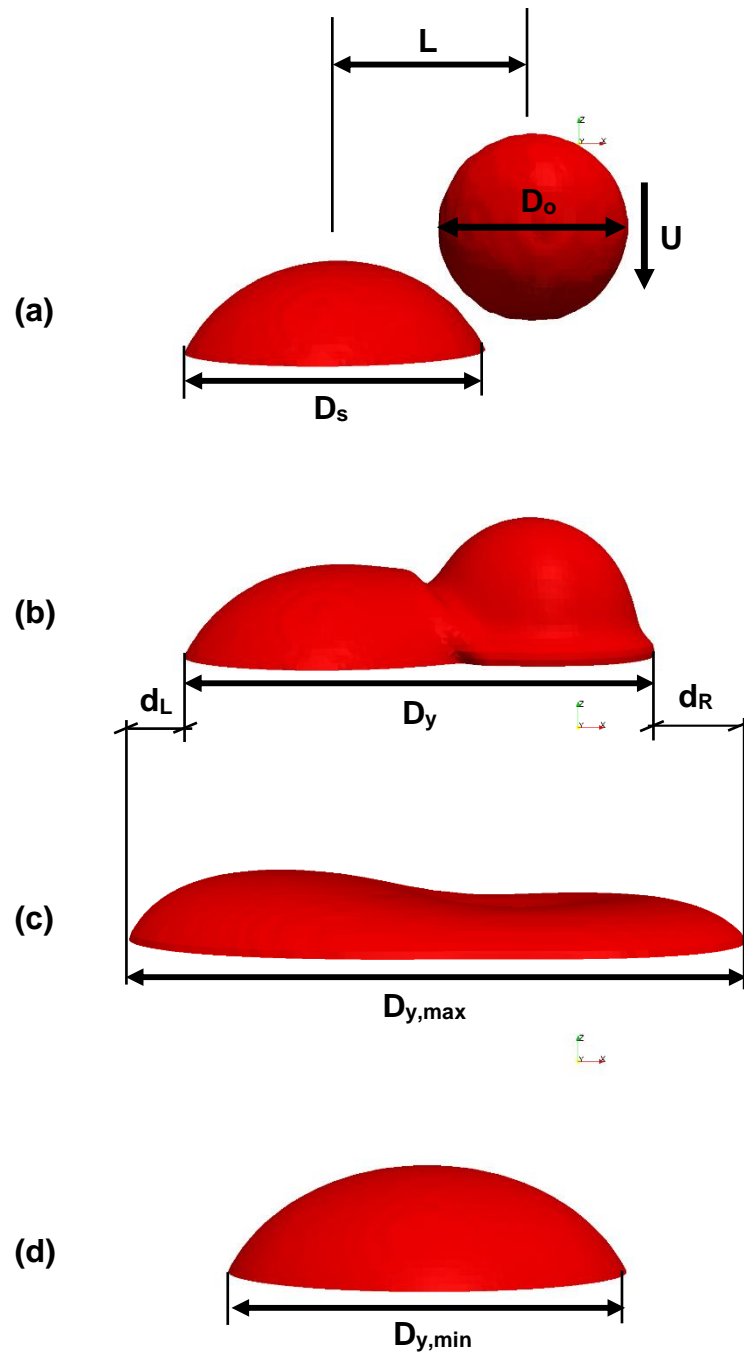


Figure 4.2 (a) Deposition of two droplets on a solid surface; (b) intermediate spread length - D_y ; (c) maximum spread length - $D_{y,max}$; (d) minimum spread length - $D_{y,min}$

Table 4.2 Three sets of overlap ratios λ used in our research

λ	D_s (mm)	L (mm)
0.5	4.4	2.2
0.34	4.4	2.9
0.18	4.4	3.6

The rationale behind adopting these three values of overlap ratio is as follows: When the droplet separation is relatively small; $L=2.2$ mm, $\lambda=0.5$ preceding impact, the centre of the impacting droplet still lies inside or at least touching the right edge of the sessile droplet. This implies that when the droplet impacts, it falls down entirely on a pre-wetted substrate first, therefore impact and coalescence occurs immediately. For a large offset; $L=2.9$, $\lambda=0.34$, the impacting droplet lands partially on a pre-wetted substrate and partially on the dry substrate, enabling coalescence and partial spread. For a larger offset; $L=3.6$, $\lambda=0.18$, the left edge of the impacting droplet lies at the right edge of the sessile droplet. This implies that when the droplet impacts, it falls down entirely on a dry substrate and therefore impacts and spreads before coalescence occurs.

Figures 4.3, 4.4 and 4.5 present the very early stage of impact and coalescence (at time=0.6 ms) and steady state condition (time=0.5 s) for different impact speeds, and at the three displacements $\lambda=0.5$, $\lambda=0.34$ and $\lambda=0.18$ respectively. From the top view contour results illustrated in those figures, it is observed that circularity is attained at time 0.5 s for the three cases $\lambda=0.5$, $\lambda=0.34$ and $\lambda=0.18$ respectively. Also from the same top view, by comparing the three overlap ratio cases, it was noticed that increasing droplet separation results in the combined droplet at its final steady state condition being located further to the right (side of impact). This corresponds to the observations of Pita et al. [21] and implies that greater spread to the right side is exhibited for larger drop separation.

Using ParaView post processing software, the edges and centre-of-mass location were quantified for the two droplet composite at its equilibrium condition. The effect of droplet spacing and impact speed on the final composite location has been analysed further. Figures 4.6, 4.7 and 4.8 illustrate, for different impact speed, the final footprint location and composite mass centre compared with initial mass centre before impact, for the three cases: $\lambda=0.5$, $\lambda=0.34$ and $\lambda=0.18$ respectively.

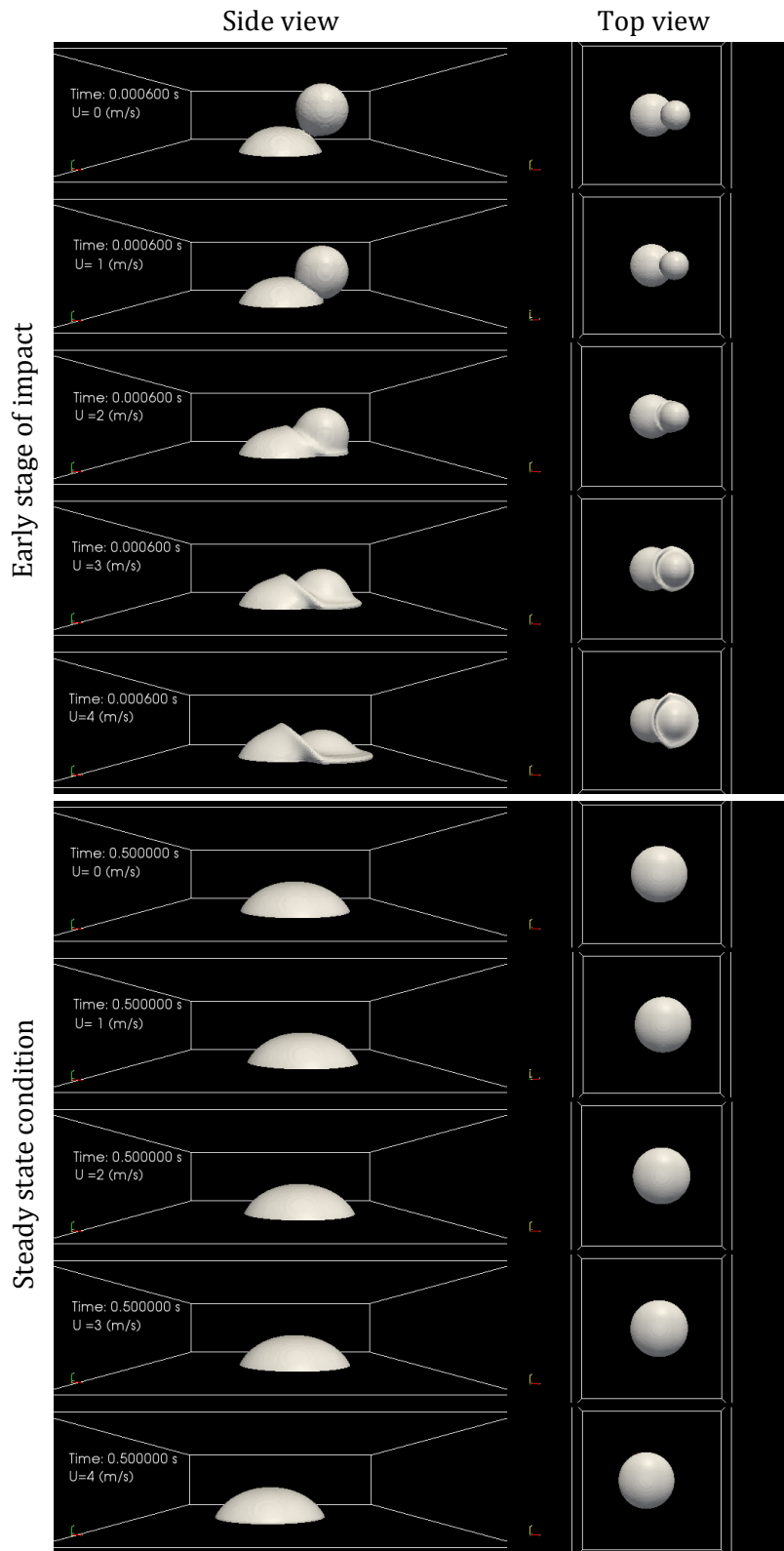


Figure 4.3 Top and side view contour of impact and coalescence droplets at different impact speed of case $\lambda=0.5$. Early stage of impact on top, steady state condition on bottom

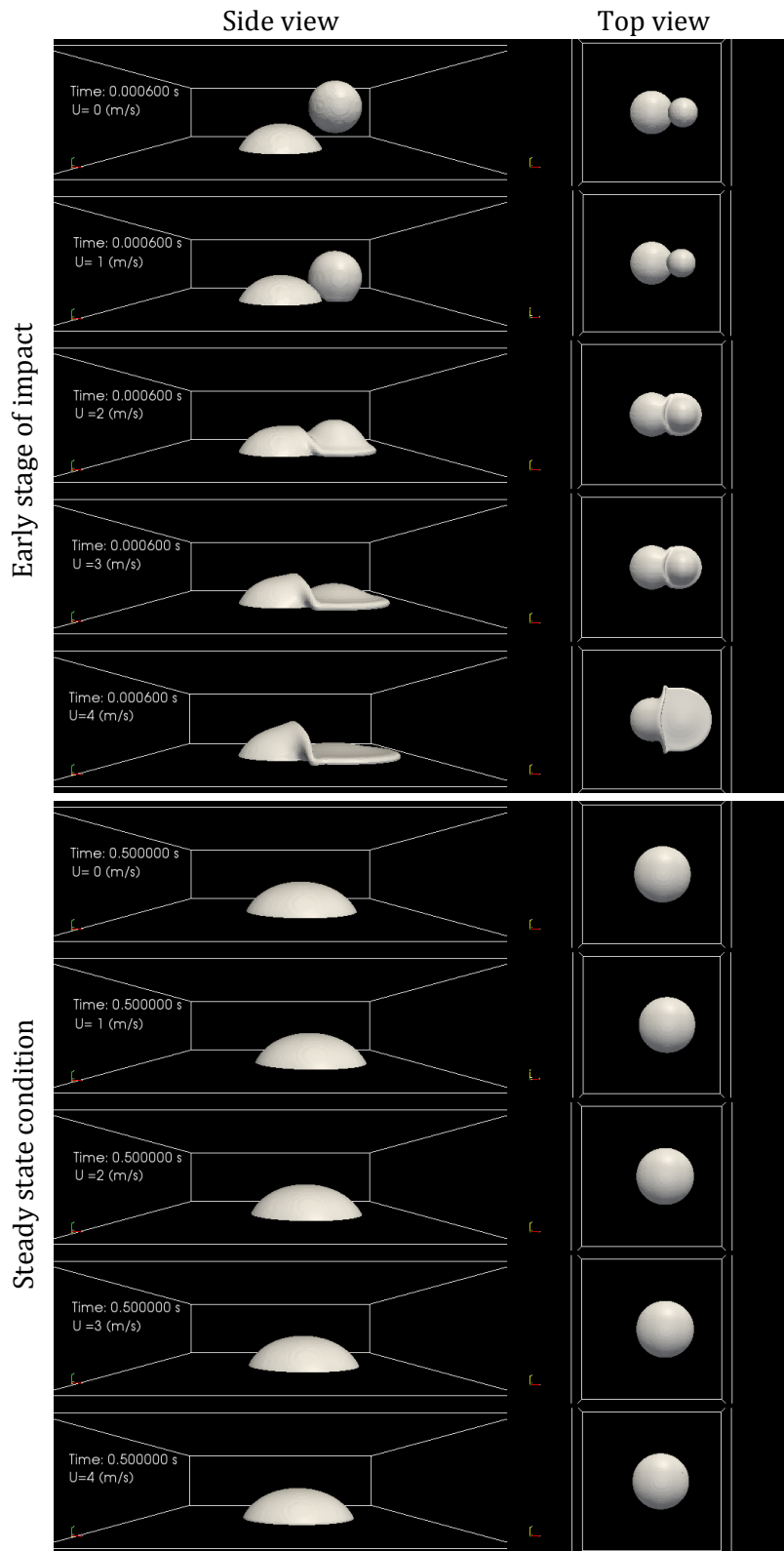


Figure 4.4 Top and side view contour of impact and coalescence droplets at different impact speed of case $\lambda=0.34$. Early stage of impact on top, steady state condition on bottom

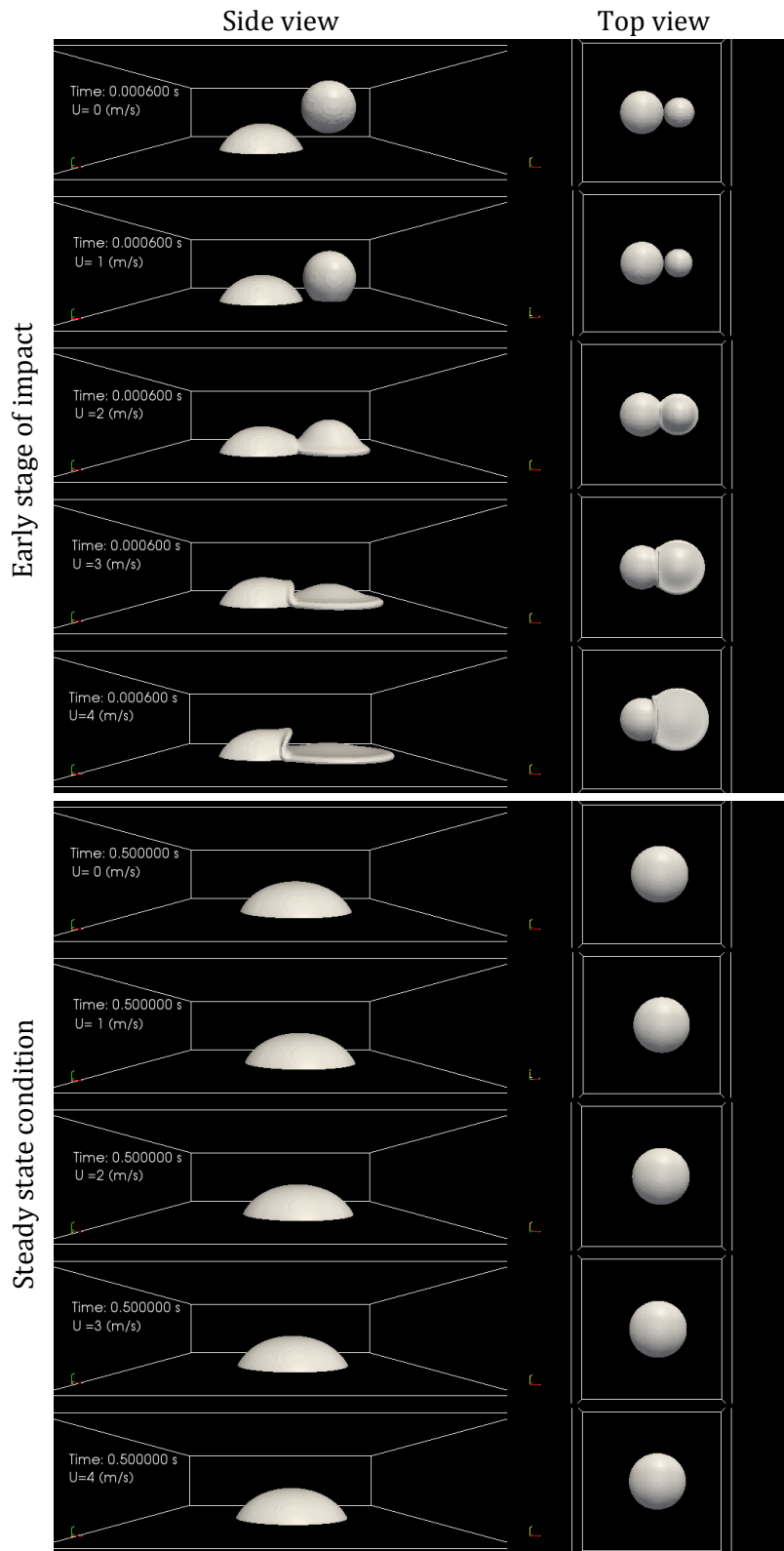


Figure 4.5 Top and side view contour of impact and coalescence droplets at different impact speed of case $\lambda=0.18$. Early stage of impact on top, steady state condition on bottom

From these figures, the effect of increasing droplet spacing results in locating the final composite to the side of the impact droplet. For $\lambda=0.5$, the centre-of-mass of the composite at equilibrium is located to the right relative to the initial centre-of-mass at low impact speed ($U=0.4-0.6$ m/s), whereas it is located to the left for higher impact speed ($U\geq 0.8$). Increasing spacing for $\lambda=0.35$, the composite centre-of-mass moves to the side of the impact droplet and then crosses the initial mass centre for higher impact speed. For the largest spacing studied, ($\lambda=0.18$), the composite droplet's final location shifted further to the side of impact droplet, locating the centre-of-mass to the right relative to the initial mass centre for broader range of impact speed ($U=0-2.4$ m/s) and showed less inertia effect from the impact side. To make a comparison between the three cases, Figure 4.9 shows the non-trivial trend movement from the right (impact side) to the left as impact speed gradually increased for the three different overlap ratios utilized as presented the side-view numerical results of a composite droplet at equilibrium condition.

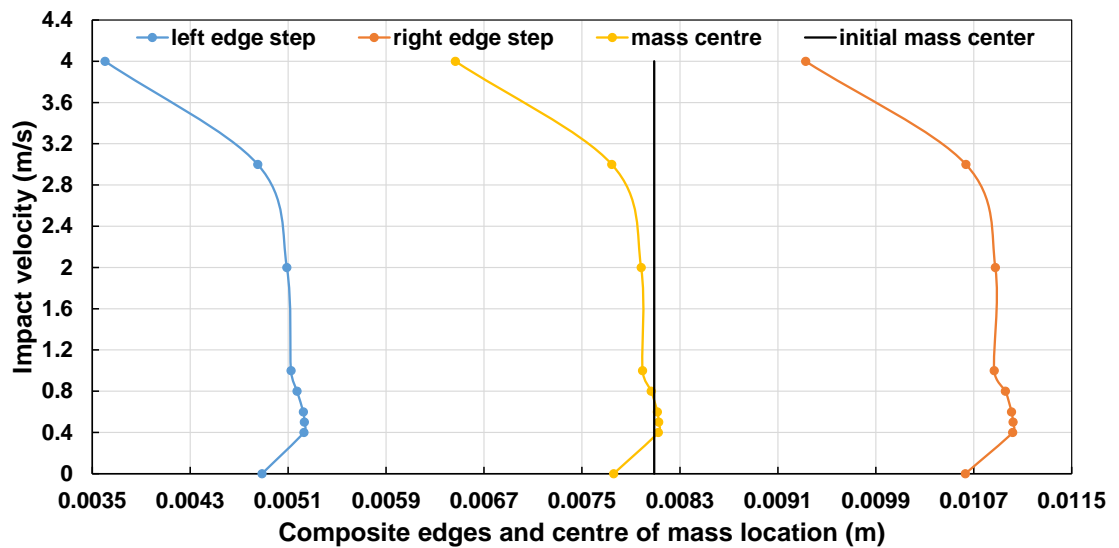


Figure 4.6 Composite droplet location details and mass centre compared with initial mass centre at different impact speed for $\lambda=0.5$

Intuitively, it would be expected that a gradual increase in impact velocity would force the final composite droplet to be located on the opposite side of impact. However, from results shown in figure 4.6, 4.7, 4.8 and 4.9 that non trivial movement is observed, whereby for small impact velocity, the composite droplet location moves gradually towards the impact side (right side), but the trend changes at a specific critical velocity.

The critical velocity needed for smaller droplet spacing ($\lambda = 0.5$) was around $U=0.4$ m/s whereas increasing droplet spacing ($\lambda = 0.34$) requires a higher impact speed of around $U=0.5$ m/s to reverse the trend. Higher critical velocity still around $U = 1$ m/s corresponds to further increase in droplet spacing ($\lambda = 0.18$). With impact speed higher than the critical one, the composite droplet moves away from the side of impact, due to the influence of inertia.

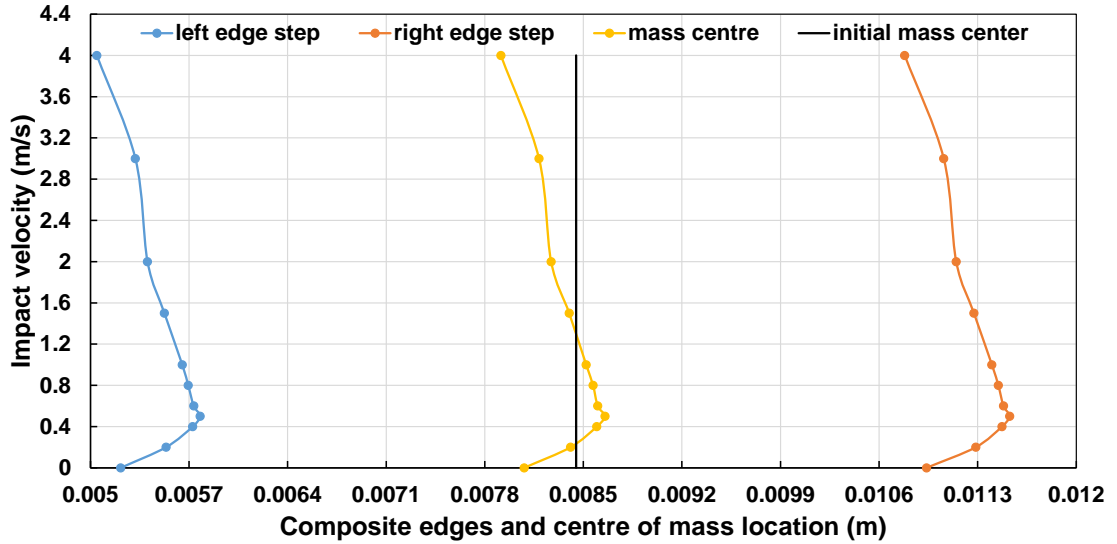


Figure 4.7 Composite droplet location details and mass centre compared with initial mass centre at different impact speed for $\lambda=0.34$

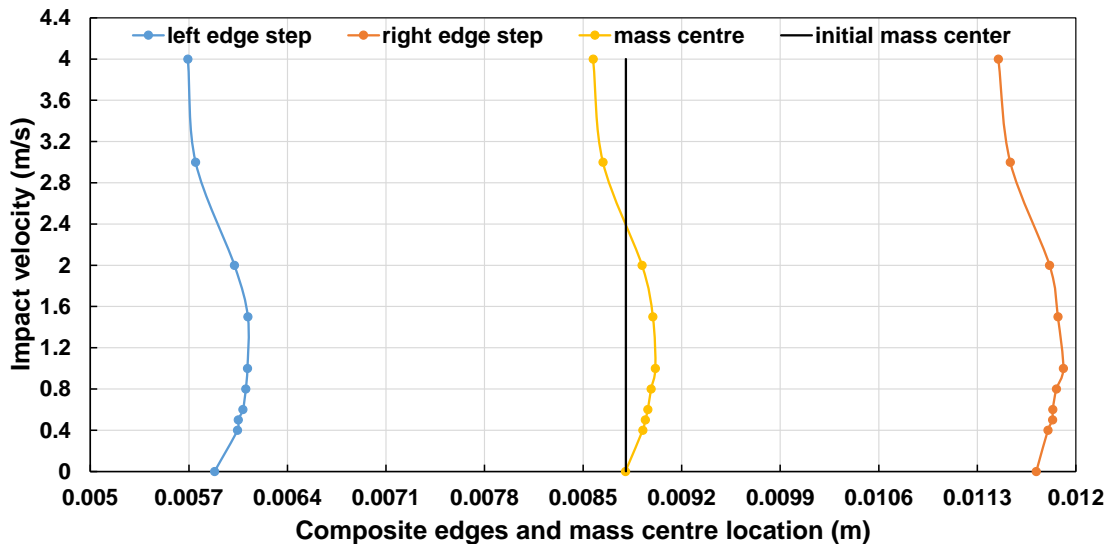


Figure 4.8 Composite droplet location details and mass centre compared with initial mass centre at different impact speed for $\lambda=0.18$

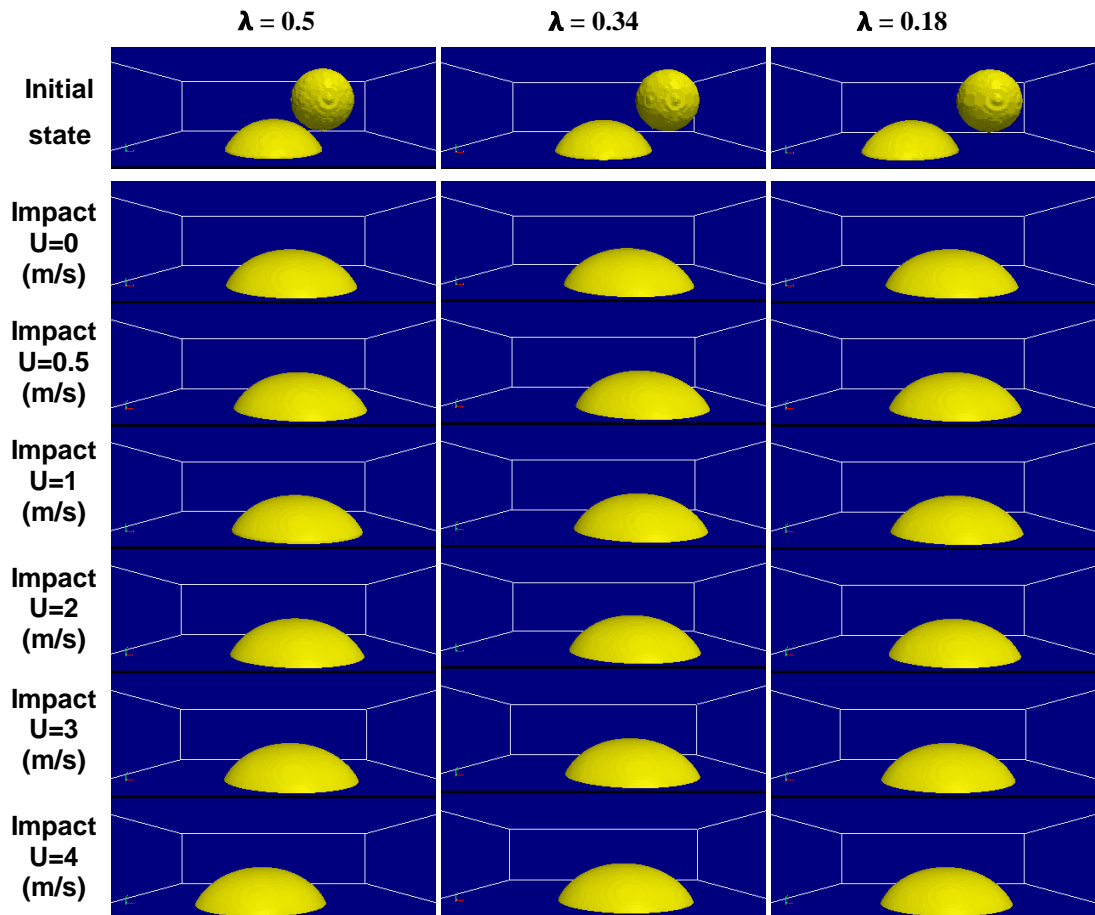


Figure 4.9 Side view contour of the two droplet composite at steady state for three different overlap ratios (λ) and different impact speeds

In their study, Yang et al.[22] commented that when the droplet impacts the sessile for different spacing between them, the sessile can act as a buffer and damp oscillations resulting from impact. Pita et al.[21] observed that through droplet coalescence, the impact droplet tries to push the sessile but the sessile resists this as the contact line to the left of the combined line does not move. The reason behind this complex behaviour of final foot print location demands further investigation, particularly regarding the moving contact line of the composite droplet with time until equilibrium is reached.

To understand the reason behind the non-trivial movement trend of composite location, the right and left edge displacement of composite droplets have been tracked with time for $\lambda = 0.34$. Across the initial centre-of-mass, the overlap ratio $\lambda = 0.34$ has

noticed a more severe change for the composite location trend than any other overlap ratio cases for an important range of impact velocity, therefore it is expected to show better representation for that purpose of investigation. The non-dimensional form utilised to calculate the displacement of the left and right edges at any time through coalescence is presented as:

$$X_L, X_R = |d_{L,R}| / (D_s + L) \quad \text{Equation 4.2}$$

Where D_L , D_s , $d_{L,R}$, and X_L, X_R are defined in the Figure 4.2. Figures 4.10, 4.11, 4.12 and 4.13 present the displacements of the right and left edges relative to their maximum points (maximum spread length of two droplets after impact ($D_{y,max}$) for velocities $U=0, 0.2, 0.4$ and 0.5 (m/s) respectively. As the definition of $X_{L,R}$ (Equation 4.2) implies, a downward slope indicates spreading, whilst an upward trend indicates retraction. For the velocity range $U = 0.0-0.5$ (m/s), tracking the right edge with time showed spread to the right side (side of impact), and this spread increases with increasing velocity. The left edge stayed pinned to the substrate showing no spread due to no observable influence of the impact droplet within this velocity range. After maximum spreading has been attained, capillary forces (surface forces) act to recoil the composite due to surface tension. This recoiling is reflected in retraction from both right and left edges. The left edge movement (displacement to the right side) through retraction results in shifting the entire composite to a final equilibrium position on the right side.

For the case $U=0$ m/s as shown in the Figure 4.10, no initial impact droplet speed with the droplet falling purely under gravitational influence, the left edge retracts earlier and further than the right edge comparing to the cases when impact speed added to the falling droplet. At this very low inertia condition, surface tension effect (throughout the retraction stage) tends to draw the sessile droplet to the right, resulting in slightly earlier or almost coincident retraction of the left edge. Increasing initial impact speed to $U=0.5$ m/s, the right edge retracts earlier and further than the left edge when the droplet falls with additional impact speed rather than just with the gravitational impact speed [17]. Here during the early stages, inertial-driven impact tends to push the sessile droplet first to the left, which causes the left edge of sessile to be delayed for a longer time before it starts to retract later than the right edge.

Hence, for this range of $U=0-0.5$ m/s, the results and observations may be summarised as:

- The sessile left edge showed no spread (stayed pinned) for all initial velocities, whilst the right edge of the impact droplet exhibited spreading.
- The impact droplet's right edge showed more spreading with increased impact speed.
- As no spread is discerned at the sessile left edge, and since the right edge of the impact droplet spreads, the net effect is that the composite droplet moves to the right (side of impact).
- As the impact speed increasing, the composite droplet tends to be located further to the right due to greater spread exhibited at the impact side.
- At highest initial impact speed which around $U=0.5$ m/s, composite maximum location occurred to the right (side of impact).

Figures 4.14 - 4.19 present the displacements of the right and left edges relative to their maximum points (points location of both edges at maximum spread after impact ($D_{y,max}$) for $U=0.6, 0.8, 1, 1.5, 2$ and 3 (m/s) respectively. For a velocity higher than the critical velocity (around $U=0.5$ m/s), the effect of inertia on the impact droplet side has induced motion on the left edge of the sessile. Although it is not clear for $U=0.6$ m/s shown in Figure 4.14, the left edge of sessile droplet has exhibited a small spread to left. This spread increases with initial velocity, and becomes more apparent as shown in Figure 4.15 - 4.19 for $U=0.8, 1, 1.5, 2$ and 3 (m/s) respectively.

Hence, in the range of $U=0.6 - 3$ (m/s), results and observations may be summarised as:

- For higher initial impact velocity ($U > 0.5$ m/s), the impact droplet influences the left edge of sessile and pushes it from right to left.
- The sessile left edge unpinned and spreads to the left. This spreading increases with an increase in the initial impact velocity.
- Droplet composite location deflected to the opposite direction of impact as expected due to inertial dominance for an impact speed $U > 0.5$ m/s.
- For higher impact speeds, the left edge of the sessile shows greater spread (displacement) and quicker response (un-pinning).

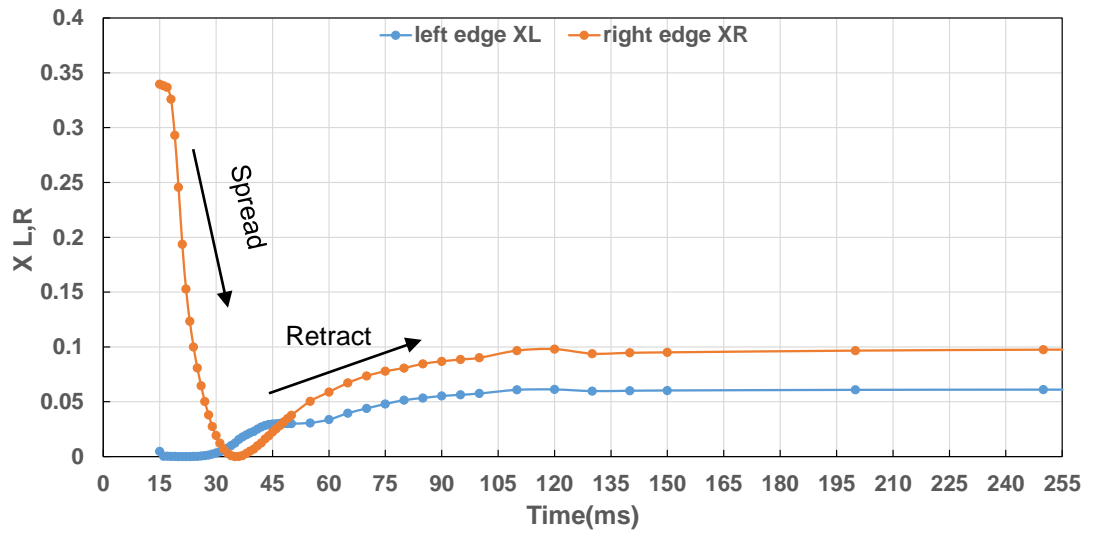


Figure 4.10 Displacement of the right and left edges of composite droplets for $U=0$ m/s

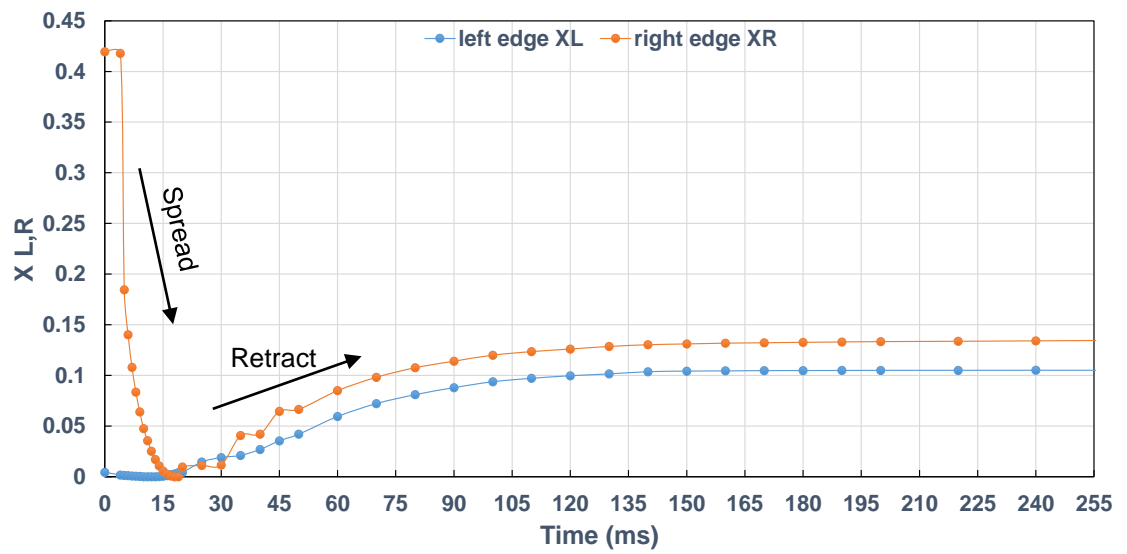


Figure 4.11 Displacement of the right and left edges of composite droplets for $U=0.2$ m/s

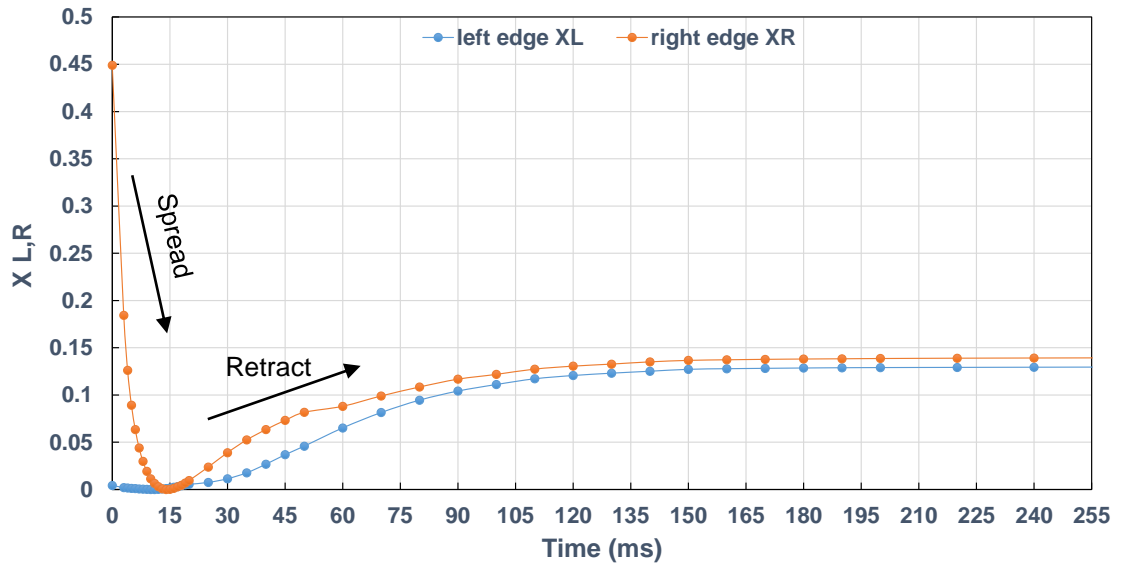


Figure 4.12 Displacement of the right and left edges of composite droplets for $U=0.4$ m/s

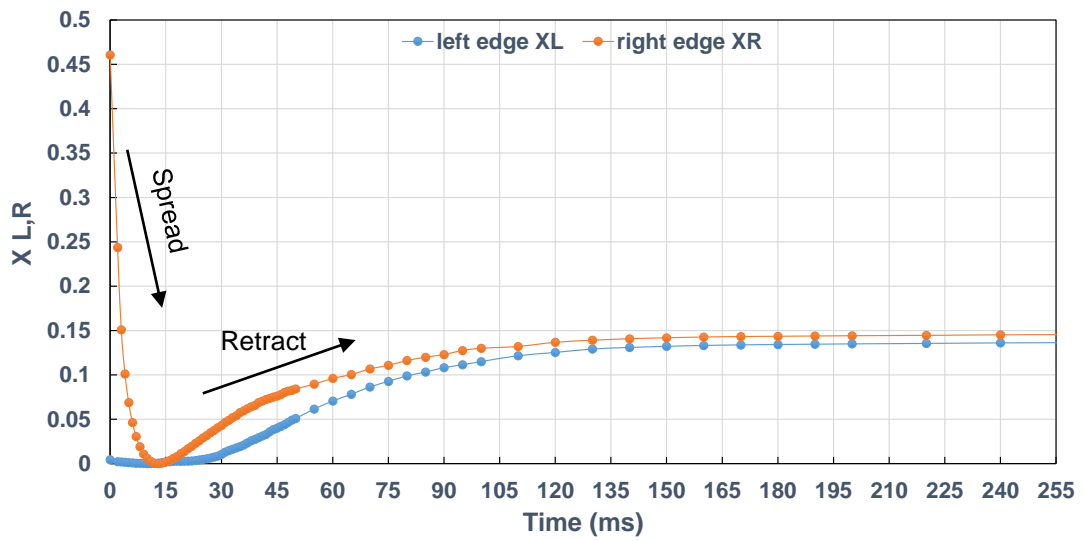


Figure 4.13 Displacement of the right and left edges of composite droplets for $U=0.5$ m/s

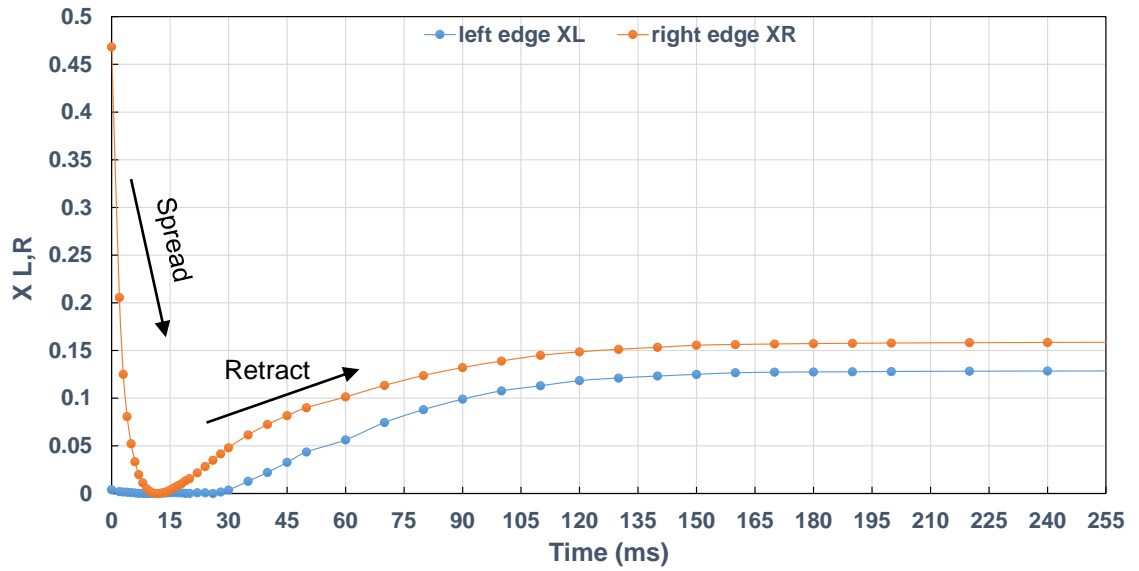


Figure 4.14 Displacement of the right and left edges of composite droplets for $U=0.6$ m/s

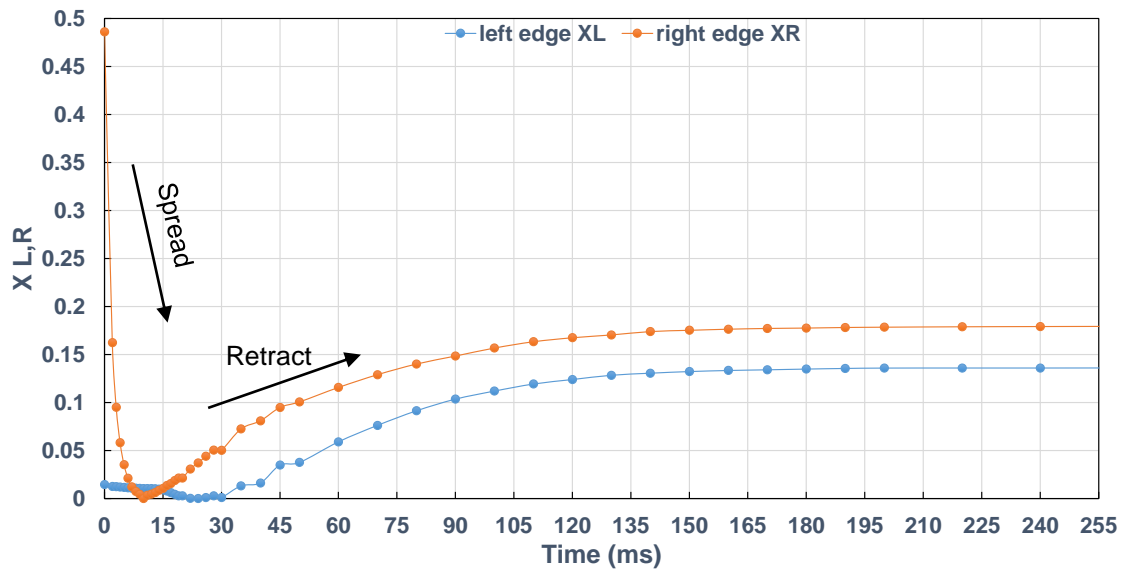


Figure 4.15 Displacement of the right and left edges of composite droplets for $U=0.8$ m/s

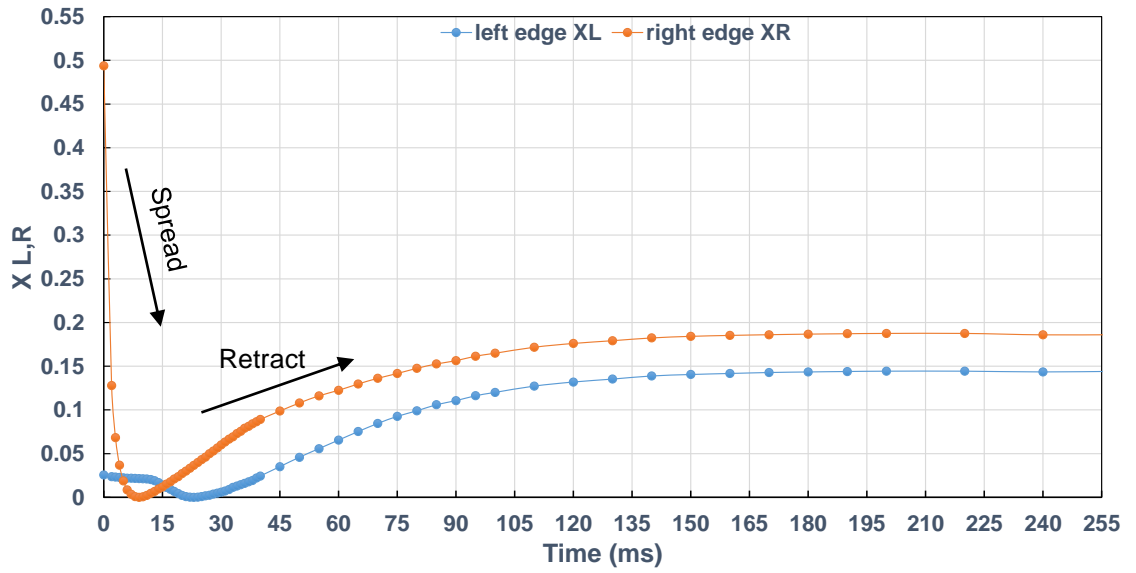


Figure 4.16 Displacement of the right and left edges of composite droplets for $U=1$ m/s

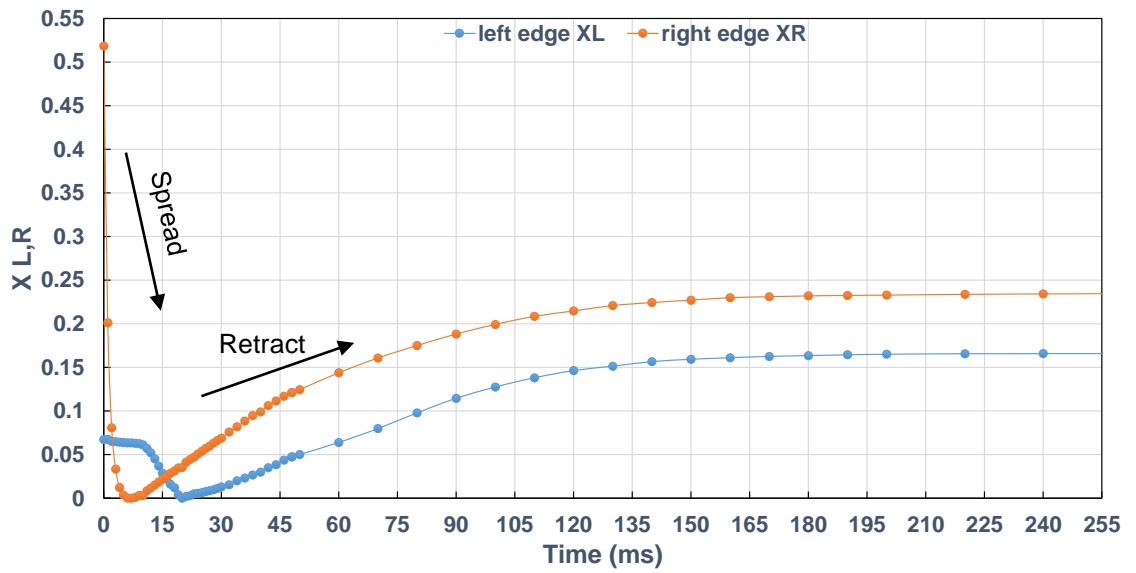


Figure 4.17 Displacement of the right and left edges of composite droplets for $U=1.5$ m/s

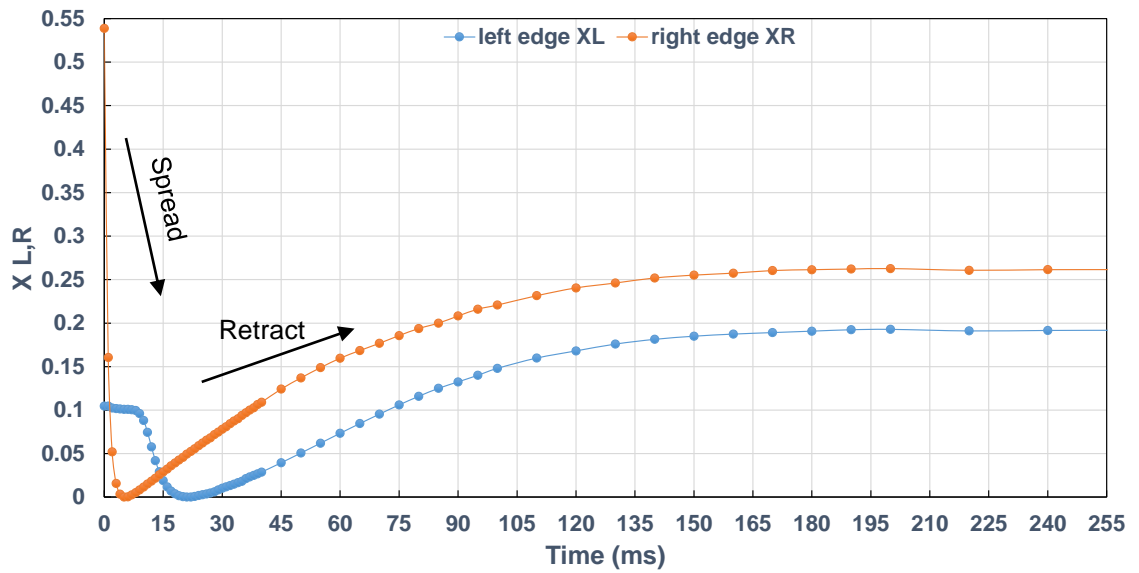


Figure 4.18 Displacement of the right and left edges of composite droplets for $U=2$ m/s

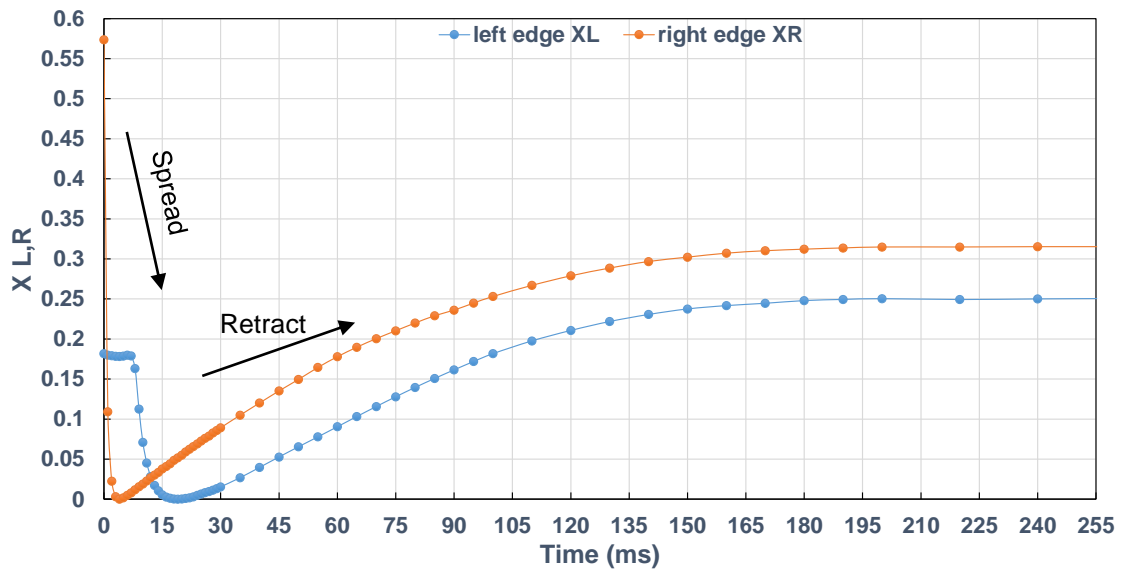


Figure 4.19 Displacement of the right and left edges of composite droplets for $U=3$ m/s

4.3.2 Effect of Surface Tension on Droplets Centre-of-Mass

In Section 4.3.1, it was found that the composite droplet location is controlled by impact velocity and liquid properties. It is also showed non-trivial trend effects (moving from right to left) in terms of the final location movement for different overlap ratios. Droplet surface tension is clearly an important variable affecting the impact process. For two droplets problem, surface tension contributes in determining the final composite location, particularly for low inertia cases. Hence, in this section, the influence of surface tension on the non-trivial trend movement and final composite location under different impact velocity for $\lambda=0.34$ is considered important.

Nominal surface tension values have been selected lower than and higher than the default value (surface tension used in section 4.3.1) in order to determine the maximum and minimum limits that defines the non-trivial trend movement at different impact velocities. Surface tension value selection relied on the systematic and calculation domain dependences but did not consider any physical applications or real surface tension values. Maximum and minimum limits have been reached determining the left and right mass centre movement for each surface tension case (Different and not real surface tension values chosen randomly for this purpose), for a particular impact velocity. Figure 4.20 specifies the different surface tension values effect on the non-trivial trend movement as presented in the composite centre-of-mass location at different impact speeds. All other parameters namely liquid viscosity, liquid density, contact angle, droplets size have been kept the same as the default case setting.

In Figure 4.20, the centre-of-mass for different surface tension cases has been compared with the initial centre-of-mass before impact takes place. For the lowest surface tension case considered ($\sigma = 4.47$ mN/m), non-trivial movement does not occur at any impact speed, with the composite centre-of-mass always located to the left side due to the effect of inertia. At the highest surface tension conducted ($\sigma = 1667.5$ mN/m), non-trivial movement almost disappeared showing the composite centre-of-mass always located to the right side at any impact speed utilized in this study due to the effect of the surface tension force. The non-trivial trend movement dominated the centre-of-mass composite location in between this range of surface tension at different initial impact speeds utilized in this study.

It is observed that at low surface tension $\sigma = 4.47, 6.71$ mN/m and low initial impact speeds of $U=0, 0.2$ m/s, the composite deposited to the right of the initial centre-of-mass. At low surface tension, the impacting droplet does not tend to be attracted to

the sessile. For low or zero impact speed, any spread after impact results in the composite moving to the right of the initial mass centre. For the low surface tension cases ($\sigma = 4.47, 6.71$ mN/m), no further centre-of-mass data was generated for velocities greater than $U=1.5$ m/s as higher impact speeds force the composite droplet further and further to the left. Similarly, no data was generated for the surface tension $\sigma = 33.55$ mN/m case for velocity greater than $U=3$ m/s.

For higher values of liquid surface tension, simulations showed that the composite droplet tends to be located to left (sessile droplet side) at zero or low initial speed ($U=0, 0.2$ m/s). This well-known process is known as “drawback” [72], and occurs when two overlapping droplets are deposited on a surface, and surface tension pulls the impact droplet toward the sessile droplet. The effect of drawback increases here as surface tension is systematically increased. This effect diminishes with increase in initial impact speed, which then dominates the competition between inertial and surface tension effects.

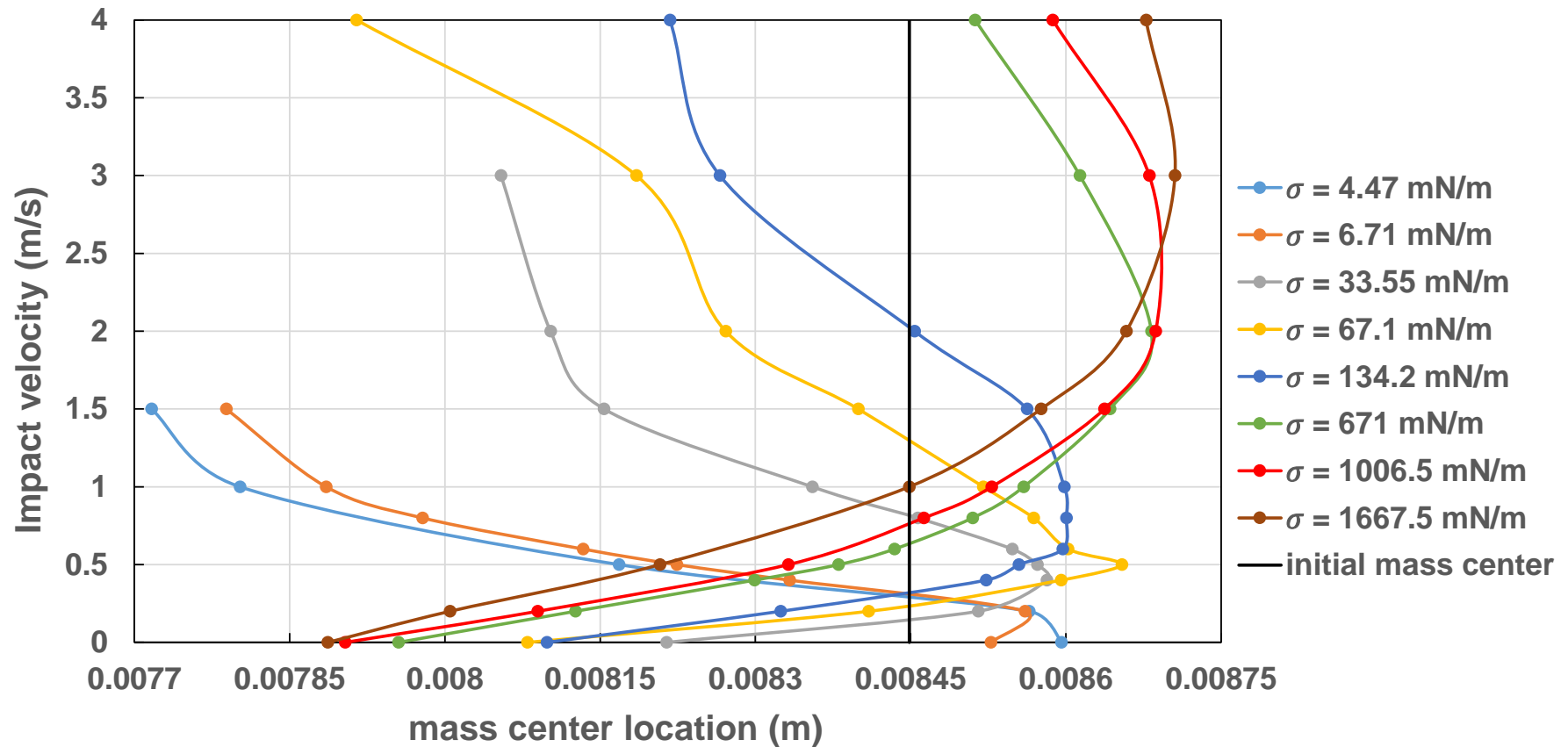


Figure 4.20 Effect of liquid surface tension on the Final Centre of Mass Location for different impact velocities

4.3.3 Effect of Viscosity on Droplets Centre-of-Mass

In Section 4.3.2, it was shown how surface tension change could affect the final foot print location indicated by the composite mass centre position. Next, all physical and geometrical parameters have been kept the same as the default values (used in section 4.3.1), apart from dynamic viscosity, which is varied to investigate its effect on the non-trivial characteristic that is final foot print location. The droplet viscosity is not important in the initial stages after impact and spreading, because the effect of inertial forces on impact dominates the process [73]. However, during the later stage of droplet coalescence, viscous forces damp motion and dissipate kinetic energy [74]. Therefore, in this section, the influence of droplet viscosity on the non-trivial trend movement and final composite location under different impact velocity for $\lambda=0.34$ is considered important.

Nominal viscosity values have been selected lower than and higher than the default value (viscosity used in section 4.3.1) in order to determine the maximum and minimum limits that defines the non-trivial trend movement at different impact velocities. Viscosity value selection relied on the systematic and calculation domain dependences but did not consider any physical applications or real viscosity values for real liquids. Maximum and minimum boundaries have been attained, determining the left and right centre-of-mass movement for each viscosity case (Different and non-real viscosities values chosen randomly for this purpose) at different impact velocities. Figure 4.21 specifies the different viscosity values effect on the non-trivial trend movement as presented in the composite centre-of-mass location at different impact speeds. All other parameters namely liquid surface tension, liquid density, contact angle, droplets size have been kept the same as the default case setting

In Figure 4.21, centre-of-mass for different viscosity cases is compared with the initial centre-of-mass before impact takes place. At the lowest viscosity considered ($\mu = 8.58$ mP.s), non-trivial movement was still dominant. Lower viscosity values resulted in droplet splashing, and so is not an appropriate case to reference the lower composite trend. For the highest viscosity case ($\mu = 3003$ mP.s), non-trivial movement has almost disappeared showing the composite centre-of-mass always located to the right side due to the influence of high viscous forces. At viscosity lower than the maximum considered, the non-trivial trend movement always dominated the centre-of-mass composite location for all impact speeds considered.

Unlike the surface tension study in the previous section, it has been shown that for all viscosity cases undertaken at $U=0$ m/s, the composite droplet located to the left of the initial centre-of-mass. The influence of viscosity becomes more prevalent when the initial impact velocity increases. By contrast with the influence of low surface tension, at low viscosities and with gradual increase, the sessile tend to be driven and the composite altimetry located to the impact droplet side. This is because the liquid becomes more adhesive to the substrate and any spread after impact results in the composite being located to the right of the initial centre-of-mass. At small values of viscosity, that is for $\mu = 8.58$ and 42.9 mP.s and highest impact speeds, no useful equilibrium droplet movement data could be generated due to droplet splashing.

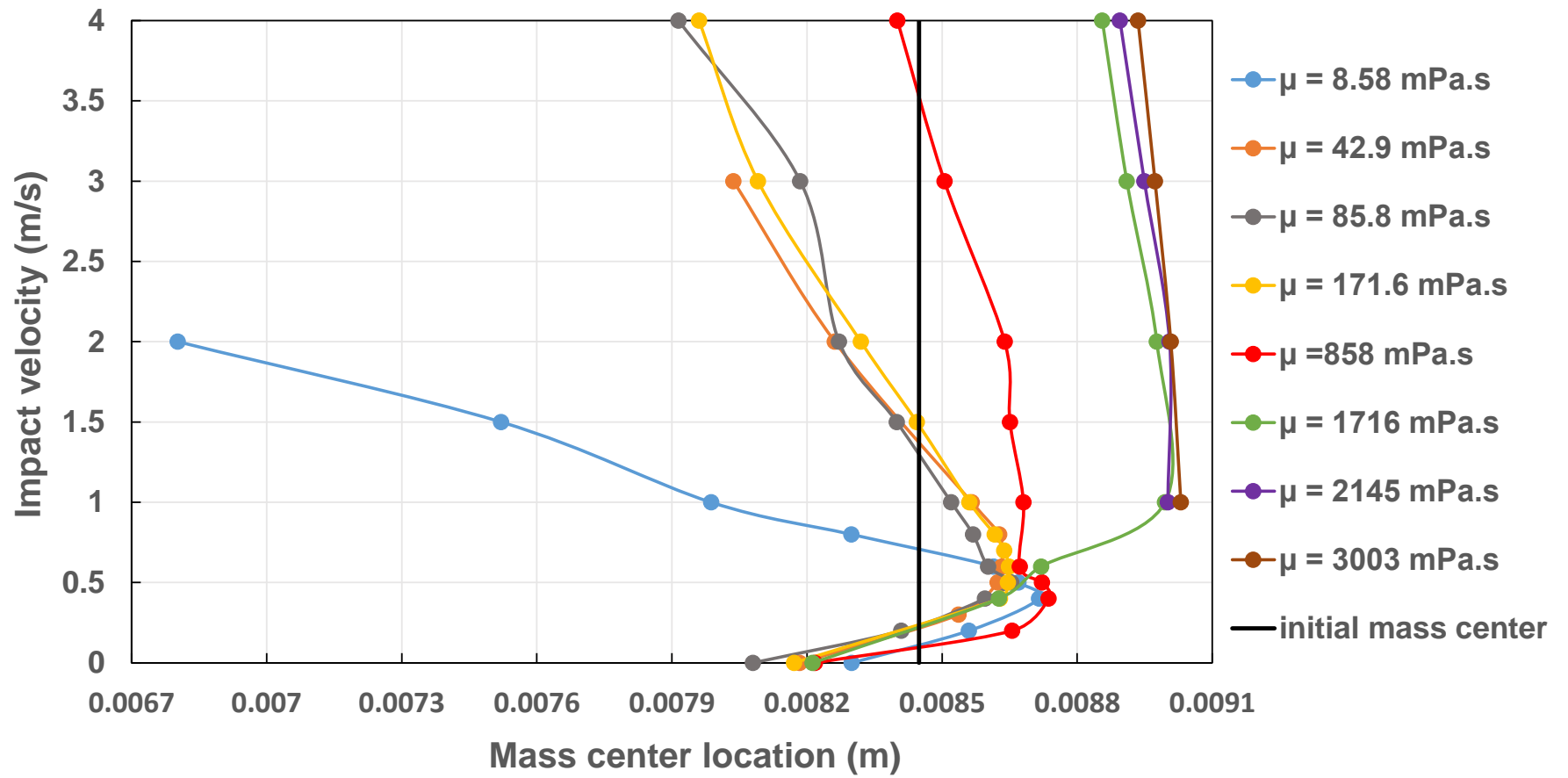


Figure 4.21 Effect of liquid viscosity property on the Final Centre of Mass Location for different impact velocities

4.3.4 Effect of Surface Tension, Viscosity and Impact Velocity on Final Composite Centre of Mass Location

The previous Sections 4.3.1 - 4.3.3 show the influence of inertia, surface tension and viscosity on the composite trend location at the final equilibrium condition. Each parameter has been shown individually to have a crucial effect on deciding the coalesced droplet movement, and has provided an indication of the composite final deposition. In this section, attention is focussed on defining a threshold line. The threshold line represents (defines) the border line that characterise whether equilibrium composite droplet located to the right or to the left relative to the initial centre-of-mass (the final composite centre-of-mass location relative to the initial centre-of-mass). It indicates the composite centre-of-mass location for the range of the real values of liquid properties (surface tension and viscosity). The threshold line has been defined for some values of velocities undertaken in this study by systematic variation of both surface tension and viscosity.

4.3.4.1 Impact Speed (U) = 0.0 m/s.

Figure 4.22 illustrates composite centre-of-mass location relative to initial centre-of-mass for $U=0$ m/s at different values of surface tension and viscosity. In general, threshold conditions have been calculated for the ranges of practical properties (surface tension as it ranges from 11.91 mN/m for Perfluorohexane to 415.41 mN/m for Mercury, and viscosity as it ranges from 0.09 mPa.s for Propylene to 950 mPa.s for Glycerine) of liquids existed and used in industrial applications. The current study considered the liquid of glycerol-water mixture as a reference for high viscous liquid and water liquid as a reference for high surface tension liquid. Therefore, the physical properties implemented in this investigation considered values of viscosity and surface tension lower than those for glycerol-water and water liquids respectively. Red spots in the figure represent a case where the composite mass centre locates to the left side relative to the initial mass centre. Green spots in the figure represent a case where the composite mass centre located on the right side relative to the initial centre-of-mass.

The threshold map presented in Figure 4.22 shows that centre-of-mass to the left was dominant for the majority of the map for the surface tension range ($\sigma = 10 - 70$ mN/m) and at any of the viscosities considered ($\mu = 5 - 90$ mPa.s); these ranges include most practical liquids. For the ink jetting applications, the physical properties for the liquid varies depending on the percentage of the water in the mixture, therefore, its surface

tension could range $\sigma = 28 - 56$ mN/m and its viscosity could range $\mu = 3 - 35$ mPa.s [75]. Changing centre-of-mass location from left to right has appeared only at very small values of surface tension (less than the minimum surface tension value for the practical liquids) $\sigma = 5 - 10$ mN/m, and relatively high range of viscosity (within the range of the practical liquids) $\mu = 40 - 90$ mPa.s. From the threshold map in Figure 4.22, final centre-of-mass composite location can be predicted at $U=0$ m/s. In fact, the threshold at $U=0$ m/s presented in a range of surface tension (5 - 10 mN/m) which are not applicable for most common liquids including those utilised in ink jet applications [76]. Moreover, the range of liquid viscosities considered in this investigation represent moderate to high viscosity liquids if compared relatively with water ($\mu=0.89$ mPa.s) or any other low liquid viscosity at room temperature $T=25$ C° [76].

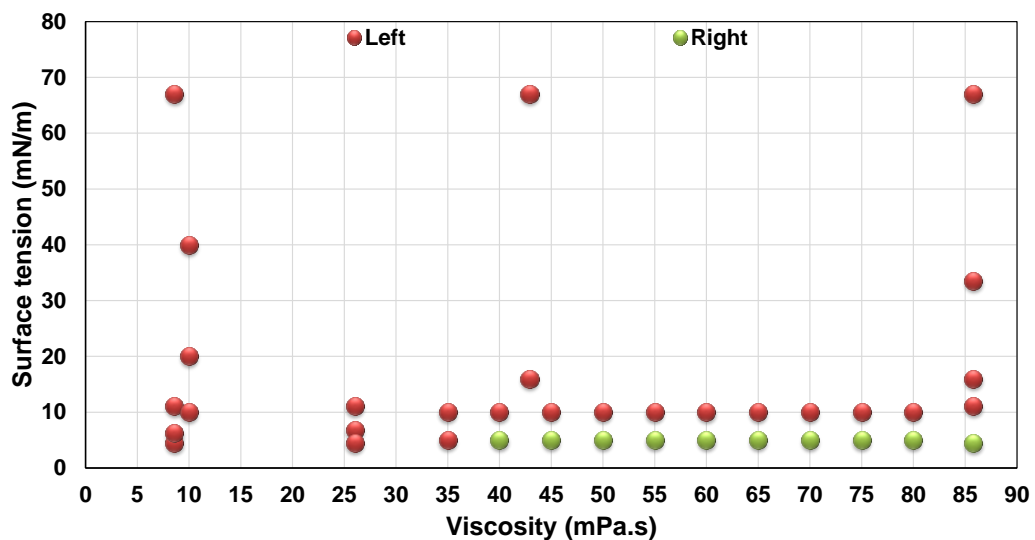


Figure 4.22 Threshold splitting between right and left composite mass centre location relative to the initial mass centre for $U=0$ m/s at different surface tension and viscosity

As shown in Figure 4.22, threshold line observed within a high range of viscosity ($\mu=40-90$ mN/m) and the composite droplet moving from the right side to the left was controlled by the influence of surface tension ($\sigma=5-10$ mN/m). These observations are consistent with those discussed in Section 4.3.3 previously for different liquid's viscosities. When surface tension increases (from 5 to 10 mN/m), the centre-of-mass location crosses the initial centre-of-mass from the right to the left. At $U=0$ m/s or very low impact speed, the sessile droplet tends to pull the falling one towards her according

to the established phenomena in literature called “drawback” [17], [77] and [78]. Therefore, the “drawback” phenomena is considered the primary reason behind locating the final composite to the left side of the initial centre-of-mass for higher surface tension values. It is well-known for high viscosity range ($\mu = 40 - 90$ mPa.s), adhesive forces increase and the composite tends to be pinned more strongly to the substrate. Hence, the composite finishes on the right side of the initial centre-of-mass at lower surface forces ($\sigma = 5$ mN/m).

4.3.4.2 Impact Speed (U) = 0.2 m/s.

Figure 4.23 illustrates the composite centre-of-mass location relative to initial centre-of-mass for $U=0.2$ m/s at different values of surface tension and viscosity. As shown in Figure 4.23, two threshold lines (lower and upper) appear within the viscosity and surface tension limits considered in this study for impact speed $U=0.2$ m/s. As for the lower threshold, kinetic energy presented via the impact speed has induced the opposite effect to that observed when $U=0$ m/s in Figure 4.22. The influence of the surface tension driven force [17], after unpinning the contact line (as also observed in Section 4.3.1), has resulted in the composite being pulled to the right for higher surface tension values and low viscosities ($\mu = 5 - 45$ mPa.s). For higher viscosities ($\mu > 45$ mPa.s), the liquid becomes more resistant to flow, with the composite droplet located to the right side at low surface tension ($\sigma < 5$ mN/m).

Representing the problem parameters in non-dimensional form may help in identifying general trends of the composite movement relative to the initial centre-of-mass. Surface tension is embedded within the Weber number (We) and viscosity is embedded within the Reynolds number (Re). Composite centre-of-mass and initial centre-of-mass have been non-dimensionalized by dividing the difference between the final composite and the initial centre-of-mass over the initial droplet diameter.

Figure 4.24 shows the composite centre-of-mass location relative to initial centre-of-mass for $U=0.2$ m/s presented in terms of Reynolds number (Re) and Weber number (We). The lower threshold line presented in Figure 4.23 corresponds to the upper threshold condition in Figure 4.24. From the upper threshold in Figure 4.24, an increase in Re (interpreted in viscosity reduction when density is constant) results in an increase in the region where, the final composite droplet position is to the left relative to the initial centre-of-mass. Hence, the areas occupied by the composed droplets to the left side

showed domination over the areas occupied by the composite located to the right side as mapped in Figure 4.24.

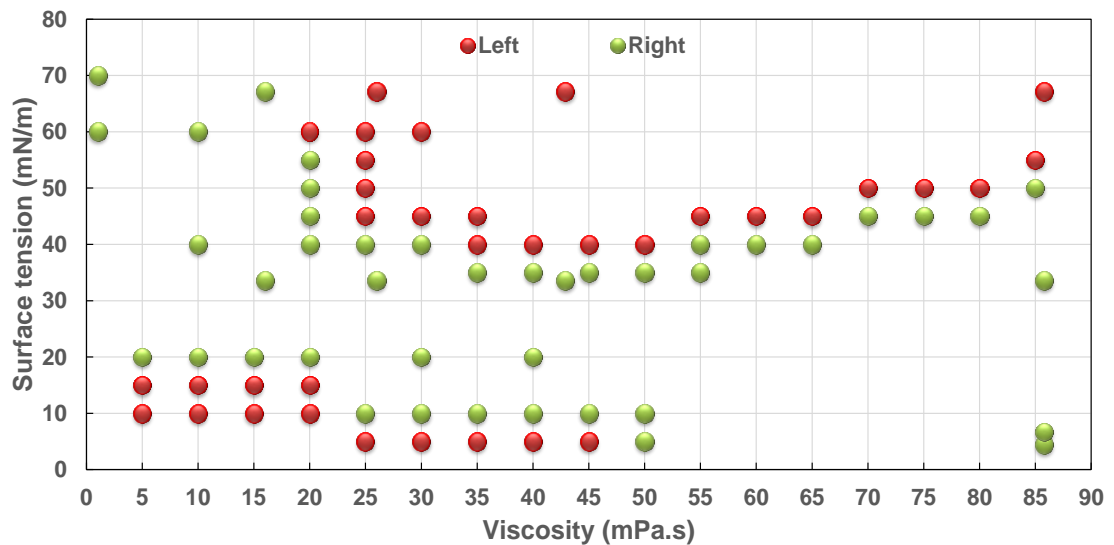


Figure 4.23 Threshold splitting between right and left composite centre-of-mass location relative to the initial centre-of-mass for $U=0.2$ m/s at different surface tension and viscosity

It is also shown in Figure 4.24 that for the upper threshold and at low Reynolds number (Re), Weber number is increased. This can be interpreted as the importance of both the viscous and surface tension forces in determining the final centre-of-mass position. The composed centre-of-mass for low Reynolds number corresponds to a threshold at high Weber number, indicating that lower surface tension forces were sufficient to balance viscous forces and hence the composite location.

The appearance of the upper threshold line in Figure 4.23 is attributed to the “drawback” phenomena discussed in Section 4.3.4.1. At zero or low impact speed of $U=0.2$ m/s, the sessile droplet tend to pull the falling droplet towards it, therefore, the final composite droplet is located to the left of the initial centre-of-mass. This occurs for higher values of surface tension, which is an influential parameter for the “drawback” phenomena. Notwithstanding the differences in the threshold line trend behaviour, it is proposed that for zero or low impact speed ($U=0$, $U=0.2$ m/s) cases, the upper threshold in Figure 4.23 corresponds in the “drawback” phenomena to the threshold line appeared in Figure 4.22 at $U=0$ m/s.

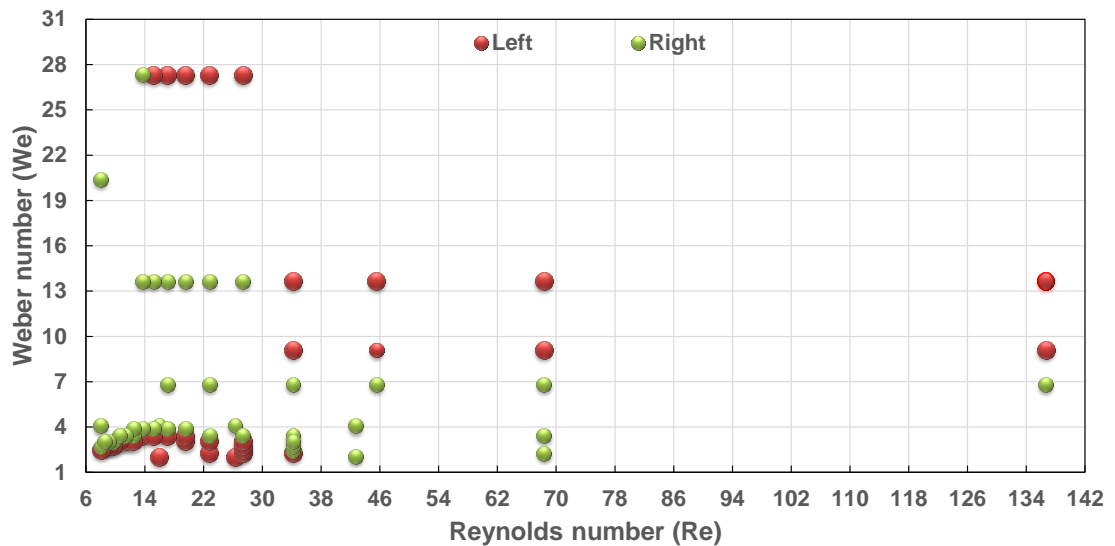


Figure 4.24 Threshold splitting between right and left non-dimensional composite mass centre location relative to the initial mass centre for $U=0.2$ m/s at different Re and We

4.3.4.3 Impact Speed (U) = 0.5 m/s.

Figure 4.25 illustrates the composite centre-of-mass location relative to initial centre-of-mass for $U=0.5$ m/s at different values of surface tension and viscosity. Figure 4.26 illustrates non-dimensionally the composite centre-of-mass location relative to initial centre-of-mass for $U=0.5$ m/s presented in terms of Reynolds number (Re) and Weber number (We). Surface tension, viscosity and impact speed are all important parameters involved in the process of droplets impact and coalescence and the effect on the final footprint location. Information from previous studies concerning the impact, coalescence and recoil droplet processes are informative and now summarised in to assist in analysing and understanding the current threshold trends.

- During the initial period of droplet spreading, inertial forces are much larger than surface tension and viscous forces [73].
- Viscous effects decrease the spread of drop impact with the time of maximum expansion, which is dependent on a balance between inertia, viscous forces and capillarity [74].
- Capillary forces become increasingly important towards the end of droplet spreading when inertial forces become small [79].

- The droplet reached its maximum extent, after which surface tension and viscous forces overcame inertia. Once droplets reached their maximum extension, surface tension forces caused recoil. Droplet recoil, though, is controlled by capillary forces [73].
- Qualitative inspection of predicted droplet shapes showed that they were sensitive to surface tension values during the period when the droplet was recoiling [73].

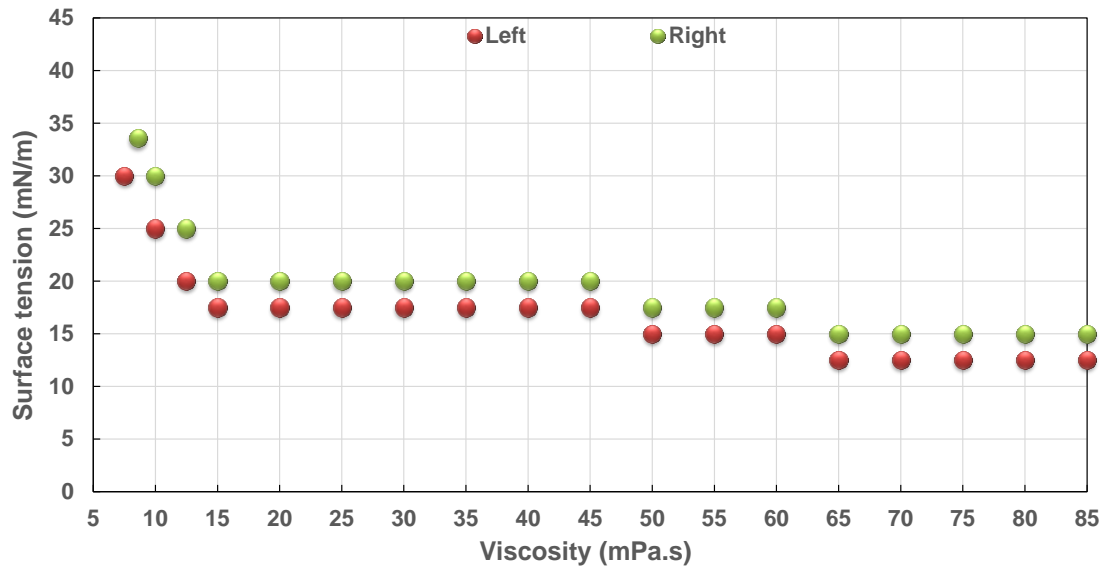


Figure 4.25 Threshold splitting between right and left composite centre-of-mass location relative to the initial centre-of-mass for $U=0.5$ m/s at different surface tension and viscosity

From data results, at low Reynolds number ($Re=20-27$ corresponding to high values of liquid viscosity $\mu = 65 - 85$ mPa.s), the threshold line for composite droplet locations associated with high values of Weber number ($We=65-68$ corresponding to low values of surface tension $\sigma = 12.5 - 15$ mN/m). For higher liquid viscosity, the coalesced droplets spread less because the liquid becomes adhesive and resists inertia. If viscosity increases further, shear stress forces increase due to higher friction forces between liquid particles which dampen the motion. Therefore, lower values of surface tension ($\sigma = 12.5 - 15$ mN/m as shown in Figure 4.25) were enough to overcome the less deformed composite resulting from coalescence of the two droplets.

As shown in Figures 4.25 and 4.26, the aforementioned details change when a small increase in Reynold number ($Re = 28-34$) takes place. Lower Weber number ($We = 48-65$) which corresponds to higher values of surface tension $\sigma = 15 - 17.5$ mN/m presented in this range for higher Reynolds number. The results showed for the threshold cases of $U=0.5$ (and similarly applicable for the threshold of case $U=0.2$) that any reduction in viscosity is accompanied by an increase in surface tension to maintain the needed equilibrium forces to overcome deformation and liquid spread after impact and coalescence.

A threshold range for higher range of Reynolds number ($Re = 37-113$) corresponds to a lower, constant Weber number range ($We = 43-84$) as observed in Figure 4.26. Beyond this Reynolds number range, any further increase in Reynold number ($Re = 138-175$) shows a continuous decrease in Weber number ($We = 45-25$). When Reynold number exceeds the value $Re=113$, two droplets showed a fairly arbitrary oscillatory movement after impact and coalescence due to the small value of dynamic viscosity which reflected in reducing the damping forces over inertia forces as represented by the higher Reynold number. Therefore any increase in Reynold number beyond $Re=113$ gives rise to lower Weber number at transition and higher surface tension forces which increases the cohesion forces more sensibly to recoil the composite to its equilibrium condition.

From investigations into the effect of impact speed on composite droplet location at different values of surface tension in Section 4.3.2, it was predicted that the composite droplet located right of the initial centre-of-mass at $U=0.5$ m/s and $\lambda=0.34$. This is applicable for liquids with surface tension ($30 \leq \sigma \leq 135$) mN/m, and for any liquid viscosity value, even for water, considered a reasonably low viscous liquid, the composite droplet would be located relatively right of the initial mass centre as shown in Figure 4.25. Based on results in Section 4.3.1, regardless of the initial centre-of-mass position, the composite located initially to the right after impact and coalescence for a low range of impact speed. This can be illustrated due to the poor dynamical effect generated from the impact side results in that a smaller wave grows after impact to move to the opposite side and unpin the far away edge (left edge of sessile). Low impact speed (low inertia) results in less particle moving from the impact side to the sessile side and hence generates lower composite spread to the opposite side of impact.

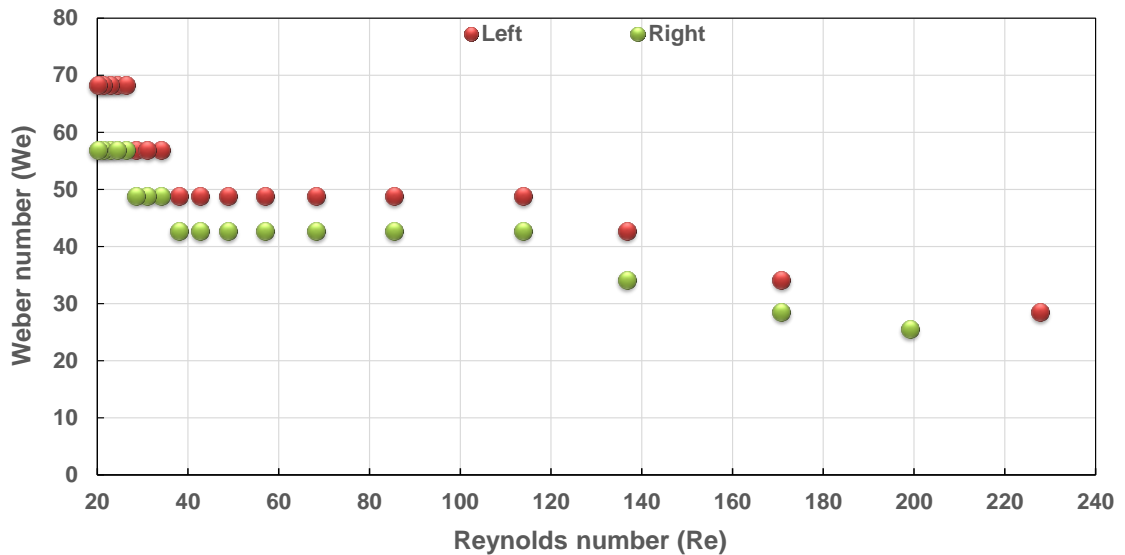


Figure 4.26 Threshold splitting between right and left non-dimensional composite mass centre location relative to the initial mass centre for $U=0.5$ m/s at different Re and We

In order to investigate the effect of surface tension on moving composite centre-of-mass from the right to the left side relative to the initial centre-of-mass at any viscosity value, two different values of surface tension cases which have same viscosity value are tracked from the early stage of coalescence until equilibrium condition is realised to illustrate that effect. The value of viscosity has been selected randomly ($\mu=25$ mPa.s) for this purpose, Figure 4.27 illustrates the effect of different surface tension values on the final composite centre-of-mass location relative to the initial centre-of-mass across the threshold line.

For the time 0-15 (ms) as shown in Figure 4.27,(a) - (d), the right edge for both cases of different surface tension are identical in location throughout the coalescence stage up to the maximum spread. When the right edge starts to recoil at time=20 ms as shown in Figure 4.27(e), differences started to appear in the contact line with the substrate showing faster recoil for the higher surface tension case. On the other hand, the left edge continues to spread up to time=35 ms as shown in Figure 4.27(h) for the lower surface tension case, whereas it has already stopped for higher surface tension case at time=30 ms, as shown in Figure 4.27(g).

Higher surface tension implies physically that higher forces are required to pull the surface back to equilibrium for a unit length of spread or unit circumference of droplet. Less spread at the left edge and faster recoil experienced for the higher surface tension

case is shown in Figures 4.27(g)-(j). Hence the two droplets at the equilibrium condition have shown the composite centre-of-mass to be located to the right of the initial centre-of-mass for the higher surface tension as shown in Figure 4.27(k) and 4.27(l). Nevertheless, the composite centre-of-mass locates to the left side of the initial centre-of-mass for the lower surface tension case due to the relative extra spread experienced to the left side for lower surface tension case.

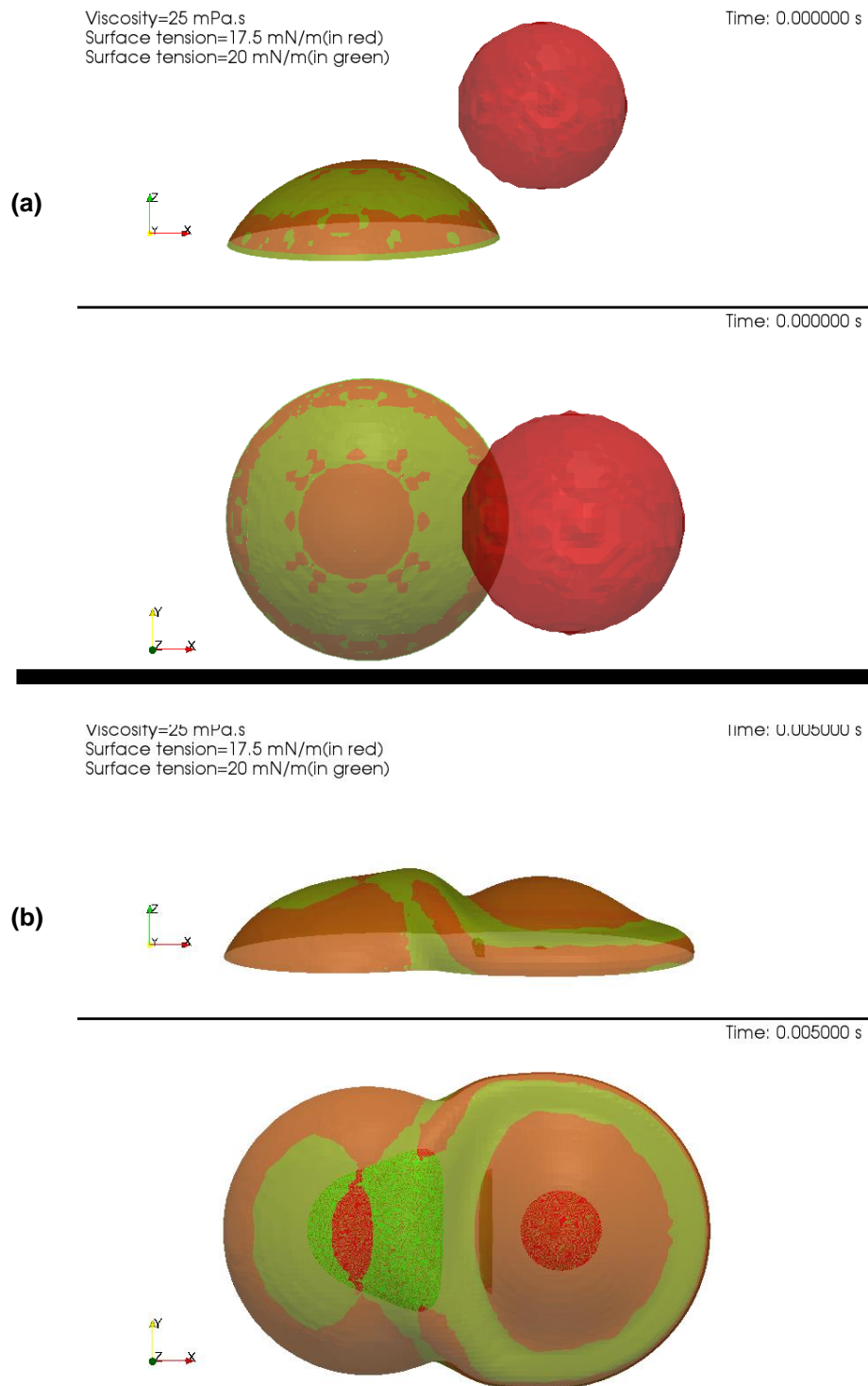
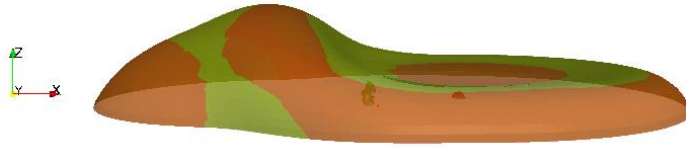


Figure 4.27 Enlarged picture showing the top and side view of local free surfaces for coalescence of two different surface tension droplets at constant viscosity. (a), (b), (c), (d), (e), (f), (g), (h), (i), (j), (k), (l) at time= 0, 5, 10, 15, 20, 25, 30, 35, 50, 100,1100 and 5100 ms respectively

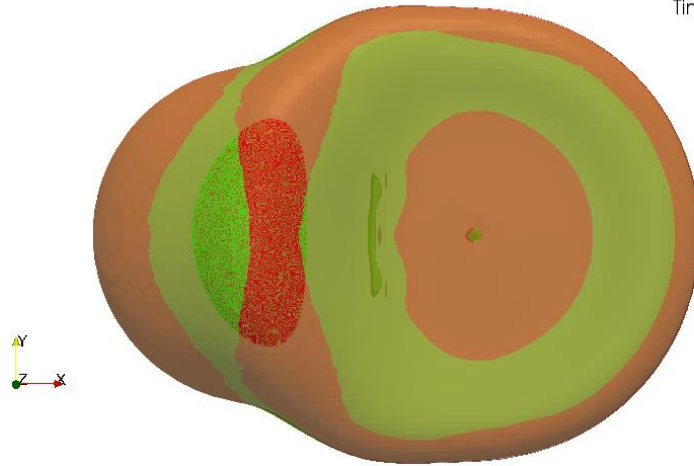
Viscosity=25 mPa.s
Surface tension=17.5 mN/m(in red)
Surface tension=20 mN/m(in green)

Time: 0.010000 s

(c)



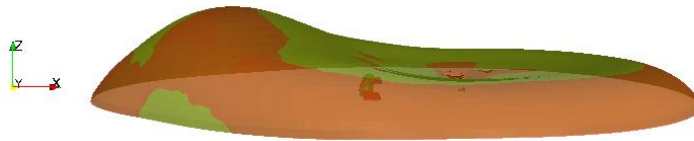
Time: 0.010000 s



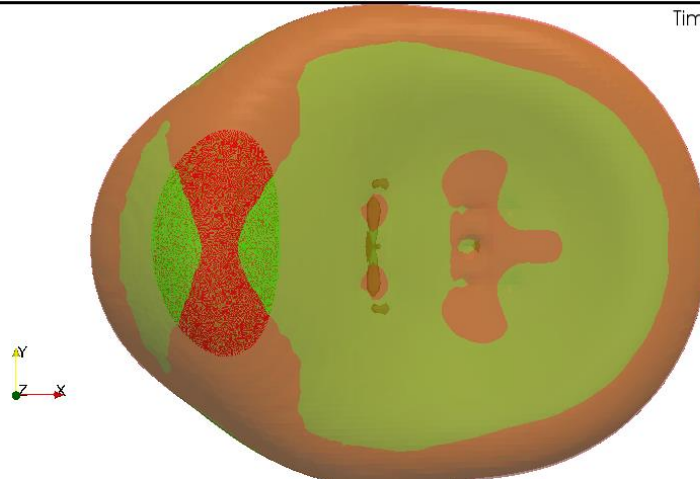
Viscosity=25 mPa.s
Surface tension=17.5 mN/m(in red)
Surface tension=20 mN/m(in green)

Time: 0.015000 s

(d)

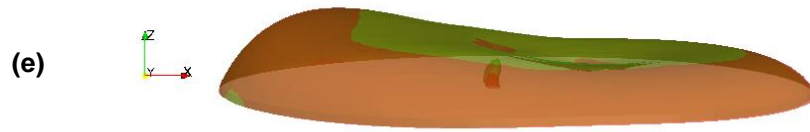


Time: 0.015000 s

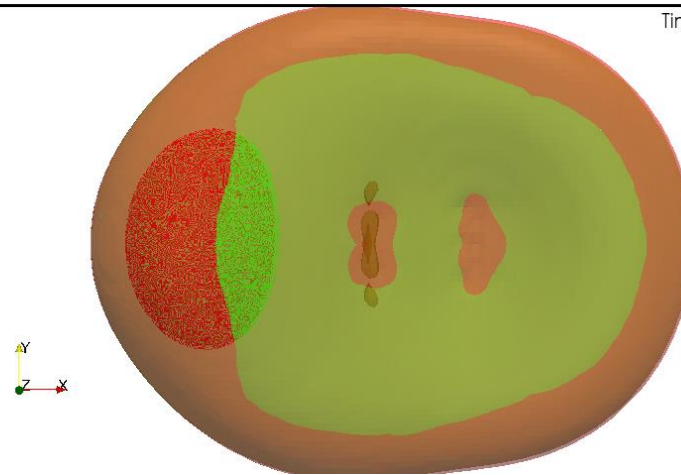


Viscosity=25 mPa.s
Surface tension=17.5 mN/m(in red)
Surface tension=20 mN/m(in green)

Time: 0.020000 s



Time: 0.020000 s

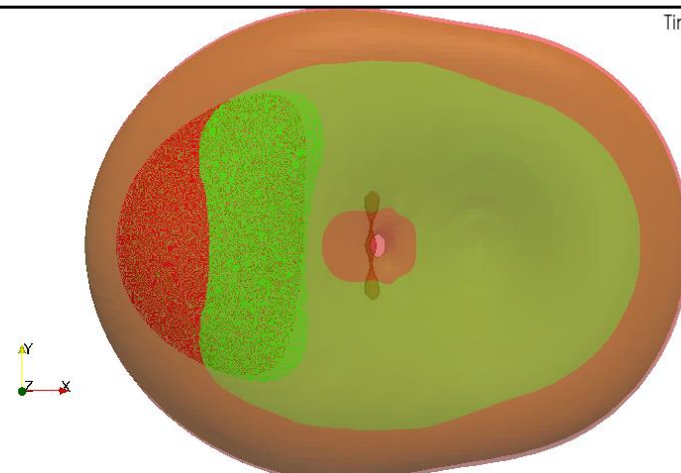


Viscosity=25 mPa.s
Surface tension=17.5 mN/m(in red)
Surface tension=20 mN/m(in green)

Time: 0.025000 s



Time: 0.025000 s

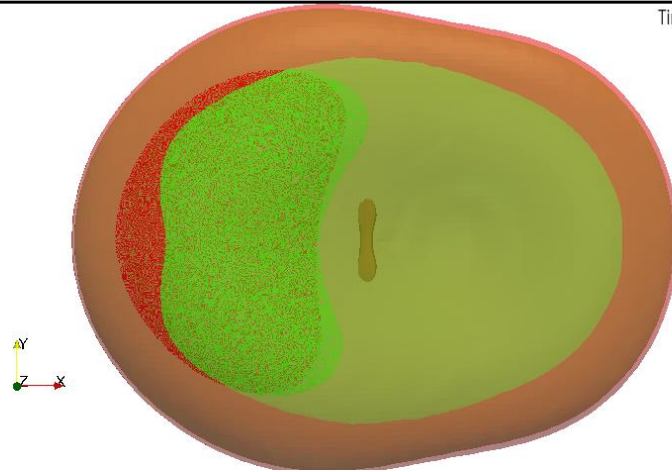


Viscosity=25 mPa.s
Surface tension=17.5 mN/m(in red)
Surface tension=20 mN/m(in green)

Time: 0.030000 s



Time: 0.030000 s

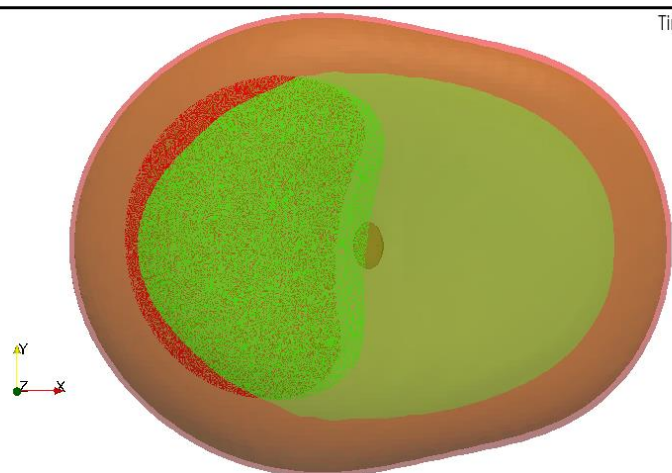


Viscosity=25 mPa.s
Surface tension=17.5 mN/m(in red)
Surface tension=20 mN/m(in green)

Time: 0.035000 s



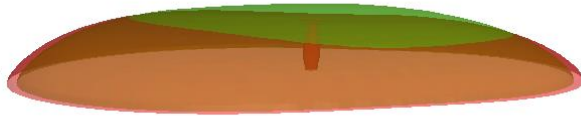
Time: 0.035000 s



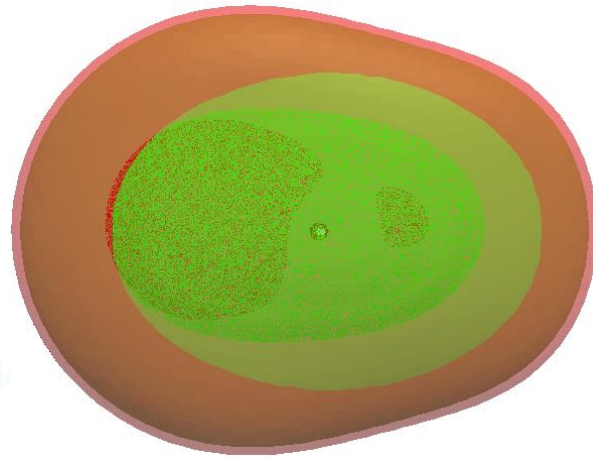
Viscosity=25 mPa.s
Surface tension=17.5 mN/m(in red)
Surface tension=20 mN/m(in green)

Time: 0.050000 s

(i)



Time: 0.050000 s



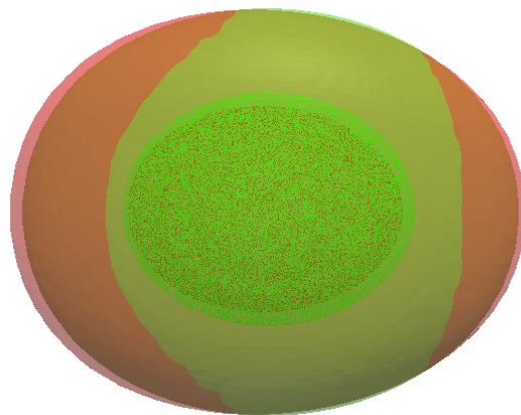
Viscosity=25 mPa.s
Surface tension=17.5 mN/m(in red)
Surface tension=20 mN/m(in green)

Time: 0.100000 s

(i)



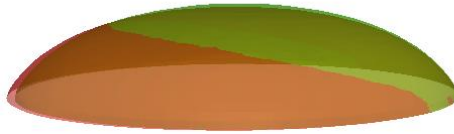
Time: 0.100000 s



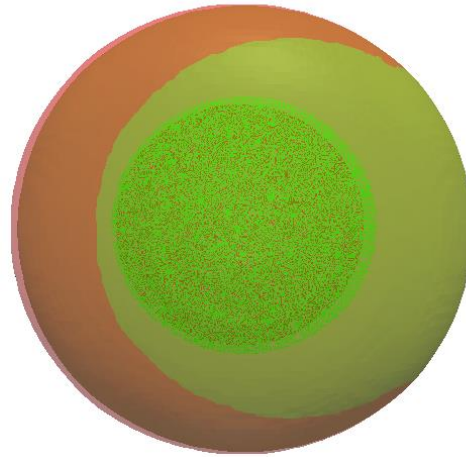
Viscosity=25 mPa.s
Surface tension=17.5 mN/m(in red)
Surface tension=20 mN/m(in green)

Time: 1.100000 s

(k)



Time: 1.100000 s



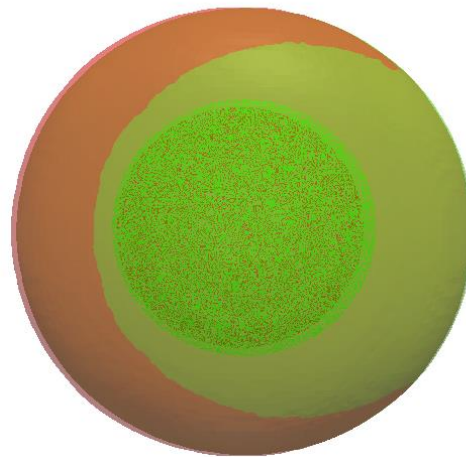
Viscosity=25 mPa.s
Surface tension=17.5 mN/m(in red)
Surface tension=20 mN/m(in green)

Time: 5.100000 s

(l)



Time: 5.100000 s



4.3.4.4 Impact Speed: U= 0.8, U=1 and U=1.2 m/s

As shown previously from the lower threshold line of the case U=0.2 in Figure 4.23 and the threshold line in Figure 4.25 of the case U=0.5, an increase in impact speed moves the threshold line up to be located at the higher range of surface tension values. In comparing both cases of U=0.2 m/s and U=0.5 m/s, it is anticipated that any further increase of impact speed would result in the area associated with left relative movement dominating over the right one. This is attributed to the higher inertia associated with higher impact speed which results in the composite being pushed further to the left. Hence it is expected that the threshold line would be located at higher range of surface tension values than those predicted at lower impact speed and for same liquid viscosity values.

Figure 4.28 illustrates the composite centre-of-mass location relative to initial centre-of-mass for U=0.8 m/s at different values of surface tension and viscosity. When impact speed increased to U=0.8, the threshold line became more linear for a wide range of liquid viscosity ($\mu=20-85$ mPa.s) when compared with the non-linear trend for U=0.5. Moreover, as anticipated, the threshold line for the U=0.8 case showed greater domination of the composite centre-of-mass to the left over the right. Therefore, the threshold line relocated as expected at higher surface tension values for the limits ($\sigma = 30-65$ mN/m) compared with the U=0.5 case.

The aforementioned observations were endorsed at higher impact speed for U=1 m/s and U=1.2 m/s as shown in Figures 4.29 and 4.30 respectively. The threshold trend remained linear for a wide viscosity range and took higher levels of surface tension as the velocity increased. This shows that the composite centre-of-mass more often located to the left side relative to the initial centre of mass. For the surface tension range undertaken in this study ($\sigma= 0-70$ mN/m), no threshold line was observed when velocity increased higher than U=1.2 m/s, and so it is reasonably assumed that the composite centre-of-mass would be always located left of the initial centre-of-mass beyond that velocity.

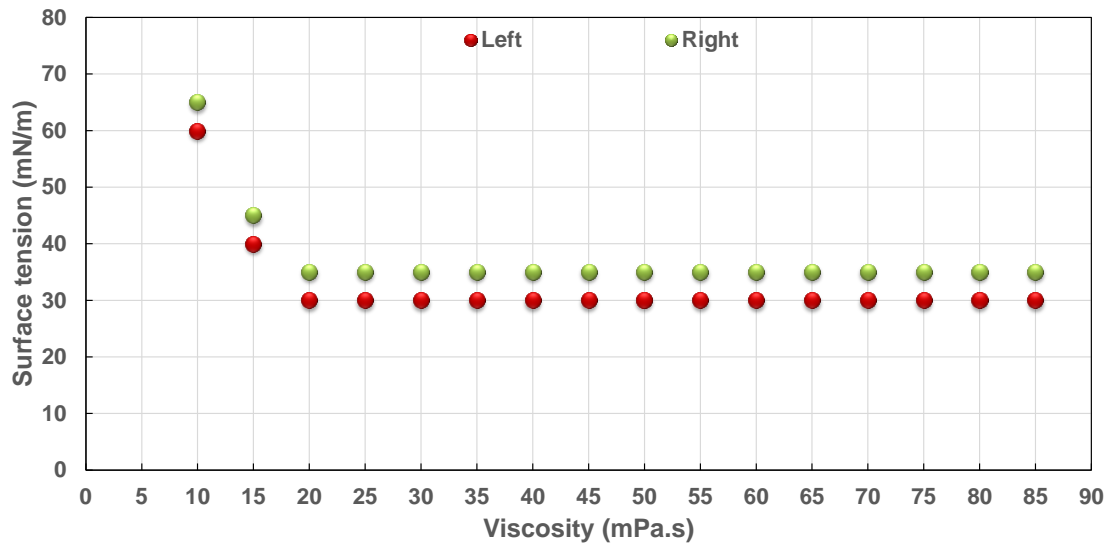


Figure 4.28 Threshold splitting between right and left composite centre-of-mass location relative to the initial centre-of-mass for $U=0.8$ m/s at different surface tension and viscosity

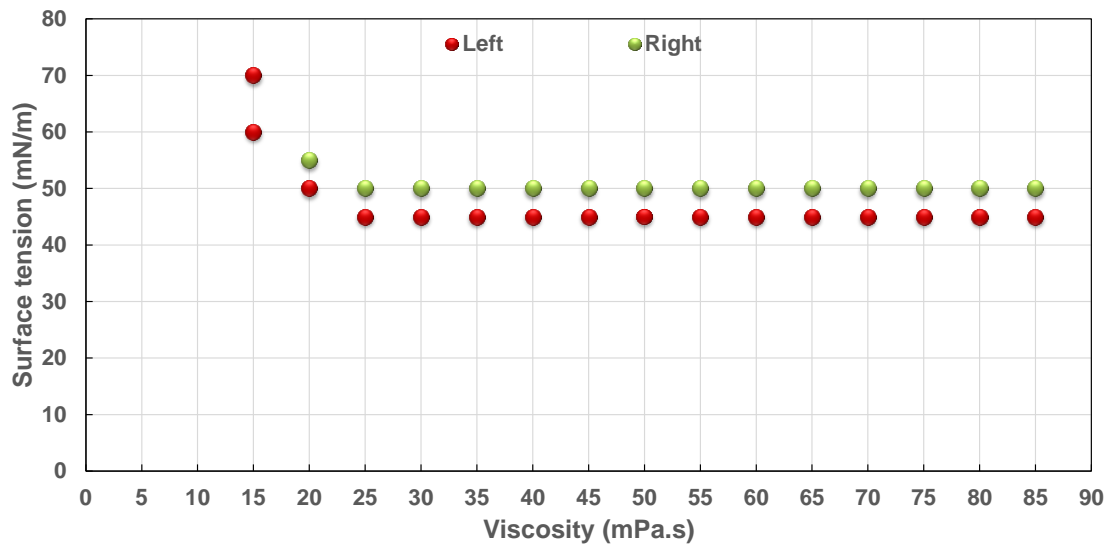


Figure 4.29 Threshold splitting between right and left composite centre-of-mass location relative to the initial centre-of-mass for $U=1$ m/s at different surface tension and viscosity

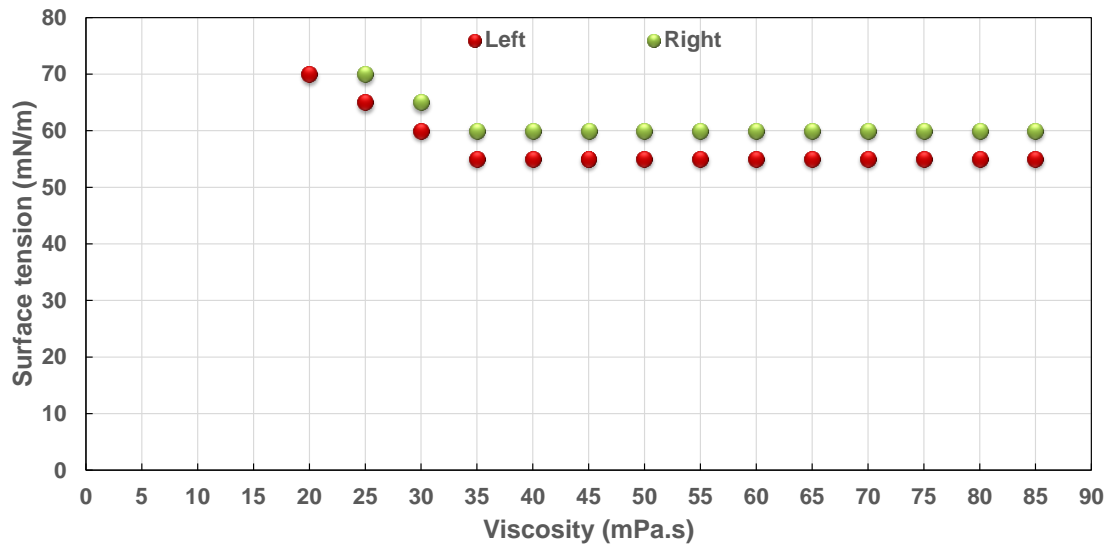


Figure 4.30 Threshold splitting between right and left composite centre-of-mass location relative to the initial centre-of-mass for $U=1.2$ m/s for different surface tension and viscosity

4.4 Summary and Conclusions

First in this chapter, the numerical setting used for two droplets problem (illustrated in Appendix A.2) was validated with experimental study [24]. Then, effect of lateral separation, impact speed and liquid properties on composite droplet location has been conducted numerically using the OpenFOAM and *sclsVOFFoam* solver. It was found that composite droplet centre-of-mass location related to initial centre-o-mass was affected by the impacting droplet velocity and liquid properties, but showed some non-trivial final location movement for different overlap ratios used in this research. The findings may be summarized thus:

- Different types of forces (inertia, viscous and surface forces) are embedded in the impact phenomena of two droplets. Those forces considered all important in the final composite droplet location.
- Left edge retraction under the effect of surface forces was considered the reason for the composite droplet locating to the side of the impact droplet at zero or low inertia conditions ($U=0-0.5$ m/s for the case of $\lambda=0.34$).
- Left edge spreading under the effect of impact speed (inertia) was considered the reason of locating composite droplet to the opposite side of impact droplet at higher velocity ($U=0.6 - 3$ m/s for the case of $\lambda=0.34$).

- For high value of surface tension, no inertia effect, composite droplet always located to impact side. Opposite happens for lower value of surface tension, inertia dominates and mass centre moves to the opposite direction.
- For high value of viscosity, no inertia effect, composite droplet always located to impact side. Right and left composite droplet trend always dominated for the lower value of viscosity, whereas at high impact speed, inertia dominates and mass centre moves to the opposite direction.
- At zero impact speed and different values of surface tension and viscosity, threshold line trend of the centre-of-mass relative to the initial centre-of-mass dominated by the “drawback” phenomena and the surface tension effect. Composite centre-of-mass located left of the initial centre-of-mass have dominated the map range of different viscosity and surface tension undertaken in this study for $U=0$ m/s.
- At low impact speed $U=0.2$, inertia influenced on the composite centre-of-mass drawing the sessile to the impact side. Therefore, due to unpinning and surface tension driven force phenomena composite located right relative of the initial centre-of-mass as presented in the lower threshold line. Effect of drawback at low inertia and high surface tension appeared in the upper threshold of the case $U=0.2$.
- At impact speed $U=0.5$, composite centre-of-mass located to the left dominated over those located to the right relative to the initial centre-of-mass due to the effect of inertia. The threshold line presented at higher surface tension values in the viscosity-surface tension map than the $U=0.2$ m/s.
- Gradual increase of impact speed as in $U=0.8, 1, 1.2$ m/s resultant in the area occupied by the composite centre-of-mass located to the left side dominated over the area for those located to the right relative to the initial centre-of-mass due to the effect of inertia as shown on the viscosity-surface tension map. Therefore, threshold line moves up to higher surface tension values as impact speed increases.
- At any value of viscosity, surface tension is the dominate parameter to decide composite droplet centre-of-mass location whether to the right or to the left relative to the initial centre-of-mass.

Chapter 5 High Speed Laminar Jet Burst Phenomena

5.1 Introduction

The aim of this research is to investigate the characteristics and mechanisms contributing to the bursting phenomena of a laminar liquid jet. Different inlet boundary condition velocity profiles ranging from fully parabolic to semi-turbulent and completely flat (top hat) turbulent are employed to study their effect on such phenomena. In this chapter, first, the numerical setting (illustrated in Appendix A.3) used to study the liquid jet problem was validated. At constant liquid jet Reynolds number $Re=2200$, various fluid properties and different ambient properties have been used to investigate their effect on the laminar jet burst phenomena. The results illustrating the mechanism of liquid jet burst phenomena have been obtained using the OpenFOAM (*scIsVOFFoam* (VOF+LS) solver) and run in parallel using High Performance Computing (HPC). Results are post-processed using ParaView software on local desktops (PCs). Each set of results are presented fully in the appendices then discussed individually. Results were compared and summarised at the end of the chapter.

5.2 Validation of the Numerical Setting Used for Liquid Jet Problem

To validate OpenFOAM solvers, 3-D numerical simulation of the breakup length of axisymmetric laminar liquid jets at low Weber number (We) are conducted. Two problems; $We=3.1$ and $We=7.45$ were modeled, and compared with experiment study [1] and the numerical result [2]. Except the dimensions, the geometrical setting used for both cases here similar to the liquid jet burst case as presented in Figure A.3.1 (Appendix A.3). The initial condition is given zero for the velocity and the pressure. The no-slip ($U=0$) and Neumann boundary condition for pressure are used at all the geometrical boundaries (wall) for the liquid jet problems. For both cases, fixed laminar (parabolic $U_{mean}=0.42$ m/s) for velocity and Neumann for pressure are given for inlet flow boundary condition. Geometrical and mesh details for both cases are presented in Table 5.1. The physical parameters for $We=3.1$ and $We=7.45$ are presented in Table 5.2 and Table 5.3, respectively.

The numerical results of $We=3.1$ obtained using *interFoam* (VOF) and *scIsVOFFoam* (VOF+LS) are presented in Figures 5.1 and 5.2, respectively. The numerical results of $We=7.45$ obtained using *scIsVOFFoam* (VOF+LS) are presented in

Figure 5.3. Figures 5.4 and 5.5 show the numerical results obtained by Pan [58] for $We=3.1$ and $We=7.45$, respectively. Also, Figure 5.6 shows the comparison between the current results using *sclsVOFFoam* and both previous experimental [80] and numerical results [58]. The numerical results showed good agreement with previous studies (experimental breakup length was calculated from Sallam [80] correlation for both Weber number cases and presented in the white bar next to the jet column) as shown in Figures 5.1-5.3.

Table 5.1 Geometrical and mesh details of $We=3.1$ and $We=7.45$ laminar jets

	<i>We=3.1 laminar jet</i>	<i>We=7.45 laminar jet</i>
Computational domain (m)	$0.3 \times 0.3 \times 0.3$	$0.3 \times 0.3 \times 0.3$
Inlet jet orifice	Diameter(D) = 0.0013	Diameter(D) = 0.0013
Mesh resolution	$34 \times 34 \times 440$	$34 \times 34 \times 880$
Mesh size (m)	5.9×10^{-5}	5.9×10^{-5}

Table 5.2 Physical parameters conducted for $We=3.1$ liquid jet case

<i>Medium</i>	<i>Density ρ (kg/m³)</i>	<i>Dynamic viscosity μ (Pa.s)</i>	<i>Surface tension σ (N/m)</i>	<i>Re</i>	<i>We</i>	<i>Oh</i>
Gas (air)	1.226	1.4519×10^{-5}				
Liquid (water)	1000	0.001137	0.073	480	3.1	3.7×10^{-3}

Table 5.3 Physical parameters conducted for $We=7.4$ liquid jet case

<i>Medium</i>	<i>Density ρ (kg/m³)</i>	<i>Dynamic viscosity μ (Pa.s)</i>	<i>Surface tension σ (N/m)</i>	<i>Re</i>	<i>We</i>	<i>Oh</i>
Gas (air)	1.226	1.4519×10^{-5}				
Liquid (water)	1000	0.001137	0.03	480	7.45	5.7×10^{-3}

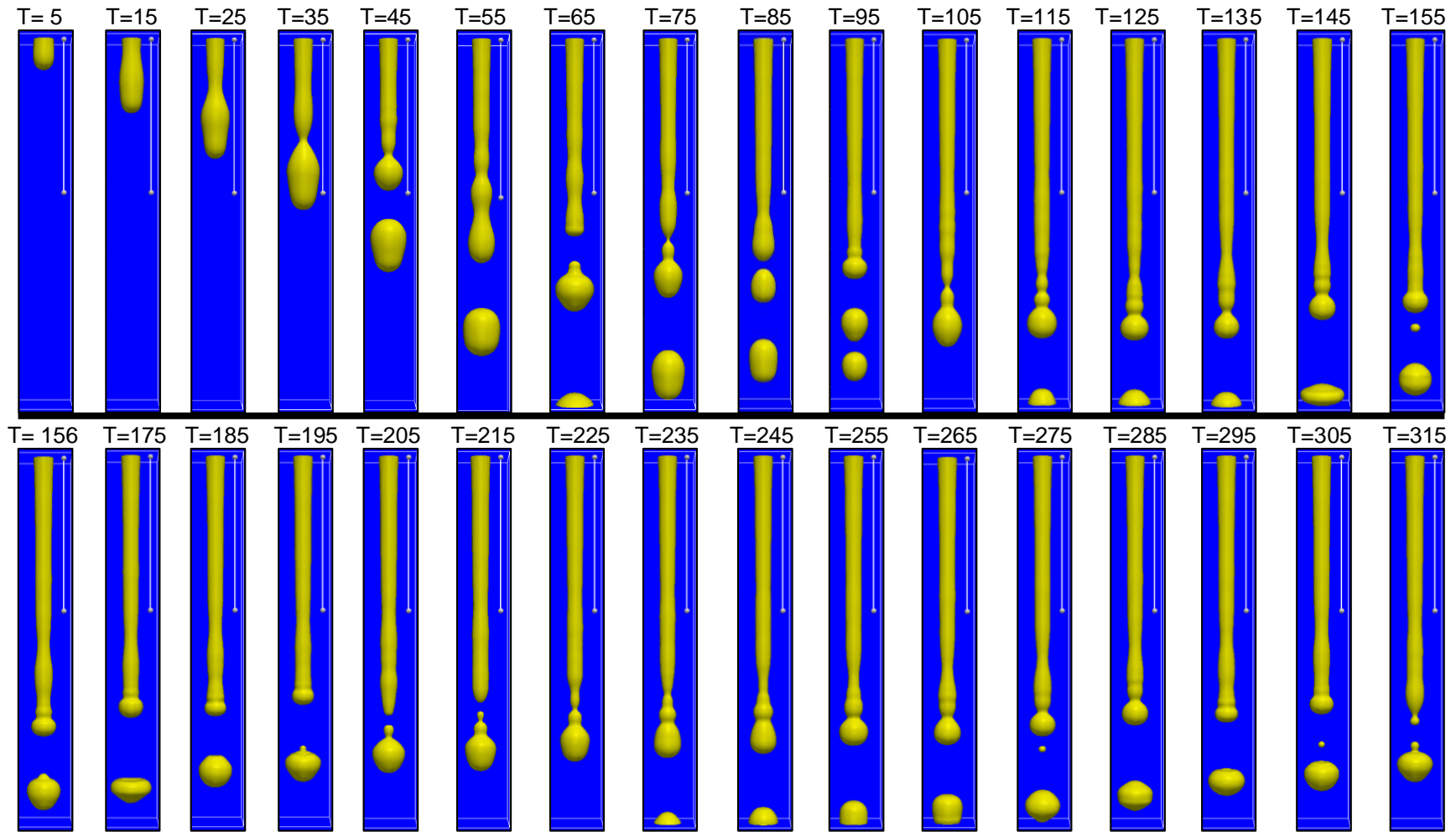


Figure 5.1 Snapshots of a 3-D liquid jet numerical simulation at $Re=480$, $We=3.1$, $Oh=3.7 \cdot 10^{-3}$, $Bo=0.23$ by the interFoam (VOF) in OpenFOAM model compared to the experimental value [80] as presented in the bars next to each time step. Time (T) in milliseconds

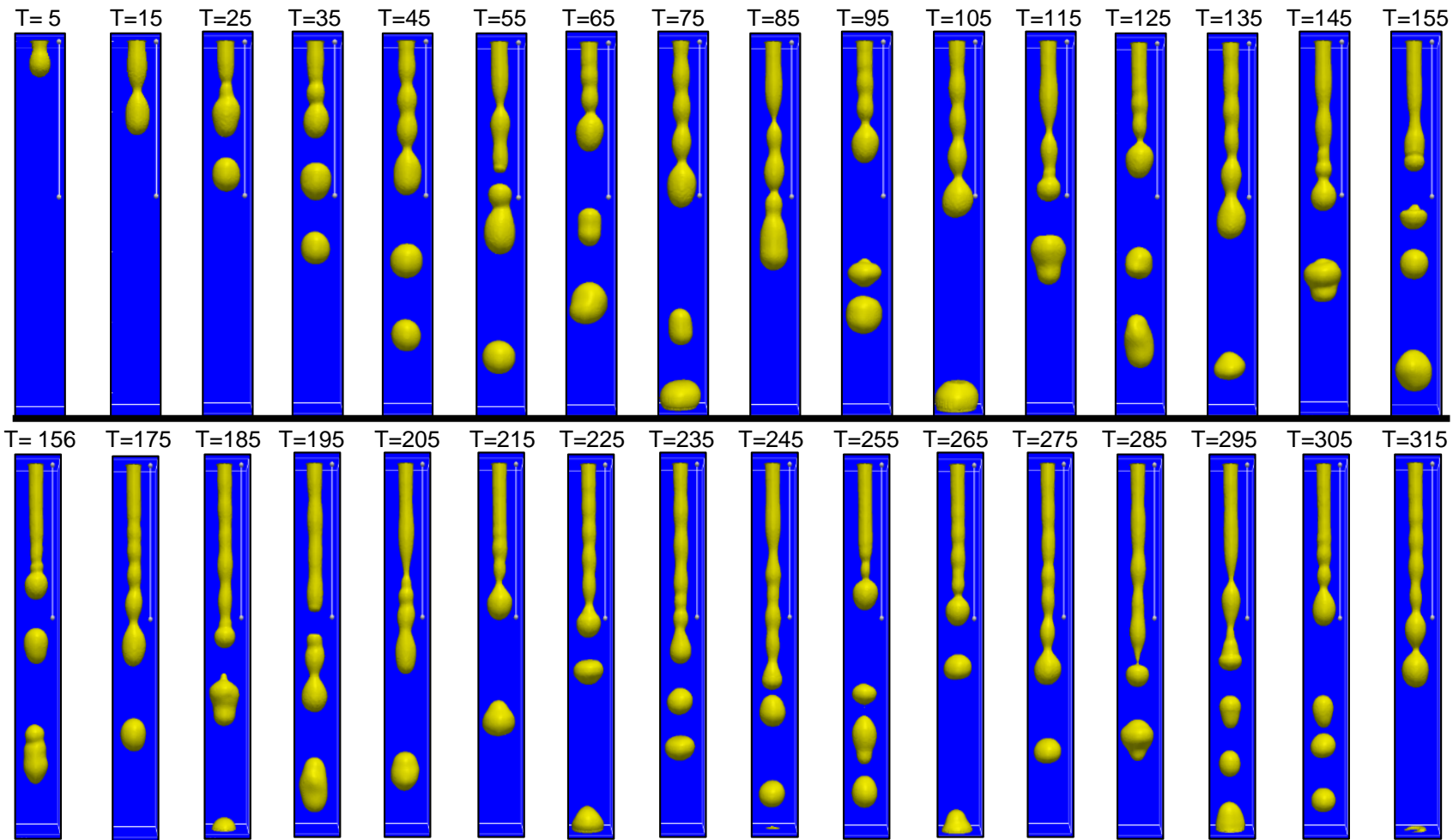


Figure 5.2 Snapshots of a 3-D liquid jet numerical simulation at $Re=480$, $We=3.1$, $Oh=3.7 \cdot 10^{-3}$, $Bo=0.23$ by the `sclsVOFFoam` (LS+VOF) in OpenFOAM model compared to the experimental value [80] as presented in the bars next to each time step. Time (T) in milliseconds

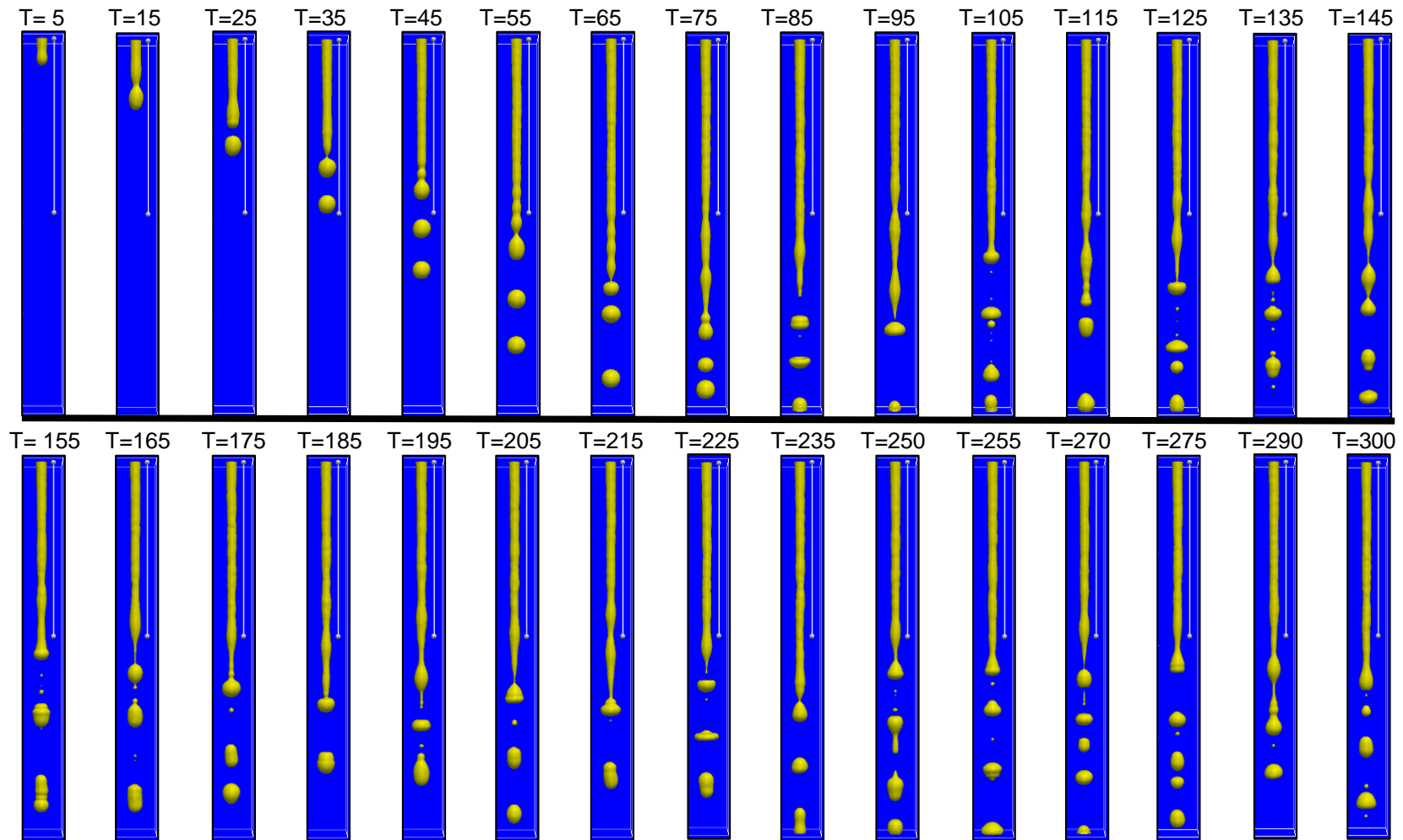


Figure 5.3 Snapshots of a 3-D liquid jet numerical simulation at $Re=480$, $We=7.45$, $Oh=5.7 \cdot 10^{-3}$, $Bo=0.55$ by the `sclsVOFFoam` (LS+VOF) in OpenFOAM model compared to the experimental value [80] as presented in the bars next to each time step. Time (T) in milliseconds

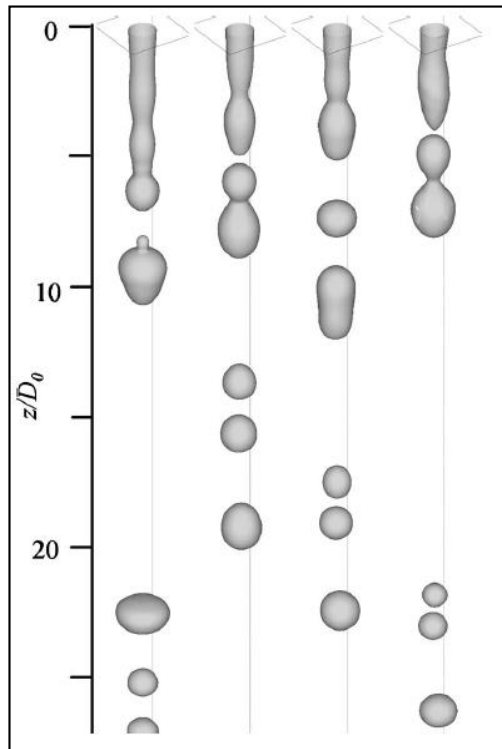


Figure 5.4 Snapshots of a 3-D liquid jet numerical simulation of water jet into air at $Re=480$, $We=3.1$, $Oh=3.7 \times 10^{-3}$. (adapted from [58])

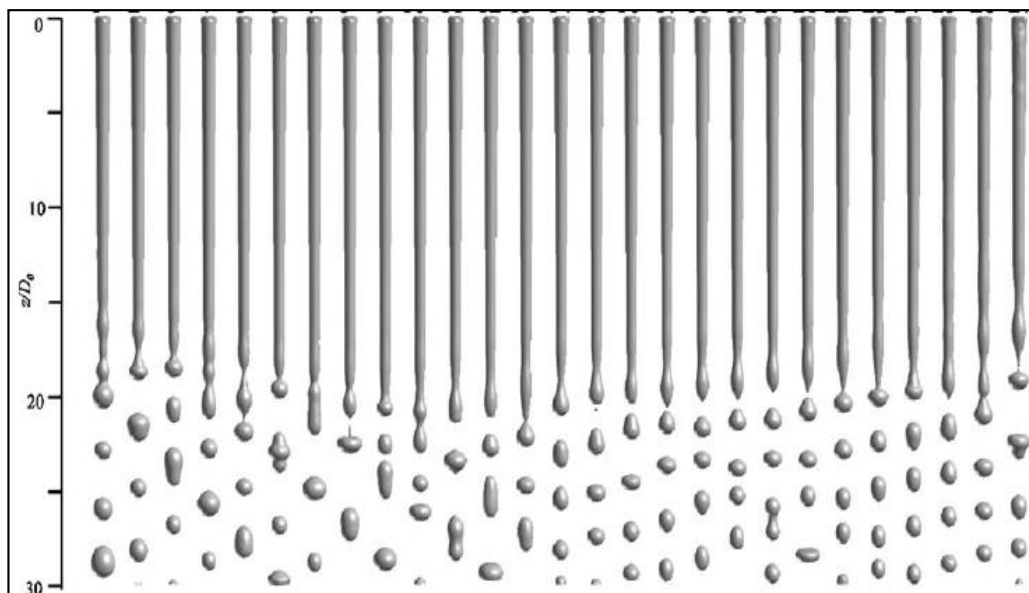


Figure 5.5 Snapshots of a 3-D liquid jet numerical simulation of water jet into air at $Re=480$, $We=7.45$, $Oh=5.7 \times 10^{-3}$. (adapted from [58])

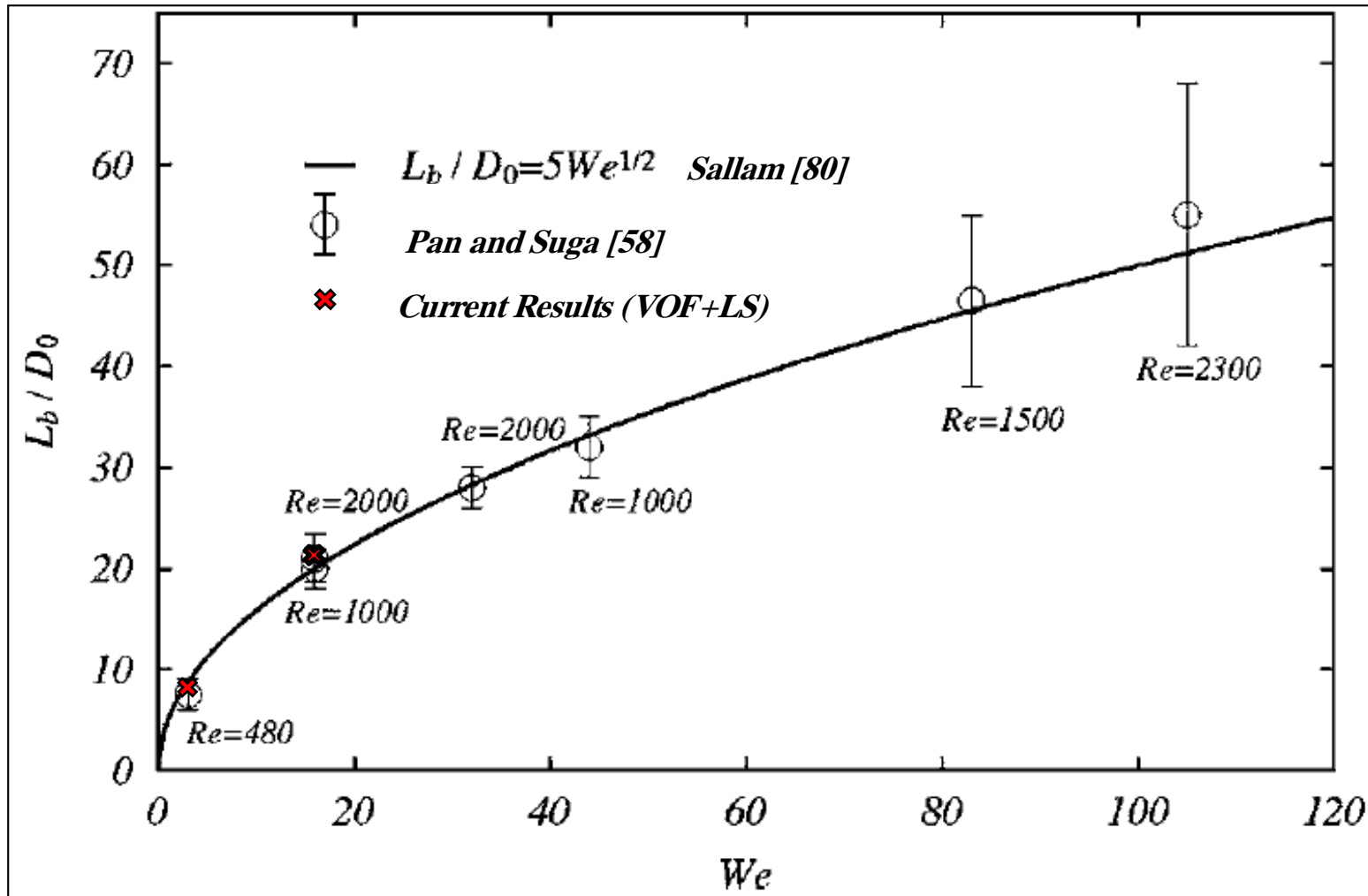


Figure 5.6 Comparison of Current results for breakup length of laminar jets at different Weber numbers studied compared with previous data [80] and [58]. (adapted from [58])

5.3 Results and Discussion

5.3.1 Fully Developed (Parabolic) Laminar Jet

Figure 5.7 benchmarks numerical simulations against previous experimental and numerical results conducted by Rupe [39] and Pan [58]. The whole bursting process is reasonably captured with the computational grid used in the current numerical simulation, whereas its resolution is not fine enough (due to computational cost) to resolve the small scale structure produced at the burst and the cell increment (Δx) is bigger by 32.4% than the one used in Pan [58] study. A series of snapshots in Figure 5.7 covers the jet process after injection and burst phenomena generation, are presented in Appendix A.4.1. As clearly shown in Figure 5.7, the images taken experimentally by Rupe [39] discovered that a fully developed laminar jet tended to disintegrate (burst) more readily than any other turbulent jet explored in his study. From Rupe [39] picture, Pan [58] estimated the location of that burst at about 46D (0.138 m) for such a jet at $Re=2200$. However, Pan [58] never noticed such a violent fashion of breakup or burst for turbulent case conducted in his numerical work at $Re=53000$.

The physical parameters for the laminar liquid jet burst phenomena and non-dimensional parameters such as Reynolds (Re), Weber (We) and Ohnesorge (Oh) number are presented in Table A.3.2 (Appendix A.3). The density of this liquid is about the same as water, whilst its viscosity is considered about 40 times as high as that of water. At these conditions, the jet exists within the laminar regime at a high Weber and Ohnesorge number. In previous and current studies for such phenomena, it is noted that the jet's release conditions considered in positions of the second-wind breakup regime of Ohnesorge/Reynolds phenomenological diagram as shown in Figure 5.8. Hence, for a jet in such conditions, the jet breakup length is expected to become shorter than that associated with the first-wind regime, as reported in the considerable literature about this. Nevertheless, unlike Rayleigh and first wind regimes, the aerodynamic effect is considered significant and important in this regime, therefore the jet may start producing liquid ligaments around the jet column [81]. As shown in Figure 5.7, one can observe that the jet breakup is not likely due to the Rayleigh instability nor the aerodynamic interaction.

In order to investigate and understand the main mechanism of such a phenomenon, the post-processing treatment was concentrated on the time (before, due and after burst) and space (the location) where liquid jet burst phenomena occurred. As shown in Figure 5.7, the jet starts with a smooth liquid column from the nozzle exit

(laminar velocity profile” Poiseuille flow”), but far in the downstream region at 0.04 m ($z/D= 13.33$) some wrinkles establish and they grow up to the burst phenomena. In order to show this surface motion and other physical characteristics more clearly where burst generated, the data has been post-processed by customizing the solution domain to focus just on the distance between 0.1 to 0.2625 m of the jet length ($z/D=33 \leq$ customized domain $\leq z/D=87.5$).

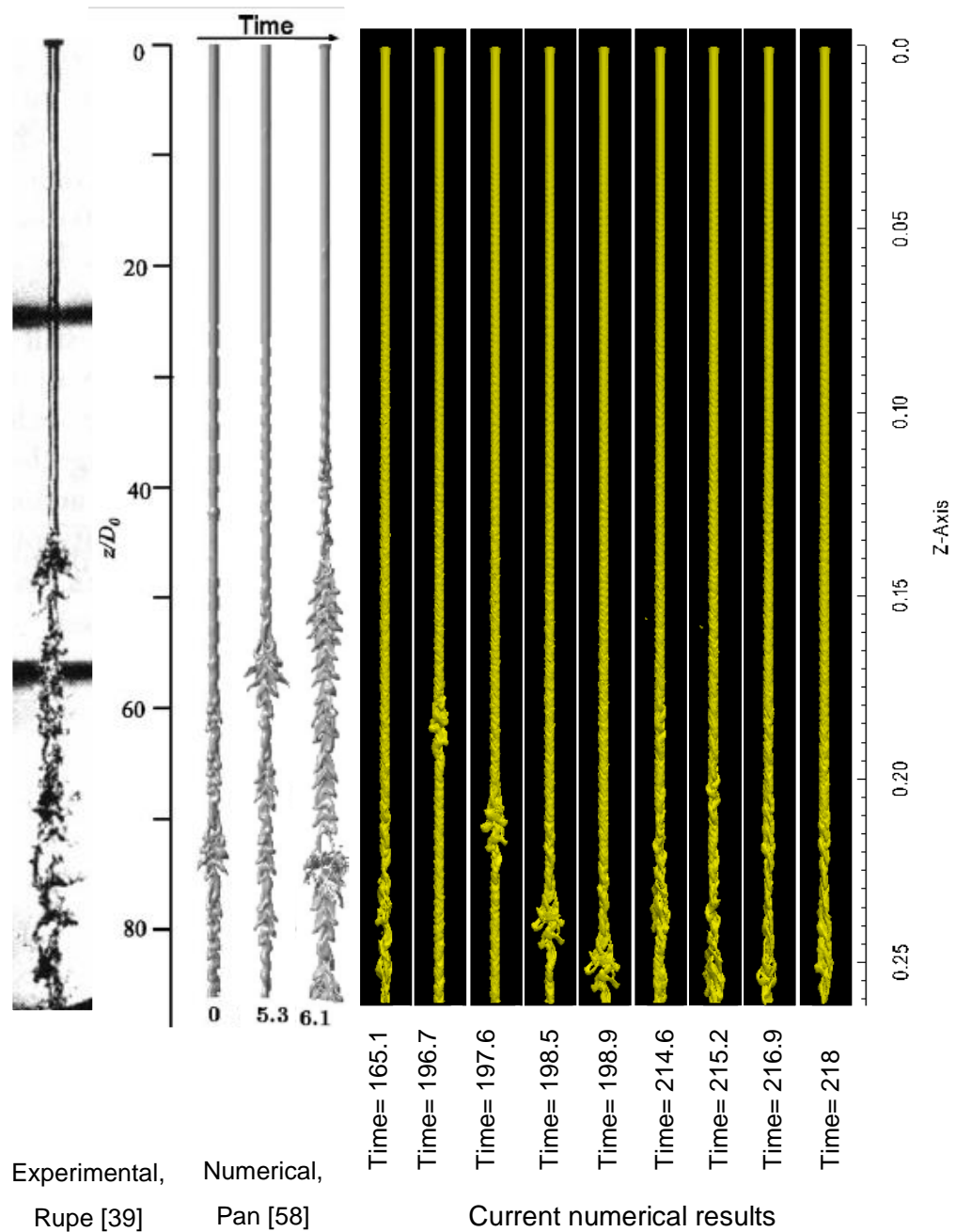


Figure 5.7 Liquid jet results for present work compared with experimental [39] and numerical [58] studies. The number next to each image indicates the dimensional physical time elapsed in milliseconds

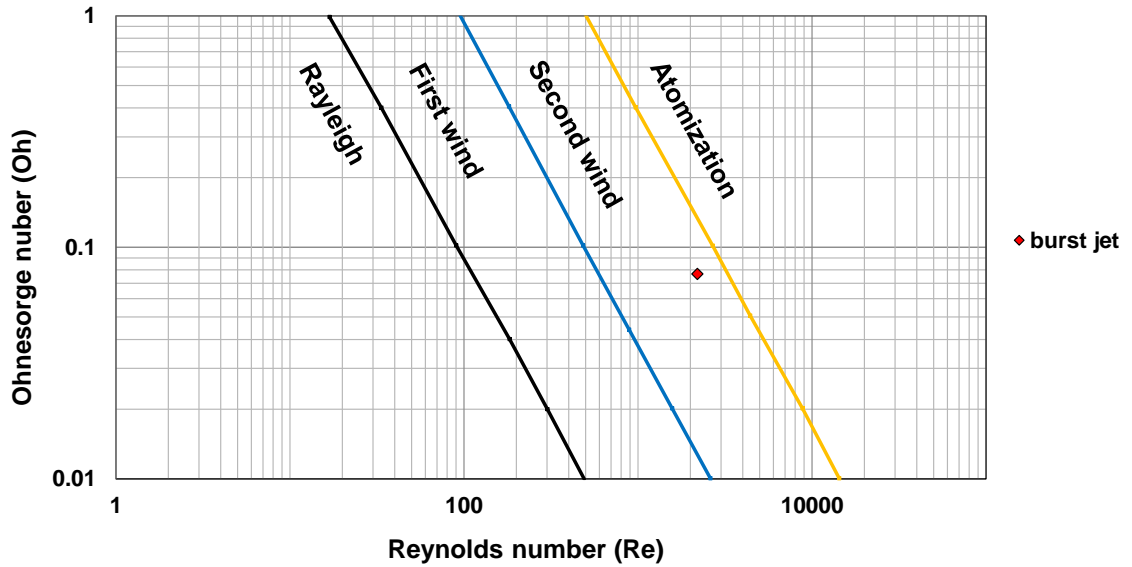


Figure 5.8 Current study physical conditions located on Ohnesorge chart and present study regime

1st row of Figure 5.9 gives close-up views of the jet column of the later stage of Figure 5.7 inside the customized domain ($z/D= 33.33 - 87.5$). Although the bursting point is not fixed in location, the first violent burst appears at the time 198 ms, and at space 0.22-24 m ($z/D= 70 - 80$) which is consistent in location with modelling snapshots images of Pan [58] showing the first strong bursting point at $z/D= 70$. As reported by Lefebvre [31], the jet burst conditions categorize the jet within the second wind-induced breakup regime. Also for the current case, the gas Weber number $We_g=28.6$ corresponds to Reitz's criteria [34] for liquid jet breakup length in the second wind induced regime as in the Equation 5.1 below:

$$13 < We_g < 40$$

Equation 5.1

The Ohnesorge chart also supports this classification as in Figure 5.8. However, the images in Figure 5.7 and 1st row of Figure 5.9 do not show typical features of the breakup mechanism by aerodynamic interactions as the jet's surface advancing the bursting point is relatively smooth in the beginning and is 'ruffled' naturally due to the normal liquid gas interaction. Undoubtedly, the jet structures in the burst area cannot be associated with the effect of either the Rayleigh instability or air friction, except for the wavy and ruffled structures in the upstream (before burst) and downstream (after burst) regions.

In order to understand this burst mechanism further, the domain in the 2nd row of Figure 5.9 is sliced through the middle longitudinally to show the instantaneous cross-

sectional velocity vector profile in the z-x plain and the liquid contour borders (two white lines). At distance 0.1 m ($z/D=33$), the liquid velocity profile was still parabolic, while on the gas side minimal movement is observed due to the low drag as the interface relative velocity was low. Development of the interface surface velocity due to liquid velocity relaxation can be observed. This relaxation results in increasing the drag force at the interface and the gas velocity respectively. Increasing the drag force resulted in the typical deformation of the liquid surface up to time 196 ms, and distance 0.16 m ($z/D=53$) where the onset of a liquid burst can be seen.

The 3rd row of Figure 5.9 represents the air field velocity vector in the 3-D domain which clarified more the observations above regarding the gas movement. The upstream air velocity is around $U=1.6$ m/s as represented in the small size of arrows and blue colour as represents low velocity intensity. Air velocity is modified further downstream and increased up to 10-15 m/s where and after burst occurs. As shown in Figure 5.7, the irregular surface deformation starts from 0.04 m ($z/D=13$) with quasi-regular perturbations formed. Up to this stage, however, the air flowfield seems not to contribute significantly to the deformation process, and the maximum liquid velocity still dominates the flow and is concentric with the liquid core.

The liquid perturbations presented by 'protrusions' excites the air flow field starting from approximately 0.18 m ($z/D=60$). This process is also confirmed in Figure 5.9, as represented by the irregular perturbations. Maximum axial liquid velocity starts to show noticeable reduction and is asymmetric with the liquid core, as shown in Figure 5.9 (2nd row). The 4th row of Figure 5.9 shows the velocity stream lines just inside the liquid column borders (two white lines) in the z-x plane. Liquid stream lines confirmed the observations of the sensible axial velocity reduction and eccentricity to the liquid core centre line.

The 5th row of Figure 5.9 shows the 3-D stream lines of velocity on the gas side surrounding the liquid contour column (coloured in pink). Reduction of the maximum liquid velocity inside the jet core due to relaxation is accompanied relatively with an increase in the axial velocity at the interface line which also increased the drag force (shear stresses) and air velocity respectively as shown in 2nd row of Figure 5.9. Due to the irregularity of the liquid's surface deformation, air dragged with liquid showed secondary flow (non-axial) movement with the liquid jet as shown in the 3rd and 5th rows of Figure 5.9. 3rd and 5th rows of Figure 5.9 illustrate the asymmetric structure of velocity profile and streamline in the gas which is consequence of the asymmetric relaxation development inside the liquid as shown in the 2nd row of Figure 5.9. A series of snapshots

in Figure 5.9, covering the evolution of the burst phenomena generation are presented in Appendix A.4.2.

In order to further understand the deformation process of the liquid core, axial and radial velocity components at the centre of the liquid core are examined along the jet, as shown in Figure 5.10. At the early stage of burst generation at 195.5 ms and space 0.15 m ($z/D=50$), axial velocity in z-axis (U_z) exhibited a sharp and sudden reduction from 38 to around 33 m/s. Sequentially, as a typical physical application to the continuity equation whilst mass and momentum are conserved, the radial velocity components in x-axis (U_x) and y-axis (U_y) direction have increased to significant values to reach around 2 m/s (between the positive and negative values).

The aero-dynamical effect of the gas on the liquid at the point (when burst commences at 195.5 ms) is very low as shown in the figures of Appendix A.4.2. This would refute the conjecture that the burst is generated initially as a result of the effects of the surrounding gas, even though the liquid jet exists in the second wind regime. This reduction of severity in the jet axial velocity (U_z) and notable high increase in radial velocities (U_x and U_y) were able to disturb the jet internally and trigger the liquid jet burst phenomena. Once the jet instabilities are initiated from the inside, disturbances then grow with space and time to eventually burst the violently liquid at 198 ms and at distance 0.22 m ($z/D=73$) as shown in Figure 5.9. A series of snapshots of Figure 5.10 covering the evolution of the burst phenomena generation are presented in Appendix A.4.3.

In order to understand the deformation process of the liquid core and to investigate the radial velocity further, Figure 5.11 shows the instantaneous lateral cross-sectional (x-y plane) velocity vector at twelve lateral locations distributed equally along the customized domain at 198 ms. The 1st row of Figure 5.11 shows the radial velocity (U_x and U_y) intensity inside the customized domain at an instantaneous longitudinal cross-sectional (x-z axis). The view orientation for the twelve lateral slices (2nd, 3rd and 4th rows) is taken as the fluid flow coming towards the observer that is moving in the negative z-direction. To make the plots clearer, the velocity vectors in the air field are removed in Figure 5.11. Furthermore, radial velocity vectors are appropriately scaled in each cross section to optimise the visualization and to see the secondary flow motion more clearly. A series of snapshots of Figure 5.11 covering the evolution of the burst phenomena generation are presented in Appendix A.4.4.

At an upper-stream section in Figure 5.11 within the customised domain at $z/D=33$, there can be seen radial motions generated from the jet core and increasing toward the interface due to the development of the axial velocity (velocity profile

relaxation). Nevertheless, a radial velocity is generated at the liquid-gas interface and directed towards the liquid side. On the interface, the directions of the velocity produced by the interface shear are already asymmetrical implying that the air flow field around the liquid column has asymmetrical structures. Although it is not shown here, it is worth mentioning that the asymmetry is progressively modified from the nozzle exit, whereas the flow structure is symmetrical even with the deficient representation of the cylindrical liquid column by the Cartesian mesh system used in this study. The contribution of the interface shear motion effect on the burst jet will be studied and confirmed later in this chapter for different gas viscosity values.

The radial velocity components encourage the generation of longitudinal-vortex (stream wise-vortex) motions (rotational motions) as shown in Figure 5.11, $z/D=37.9$. It seems that the shear motions at the interface are weakened while the vortex motions seem to be magnified by the momentum supplied from the radial motion in the short distance downstream region as shown in Figure 5.11, $z/D= 42.9$ and $z/D= 47.8$.

Although it is not shown at 198 ms, strong transverse vortex motions exist in the inner region as indicated by the vector directions. As shown in Appendix A.4.4, the transverse vortices can be seen at 195 ms (at $z/D=62.7$ which is almost the reverse of those of $z/D 67.6$) and also at 197.5 ms (at $z/D=52.8$, $z/D=57.5$). In Figure 5.11, at $z/D=52.8$, $z/D=57.7$ and $z/D=62.7$, strong longitudinal twin vortex motions are obviously generated. Once the interface is strongly distorted in a very rapid and violent fashion, unstable distorting and/or stretching motions of the liquid core are amplified further. Longitudinal twin vortex overcomes the inertial and surface tension forces, ultimately distorting the shape of the interface leading to burst the jet as in Figure 5.11, $z/D=67.6$.

Except for the opposite transverse vortex motions in our study, all of the aforementioned vortex motion observations have been noticed in Pan [58] study at one physical time step. Generally, any physical phenomena generate and modify or disappear through space and time. Although the transverse vortex has been captured at other physical time steps as shown in Appendix A.4.4, it is likely that the opposite transverse vortex is not present from the view at 198 ms due to the post-processed frames selected. In this study, the view can miss any phenomena because the lateral slices were chosen and distributed uniformly along the customized domain, while in the Pan [58] study, the lateral slices have been adapted carefully to consider the different physical phenomena.

Eventually, when jet burst occurs, the jet disintegrates and the ligaments were thrown out from the core and successively broken down by aerodynamic drag. From

different types of liquid jet studied in his research, Pan [58] hypothesised that the liquid jet burst phenomena will never occur if Weber number (We) was low. The jet will produce different breakup phenomena because the vortex motion will not be able to overcome the surface tension force at lower Weber number (We).

The radial velocity is generated as a result of the axial velocity relaxation from parabolic to flat profile and the initiation of secondary motion inside the liquid. This requires appropriate choice for the presentation of results to elucidate the different vortex structures of different origin throughout the flow field. In order to focus on how the burst generated, attention has been paid to perturbations existing within the liquid due to different vortex structure generation. Figures 5.12 (the onset of burst represented in the liquid core perturbations at time 194.6 ms) and 5.13 (where liquid jet burst phenomena eventually occurred at time 198 ms) show the instantaneous comparison between the velocity field and the vortical field.

The 1st row of Figure 5.12 and Figure 5.13 shows a longitudinal slice (x - z plane) taken along the customized domain of velocity field, whereas the 2nd row shows the velocity field distribution at eight lateral slices (x - y plane) uniformly distributed along the customized domain. On the other hand, the 3rd row of Figure 5.12 and 5.13 shows a longitudinal slice (x - z plane) taken along the customized domain of the vortices' field distribution, whereas the 4th row shows eight slices taken horizontally (in the x - y plane) along the customized domain for the vortices' field distribution. In order to show a better view of the vorticity inside the domain, the maximum value of vorticity has been rescaled on a reduced range, as shown in the 3rd and 4th rows of Figures 5.12 and 5.13. The white lines in Figures 5.12 and 5.13 represent the liquid contour borders as sliced longitudinally or laterally across the customized domain.

As shown in the 1st and 2nd rows of Figure 5.12, the maximum liquid velocity is concentric with the liquid core axis line and its intensity reduces from upstream to downstream due to the velocity relaxation. As the result of the high viscosity liquid and non-uniform velocity profile (parabolic), drag forces are generated between the liquid layers where there is maximum velocity at the centre of the jet and the nearby layers. Different velocities pertaining between the liquid layers on both sides of the centre line of the jet start to generate shear stresses and/or span-wise vortices. The direction of the span-wise vortices perpendicular to the axial direction of the fluid flow in which the vortices rotate anti-clockwise above the centre line of the liquid core and the rotation is clockwise for vortices below the centre line of the liquid core. Just after ejection, liquid jet has inherited high drag forces between the liquid and nozzle walls, which explains the

higher vortices' intensity near the interface lines and reduces to zero where no shear force or drag exists at the centre of the liquid core (maximum velocity).

Figure 5.12 shows the onset of the burst phenomena at 194.6 ms and location 0.122 m ($z/D= 40.7$). Maximum velocity becomes eccentric to the liquid jet centre line and starts to show oscillations. The same behaviour of oscillation can be observed on the vorticity as shown in the 3rd row of Figure 5.12 in the form of a sinuous wave. Moreover, the vorticity intensity shows a non-uniform distribution as clearly seen in the 4th row at $z/D= 40.7$. The observations above are identical in location to where the axial velocity starts to show abrupt reduction, whereas the radial velocities increase noticeably as shown in Figure 5.10 in Appendix A.4.3. This explains the reason for the significant axial velocity reduction noticed in the centre line of the liquid core as the maximum velocity is no longer concentric.

The eccentricity of the axial velocity means that the maximum velocity has moved to a different location. At $z/D= 40.7$, the maximum axial velocity is still appreciably high (around $U=37$ m/s) compared to other velocities' values further downstream. Relocation of the maximum axial velocity results deforming the shear stress structure and the span-wise vortices which generally leads to generating instabilities inside the liquid as indicated by the higher liquid surface deformation. Nevertheless, increasing the radial velocity inside the liquid was responsible for generating another type of vortex (stream-wise vortices). Also, the above instabilities may be observed downstream of the jet. The downstream instabilities resulted in producing a very deformed liquid surface rather than an obvious liquid jet burst phenomena.

It is proposed here that once instabilities are generated upstream, they modify in space and end up producing the burst phenomena. The maximum velocity of the liquid jet upstream is, of course, moving relatively faster than the one downstream, therefore it disturbs the liquid core more strongly, thus generating high perturbations which grow more intensive with space leading to the jet burst. A series of snapshots in Figures 5.12 and 5.13 covering the evolution of the burst phenomena generation are presented in Appendix A.4.5.

Figures 5.14 (shows the onset of the jet burst at 194.6 ms) and 5.15 (shows liquid jet burst phenomena eventually occurred at time 198 ms) show the instantaneous vortices field in the gas side (1st row), in the liquid side (2nd row) and liquid vorticity components field distribution as in ω_x (3rd row), ω_y (4th row) and ω_z (5th row). The five rows are sliced longitudinally (x - z plain) across the customized domain. The liquid contour has been presented in the 1st row of Figures 5.14 and 5.15, while the white lines

in the rest of the rows represent the liquid contour borders as sliced longitudinally across the customized domain. Vorticity have been scaled appropriately in each row results for better vorticity distribution display.

As observed in Figure 5.13, the liquid surface roughness excites the air flow field to be rough and increasing its speed as liquid jet relaxation progresses. This process is confirmed in the 1st row of Figure 5.14, which shows strong air vorticity induced around the liquid surface. Such air vortices could enhance the liquid column deformation as seen at 0.22 m in the 2nd row of Figure 5.14, leading to the possible breakup further downstream. Presenting the liquid vorticity as in the 2nd row of Figure 5.14 confirmed the process of the onset of liquid jet burst phenomena. It is obvious that strong instabilities are generated inside the liquid at $z/D= 40.7$ and broke the uniform shear stress structure and/or the span wise vortices around the liquid jet centre line and generate sinuous waves, as shown in the 1st row of Figure 5.12.

The transverse vortex structure is more clearly observed in the region of $40 < z/D < 47$ in the 3rd row of Figure 5.14 which shows the vorticity (ω_x) distribution in the x-z plane. In fact, positive and negative regions of vorticity field in the x-z plane appear in sequence along the (ω_x) distribution. The 4th row of Figure 5.14 indicates the development of the sinuous wave motion as shown from the vorticity (ω_y) distribution. Furthermore, the strong longitudinal twin vortex motions noticed before as in Figure 5.11 are also clearly shown in the 5th row of Figure 5.14 throughout the vorticity ω_z distribution within the region of $40 < z/D < 47$ in the x-z plane. These characteristics are fully consistent with the physical observations in time or space observed in Figures 5.9, 5.10, 5.11, 5.12 and 5.13. A series of snapshots of Figures 5.14 and 5.15 covering the evolution of the burst phenomena generation are presented in Appendix A.4.6.

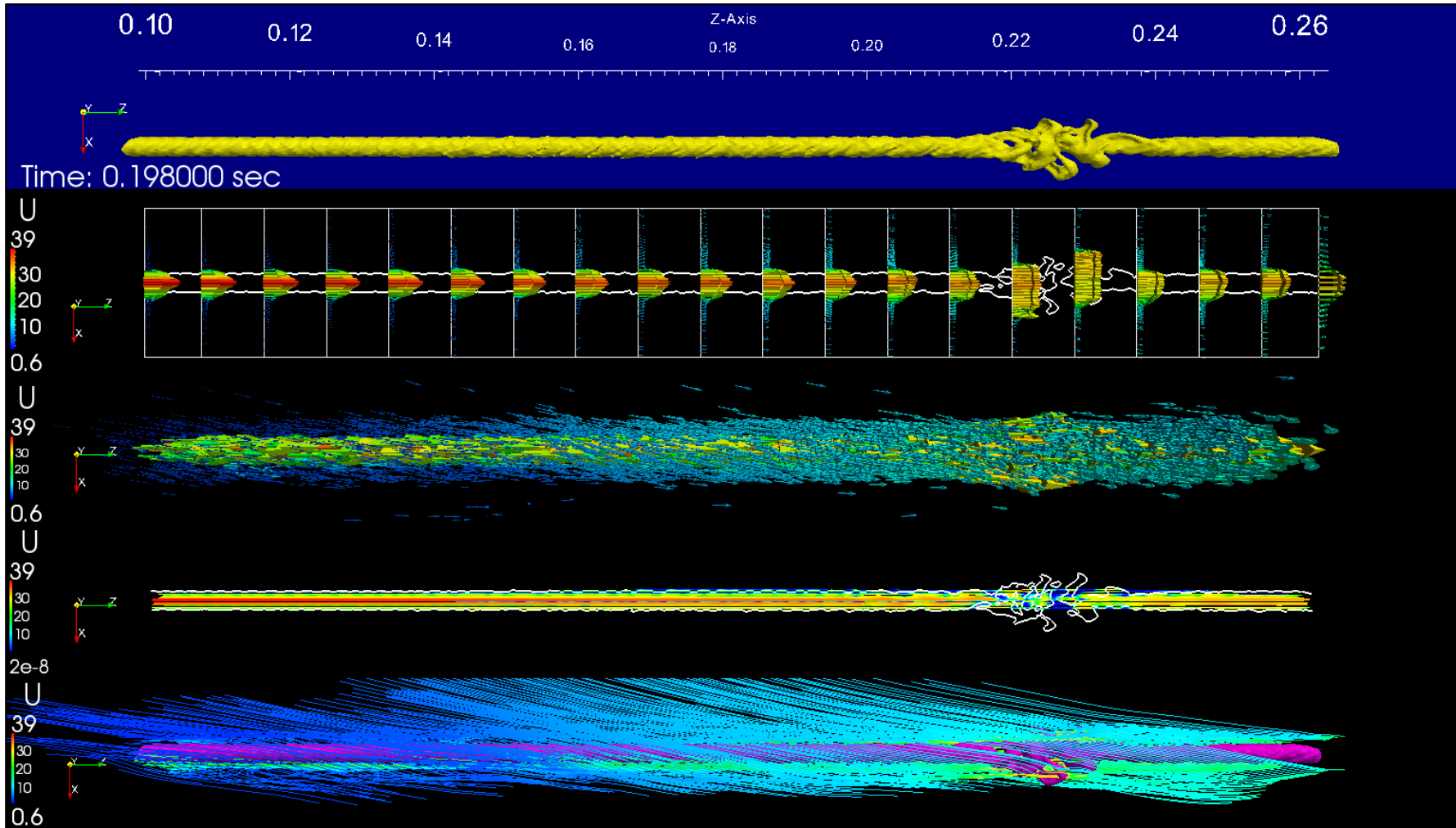


Figure 5.9 Liquid column (1st row), domain velocity profile (2nd row), domain velocity field (3rd row), liquid velocity stream lines (4th row) and gas velocity stream lines (5th row)

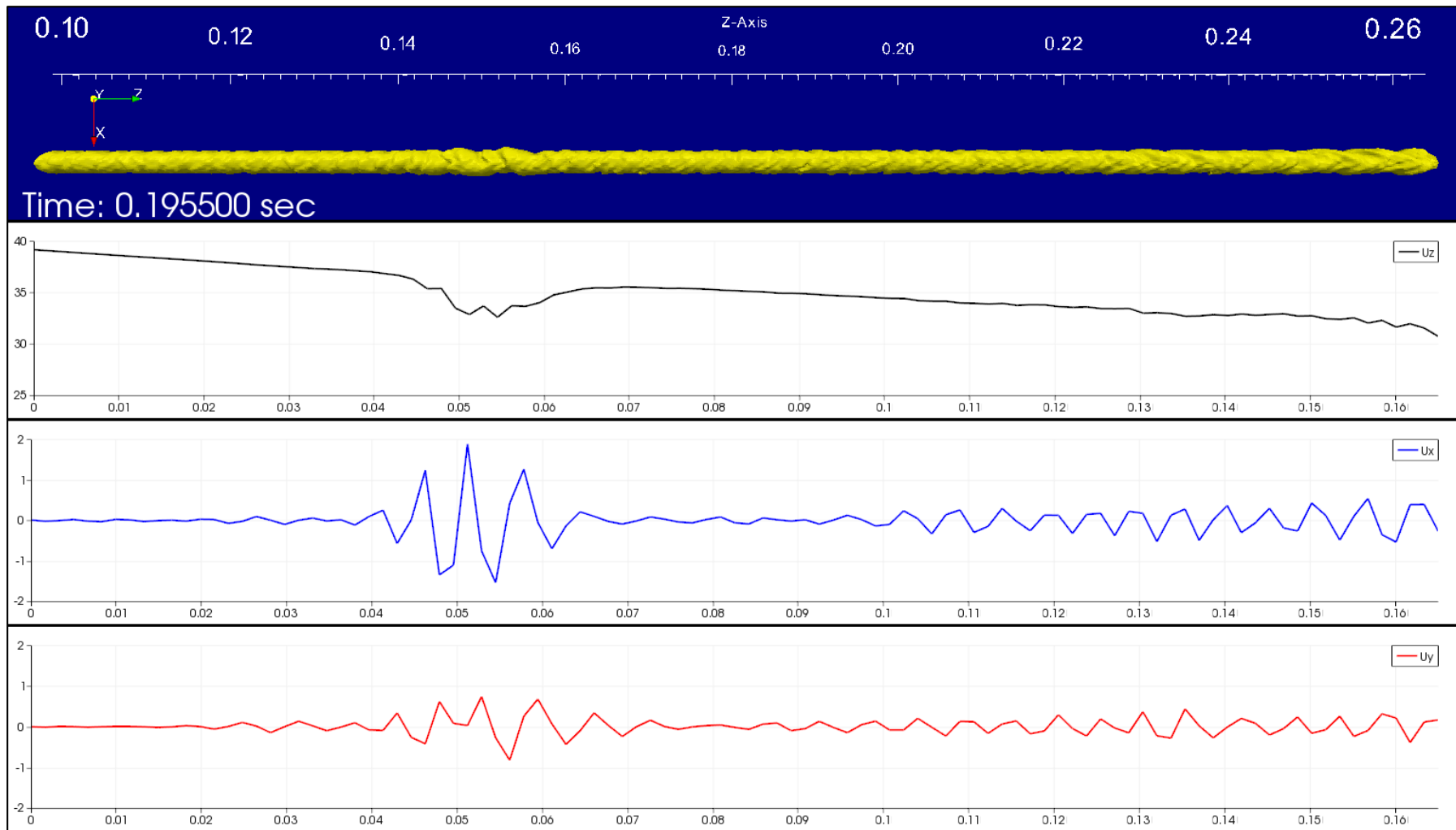


Figure 5.10 Liquid jet core velocity components (U_x , U_y and U_z at the early time (Time =0.195.5 seconds) of liquid jet burst phenomena

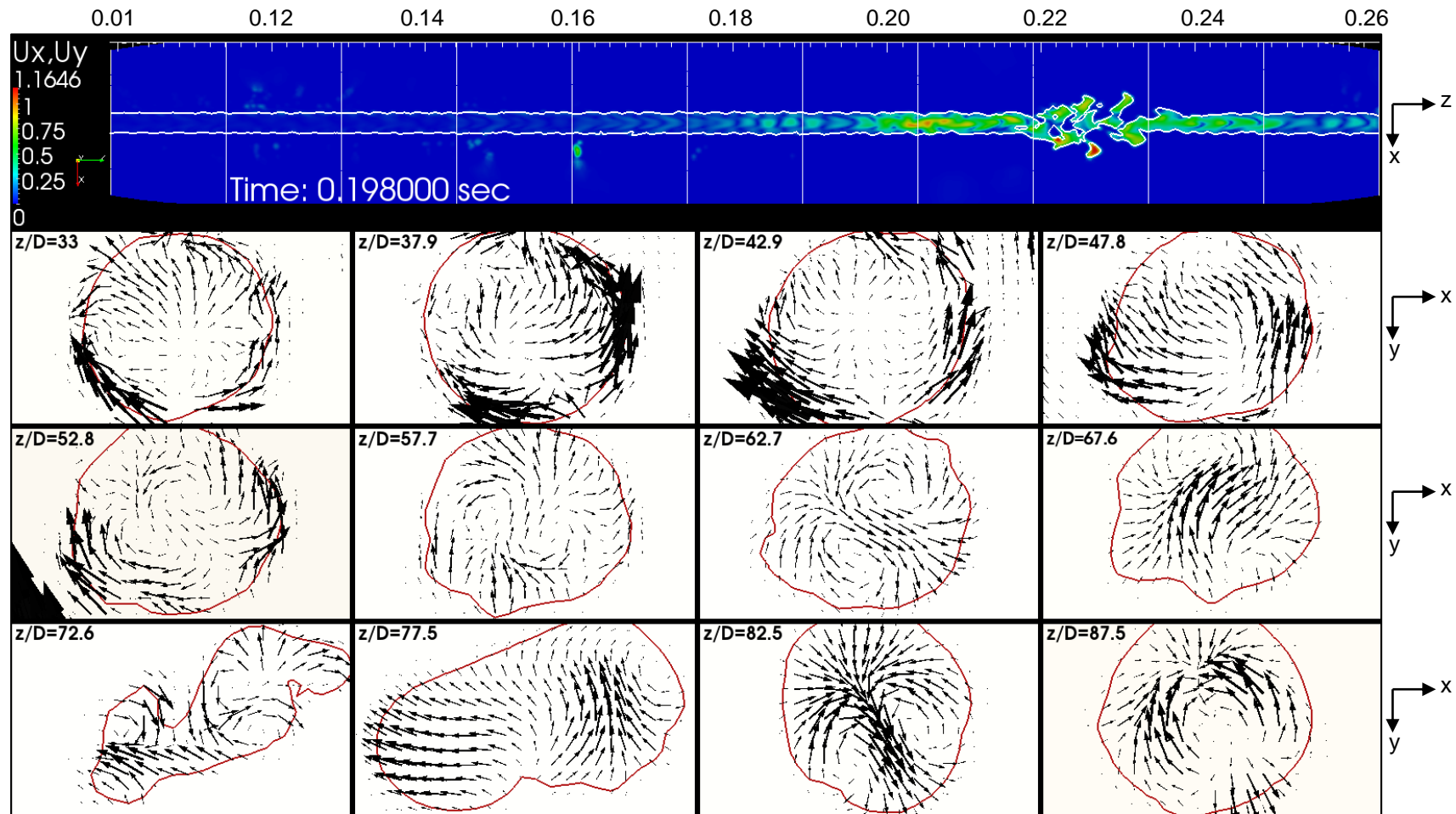


Figure 5.11 Distribution of instantaneous liquid velocity vectors projected onto longitudinal and cross-sectional planes at different axis locations. The vector length is scaled appropriately in each cross-section to show the radial motion in the liquid core

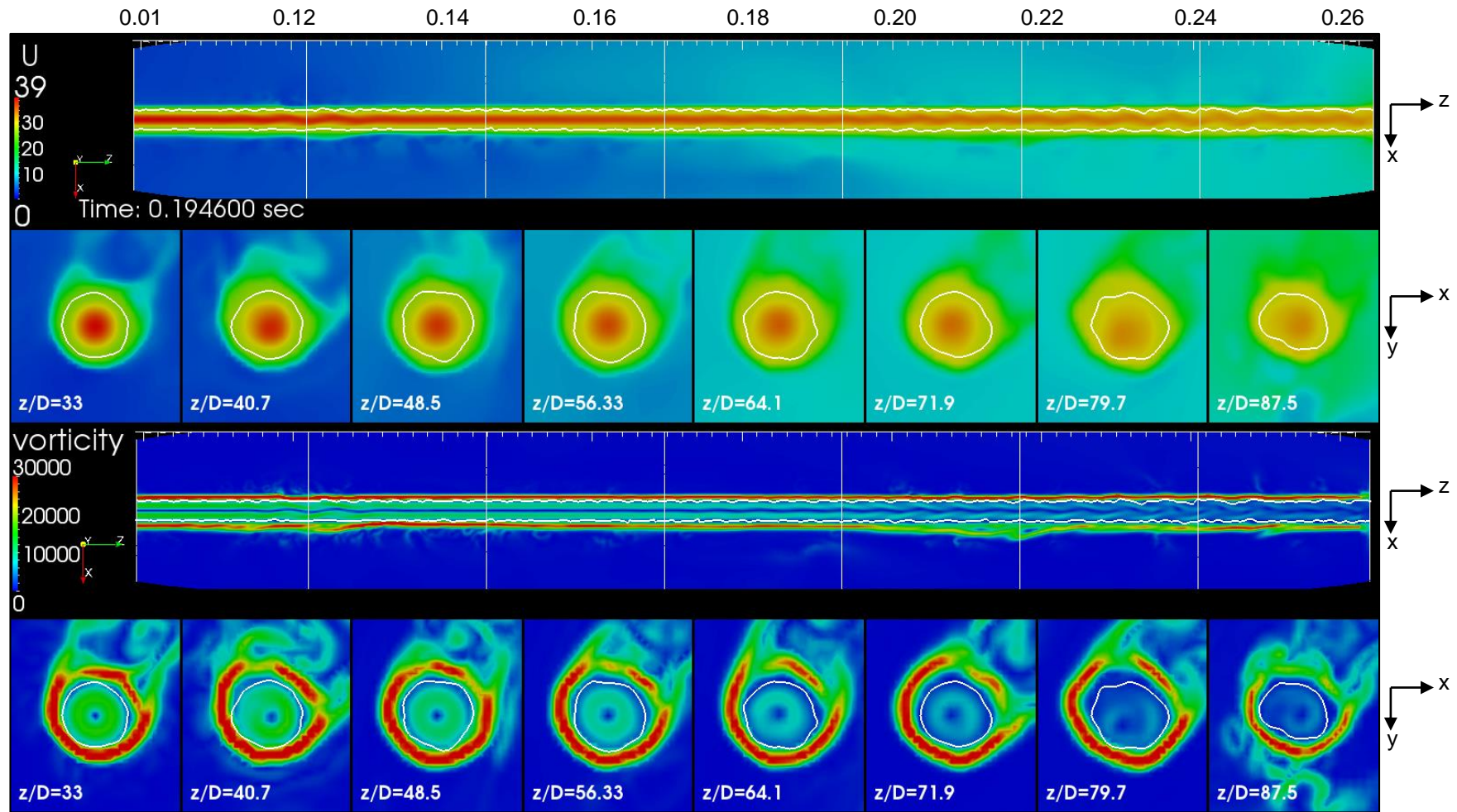


Figure 5.12 Longitudinal and lateral velocity (1st and 2nd rows) and vorticity (3rd and 4th rows) field's distribution at the onset of liquid jet burst phenomena

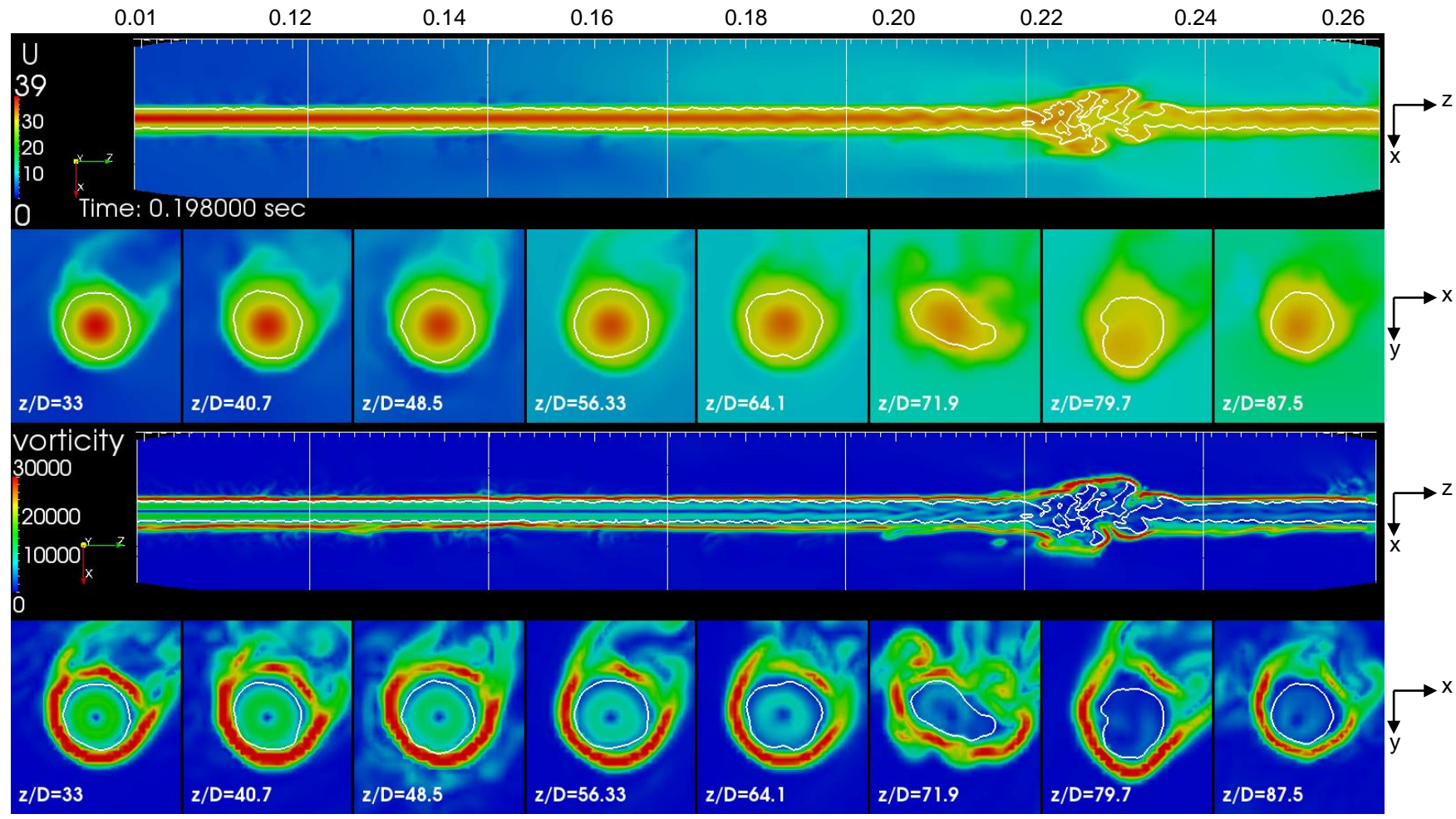


Figure 5.13 Longitudinal and lateral velocity (1st and 2nd rows) and vorticity (3rd and 4th rows) field's distribution of liquid jet burst phenomena

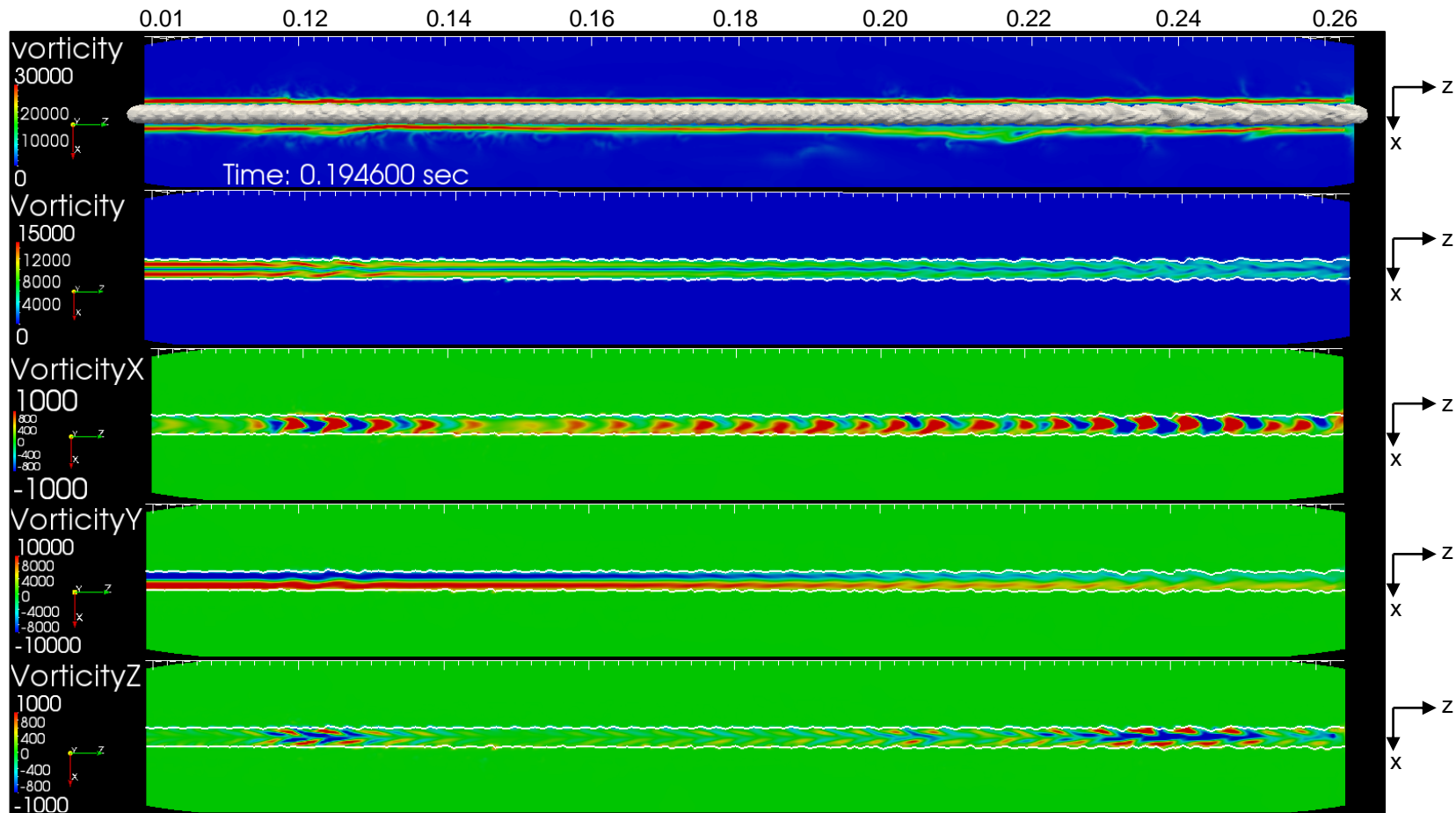


Figure 5.14 Distribution of instantaneous vorticity fields in an axis plan at the onset of the liquid jet burst phenomena. 1st row in the gas phase, 2nd row in the liquid phase, 3rd row vorticity-x distribution in the liquid phase, 4th row vorticity-y distribution in the liquid phase and 5th row vorticity-z component distribution in the liquid phase

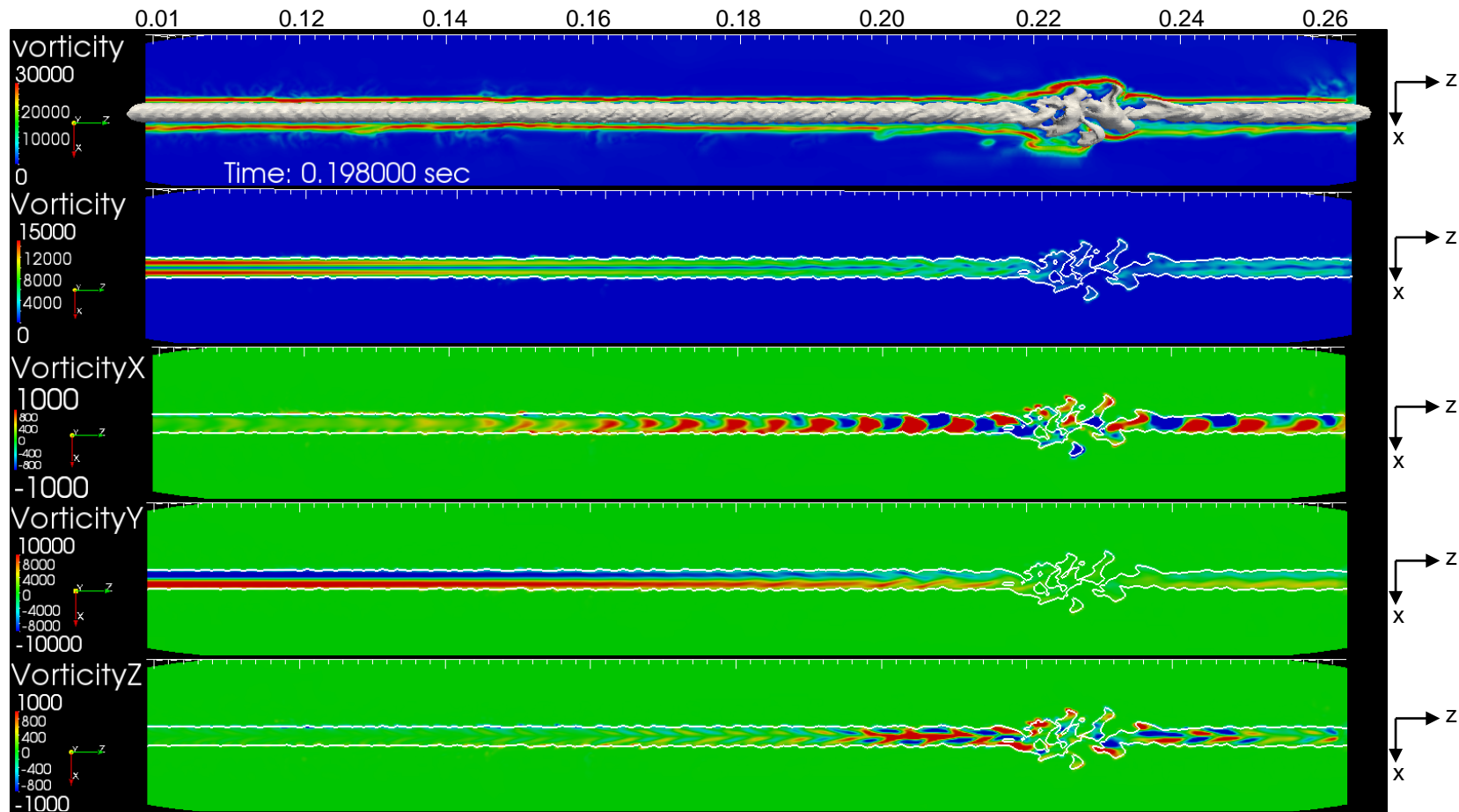


Figure 5.15 Distribution of instantaneous vorticity fields in an axis plain of the liquid jet burst phenomena. 1st row in the gas phase, 2nd row in the liquid phase, 3rd row vorticity-x distribution in the liquid phase, 4th row vorticity-y distribution in the liquid phase and 5th row vorticity-z component distribution in the liquid phase

5.3.1.1 Vorticity

It has been shown that the onset of instabilities which have led to violent perturbations and ultimately burst the jet occur as a result of increasing the radial velocity and stream wise vortex formation inside the liquid core. The results showed different vortex structures within the liquid jet represented in span-wise vortices perpendicular to the fluid flow direction and stream wise vortex parallel to the fluid flow which is considered a primary reason leading to the burst phenomena. In order to characterize and explore the burst phenomena further, information about the flow field inside the liquid can be expanded by distinguishing between the span and stream wise vortices.

The fluid motion of practical interest generally has complicated temporal structures which are 3-D and transient with time. Understanding the dynamics of fluid motion may be difficult without knowing the structure of any physical phenomena. Investigating vorticity magnitude in the fluid flow provides an indication of the presence of vortical structures. There have been many attempts to visualize them, either by using stream lines, path lines, vorticity, the Laplacian of pressure, the rate of rotation and strain stresses or others. Historically, the existence of vortices has been distinguished as high vorticity concentrated regions and visualised by plotting iso-surfaces of magnitude or a single element of vorticity. However, high vorticity regions do not always capture swirling circular vortices alone but also vortex shear layers [82].

To describe the local spinning motion of a continuum near some point (the tendency of something to rotate) we need vorticity. Vorticity is a rotation of the velocity vector. Mathematically, it is the curl of the velocity vector. The features of the vorticity vector (length and direction) characterise the rotation at that point. The direction of the curl is the axis of rotation, as determined by the right-hand rule, and the magnitude of the curl is the magnitude of rotation.

The first post processing tool used to calculate vorticity in OpenFOAM is to run the utility: *vorticity* tool in terminal window of the results case directory. The vorticity code will start calculating and writing the vorticity vector of velocity field (U) for each time step of the data results. This utility will also generate the magVorticity file as a scalar field to present the vorticity contour. One can produce the vorticity scalar field components, i.e. vorticity-x, vorticity-y and vorticity-z by running the utility: *foamCalc components vorticity*. The second tool which produces just the vorticity scalar field: *foamCalcEx mag vorticity*. This utility works the same way as the standard *foamCalc* tool, but accepts extra parameters. It does not come as a standard utility supported with OpenFOAM versions.

5.3.1.1.1 Vortex Detection via Helicity and Normalized Helicity

In order to develop our understanding and interpreting the computation of vortex interactions, an improved method for vortex detection criteria is desirable. Therefore, helicity density and normalized helicity are introduced. These are both scalar quantities derived from velocity so that its representation will not be difficult in terms of different components or cross sections. They introduce new variables, highlight complex parts of the flow field, identify vortices, distinguish between primary and secondary vortices, and detect swirling motion [83].

To use helicity density H_d , one should include the integral of helicity density ($\mathbf{U} \cdot \boldsymbol{\omega}$), as a conservation condition as they move in the flow inside material volumes [84]. Helicity is a scalar property field defined as the dot-product of the vorticity vector and the velocity vector. It defines the component of vorticity which is parallel to the local velocity vector. Helicity has been a subject of active research with regard to its possible utilisation regarding fluid dynamics. The “relative helicity” or more properly named “normalized helicity” is defined as [85];

$$H_n = \mathbf{U} \cdot \boldsymbol{\omega} / |\mathbf{U}| |\boldsymbol{\omega}| \quad \text{Equation 5.2}$$

where \mathbf{U} is velocity vector, $\boldsymbol{\omega}$ is vorticity vector and $|\mathbf{U}|$ and $|\boldsymbol{\omega}|$ are their magnitudes. The value of normalized helicity by definition range from -1 to 1. The H_n value could be interpreted as a balance between the swirling direction and the flow direction [86]. Besides just being simple scalar quantities, the big feature of helicity density and normalized helicity is that their magnitudes and sense (direction) are meaningful. High values of vorticity and speed represents high values of helicity density when the relative angle between them is small [83].

The sign of normalized helicity indicates the direction of swirl (clockwise or counter-clockwise) of the vortex with respect to the stream wise velocity component. It switches whenever a transition occurs between primary and secondary vortices [87]. For $|H_n| \simeq 1$, the vorticity is aligned with the direction of the velocity, i.e. swirl, where centre axes of rotation are parallel to flow direction, whereas, for $|H_n| = 0$, the vorticity is perpendicular to the flow. As such, normalized helicity can be used as a useful indicator of how the velocity vector field is oriented with respect to the vorticity vector field for a given flow field. Computing helicity and normalized helicity within OpenFOAM has been derived explicitly because there is not a standard tool to do so. Within ParaView, the Calculator filter is used to extract the dot product for the vorticity vector ($\text{curl}\mathbf{U}$) and velocity vector (\mathbf{U}) to obtain helicity (H_d). The helicity (H_d) divided on the multiplication of

absolute values for the vorticity ($\text{curl}U$) and velocity (U) to obtain normalized helicity (H_n) as presented in Equation 5.2.

The data are post-processed by extracting several snapshots of helicity results as presented in appendix A.4.7. Each snapshot represents four lines or rows of data types which are considered more beneficial to look at liquid jet phenomena from the inside. In the 1st row, the *Glygh* filter is used to present the vorticity vector component in the z-axis (axial liquid jet direction) which represents the stream-wise vortices within the liquid (represented by the two white lines as shown in Figure 5.16 at 194.6 ms and Figure 5.17 at time 198 ms). In the 2nd row of Figures 5.16 and 5.17, the helicity structure (contour) is presented just inside the liquid with a helicity density threshold value of 50000 to highlight the peaks. This method showed more clearly the location and direction of the strong vortex structures, which is further enhanced by presenting the helicity density within the liquid boundary, through reduction of the post-processed liquid 'opacity'.

In the 3rd row, Figures 5.16 and 5.17, the normalized helicity structure (contour) has been sliced longitudinally across the domain to reflect the location where vorticity was in parallel (stream-wise) or perpendicular (span-wise) to the liquid jet flow. This gives an indication of the location and type of vortices, i.e. spinning or shearing based on the normalized helicity configuration and colouring range in both the gas and the liquid. Visualizing normalized helicity has successfully highlighted the 3-D effects, or conversely which parts of the flow are mainly 2-D. In the presentation, the colour extremes of blue or red indicate where the flow is highly 3-D, whereas a green colour (normalised helicity is zero) means the flow is broadly 2-D and the vorticity is normal to the main fluid velocity. In the 4th row, of Figures 5.16 and 5.17, the *Stream Tracer* filter used to visualize the global vorticity just inside the liquid.

In the 1st row of Figure 5.16, at 0.12 m ($z/D=40$) a strong stream wise vorticity (vorticity-z) field is observed. The larger vector sizes and colour here represents how strong the vorticity is in the direction of the liquid flow. Starting from time 195 ms (see Appendix A.4.7), strong axial vorticity appears, which implies the generation of the twin vortex structure previously observed in Figure 5.11. In the 2nd row of Figure 5.16, a large, relatively long structure of helicity appears at $z/D=40$ (0.12 m). This indicates the magnitude of the vorticity and more specifically identifies the stream wise rotational vortices generated in the axial direction of the fluid flow inside the liquid core. In the 3rd row of Figure 5.16, at 0.2 m ($z/D=66$) downstream and outward, normalized helicity structure presented (mostly coloured in green) as a result of span-wise vortices. The

span-wise vorticity (as represented in the shear strain vortex without or with low rotation) presented perpendicularly to the jet flow axial direction. The strong normalized helicity located upstream at $z/D=40$ (0.12 m) as a result of span-wise vorticity disturbed the liquid layers structure as presented in the shear stresses and or spinning perpendicular to the flow direction.

The 4th row of Figure 5.16 shows the vorticity represented in stream lines inside the liquid, which explain the axial spinning and liquid local rotation around the liquid axis as shown previously in Figures 5.11 and 5.14. The strong spinning presented upstream at $z/D=40$ (0.12 m) is identical in location to the strong helicity structure observed. The vorticity structure initiated at time 194.6 ms and $z/D=40$ (0.12 m) modified with space and time to burst the jet at time 198 ms as shown in Figure 5.17.

The main purpose of this investigation is to examine the burst's onset and characterize the mechanism of the liquid jet burst phenomena. The aforementioned discussion as presented in the velocity relaxation and vorticity data analysis has revealed the reasons behind the liquid jet burst phenomena. From results, the burst initiated due to the axial velocity relaxation and generating the radial (secondary) movement which led to generating instabilities inside the liquid as represented in the different vortex structures. Also, the results showed that those disturbances initiated inside the liquid occurred at a very low relative velocity between the two phases at the interface. Investigating the liquid jet interaction with the surrounding gas after the jet burst is not the purpose of this investigation. However, the aerodynamic turbulence effect on the initiation of the liquid jet burst phenomena still considered important and will be considered later in this study as represented in Section 5.3.3.

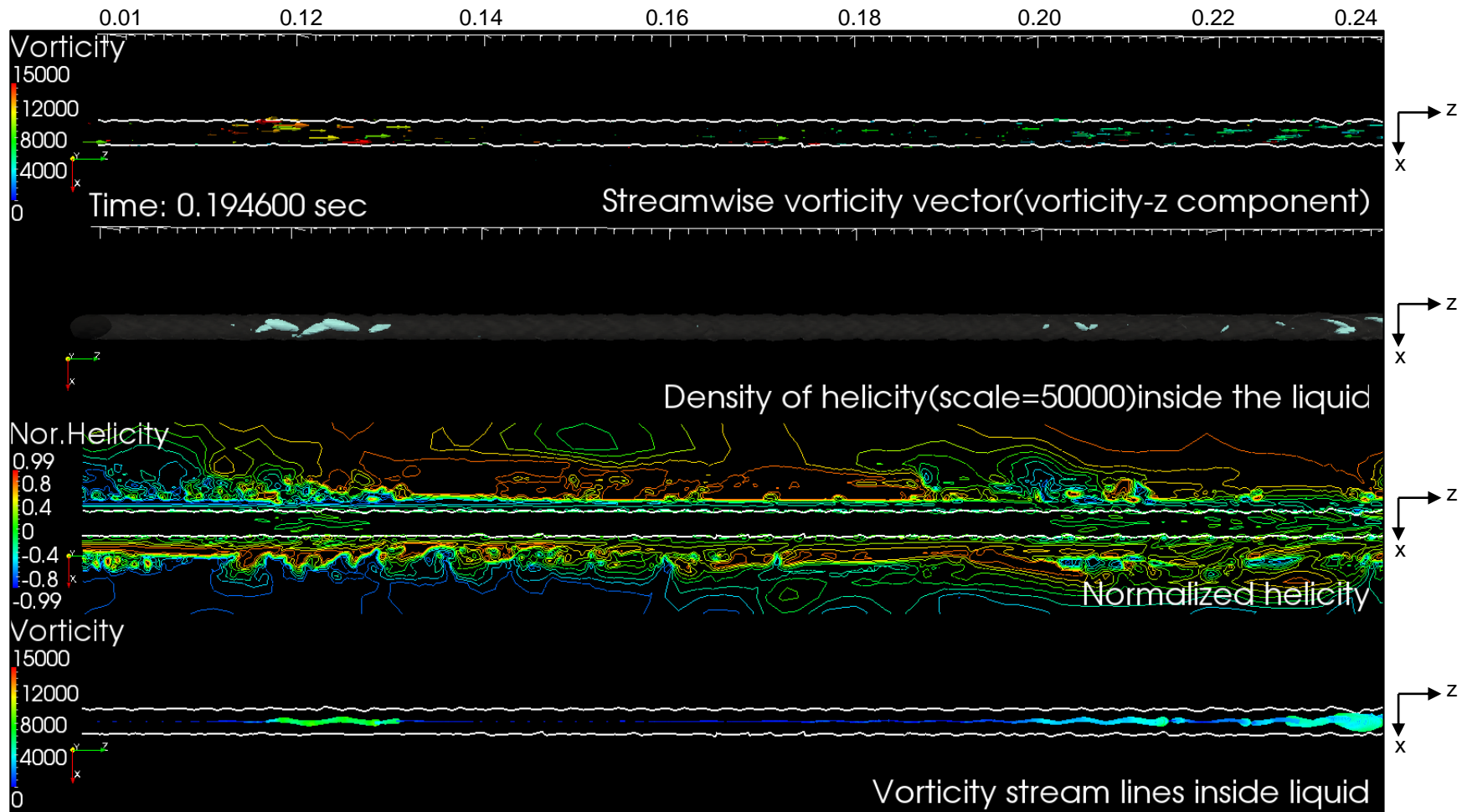


Figure 5.16 Liquid different vortex structures at time 194.6 ms. 1st row: axial vorticity vector (ω_z) in the liquid side, 2nd row: Helicity vortex structure in the liquid side, 3rd row: normalized helicity structure sliced longitudinally across the customized domain, 4th row: vorticity stream lines in the liquid side

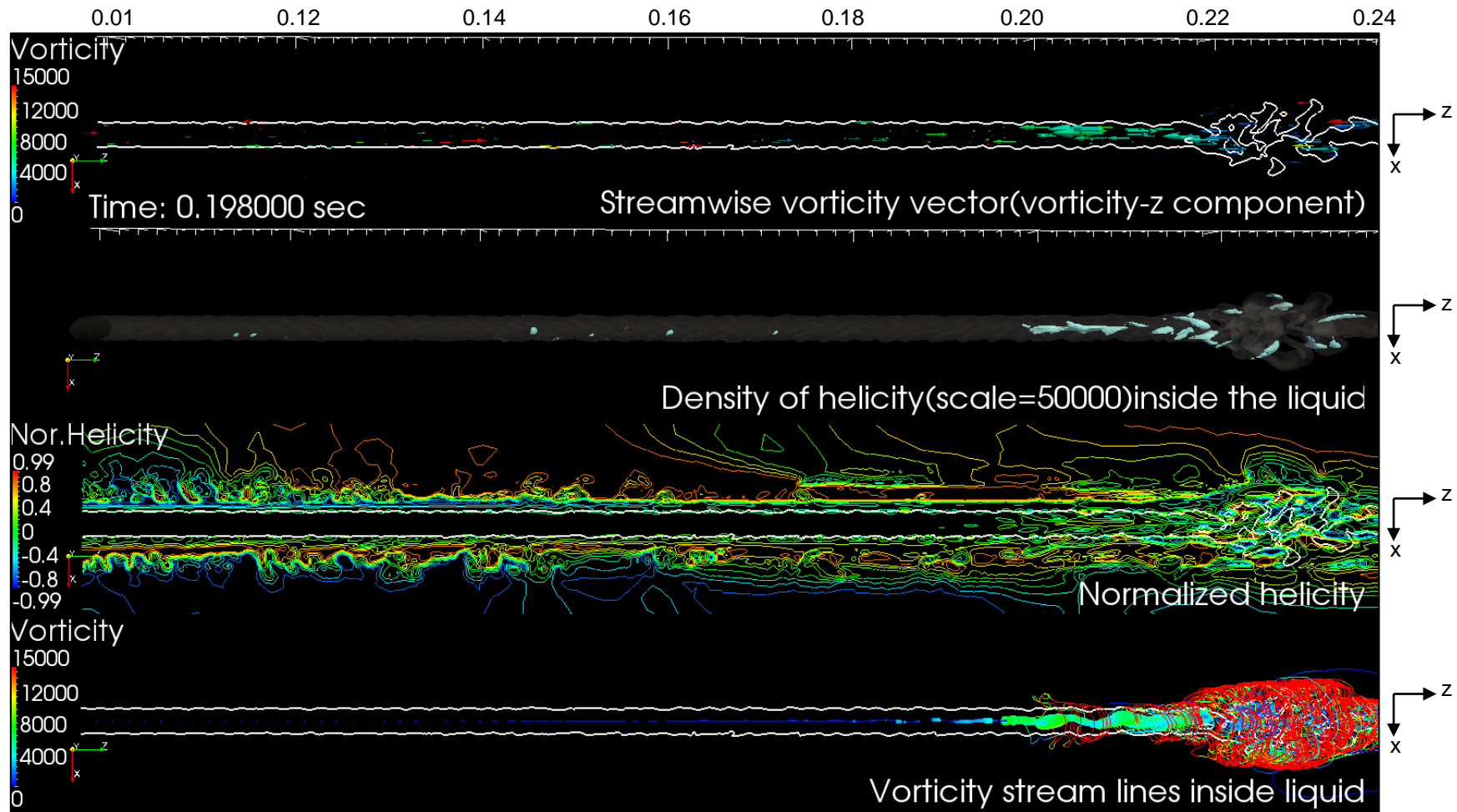


Figure 5.17 Liquid different vortex structures at time 198 ms. 1st row: axial vorticity vector (ω_z) in the liquid side, 2nd row: Helicity vortex structure in the liquid side, 3rd row: normalized helicity structure sliced longitudinally across the customized domain, 4th row: vorticity stream lines in the liquid side

5.3.2 Inflow Velocity Profile Effect on Burst Phenomena

In the previous section, results showed that the jet axial velocity reduction due to the parabolic (laminar) velocity profile relaxation to a flat profile and the radial movement generation is considered highly influential to burst the liquid jet. Therefore, it was decided to study two different cases: first, the jet ejected with a flat (top hat) inlet profile and secondly, a semi-turbulent inlet velocity profile conditions, hence suppressing flow relaxation. In this section, direct numerical simulation (DNS) based on the simple coupled level set and volume of fluid (S-CLSVOF) is performed in order to identify the influence of the jet inflow velocity profile conditions on the sensitivity on initiating the liquid jet burst phenomena.

This investigation has been undertaken under the same model set-up, flow, liquid and gas conditions used in the parabolic (default) liquid jet burst case in Section 5.3.1 unless specifically cited otherwise. The numerical setup used in this study allows any physical parameter to be varied individually so that “numerical experiments” may be performed by varying each of the potential influencing parameters separately. The focus of the present investigation was concerned with identifying those physical phenomena and observations that most strongly prevail and enhance the burst phenomena. The same strategy used previously in Section 5.3.1 is used again here to post-process the data including the same fixed scales or threshold values in order to have fair and reasonable physical comparisons with the parabolic (default) jet case.

5.3.2.1 Turbulent (Top Hat) Inflow Velocity Profile Jet

In contrast with laminar flow, the definition of the velocity profile in turbulent flow is based on both analysis and measurements, and so is empirical in nature. Velocity profiles for laminar and top hat flat turbulent profile inflow used in the current study are compared with the typical turbulent profile inflow in Figure 5.18. The approach used to identify the inflow profile for laminar flow and fully developed turbulent flow is to use the power-law velocity profile approximation [88] as shown schematically in Figure 5.19 and expressed as:

$$\frac{u}{u_{max}} = \left(1 - \frac{r}{R}\right)^{1/n}$$

Equation 5.3

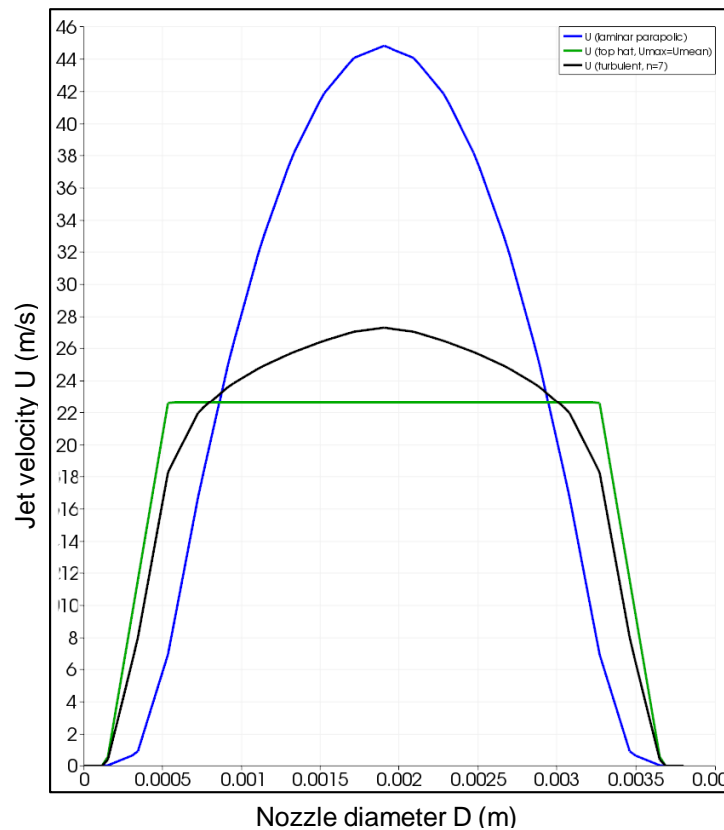


Figure 5.18 Laminar (blue), top hat turbulent (green) and typical turbulent (black) velocity profile produced by the current modelling benchmark

where the exponent n is a constant whose value depends on the Reynolds number. The value of n increases with increasing Reynolds number. The value $n = 7$ generally approximates many turbulent flows in practice, giving rise to the term one-seventh power-law velocity profile. From the literature [88], various power-law velocity profiles are shown in Figure 5.20 for $n = 6, 8,$ and 10 together with the velocity profile for laminar flow for comparison. As shown, the turbulent velocity profile is broader than the laminar one, and it becomes flattened as n increases.

The equivalent top hat velocity profile (turbulent) can be easily identified in the current modelling by imposing constant axial velocity value ($U = 22.6$ m/s) at each grid point across the inflow region or boundary at the nozzle exit. The top hat velocity profile is not the realistic turbulent profile jet case that could result from a simple orifice nozzle even for a flow through a short nozzle or pipe. However, a top hat inflow velocity profile is an idealised representation which still can be reproduced from other nozzle types such as conical contraction nozzle [89].

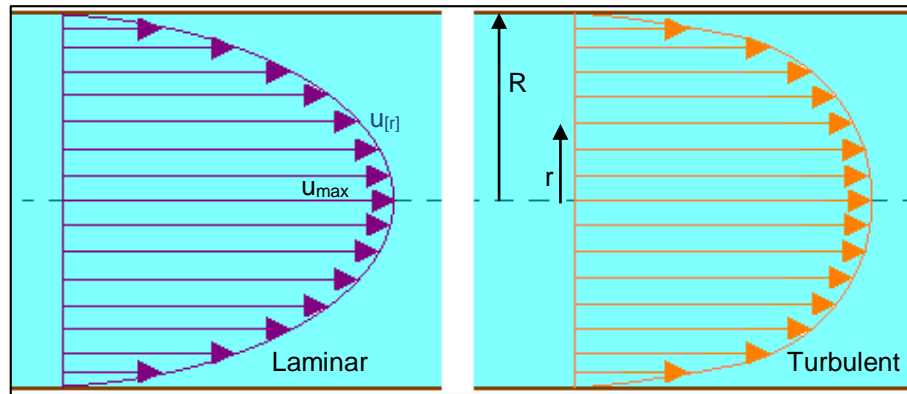


Figure 5.19 Schematic diagram for laminar and turbulent velocity profile

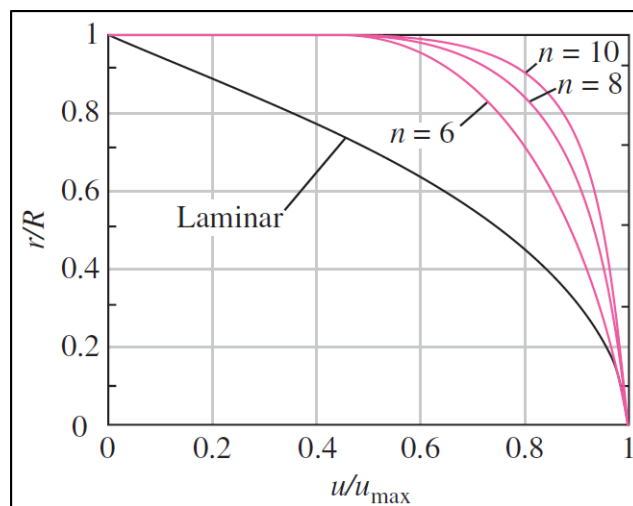


Figure 5.20 Power-law velocity profiles for turbulent flow in a pipe for different exponents, and its comparison with the laminar velocity profile. (adapted from [88])

Figure 5.21 displays the numerical simulations results of a top hat inflow velocity profile jet at Reynolds number $Re=2200$ at an advanced time period of ejection. One can note that the jet starts with a smooth surface upstream but later in the downstream region at 0.05 m ($z/D= 16.66$) some wrinkles appear and they develop but do not breakup or burst. By contrast with the burst case, the jet, in this case, showed a stable and coherent structure with uniform ruffled surface due to the normal liquid gas interaction. The simulation was run for a longer physical time than achieved for parabolic burst case and stopped after 225 ms . A series of snapshots covering the jet process at shorter fractions of time to those showed in Figure 5.21 is presented in Appendix A.5.1.

As the first 100 ms of the jet development did not show significant phenomena or high jet surface deformation, post-processing treatment is emphasised on the last 125

ms in order to minimise computational expense. It has been focused on the area where instabilities initiated at the interface upstream till the end of the jet downstream for the distance between 0.1 to 0.2625 m within the customised domain of the jet length. In order to have a reasonable comparison with the default burst jet case, the top hat turbulent jet results discussion is focused on the time where the jet showed a burst in the laminar parabolic (default) case around 198 ms.

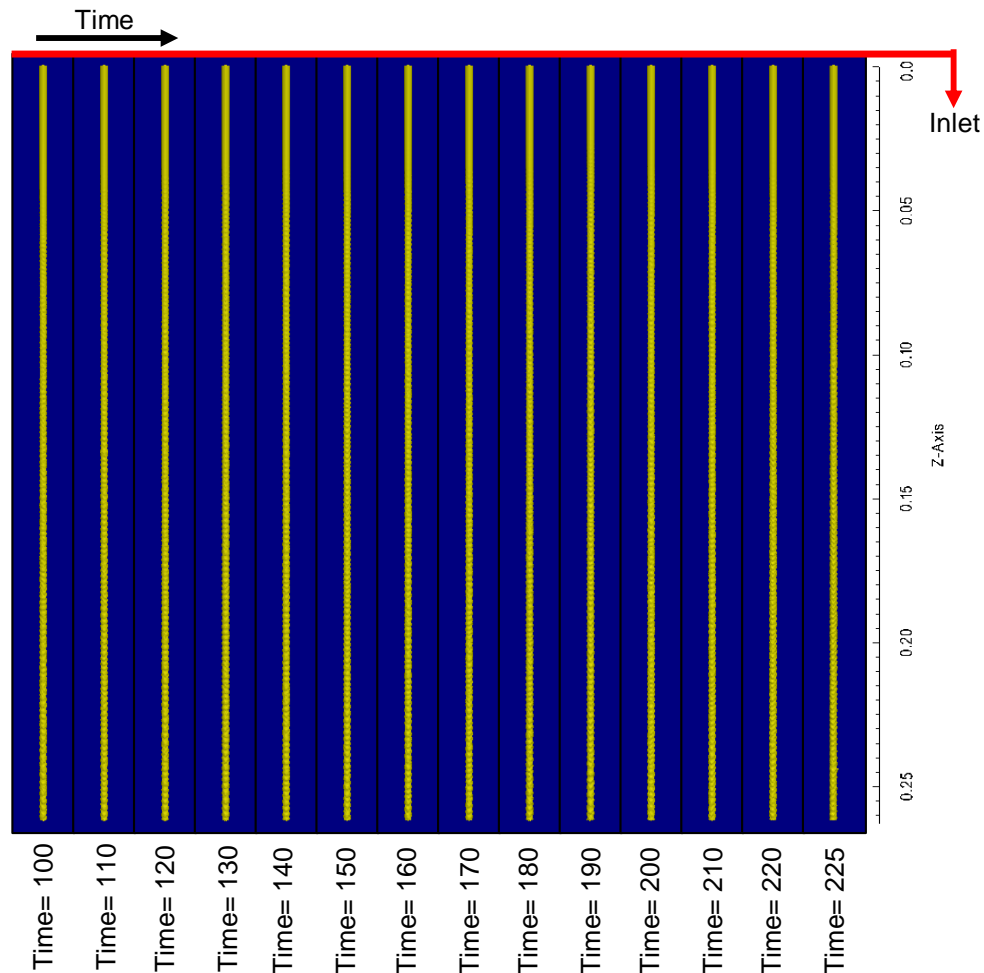


Figure 5.21 Liquid jet column ejected with an inflow condition of the top hat (turbulent) velocity profile. The number next to each image indicates the dimensional physical time elapsed in milliseconds

In Figure 5.22, the liquid jet velocity profile maintained a flat profile throughout the jet. In contrast to the laminar parabolic case, the turbulent flat velocity profile dragged the gas immediately after the liquid was injected from the nozzle. Air velocity is modified further downstream and increased up to 10-15 m/s. Liquid stream lines confirmed the observations of the uniform axial velocity inside the liquid shown in the 2nd row of this figure. The liquid jet surface deformation showed a high degree of symmetry, which results in uniformity of the velocity profile structure and streamline in gas as shown in the

2nd and 5th rows of Figure 5.22. A series of snapshots associated with Figure 5.22 are presented in Appendix A.5.2.

Axial and radial velocity components at the centre of the liquid core are examined along with the jet as shown in Figure 5.23. At time 198 ms, axial velocity in the z-axis (U_z) exhibited a gradual and uniform increase from $U=22.6$ to around $U=22.7$ m/s due to acceleration results from the effect of gravity. By contrast, the velocity components in the radial plane were insignificant. A series of snapshots relating to Figure 5.23 covering the time process of the jet is presented in Appendix A.5.3.

Figure 5.24 shows the instantaneous lateral cross-sectional (x-y plane) velocity vector at twelve lateral locations distributed equally along the customized domain at time 198 ms. A series of snapshots relating to Figure 5.24 covering the time process of the jet is presented in Appendix A.5.4. In Figure 5.24, at $z/D=33$ to $z/D=52.8$ (an upstream section within the customized domain), very little radial velocity is generated at the liquid gas interface and directed towards the liquid side. On the interface, the directions of the velocity produced by the interface shear are already asymmetrical, implying that the air flow field around the liquid column is not perfectly symmetrically structured. This asymmetry is progressively modified from the nozzle exit, whereas the flow structure is symmetrical. As noticed in Figure 5.23, no significant radial motion observed as shown in Figure 5.24. The difference in the radial motion observed here compared with the laminar parabolic case is because no velocity relaxation occurs in the top hat (flat) velocity profile case. Hence, the transverse or the twin vortex motion structure observed in the parabolic laminar jet do not evolve either.

To clarify the differences between the parabolic and top-hat cases further, the focus has been put on velocity and vortices inside the flow field. Figure 5.25 shows the instantaneous comparison between the velocity field and the vortices field at time 198 ms. As shown in the 1st and 2nd rows of Figure 5.25, the liquid velocity is uniformly distributed inside the liquid, and its magnitude stays constant along the length of the jet due to the suppression of velocity relaxation. Figure 5.25 confirms the results presented in Figures 5.23 and 5.24, where axial velocity flow dominates with effectively no radial movement. This is considered the reason behind the high stability observed for the turbulent jet and low surface deformation if compared with laminar burst jet case. A series of snapshots associated with Figures 5.25 covering the time process of the jet is presented in Appendix A.5.5.

As observed in Figure 5.26, the liquid surface roughness excites the air flow field, increasing its speed as the liquid jet moves downstream. This process is confirmed in

the 1st row of Figure 5.26 which shows strong air vorticity induced around the liquid surface. Such air vortices could enhance the liquid column deformation as seen at 0.14 m in the 1st row of Figure 5.22. The 2nd row of Figure 5.26 reassuringly confirms the lack of vorticity existing in liquid, also shown in Figure 5.25, when compared with the laminar burst case.

If compared to the laminar burst case (cf. Figures 5.14 and 5.15), no transverse vortex structure is observed in the 3rd row of Figure 5.26 showing the zero vorticity field (ω_x , and ω_y). Also, positive and negative vorticity regions that appeared in sequence in the laminar burst case have disappeared here for the turbulent jet. The 4th row of Figure 5.26 shows no ω_y , in contrast with the sinuous motion disturbances observed for the laminar burst case (Figures 5.14 and 5.15). Furthermore, strong longitudinal twin vortex motions prevalent in the laminar case are not present in this case, as shown in the 5th row of Figure 5.26 in the vorticity field ω_z . The aforementioned observations are fully consistent with the physical observation noticed in Figures 5.23, 5.24, and 5.25. A series of snapshots relating to Figure 5.26 covering the time process of the jet is presented in Appendix A.5.6.

From the vortex field presented in Figure 5.27, the 1st row showed no noticeable stream-wise vorticity vector inside the liquid if compared with the same situation for the laminar burst jet. In the 2nd row of Figure 5.27, no vortex structure was observed inside the liquid in contrast to the strong vortex structure existed for the laminar jet burst. Throughout the normalized helicity presented in the 3rd row of Figure 5.27, no clear span-wise vortex structure is identified within the liquid if compared with the obvious span-wise vortex structure noticed for the laminar burst jet. In contrast with the laminar jet burst, no clear rotation is generated inside the liquid for the stream-wise vorticity presented in the 4th row of Figure 5.27. A series of snapshots relating to Figure 5.27 covering the time process of the jet is presented in Appendix A.5.7.

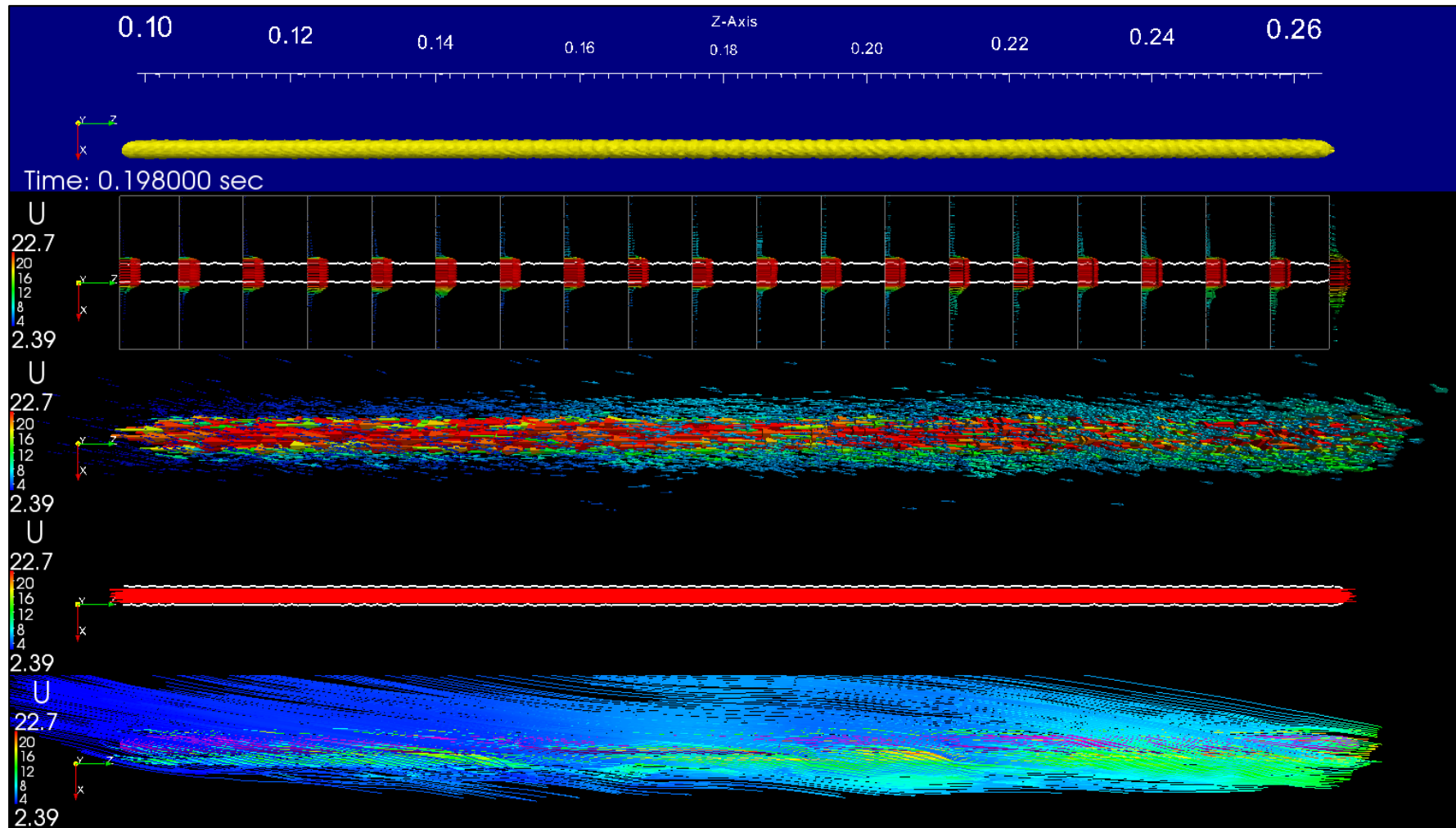


Figure 5.22 Top hat turbulent case results show the liquid column (1st row), domain velocity profile (2nd row), domain velocity field (3rd row), liquid velocity stream lines (4th row) and gas velocity stream lines (5th row)

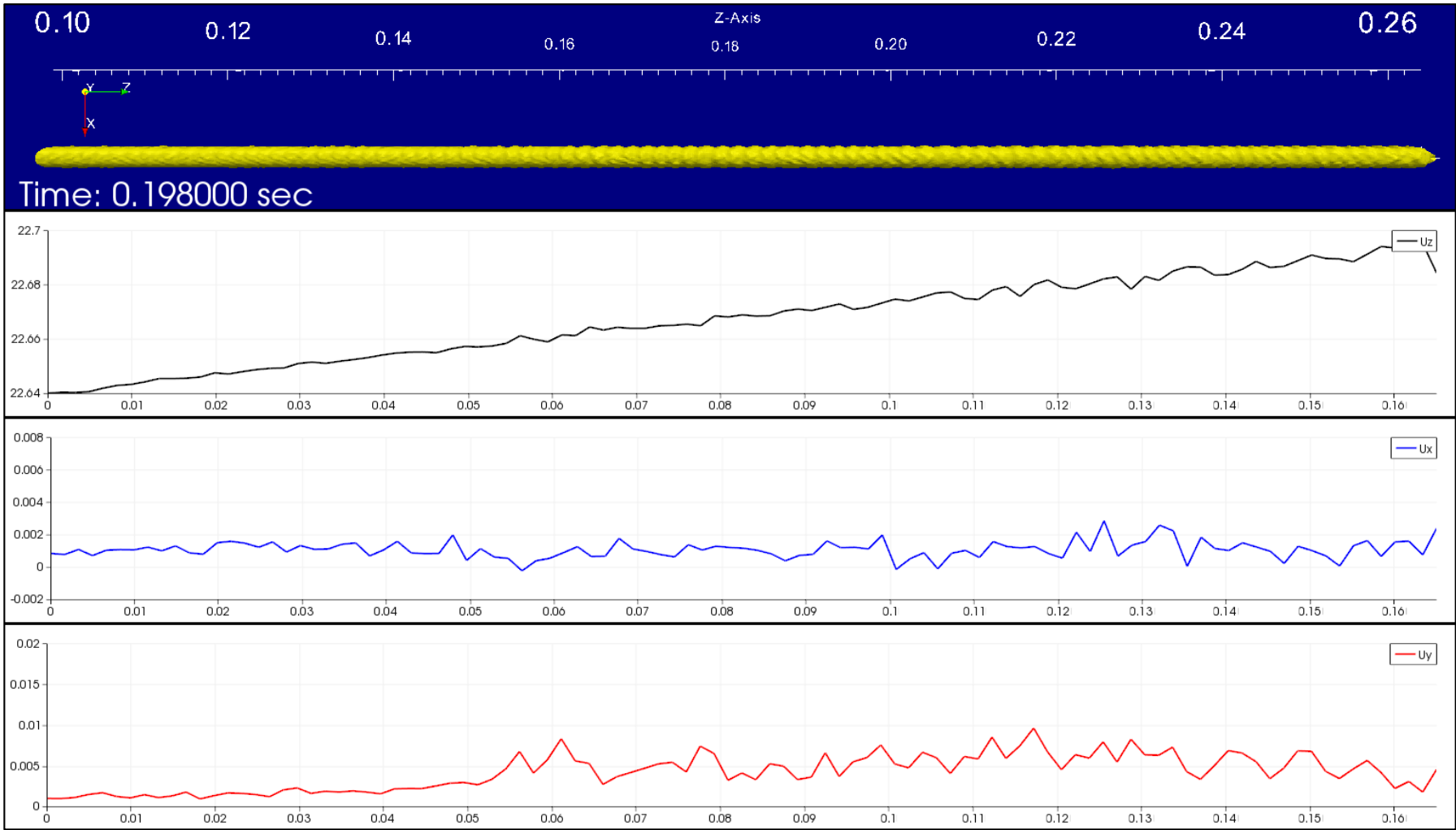


Figure 5.23 Liquid jet core velocity components (U_x , U_y and U_z) at time 198 ms of liquid jet top hat (flat) inflow turbulent condition

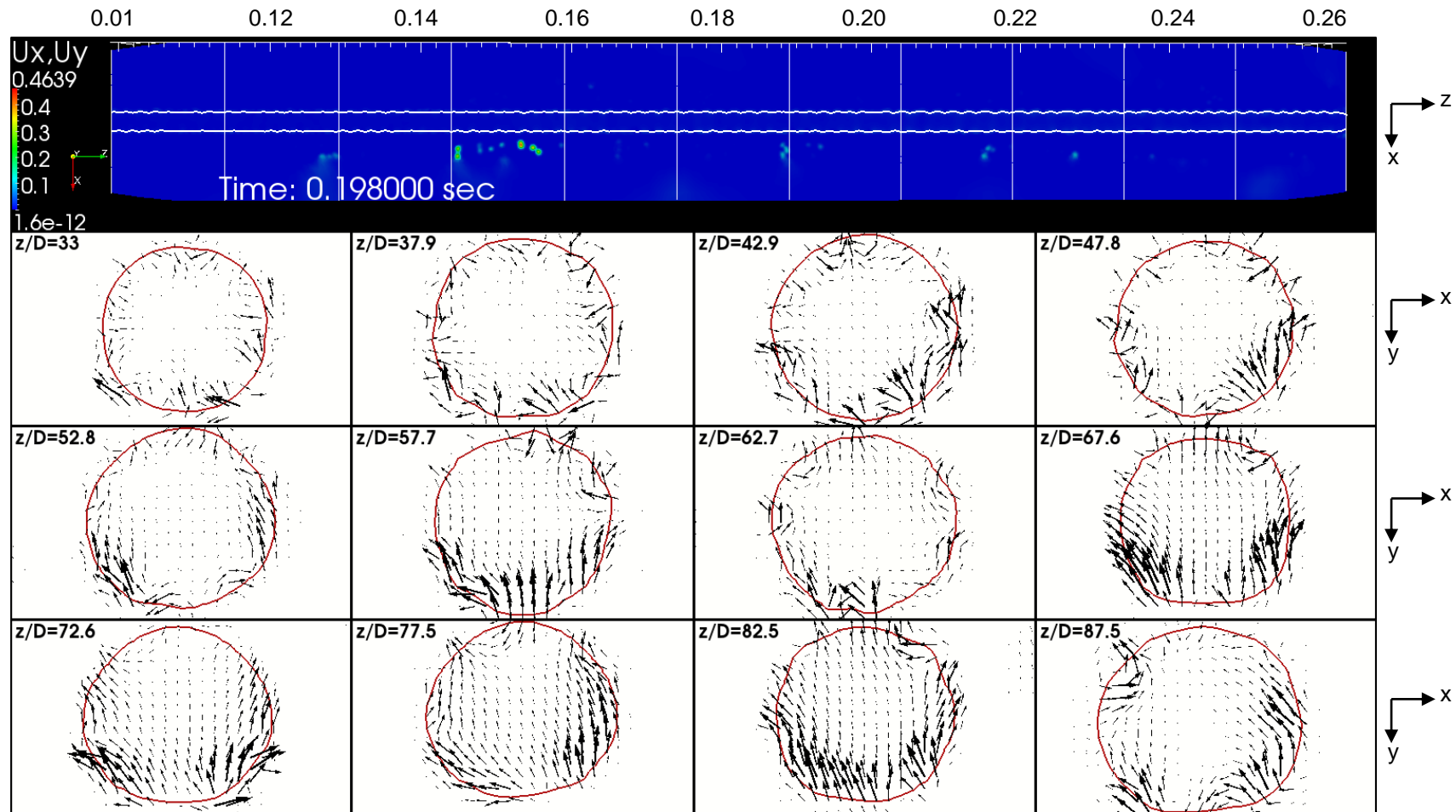


Figure 5.24 Distribution of instantaneous liquid velocity vectors projected onto longitudinal and cross-sectional planes at different axis locations for top (flat) inflow turbulent condition

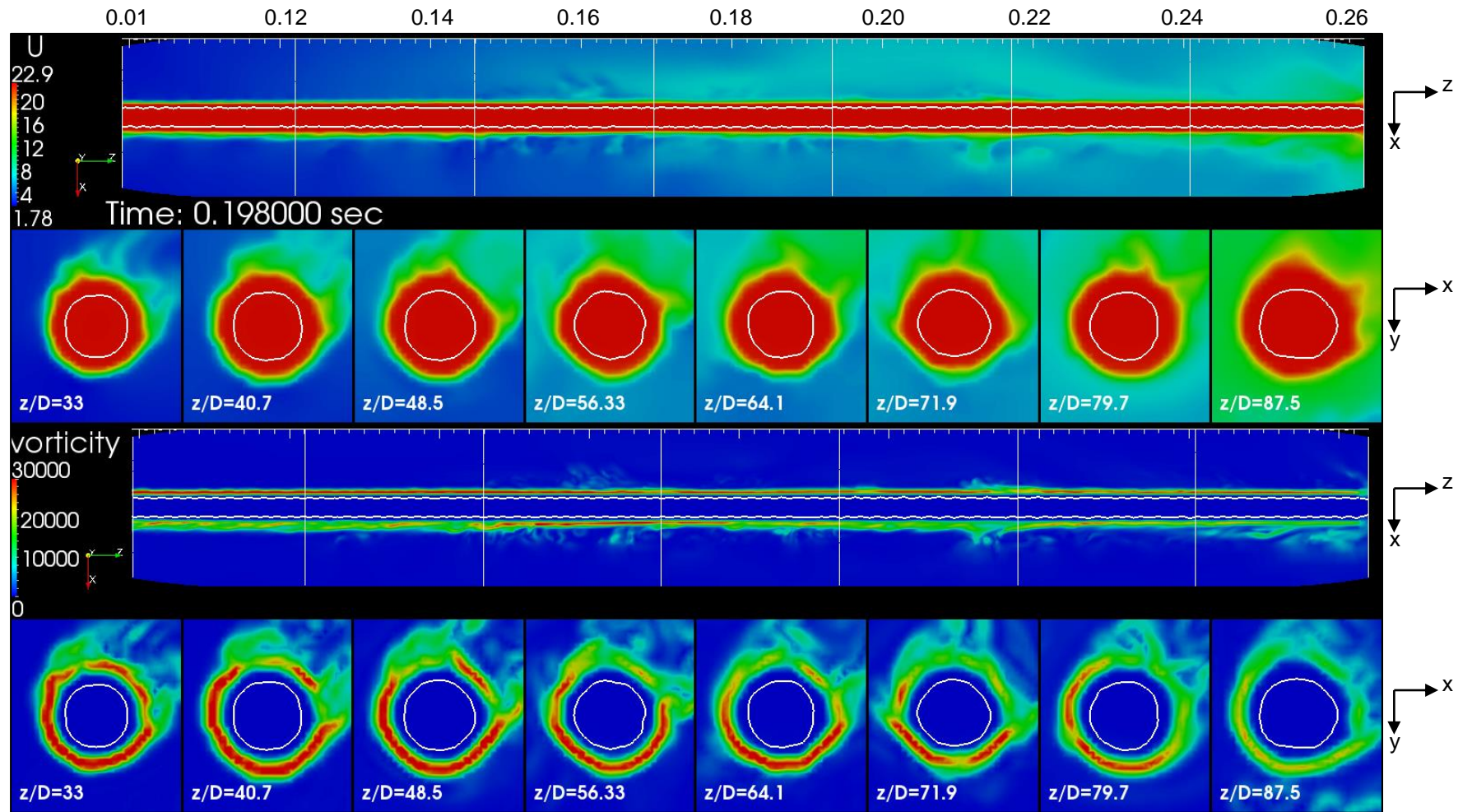


Figure 5.25 Longitudinal and lateral velocity (1st and 2nd rows) and vorticity (3rd and 4th rows) field's distribution of turbulent liquid jet problem

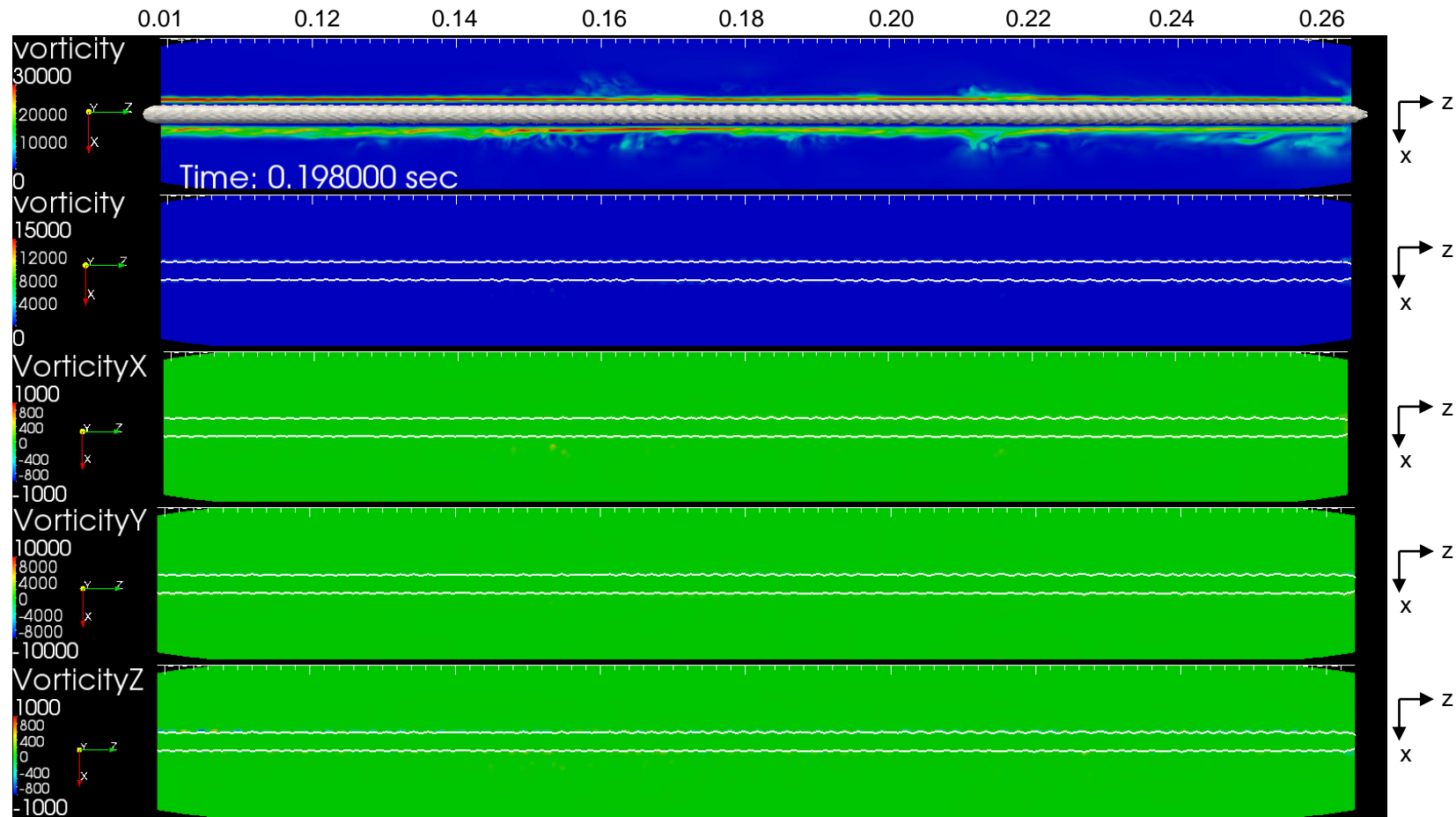


Figure 5.26 Distribution of instantaneous vorticity fields in an axis plain of the turbulent liquid case. 1st row in the gas phase, 2nd row in the liquid phase, 3rd row vorticity-x distribution in the liquid phase, 4th row vorticity-y distribution in the liquid phase and 5th row vorticity-z component distribution in the liquid phase

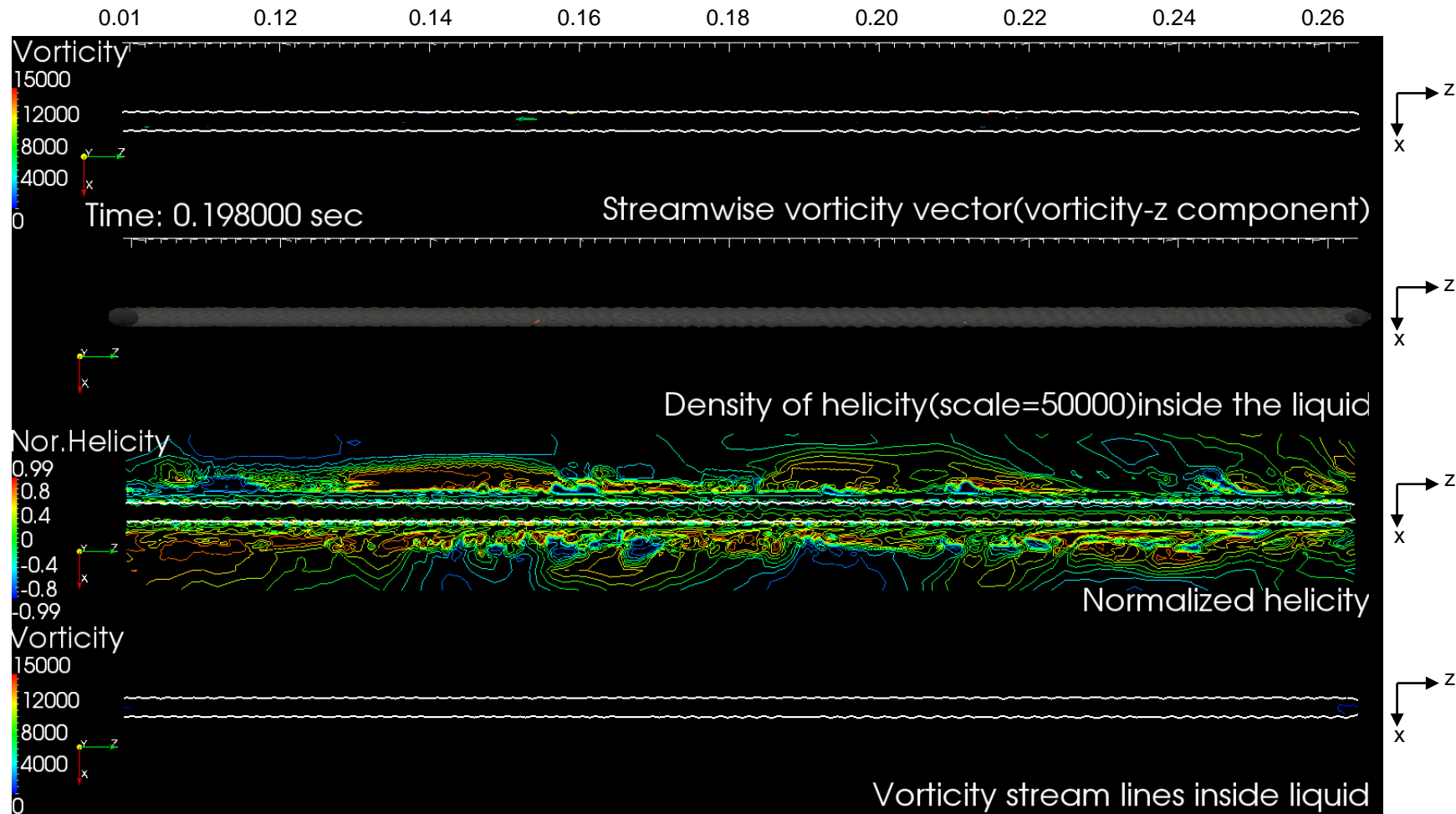


Figure 5.27 Different vortex structures for top flat turbulent liquid jet case at time 198 ms. 1st row: axial vorticity vector (ω_z) in the liquid side, 2nd row: Helicity vortex structure in the liquid side, 3rd row: normalized helicity structure sliced longitudinally across the customized domain, 4th row: vorticity stream lines in the liquid side

5.3.2.2 Semi-turbulent Inflow Velocity Profile Jet

There is no direct or exact definition for the semi-turbulent velocity profile because it has undefined degrees as it ranges from fully laminar (parabolic profile) to fully turbulent profile where $n=7$ according to the power law approximation. The semi-turbulent velocity profile adopted through using the power law approximation is based on the maximum velocity difference between laminar and turbulent cases. The idea is to propose a maximum velocity for the semi-turbulent profile equal to some value in between the maximum velocities used for the laminar and turbulent (top hat) profiles whilst maintaining fixed mean velocity and hence Reynolds number. Therefore, at constant $Re=2200$ and $u_{mean}=22.6$ m/s, n should be some value less than 7 which represents the turbulent inflow case. As illustrated in Figure 5.28 below, $n=3$ is the power law approximation adopted for the semi-turbulent inflow velocity profile. The maximum velocity for this case is $u_{max}=34$ m/s, which is almost midway between the maximum velocities for the parabolic (laminar) and the top hat (turbulent) case.

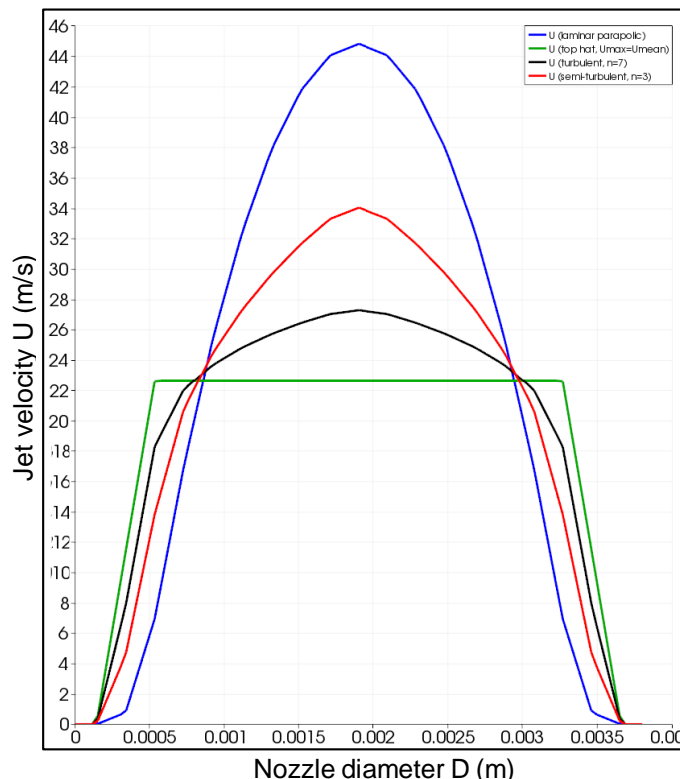


Figure 5.28 Laminar (blue), top hat turbulent (green), typical turbulent $n=7$ (black) and semi-turbulent $n=3$ (red) velocity profile produced by the current modelling benchmark

The equivalent semi-turbulent velocity profile can be easily identified in the current modelling through using Equation 5.3 at each grid point across the inflow region

or boundary at the nozzle exit through using axial mean velocity $U_{mean}= 22.6$ m/s, and $n=3$. Considering semi-turbulent inflow velocity profile, the current simulations have been performed under the same corresponding jet initial, boundary and control settings conditions to those of the laminar (parabolic) inflow velocity condition.

Figure 5.29 shows the numerical simulation results of the semi-turbulent inflow velocity profile jet at Reynolds number $Re=2200$ at an advanced time period after ejection. One observes that the jet starts with a smooth surface upstream, but later in the downstream region at 0.03 m ($z/D= 10$) some wrinkles establish and develop but do not breakup or burst. In contrast to the burst case and similar to the turbulent case, the jet showed stable and coherent structure with uniform ruffled surface due to the conventional liquid-gas interaction. Hence, as there are no signs of strong instabilities or jet burst, simulations have been allowed to run for longer physical time than achieved for laminar or turbulent cases and stopped after 245 ms. A series of snapshots covering the jet process at shorter fractions of time to those showed in Figure 5.29 is presented in Appendix A.6.1.

The same treatment has been considered in the post-processing stage similar to the one used in the parabolic burst case. As the first 100 ms after release did not show any important phenomena or high jet surface deformation, post-processing treatment is concentrated on the last 145 ms in order to reduce computational cost. The region which is being focussed on is where instabilities are initiated at the interface upstream to the end of the jet downstream for the distance between 0.1 to 0.2625 m. In order to have a reasonable comparison with the default jet burst case, the semi-turbulent jet results discussions are focused on the time where the jet showed burst for the laminar parabolic case at 198 ms.

In the 2nd row of Figure 5.30, despite the presence of the velocity relaxation, the liquid jet velocity profile not flattened along the length of the jet. If compared with the parabolic case, the rate of velocity relaxation in the semi-turbulent is lower than that noticed for the laminar (parabolic) burst case. The liquid stream lines confirm the observations of the non-uniform axial velocity inside the liquid shown in the 4th row of the same figure. A series of snapshots of Figure 5.30 is presented in Appendix A.6.2.

As shown in the Figure 5.31 at time 198 ms, the axial velocity (U_z) exhibited a gradual, smooth and uniform decrease from $u_{max}=34$ m/s to around $U=26.2$ m/s due to the local deceleration results from the effect of velocity relaxation. On the other hand, the radial velocity components in the x-axis (U_x) and y-axis (U_y) direction showed moderate radial movement with increase in radial velocity components to a maximum

$U_{x,y}=0.02$ m/s observed at different time steps results. A series of snapshots relating to Figure 5.31 covering the time process of the semi-turbulent jet is presented in Appendix A.6.3.

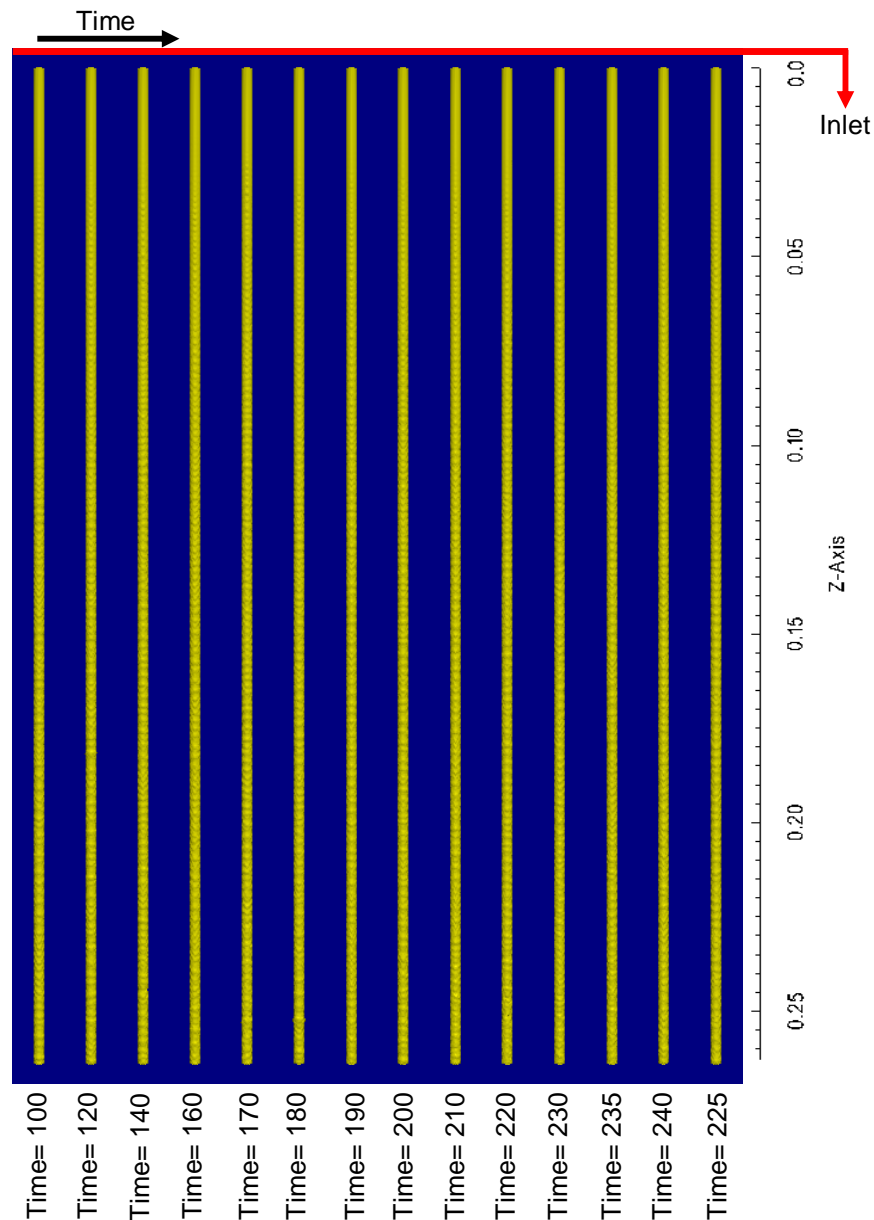


Figure 5.29 Liquid jet column ejected with an inflow condition of semi-turbulent velocity profile. The number next to each image indicates the dimensional physical time elapsed in milliseconds

No vortex structure is observed in Figure 5.32, despite the existence of the radial motion due to the axial velocity relaxation which contrasts with the top hat inflow velocity case. It is noticed that very little radial velocity is generated at the liquid-gas interface

and directed towards the liquid side or the opposite direction. At some locations on the interface, the behaviour of the radial movement produced by the interface shear showed asymmetry implying that the air flow field around the liquid column has asymmetrical structures. Less effective velocity relaxation occurs in the semi-turbulent velocity profile indicated by the differences in the radial motion when compared with the laminar case. These differences include the lack of transverse or the twin vortex motion structure observed in the parabolic laminar jet case. However, the semi-turbulent jet case shows radial motion more akin to that associated with the top hat turbulent case. A series of snapshots of Figure 5.32 covering the time process of the semi-turbulent jet is presented in Appendix A.6.4.

Figure 5.33 shows the instantaneous comparison between the velocity field and the vorticity field at time 198 ms. As shown in the 1st and 2nd rows of Figure 5.33, the liquid velocity is not uniformly distributed inside the liquid, and its higher magnitude pervades the centre of the liquid core along its length. Their velocity profile does not completely relax by the end of the jet. The results presented in Figure 5.33 agree with the results presented in the Figures 5.31 and 5.32. The jet is considered stable and showed no burst in the semi-turbulent study case as no secondary flow effectively existed when comparing with the laminar case. A series of snapshots of Figures 5.33 covering the time process of the semi-turbulent jet are presented in Appendix A.6.5.

As for the turbulent case, the liquid surface roughness indicated and modified as liquid jet move downstream as shown Figure 5.34. Presenting only the liquid vorticity as in the 2nd row of Figure 5.34, it indicated the less effective vorticity existed within the liquid as shown in Figure 5.33 when comparing with the laminar case. In the semi-turbulent jet case, the liquid velocity profile showed, but with less effective relaxation (no significant secondary flow noticed) when comparing with the laminar case, therefore, the vorticity was less effective in the semi-turbulent jet than the laminar burst jet (see Figures 5.14 and 5.15 for comparison with Figures 5.33 and 5.34). This indicated also in not existing the transverse vortex structure similar to those positive and negative regions (red and blue) appeared in sequence in the 3rd row along the z-x plane for the laminar burst jet case (see Figures 5.14 and 5.15 for comparison with Figures 5.34). Less effective vorticity was noticed in the 4th row and no strong longitudinal twin vortex motions observed in the 5th row of Figure 5.34 when compared with the laminar case as a result of relatively less effective velocity relaxation indicated in the semi-turbulent case. A series of snapshots of Figures 5.34 covering the time process of the semi-turbulent jet are presented in Appendix A.6.6.

In contrast to the laminar burst case, the vorticity component in the z-axis showed no stream-wise vorticity vector effect inside the liquid as shown in the 1st row of Figure 5.35. In contrast to the laminar burst case, as shown in the 2nd row, no helicity presented as an indication of less effective vortex generation within the liquid. Likewise, the normalized helicity presented in the 3rd row showed less effective span-wise vortex within the liquid in contrast to the laminar burst case. Moreover, the vorticity streamlines presented in the 4th row showed no spiral or rotation within the liquid when compared with the appreciable stream-wise spiral movement observed in the laminar burst jet. A series of snapshots of Figures 5.35 covering the time process of the semi-turbulent jet are presented in Appendix A.6.7.

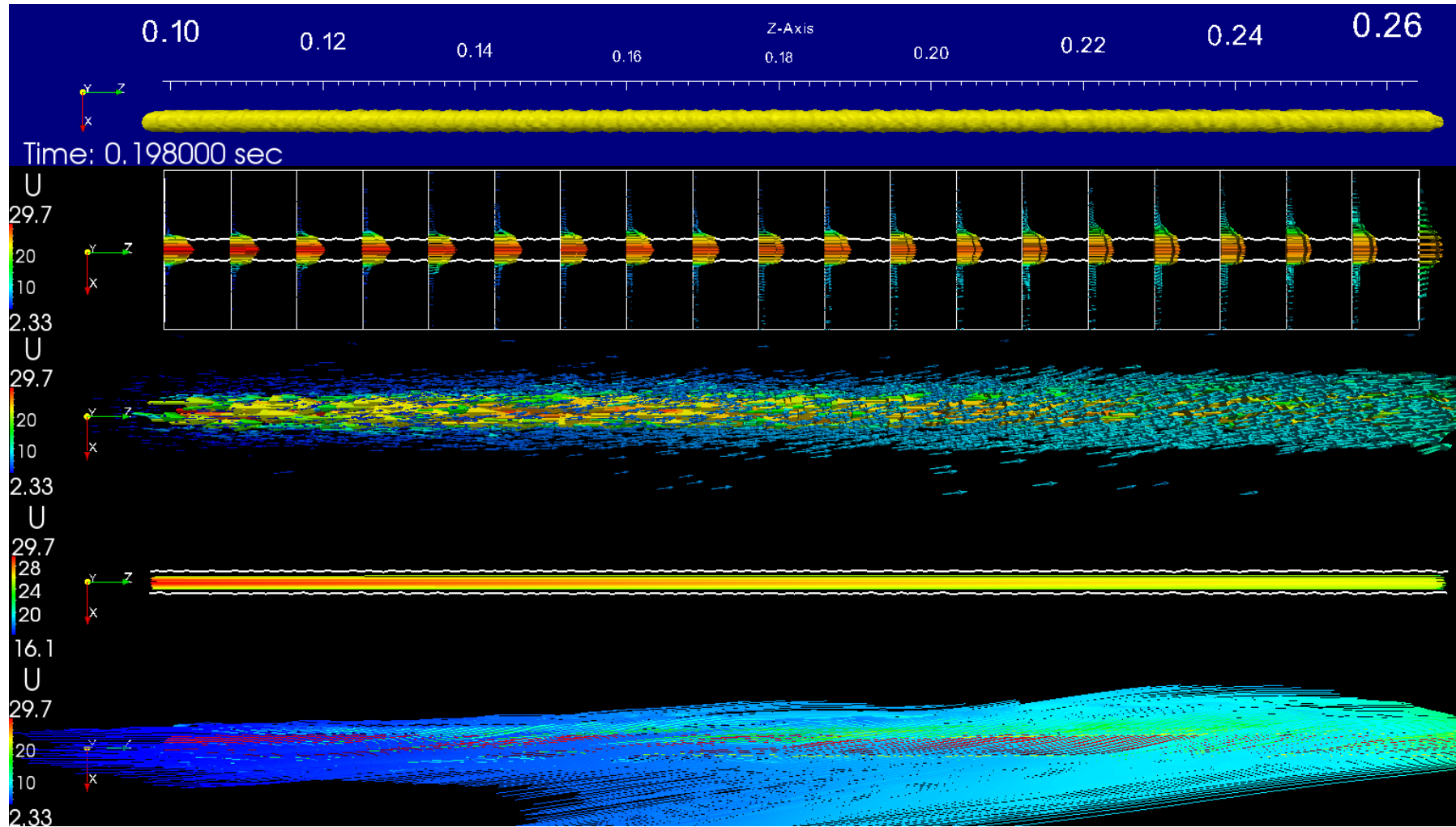


Figure 5.30 Semi-turbulent case results show the liquid column (1st row), domain velocity profile (2nd row), domain velocity field (3rd row), liquid velocity stream lines (4th row) and gas velocity stream lines (5th row)

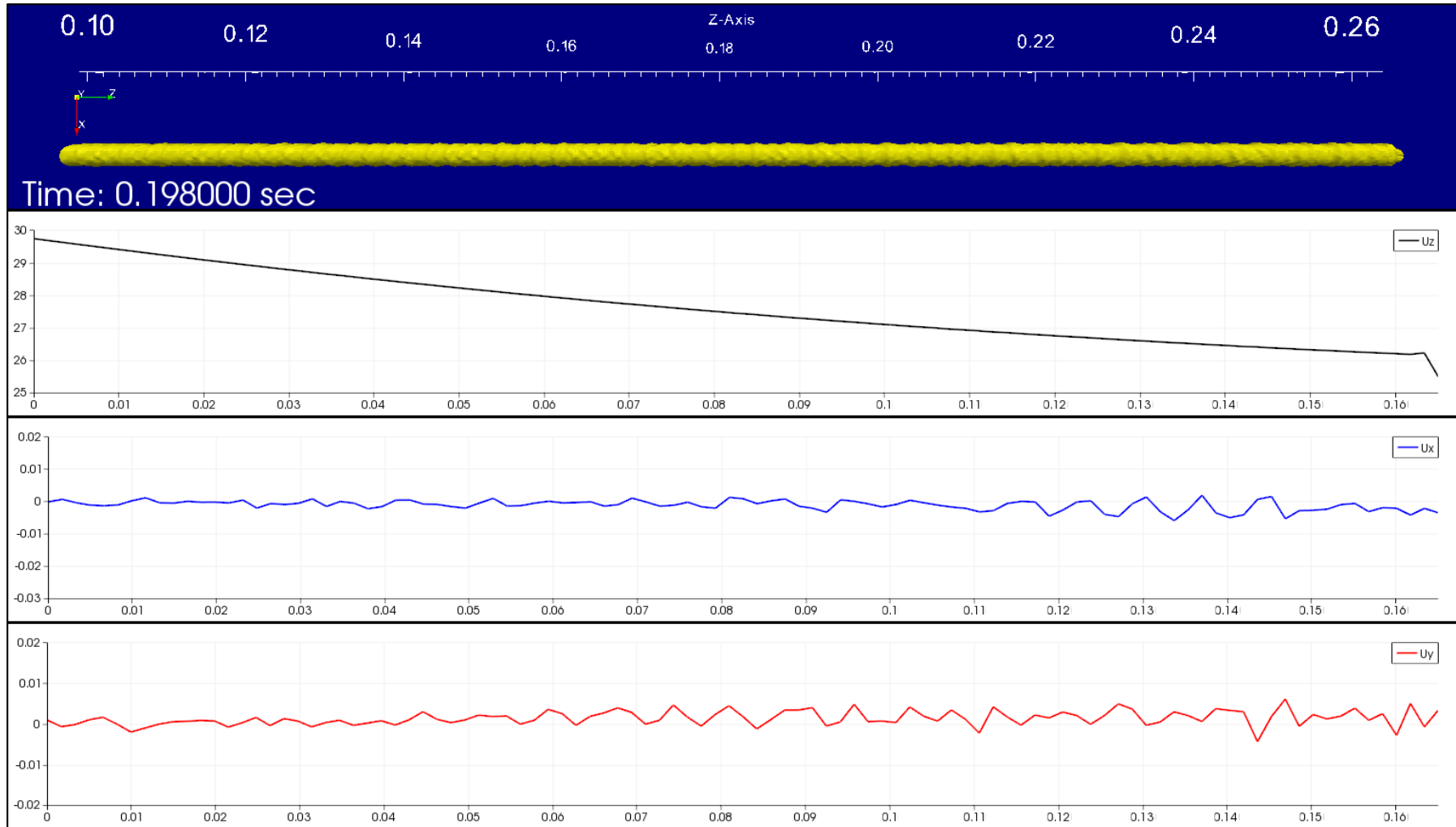


Figure 5.31 Liquid jet core velocity components (U_x U_y and U_z) at time 198 ms of liquid jet semi-turbulent inflow condition

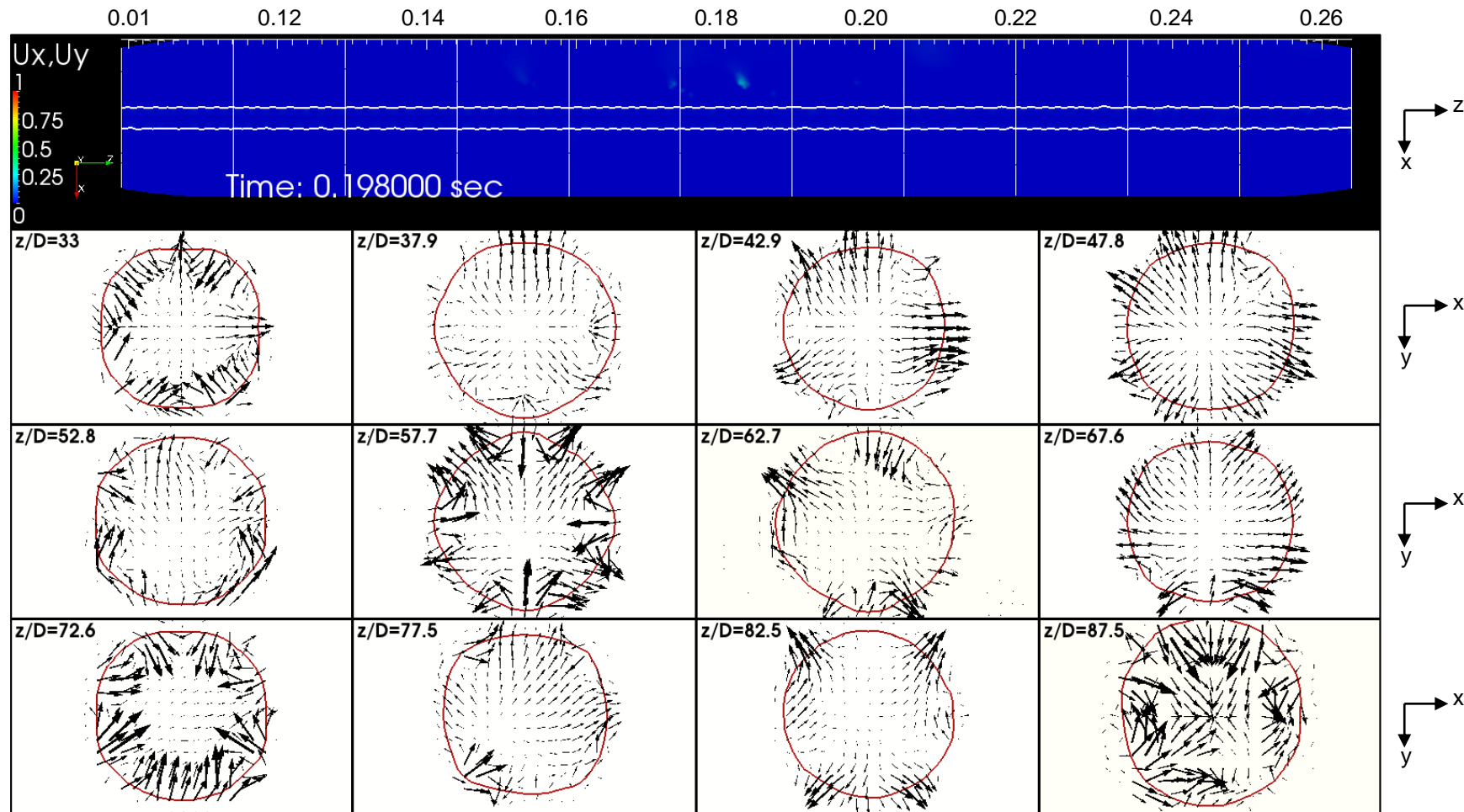


Figure 5.32 Distribution of instantaneous liquid velocity vectors projected onto longitudinal and cross-sectional planes at different axis locations for the semi-turbulent inflow condition

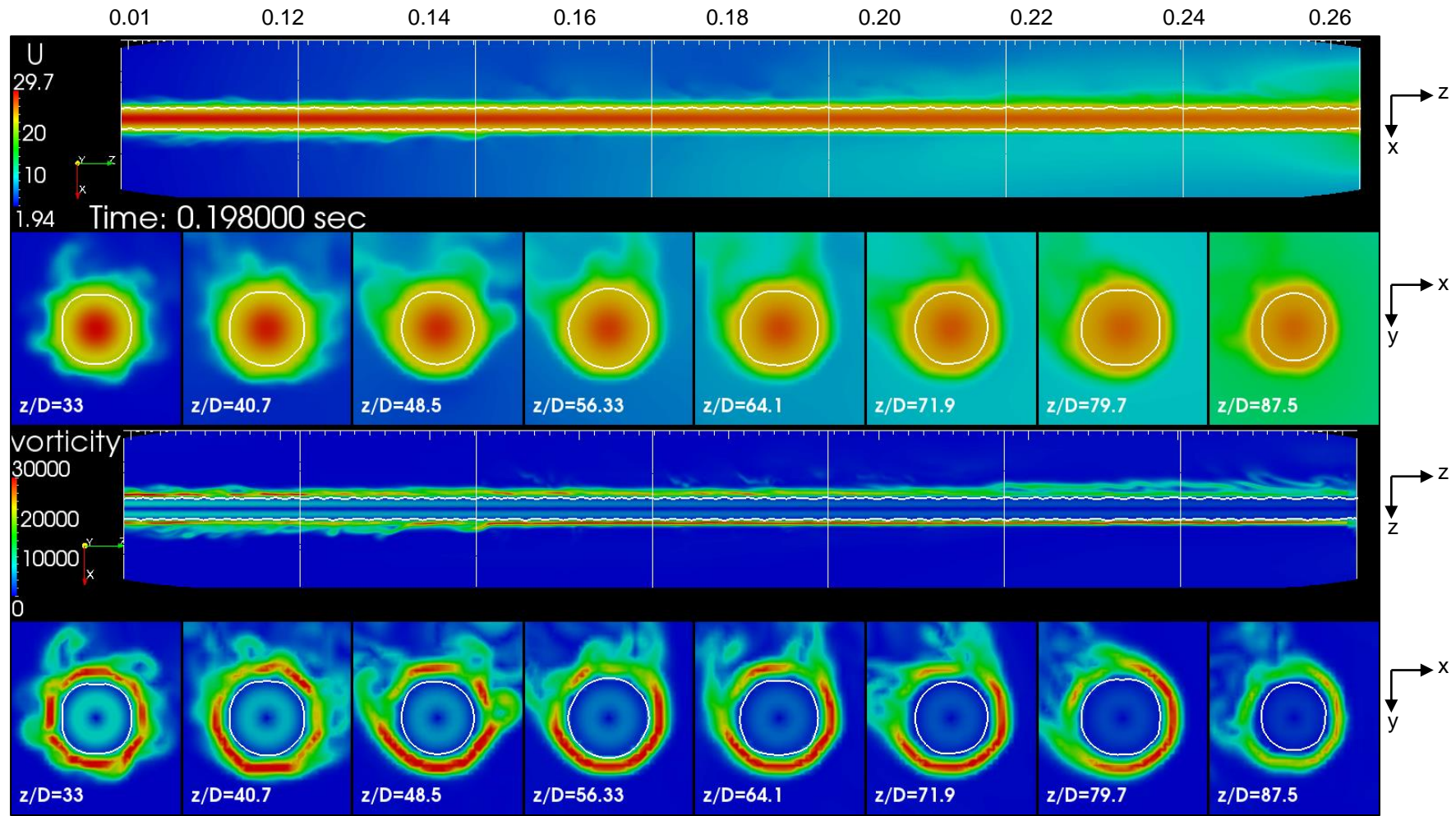


Figure 5.33 Longitudinal and lateral velocity (1st and 2nd rows) and vorticity (3rd and 4th rows) field's distribution of semi-turbulent liquid jet case

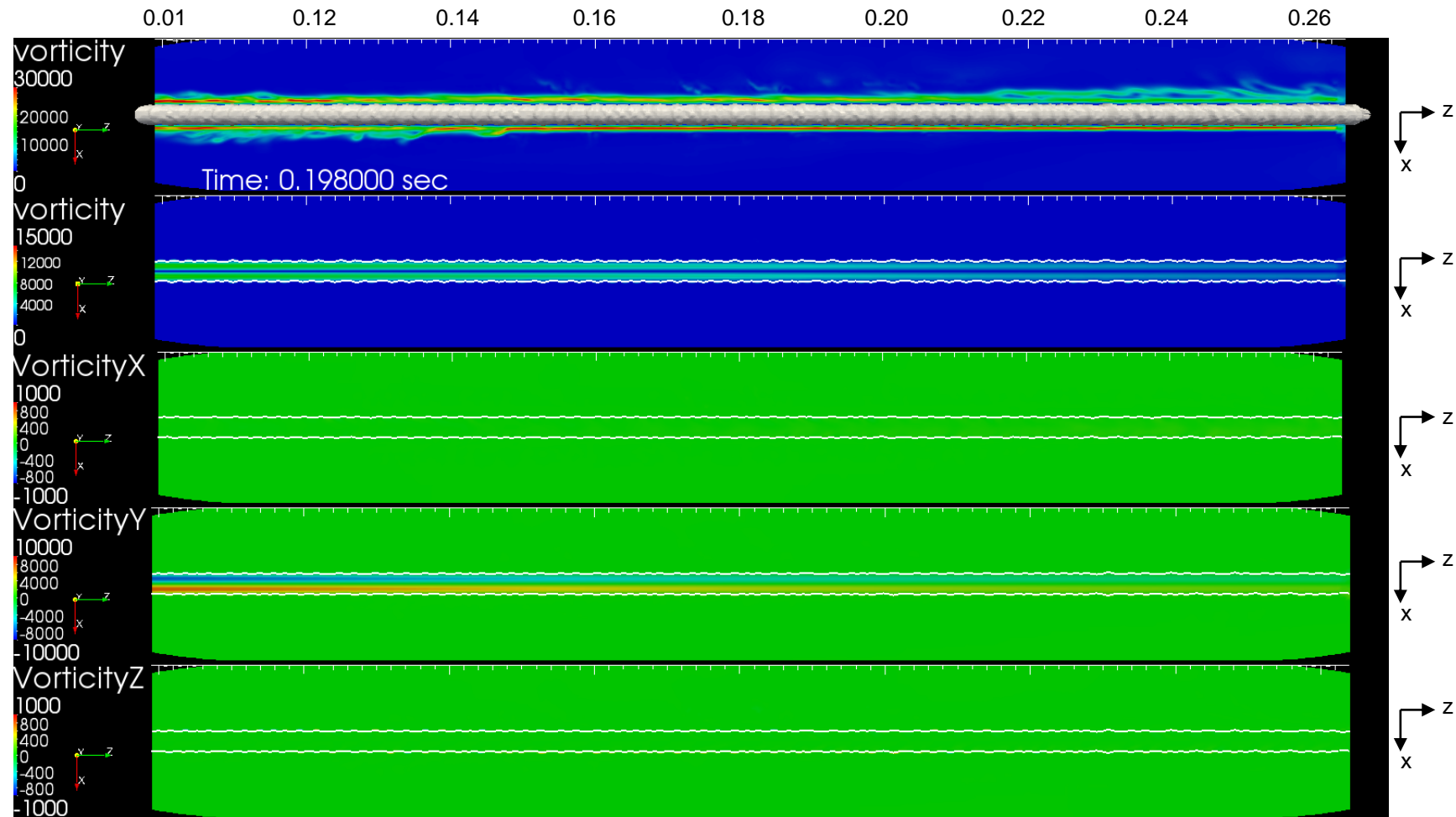


Figure 5.34 Distribution of instantaneous vorticity fields in an axis plain of the semi-turbulent liquid case. 1st row in the gas phase, 2nd row in the liquid phase, 3rd row vorticity-x distribution in the liquid phase, 4th row vorticity-y distribution in the liquid phase and 5th row vorticity-z component distribution in the liquid phase

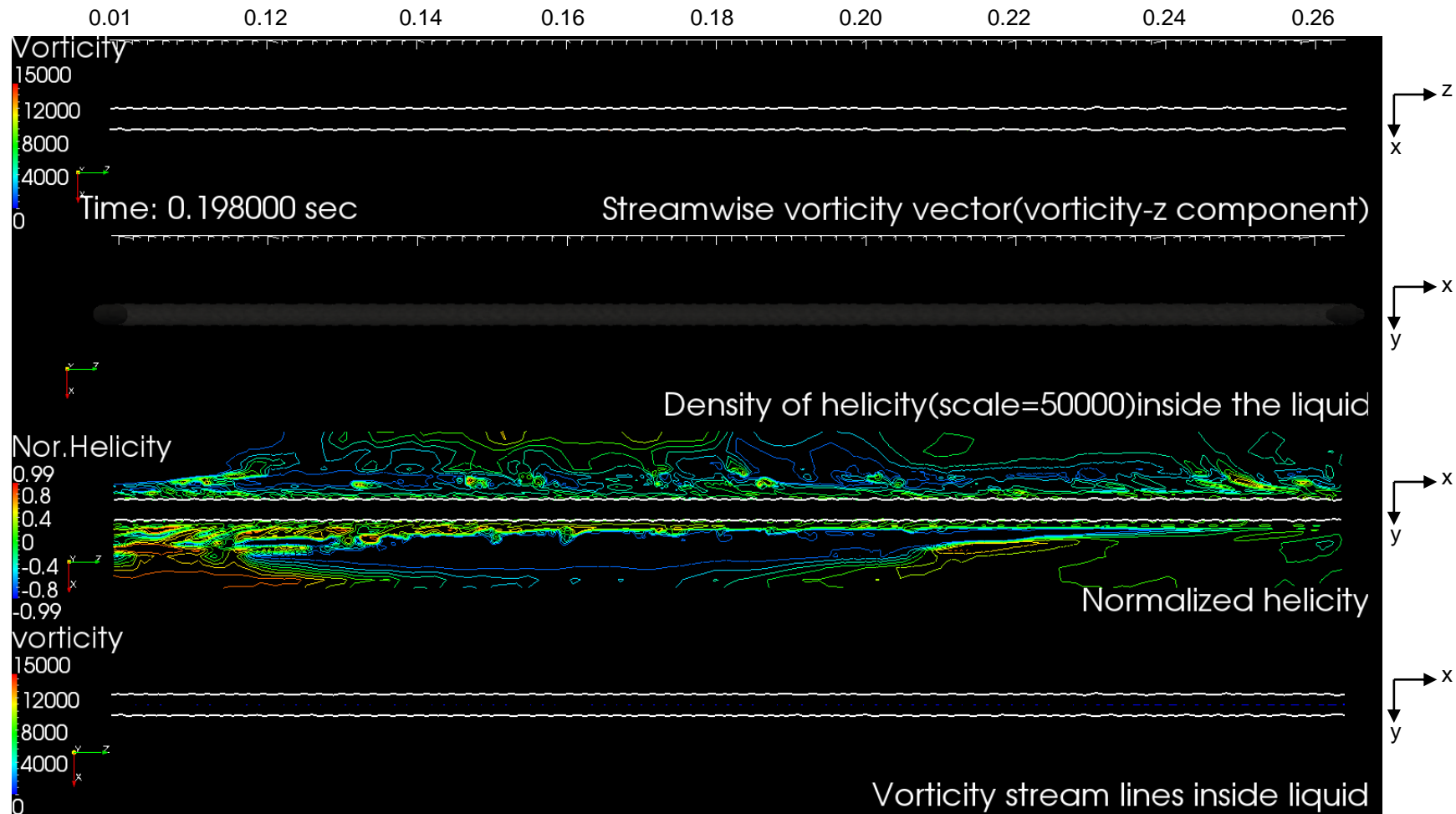


Figure 5.35 Different vortex structures for top semi-turbulent liquid jet case at time 198 ms. 1st row: axial vorticity vector (ω_z) in the liquid side, 2nd row: Helicity vortex structure in the liquid side, 3rd row: normalized of helicity structure sliced longitudinally across the customized domain, 4th row: vorticity stream lines in the liquid side

5.3.3 Effect of the Gas Ambient Conditions on the Liquid Jet Burst

As illustrated in Section 5.3.1, liquid jet burst phenomena occur naturally at an atmospheric condition. With the corresponding application, if this phenomenon exists without enough or considerable safety standards, it could lead to disasters if liquid fuel release accidentally occurred in industry. Hence, it is essential to also investigate the physical parameter effect of the surrounding gas on the jet burst phenomena. Attention will be focussed on the gas parameters that could magnify or damp down burst phenomena, and may produce another type of liquid jet breakup. From the relative literature, the data concerning the effect of the viscosity of the surrounding gas on the liquid jet are rare. In the laminar burst jet case, atmospheric viscosity has an influence on the velocity relaxation of the laminar (parabolic) profile as contributed to the drag force at the interface line and or to the aerodynamic turbulence effect, hence, such an investigation could be impactful on the liquid jet burst phenomena.

This investigation is important to derive broader conclusion concerning the physical characterisation of the burst jet. For example, as illustrated in Section 5.3.2, it cannot be concluded with high certainty whether the influence of the injection (inflow velocity profile) conditions on the jet burst is caused only due to the changes in the nozzle exit flow. It is arguably other parameters such as aerodynamic turbulence or the liquid and gas physical parameter that could impact towards to burst the jet.

5.3.3.1 Laminar Jet Burst Released at Higher Ambient Gas Viscosity

Viscosity in gases arises principally from the molecular diffusion that transports momentum between layers of flow. From an application point of view, different gaseous viscosity values change or range between half to double relative to the air viscosity value. Viscosity as a gas property does not depend on the gas pressure while it is dependent on the gas temperature. Gaseous viscosity increases as temperature increases, and decreases as the temperature decreases. As the gas temperature increases, the gas molecules move faster and more momentum is transferred between the gas layers, thereby increasing the viscosity (internal friction) of the gas. This differs in liquids because liquids have different frictional mechanisms at the molecular level.

Viscosity is related to shear stress and the rate of shear in a fluid, which illustrates its dependence on the mean free path of the diffusing particles. Increasing the gas viscosity would increase the shear stress (increasing drag and friction with the liquid surface across the interface) and probably modify the burst phenomena. On the other hand, increasing the gas viscosity would reduce the turbulence in the gas phase and

may decrease the aerodynamic gas effect on the liquid jet (if it is influential on such phenomena).

In order to investigate the effect of ejecting burst jet phenomena into a higher ambient gas viscosity, the viscosity has been increased 10 times that of atmospheric air viscosity utilized in the default laminar burst jet case. Table 5.4 below shows the gas physical properties used in the default burst case where liquid to gas viscosity ratio is $\mu_l/\mu_g = 2089.88$ (1st row), gas properties used for higher gas viscosity and low liquid to gas viscosity ratio as in the Table 5.4 (2nd row) and gas properties used for lower gas viscosity and high liquid to gas viscosity ratio (Section 5.3.3.2) as in the Table 5.4 (3rd row).

Table 5.4 physical properties and non-dimensional parameters used for high and low liquid to gas viscosity ratio

cases	<i>Physical properties and non-dimensional parameters</i>					
	Liquid viscosity μ_L (kg/m.s)	Gas viscosity μ_g (kg/m.s)	Liquid to gas viscosity ratio μ_L/μ_g	Gas Reynolds number Re_g	Gas Weber number We_g	Gas Ohnesorge number Oh_g
Laminar burst jet (Section 5.3.1)	0.0372	0.0000178	2089.88	4669.8	28.9	0.0012
Laminar jet at Higher gas viscosity (Section 5.3.3.1)	0.0372	0.000178	208.98	466.98	28.9	0.0115
Laminar jet at lower gas viscosity (Section 5.3.3.2)	0.0372	0.00000178	20898.8	46698	28.9	0.000115

Figure 5.36 shows the results of a laminar inflow velocity profile jet at Reynolds number $Re=2200$ released to a high viscous ambient condition at an advanced period of ejection time. In Figure. 5.36, the jet starts with a smooth surface upstream, but downstream at 0.04 m ($z/D= 13.33$) some wrinkles establish and grow up to produce the jet burst downstream at 0.23 m ($z/D= 76.5$). The jet instability (represented by the ruffled surface) is modified and deformed, certainly due to the laminar velocity relaxation as the aerodynamic movement has been reduced tremendously for higher viscous gas. It is noticed that the jet burst, in this case, occurred at 182 ms which is considerably faster than the default burst jet by 16 ms. A series of snapshots covering the jet process at shorter fractions of time to those showed in Figure 5.36 is presented in Appendix A.7.1.

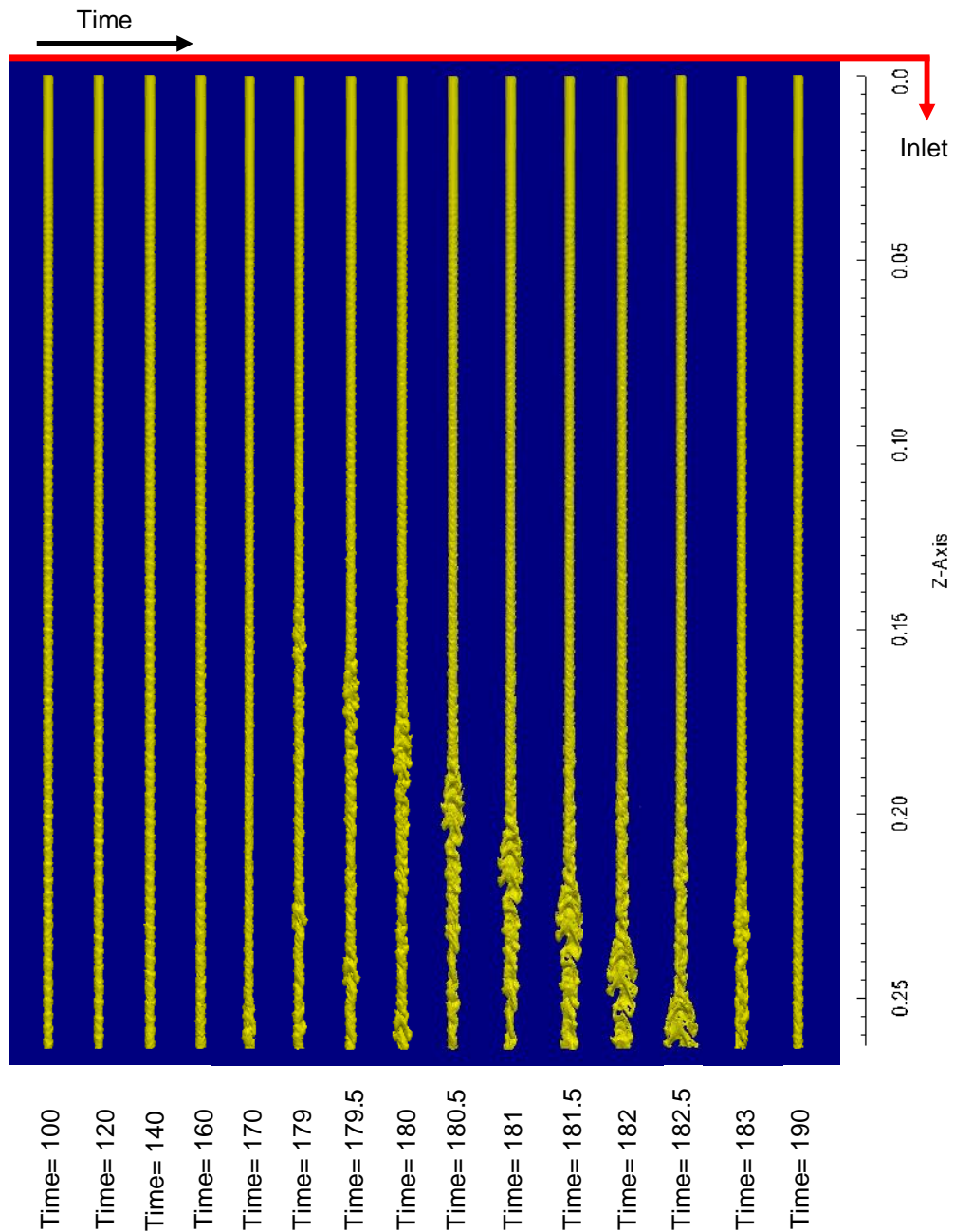


Figure 5.36 Liquid jet column ejected with laminar (parabolic velocity profile) inflow condition to a high viscous ambient (10 times higher than air viscosity). The number next to each image indicates the dimensional physical time elapsed in milliseconds

Exactly the same post-processing treatment has been taken into account in this case, similar to that used in the parabolic burst case. Physical observations and the discussion mentioned in the laminar burst jet in section 5.3.1 are applied to the current case. Hence, no further data comments or discussion are needed or mentioned unless it is necessary.

Figure 5.37 shows a close-up view to the liquid contour (1st row), domain velocity profile (2nd row), domain velocity field (3rd row), liquid stream lines (4th row) and gas stream lines (5th row) at time 181.5 ms. A series of snapshots covering the jet process at shorter fractions of time to those showed in Figure 5.37 is presented in Appendix A.7.2. Axial and radial velocity components at the centre of the liquid core are examined along with the jet as presented in Figure 5.38 at time 181.5 ms. Liquid burst contour ejected to a high viscous ambient gas condition viewed in the 1st row of Figure 5.38. Axial velocity in the z-axis (U_z) and radial velocity components in the x-axis (U_x) and y-axis (U_y) direction showed in the 2nd, 3rd and 4th rows respectively. A series of snapshots covering the jet process at shorter fractions of time to those showed in Figure 5.38 is presented in Appendix A.7.3.

The 2nd, 3rd and 4th rows respectively of Figure 5.39 show the instantaneous lateral cross-sectional (x-y plane) velocity vector at twelve lateral locations distributed equally along the customized domain at time 181.5 ms. Whereas the 1st row of Figure 5.39 shows the radial velocity (U_x and U_y) intensity at an instantaneous longitudinal cross-sectional (x-z plane). A series of snapshots covering the jet process at shorter fractions of time to those showed in Figure 5.39 is presented in Appendix A.7.4. The 1st row of Figure 5.40 shows a longitudinal slice (x-z plane) of velocity field distribution, whereas the 2nd row shows eight slices laterally (x-y plane) for the velocity field distribution at a time 181.5 ms. The 3rd row of Figure 5.40 shows a longitudinal slice (x-z plane) of the vortices' field distribution, whereas the 4th row shows the lateral eight slices (x-y plane) for the vortices field distribution. A series of snapshots covering the jet process at shorter fractions of time to those showed in Figure 5.40 is presented in Appendix A.7.5.

Figure 5.41 shows the instantaneous vorticity field within the gas side (1st row), within the liquid side (2nd row), liquid vortices fields ω_x in x-z plane (3rd row), ω_y in x-z plane (4th row) and ω_z in x-z plane (5th row), at a time 181.5 ms. A series of snapshots covering the jet process at shorter fractions of time to those showed in Figure 5.41 is presented in Appendix A.7.6. The vorticity flow field vector component in the z-axis (axial liquid jet direction) is presented in the 1st row of Figure 5.42, while the 2nd row showed the contour of the helicity structure within the liquid. The normalized helicity is presented in the 3rd row, and the vorticity streamlines within the liquid presented in the 4th row. A series of snapshots covering the jet process at shorter fractions of time to those showed in Figure 5.42 is presented in Appendix A.7.7.

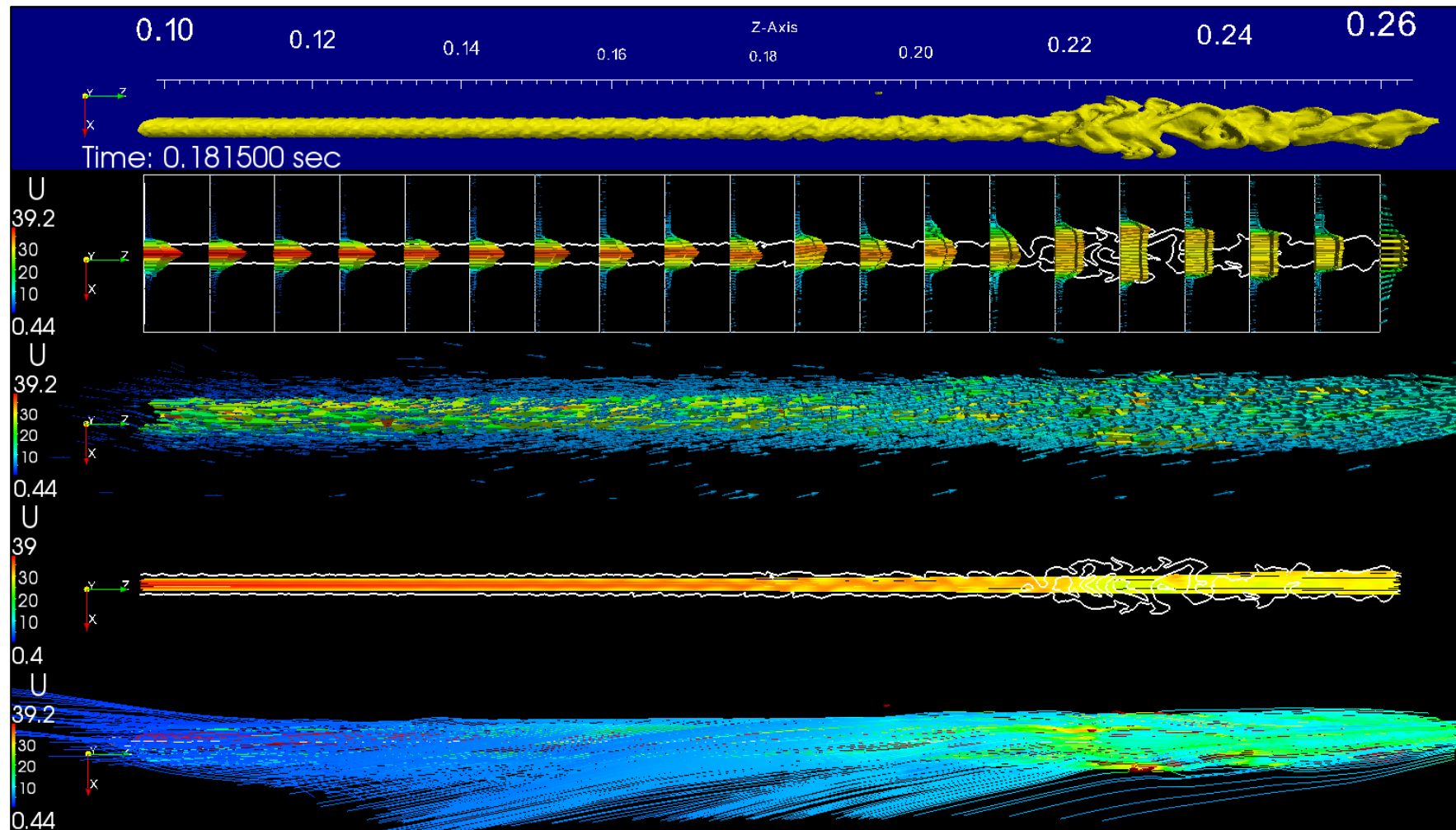


Figure 5.37 Laminar burst jet at high ambient gas viscosity; results show the liquid column (1st row), domain velocity profile (2nd row), domain velocity field (3rd row), liquid velocity stream lines (4th row) and gas velocity stream lines (5th row)

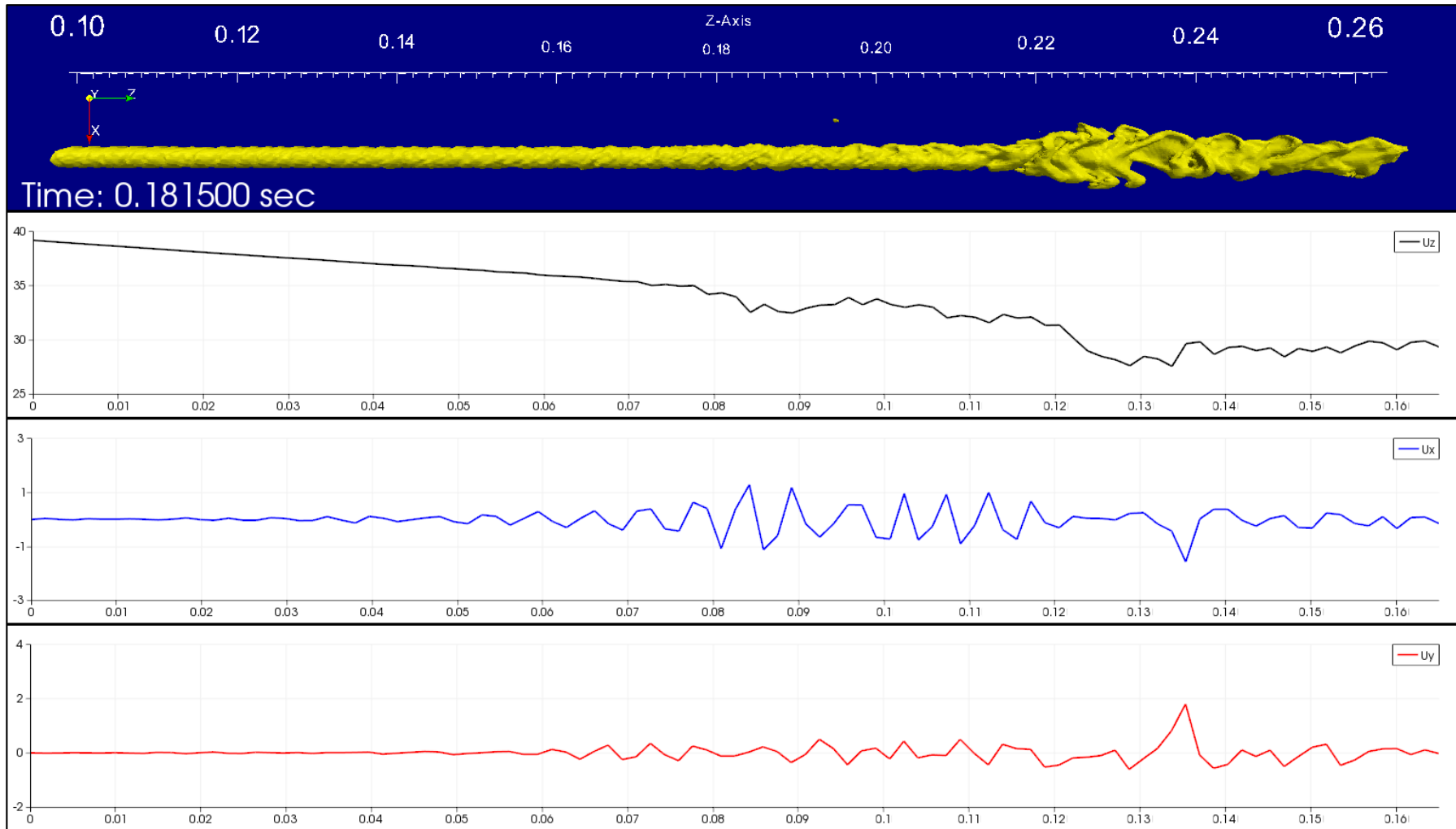


Figure 5.38 Liquid jet core velocity components (U_x U_y and U_z) at time 181.5 ms of a laminar burst jet at high ambient gas viscosity

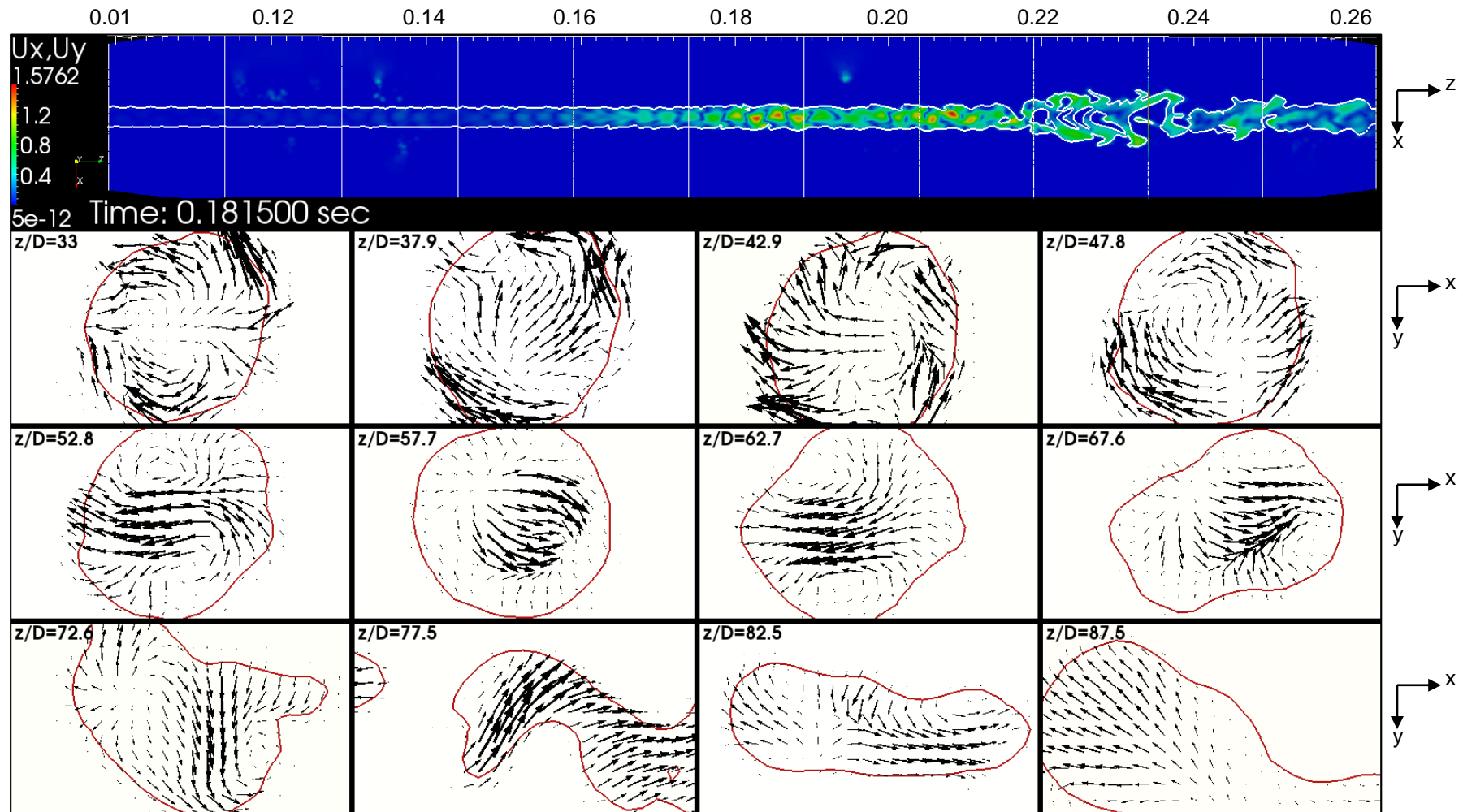


Figure 5.39 Distribution of instantaneous liquid velocity vectors projected onto longitudinal and cross-sectional planes at different axis locations for a laminar burst jet at high ambient gas viscosity

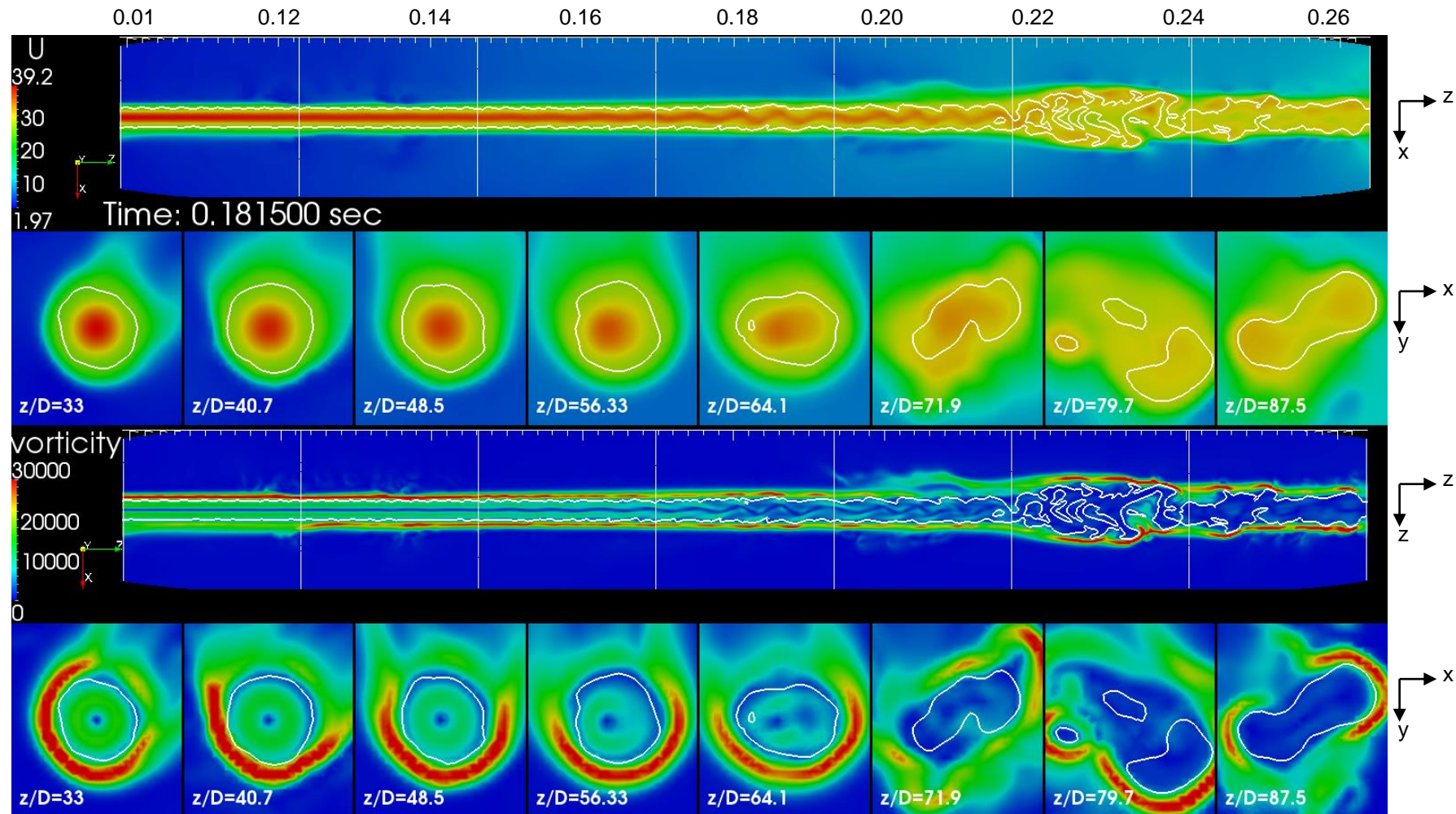


Figure 5.40 Longitudinal and lateral velocity (1st and 2nd rows) and vorticity (3rd and 4th rows) field's distribution for a laminar burst jet at high ambient gas viscosity

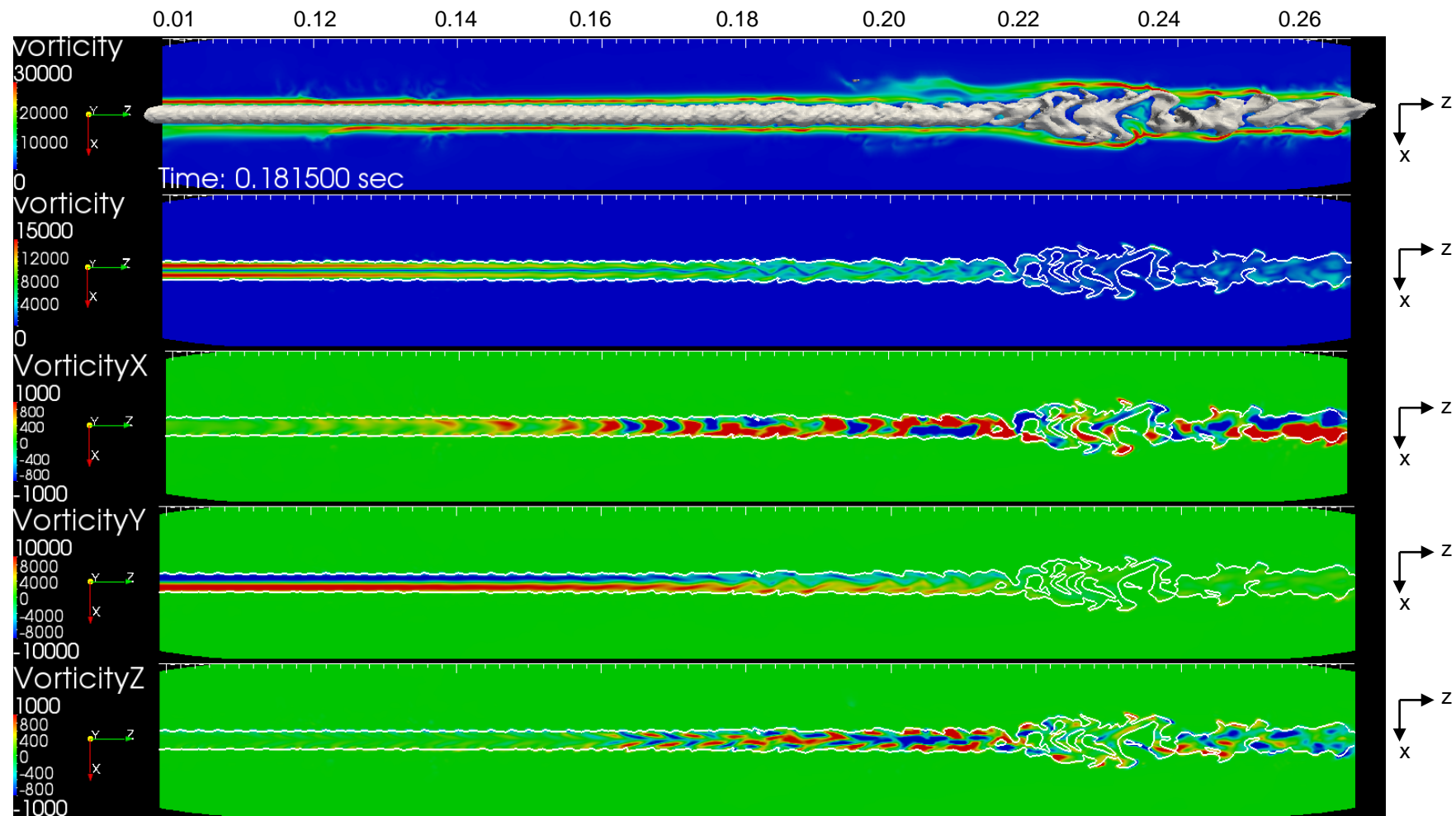


Figure 5.41 Distribution of instantaneous vorticity fields in an axis plane for a laminar burst jet at high ambient gas viscosity at time 181.5 ms. 1st row in the gas phase, 2nd row in the liquid phase, 3rd row vorticity-x distribution in the liquid phase, 4th row vorticity-y distribution in the liquid phase and 5th row vorticity-z component distribution in the liquid phase

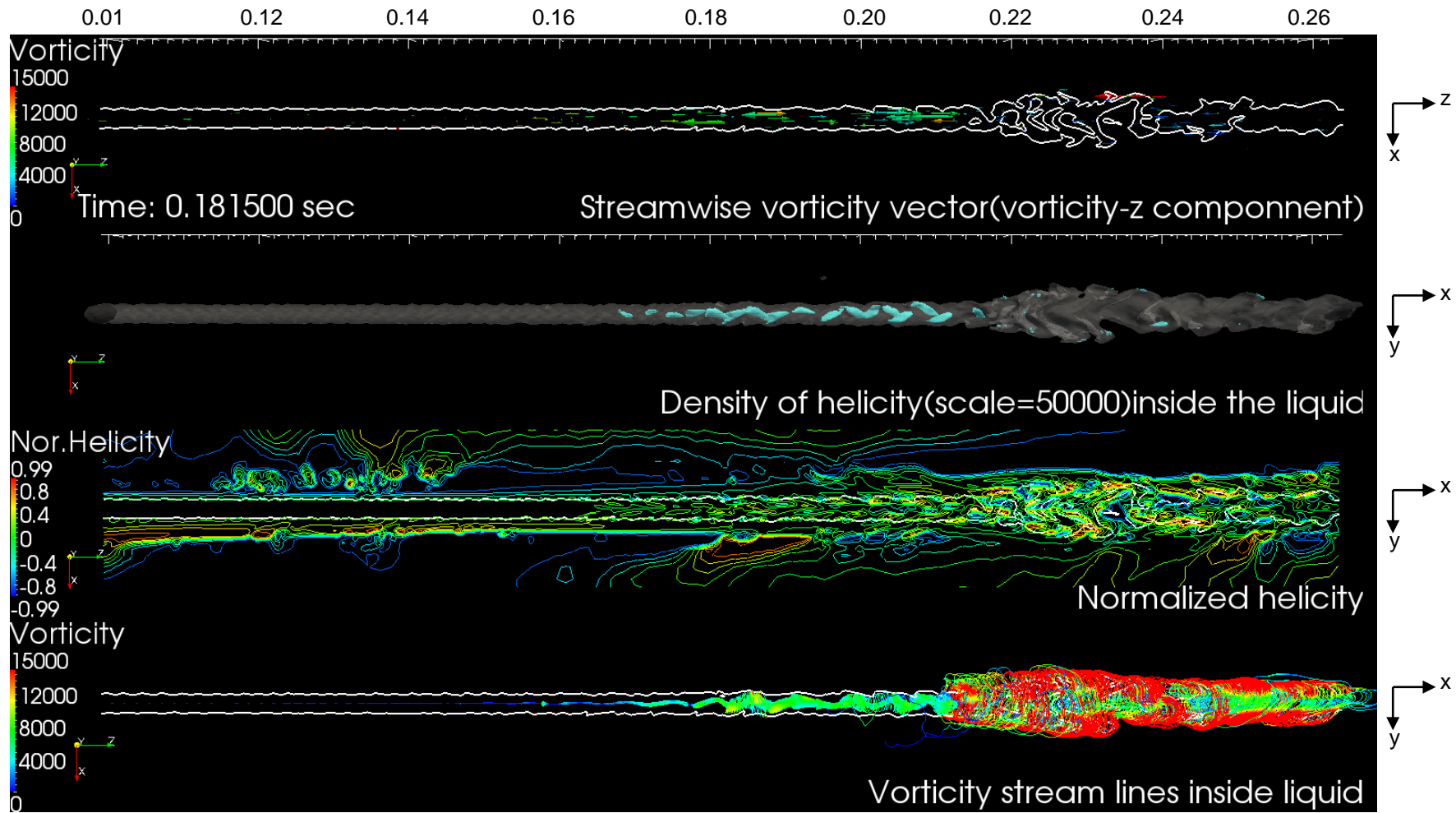


Figure 5.42 Different vortex structures for a laminar burst jet at higher ambient gas viscosity at time 181.5 ms. 1st row: axial vorticity vector (ω_z) in the liquid side, 2nd row: Helicity vortex structure in the liquid side, 3rd row: normalized of helicity structure sliced longitudinally across the customized domain, 4th row: vorticity stream lines in the liquid side

5.3.3.2 Laminar Jet Burst Released at Lower Ambient Gas Viscosity

In contrast to the test case conducted in Section 5.3.3.1, any decrease in the gas viscosity would decrease the shear stress (drag and friction) and may weaken or completely suppress the burst phenomena as a result of reducing the gas friction at the liquid surface across the interface. On the other hand, gas viscosity reduction would improve the turbulence in the gas phase and may increase the aerodynamic gas effect on the liquid jet (if it influential on such phenomena). Hence, an investigation was conducted whereby the gas viscosity has been reduced to 10 times lower than the atmospheric air viscosity utilized by default in laminar burst jet case. Table 5.4 (3rd row) in Section 5.3.3.1 shows the gas physical properties used throughout this case for lower gas viscosity and high liquid to gas viscosity ratio.

Figure 5.43 shows the results of a laminar inflow velocity profile jet at Reynolds number $Re=2200$ released to a low viscous ambient condition at an advanced period of ejection time. In Figure. 5.43, the jet starts with a smooth surface upstream, but downstream at 0.04 m ($z/D= 13.33$), some wrinkles establish and grow up to produce the jet burst downstream roughly at the same location as observed in the default burst case and high ambient gas viscosity case. As illustrated previously in Section 5.3.3.1, although the aerodynamic effect reduced as the jet injected into higher ambient viscous gas, the liquid jet burst phenomena was noticed, but was faster in time when compared with the default burst case. This could be ascribed to the increase in the interfacial shear (friction) at the liquid-gas interface. The opposite process occurred for injection laminar burst jet into lower viscous ambient condition, whereas burst phenomena was noticed but was slower in time when compared with the default burst case. This corresponds to the decrease in the interfacial shear (friction) at the liquid-gas interface despite increasing the aerodynamic gas or the gas turbulence effect.

Although gas turbulence and aerodynamic movement has been increased tremendously for lower viscous gas, the jet showed conventional instability represented in the ruffled surface and the column structure deformed certainly due to the relaxation as shown from Figure 5.43. Lower shear stress (less friction) at the interface for the lower gas viscosity reflected on the burst jet appearance interpreted as a burst jet delay appearance by 59 ms (jet burst occurred at 257 ms) comparing with the default burst jet injected to air (jet burst occurred at 198 ms). A series of snapshots covering the jet process at shorter fractions of time to those showed in Figure 5.43 is presented in Appendix A.8.1.

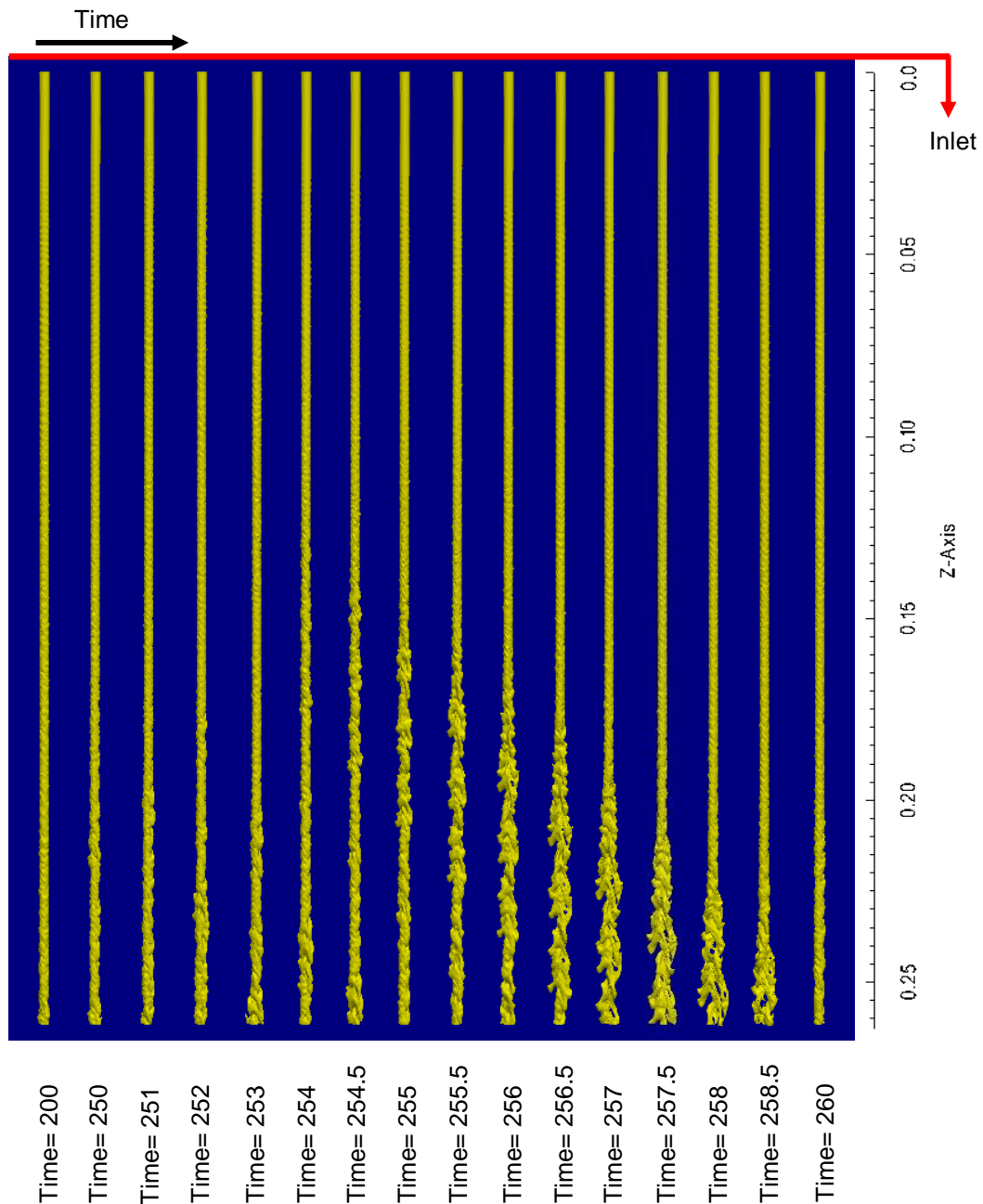


Figure 5.43 Liquid jet column ejected with laminar (parabolic velocity profile) inflow condition to a low viscous ambient (10 times less than air viscosity). The number next to each image indicates the dimensional physical time elapsed in milliseconds.

The post-processing treatment has been taken into account in this case, same to the one used in the parabolic burst case. Physical observations and the discussion mentioned in the laminar burst jet in section 5.3.1 are applied to the current case. Hence, no further data comments or discussion are needed or mentioned unless it is necessary.

Figure 5.44 shows a close-up view to the liquid contour (1st row), domain velocity profile (2nd row), domain velocity field (3rd row), liquid stream lines (4th row) and liquid stream lines (5th row) at time 257 ms. A series of snapshots covering the jet process at shorter fractions of time to those showed in Figure 5.44 is presented in Appendix A.8.2. Axial and radial velocity components at the centre of the liquid core are examined along side the jet as presented in Figure 5.45 at time 257 ms. Liquid burst jet ejected to a lower viscous ambient gas condition viewed in the 1st row of Figure 5.45. Axial velocity in the z-axis (U_z) and radial velocity components in the x-axis (U_x) and y-axis (U_y) direction showed in the 2nd, 3rd and 4th rows respectively. A series of snapshots covering the jet process at shorter fractions of time to those showed in Figure 5.45 is presented in Appendix A.8.3.

The 2nd, 3rd and 4th rows respectively of Figure 5.46 show the instantaneous lateral cross-sectional (x-y plane) velocity vector at twelve lateral locations distributed equally along the customized domain at time 257 ms. Whereas, the 1st row of Figure 5.46 shows the radial velocity (U_x and U_y) intensity at an instantaneous longitudinal cross-sectional (x-z plane). A series of snapshots covering the jet process at shorter fractions of time to those showed in Figure 5.46 is presented in Appendix A.8.4. 1st row of Figure 5.47 shows a longitudinal slice (x-z plane) of velocity field distribution whereas the 2nd row shows eight slices laterally (x-y plane) for the velocity field distribution at a time 257 ms. The 3rd row of Figure 5.47 shows a longitudinal slice (x-z plane) of vortices field distribution whereas the 4th row shows lateral eight slices (x-y plane) for the vortices field distribution. A series of snapshots covering the jet process at shorter fractions of time to those showed in Figure 5.47 is presented in Appendix A.8.5.

Figure 5.48 shows the instantaneous vorticity field within the gas side (1st row), within the liquid side (2nd row), liquid vortices fields ω_x in x-z plane (3rd row), ω_y in x-z plane (4th row) and ω_z in x-z plane (5th row), at a time 257 ms. A series of snapshots covering the jet process at shorter fractions of time to those showed in Figure 5.48 is presented in Appendix A.8.6. The vorticity flow field vector component in the z-axis (axial liquid jet direction) is presented in the 1st row of Figure 5.49, while the 2nd row showed the contour of the helicity structure within the liquid. The normalized helicity is presented in the 3rd row, and the vorticity streamlines within the liquid presented in the 4th row. A series of snapshots covering the jet process at shorter fractions of time to those showed in Figure 5.49 is presented in Appendix A.8.7.

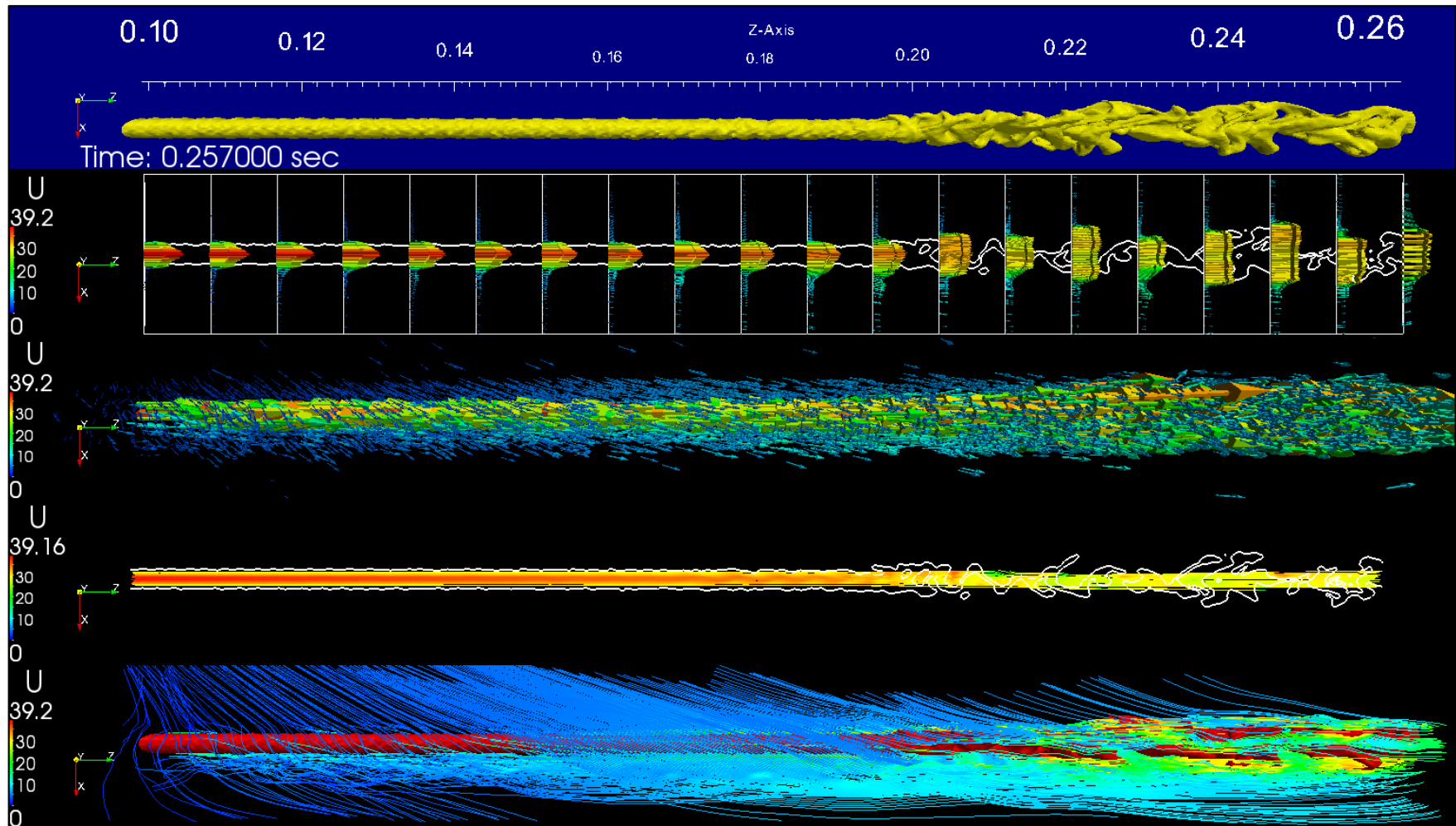


Figure 5.44 Laminar burst jet at low ambient gas viscosity case results show the liquid column (1st row), domain velocity profile (2nd row), domain velocity field (3rd row), liquid velocity stream lines (4th row) and gas velocity stream lines (5th row)

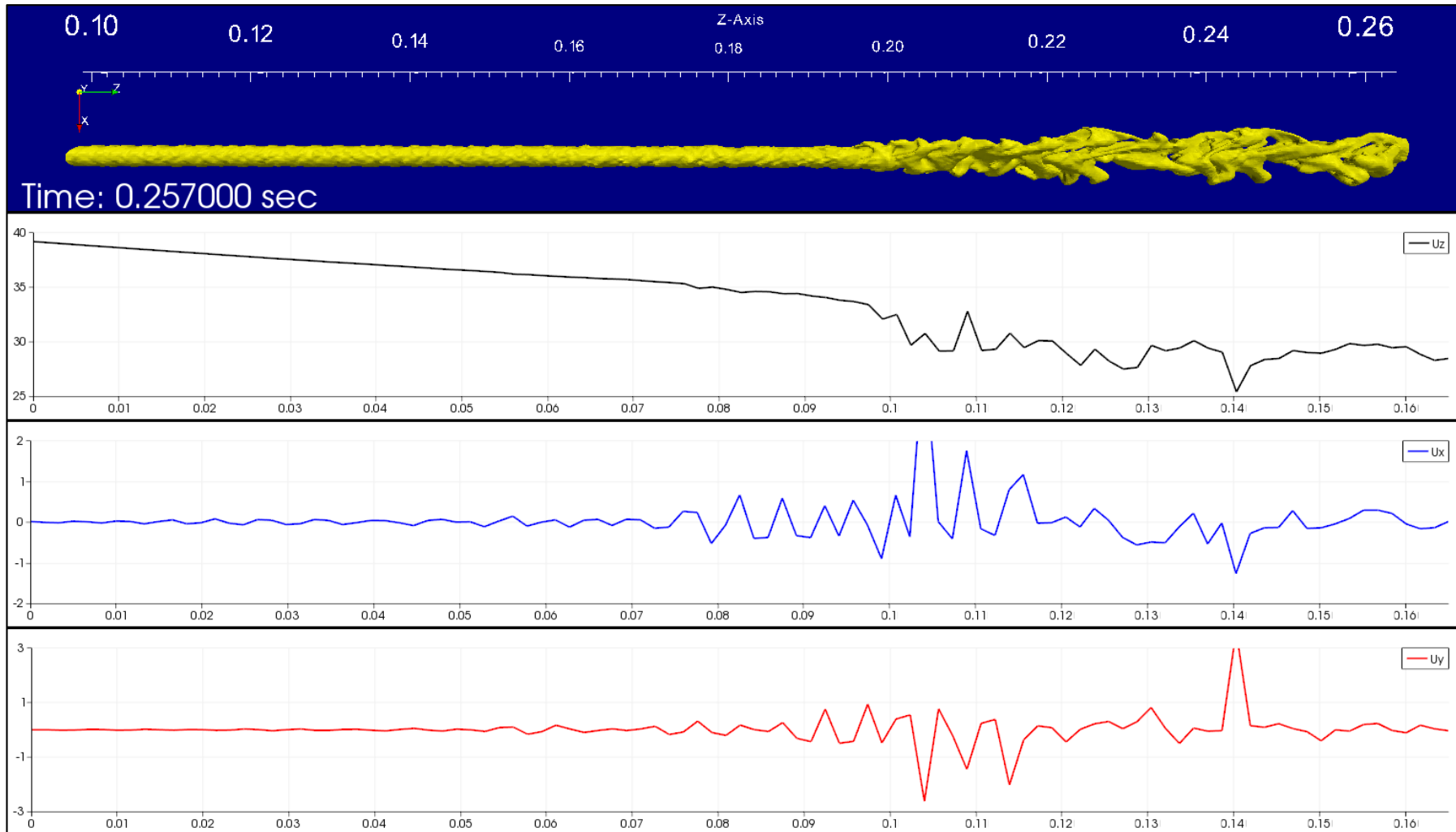


Figure 5.45 Liquid jet core velocity components (U_x U_y and U_z) at time 257 ms of a laminar burst jet at low ambient gas viscosity

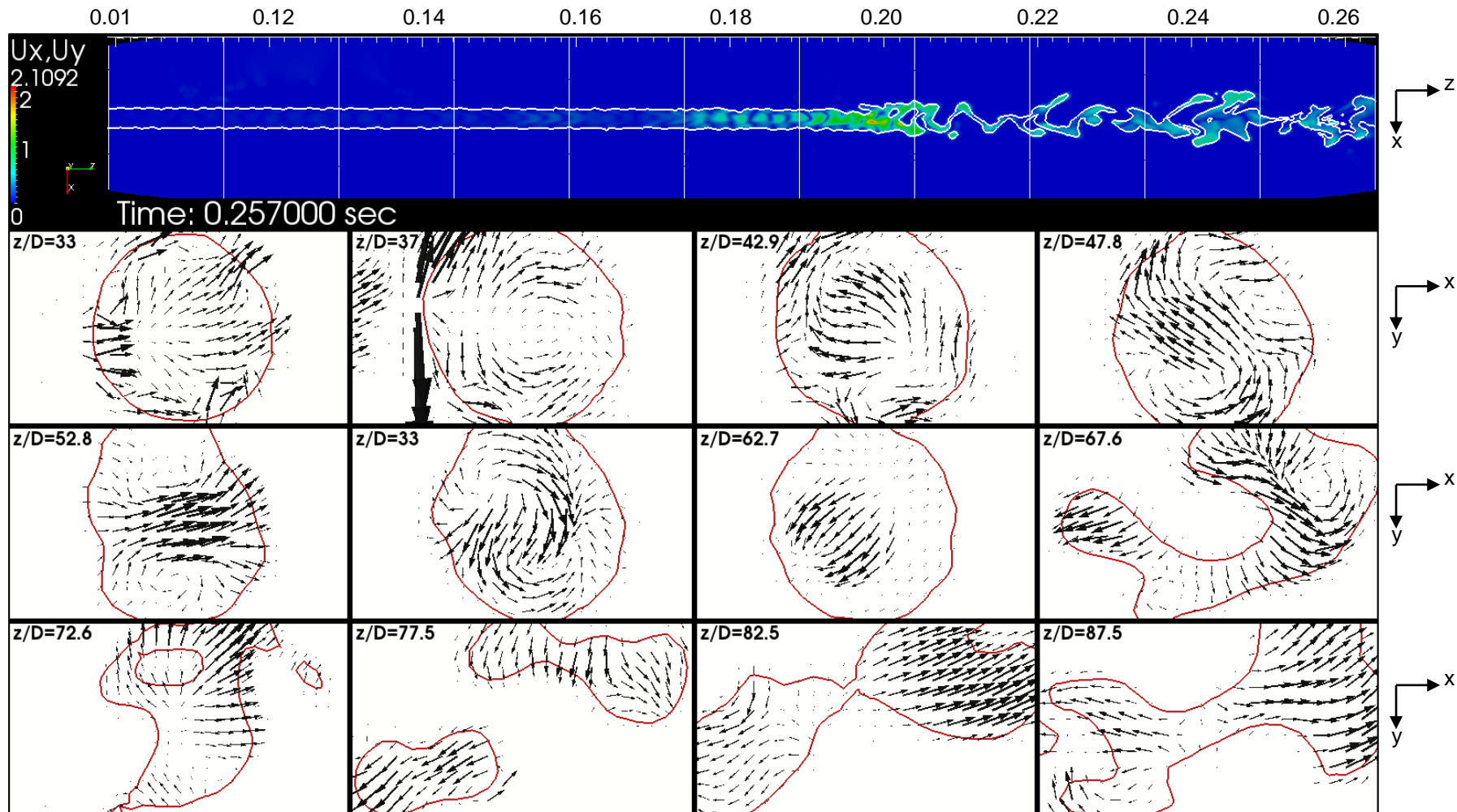


Figure 5.46 Distribution of instantaneous liquid velocity vectors projected onto longitudinal and cross-sectional planes at different axis locations for a laminar burst jet at low ambient gas viscosity

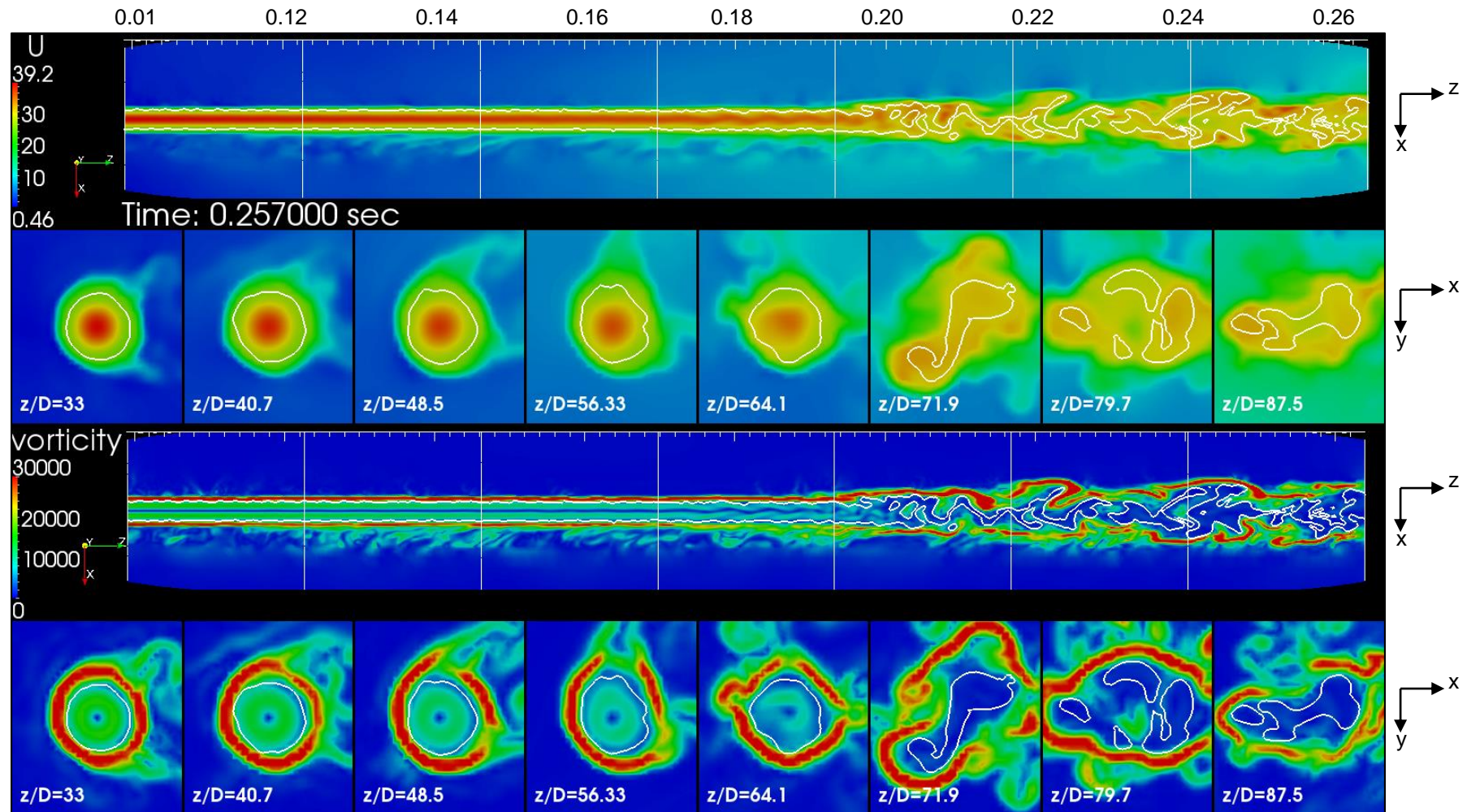


Figure 5.47 Longitudinal and lateral velocity (1st and 2nd rows) and vorticity (3rd and 4th rows) field's distribution for a laminar burst jet at low ambient gas viscosity

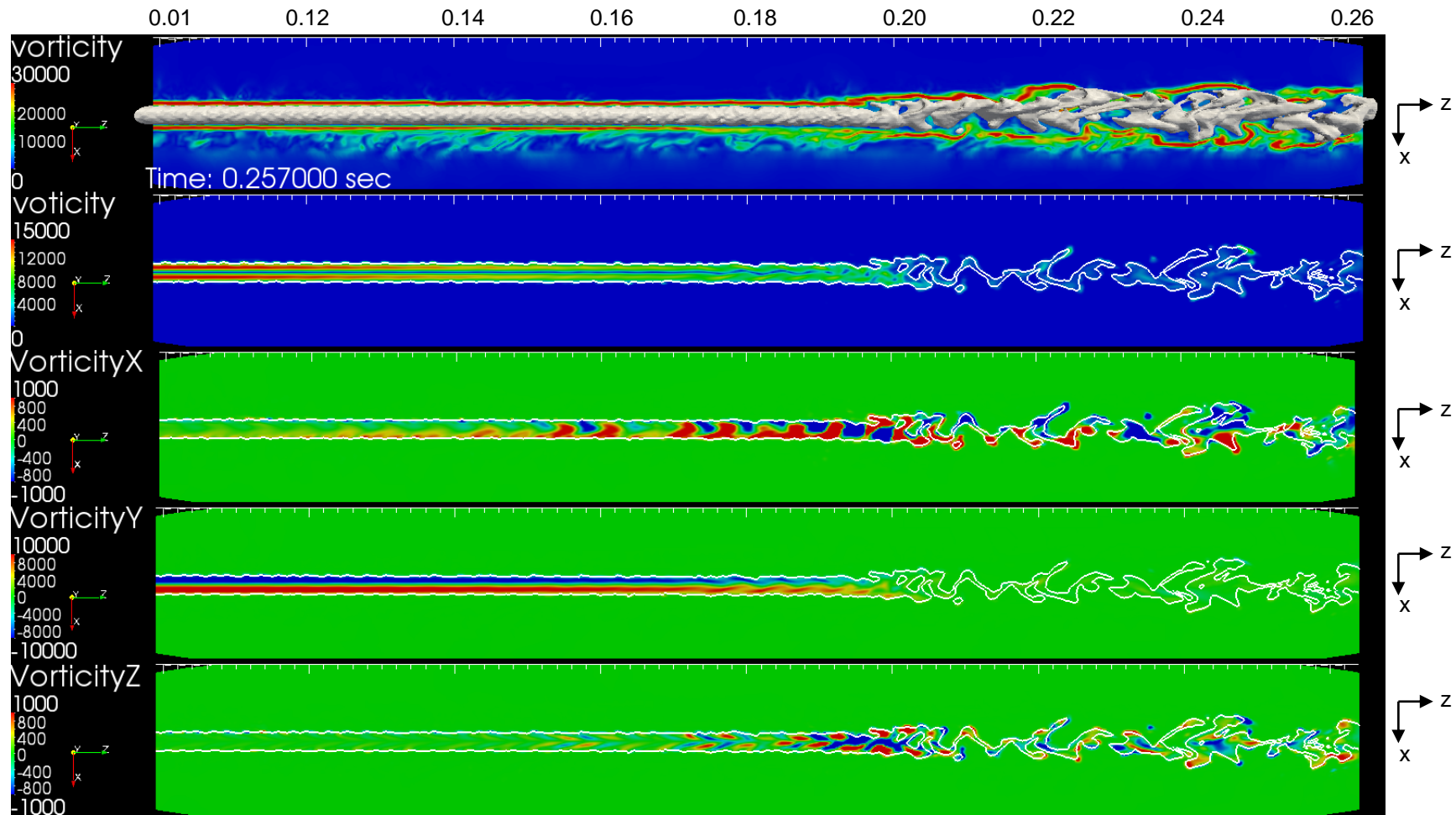


Figure 5.48 Distribution of instantaneous vorticity fields in an axis plain for a laminar burst jet at low ambient gas viscosity at time 257 ms. 1st row in the gas phase, 2nd row in the liquid phase, 3rd row vorticity-x distribution in the liquid phase, 4th row vorticity-y distribution in the liquid phase and 5th row vorticity-z component distribution in the liquid phase

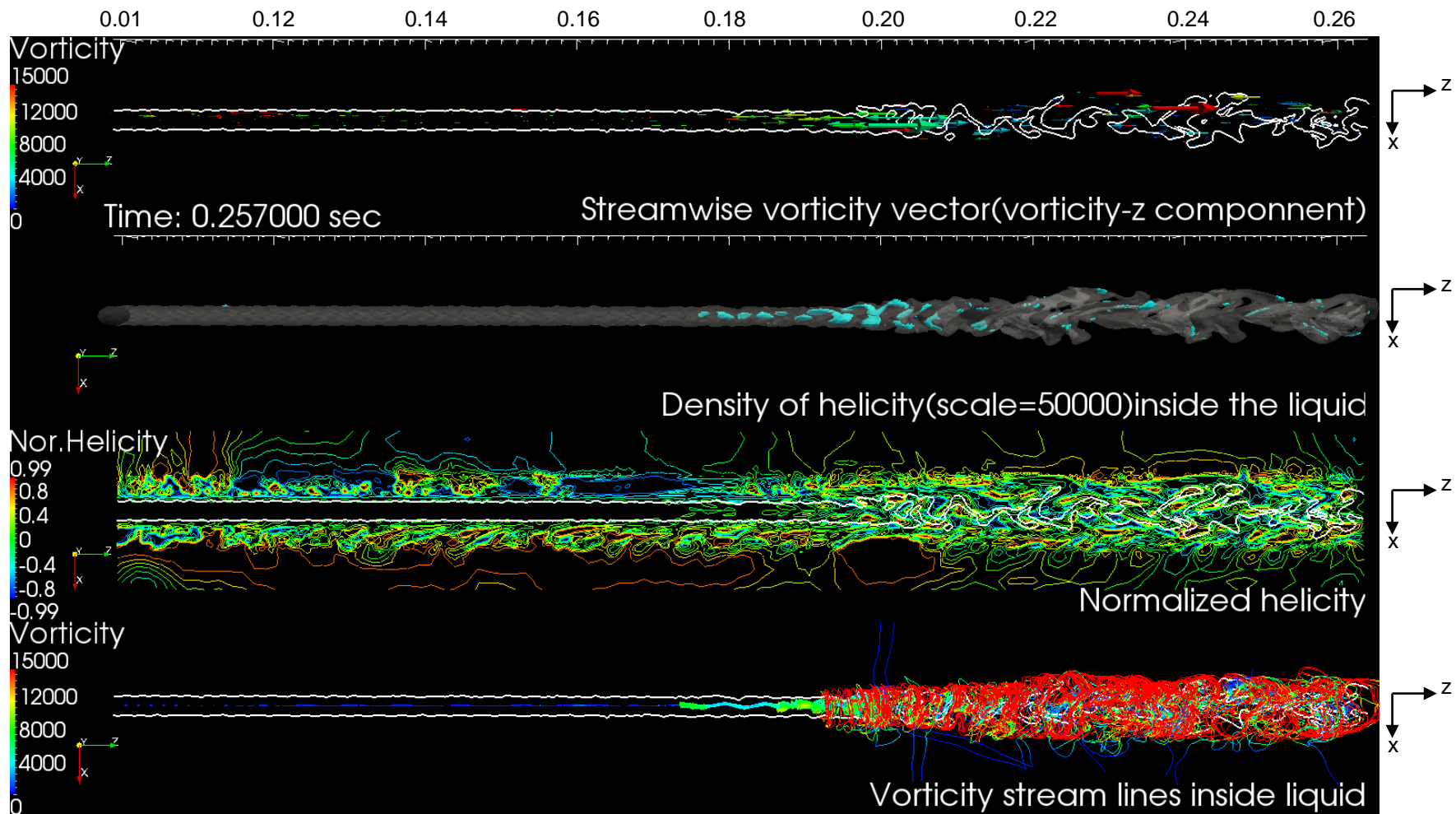


Figure 5.49 Different vortex structures for a laminar burst jet at higher ambient gas viscosity at time 257 ms. 1st row: axial vorticity vector (ω_z) in the liquid side, 2nd row: Helicity vortex structure in the liquid side, 3rd row: normalized of helicity structure sliced longitudinally across the customized domain, 4th row: vorticity stream lines in the liquid side

5.3.4 Effect of Low Viscous Liquid on Laminar Burst Jet

From the practical point of view, the liquid utilized (Glycerine in water 79% by weight) to produce the laminar jet burst phenomena is a considerably high viscous liquid if compared with other types of liquids used in many engineering applications. Pan and Suga [58] reported that the liquid jet burst phenomena occur in such a jet with high liquid viscosity accompanied by high Weber number and relatively high Ohnesorge number. Furthermore, Pan and Suga [58] reported that, due to the high liquid viscosity, the vortex structure generated inside the liquid core keeps its large scale. Hence, investigation of the effect of liquid viscosity, Weber number and accordingly Ohnesorge number is considered essential for the comprehensive understanding of laminar burst jet phenomena.

This investigation was conducted by utilizing the same settings and the benchmark used in the former cases except for the liquid viscosity as it is reduced by ten times to replicate the water viscosity. The Reynolds number was kept constant ($Re=2200$) as in the default case, with the nozzle diameter $D=0.003$ m and the liquid density constants as in the default case, but the injection speed decreased from $u_{mean}=22.6$ m/s to $u_{mean}=2.26$ m/s. Hence the reduction in the inertial force resultant in reducing the liquid's Weber number and Ohnesorge number. Table 5.5 below illustrates the physical properties and the non-dimensional parameters used in the lower viscous liquid study case. According to the non-dimensional parameters in Table 5.5, the release conditions for lower viscous liquid transferred from the second wind induced regime (as for the laminar burst jet case) to the first wind induced regime as shown in Figure 5.50.

Table 5.5 Properties and non-dimensional parameters used for low viscous liquid case

<i>Phase</i>	<i>Physical properties and non-dimensional parameters</i>					
	<i>Viscosity μ (kg/m.s)</i>	<i>Density ρ (kg/m³)</i>	<i>Surface tension σ (N/m)</i>	<i>Reynolds number Re</i>	<i>Weber number We</i>	<i>Ohnesorge number Oh</i>
Liquid	0.00372	1206	0.065	2200	284.29	0.00766
Gas	0.0000178	1.226		466.98	0.289	0.00115

Although Reynolds number is high ($Re=2200$), the release condition categorized in the first wind induced region as Weber number and Ohnesorge number is low. As the nozzle exit velocity reduced in this case, the surface tension forces would dominate the inertia forces, and it was anticipated that it would exhibit laminar jet breakup. Moreover,

laminar burst jet and its high instabilities are expected to disappear in this case according to Pan and Suga [58] as for lower liquid viscosity and Weber number. Modelling this case has been accomplished for a longer physical time in order to have more certainty about the jet behaviour until it is stopped at 254 ms.

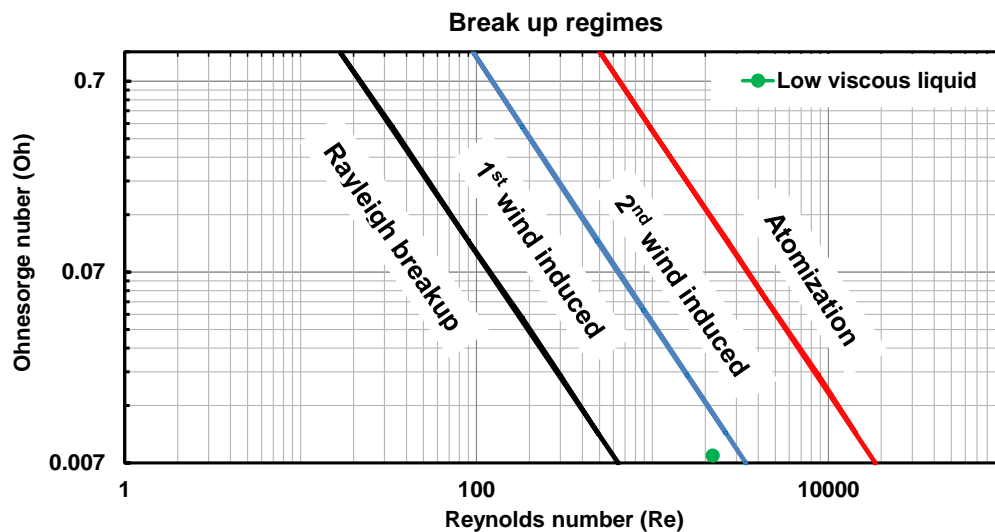


Figure 5.50 Low viscous liquid physical conditions located on Ohnesorge chart and the present investigation regime

Figure 5.51 shows the results of a laminar inflow velocity profile jet at Reynolds number $Re=2200$ released with low liquid viscosity condition at different period of ejection time. In Figure 5.51, the jet starts with a smooth surface upstream, then in the downstream region 0.04 m ($z/D=13.33$), wrinkles establish and grow up to break up the jet at a distance nearly at the edge or out of range of the investigation domain. Although the mesh resolution was still not high enough, the breakup length from the consequences is around $L_B/D=86-89$. This breakup value is very close (it could be more accurate with higher resolution) with the experimental breakup length value $L_B/D=84.3$ for liquid release cases of $We < 400$ proposed by Sallam [80]. Pan and Suga [58] studied numerically with adequate mesh several cases for laminar breakup, and found that breakup length values results oscillate around the experimental value of Sallam [80]. Therefore, it is considered here that the current results accurately enough correspond to the breakup length measurements for a laminar jet compared with Pan and Suga [58] results as clearly shown in Figures 5.4-5.6. A series of snapshots covering the jet process at shorter fractions of time to those showed in Figure 5.51 is presented in Appendix A.9.1.

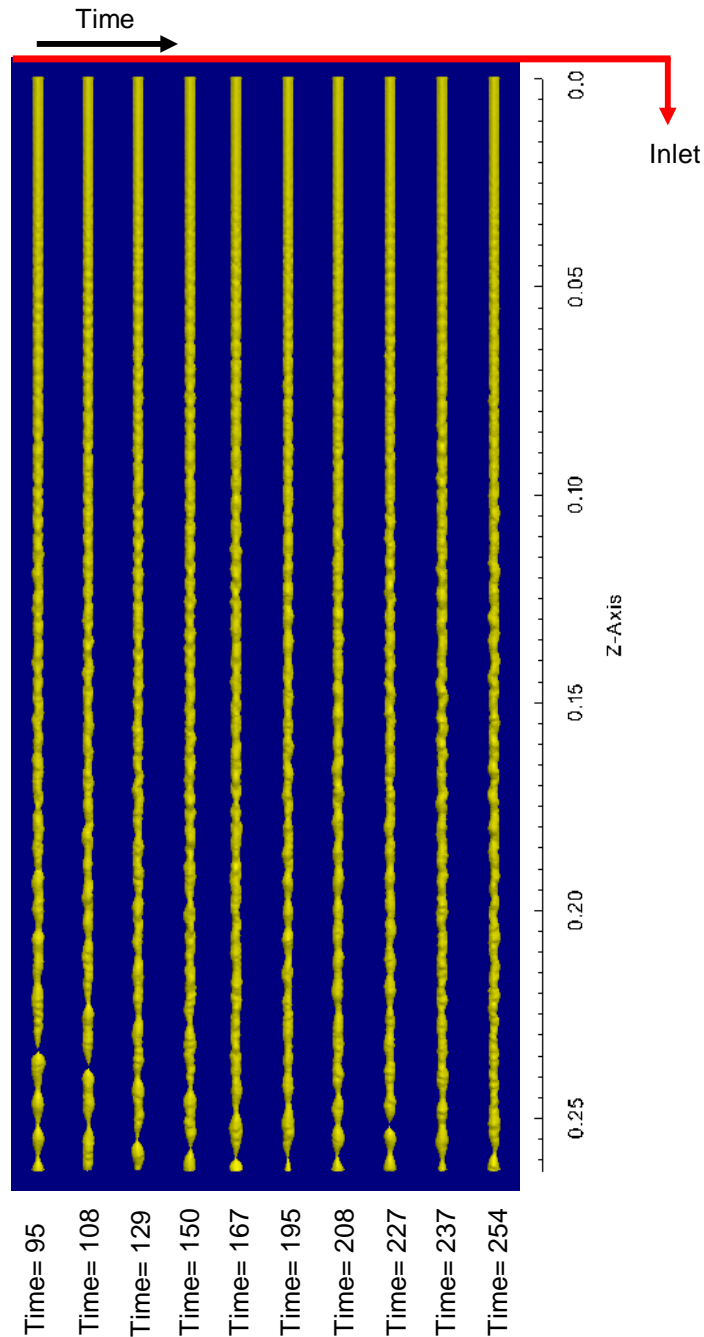


Figure 5.51 Low viscosity liquid jet column ejected with inflow condition of laminar (parabolic velocity profile). The number next to each image indicates the dimensional physical time elapsed in milliseconds

Exactly the same post-processing treatment has been taken into account in this case similar to that used in the parabolic burst case. This time, post-processing included the entire jet length instead focusing on the specific area as in the former cases. The first 100 ms of the jet development time is considered a transitional stage; beyond it, the jet breakup length tended to be stabilized (see Appendix A.9.1), hence, the results

discussion will be focused on the jet at the latest time step results especially on the last 227 ms. of the jet time results.

The 1st row of Figure 5.52 shows the jet column contour at time 227 ms. In the 2nd row, the liquid jet velocity profile relaxes from laminar profile upstream to almost flat profile downstream. As the liquid injection velocity is low, the aerodynamic forces have no effect on the jet breakup if compared with the high speed laminar burst jet. The 3rd row represents the air field velocity vector in the 3-D domain. Observations regarding the low aerodynamic effect are clarified more in the 3rd row. The 4th row shows the velocity streamlines within the liquid column in the z-x plane. Liquid stream lines have confirmed the observations of the velocity relaxation which occur inside the liquid. As shown from the liquid streamlines, liquid jet surface deformation increased when maximum velocity became non-concentric and was exhibiting sinusoidal or wavy movement. Wavy movement occurs at 0.1 m ($z/D=33.33$) and ends at 0.15 m ($z/D=50$) when the liquid velocity profile relaxed totally from parabolic to flat. No breakup occurs until inertia overcame surface tension force downstream and breakup the jet at 0.25 m ($z/D=83.33$). The 5th row shows the 3-D streamlines within the gas side surrounding the liquid contour column (in red). A series of snapshots covering the jet process at shorter fractions of time to those showed in Figure 5.52 is presented in Appendix A.9.2.

Axial and radial velocity components at the centre of the liquid core are examined along with the jet as shown in Figure 5.53 at time 227 ms. As shown in the 2nd row, axial velocity in the z-axis (U_z) exhibited a gradual decrease due to relaxation. The trend of axial velocity reduction changed at the distance between 0.1m ($z/D=33.33$) till the end, whereas wavy movement inside the liquid occurred and complete velocity flattening was observed. The radial velocity components in the x-axis (U_x) and y-axis (U_y) showed radial activity resultant in an increase in the radial velocity components precisely where the high and non-regular axial velocity reduction occurred. A series of snapshots covering the jet process at shorter fractions of time to those showed in Figure 5.53 is presented in Appendix A.9.3.

The 2nd, 3rd and 4th rows respectively of Figure 5.54 show the instantaneous lateral cross-sectional (x-y plane) velocity vector at twelve lateral locations distributed equally along the domain of time 227 ms, whereas, the 1st row of Figure 5.54 shows the radial velocity (U_x and U_y) intensity at an instantaneous longitudinal cross-sectional (x-z plane). Symmetric interface shear velocity and uniform jet structures were observed up stream at $z/D=0$, implying insignificant velocity relaxation or aerodynamic influence at the interface. The jet deformed gradually downstream as relaxation occurred and

modified, hence the surrounding air dragged with the jet, and radial movement appeared inside the liquid core. The Interface shear velocity became asymmetrical which is gradually modified from the nozzle exit, whereas the flow structure is symmetrical.

The difference in the radial motion observed here with the laminar burst jet case is that the velocity relaxation occurs at lower injection velocity. Moreover, no strong vortices (transverse or twin vortex structure) were generated clearly inside the liquid column. At high injection speed and viscous liquids, the disturbances generated inside the liquid were influential due to the high drag and shear forces between the liquid layers. Hence, a strong vortex structure was generated when the radial velocity increased and the liquid jet exhibited burst as illustrated in Section 5.3.1. However, in this case, the viscosity and the injection speed were low, hence the radial movement generated was not effective enough to produce the strong vortex structure and burst the jet. A series of snapshots covering the jet process at shorter fractions of time to those showed in Figure 5.54 is presented in Appendix A.9.4.

Figures 5.55 shows the instantaneous comparison between the velocity field and the vortices field at the time of 227 ms. The 1st row of Figure 5.55 shows a longitudinal slice (x-z plane) of velocity field distribution, whereas the 2nd row shows eight slices laterally (x-y plane) for the velocity field distribution at a time 227 ms. The 3rd row shows a longitudinal slice (x-z plane) of the vortices field distribution, whereas the 4th row shows lateral eight slices (x-y plane) for the vortices field distribution. The injection speed and the vorticity within the liquid showed the insignificant effect as interpreted in lower shear stress (low viscous liquid) if compared with liquid utilized to produce the jet case (high viscous liquid). Hence, the vorticity values range has been rescaled (reduced) to present a better view, as seen in Figure 5.55. This explains the reasons behind the conventional liquid jet breakup if compared with a high viscous laminar burst case. A series of snapshots covering the jet process at shorter fractions of time to those showed in Figure 5.55 is presented in Appendix A.9.5.

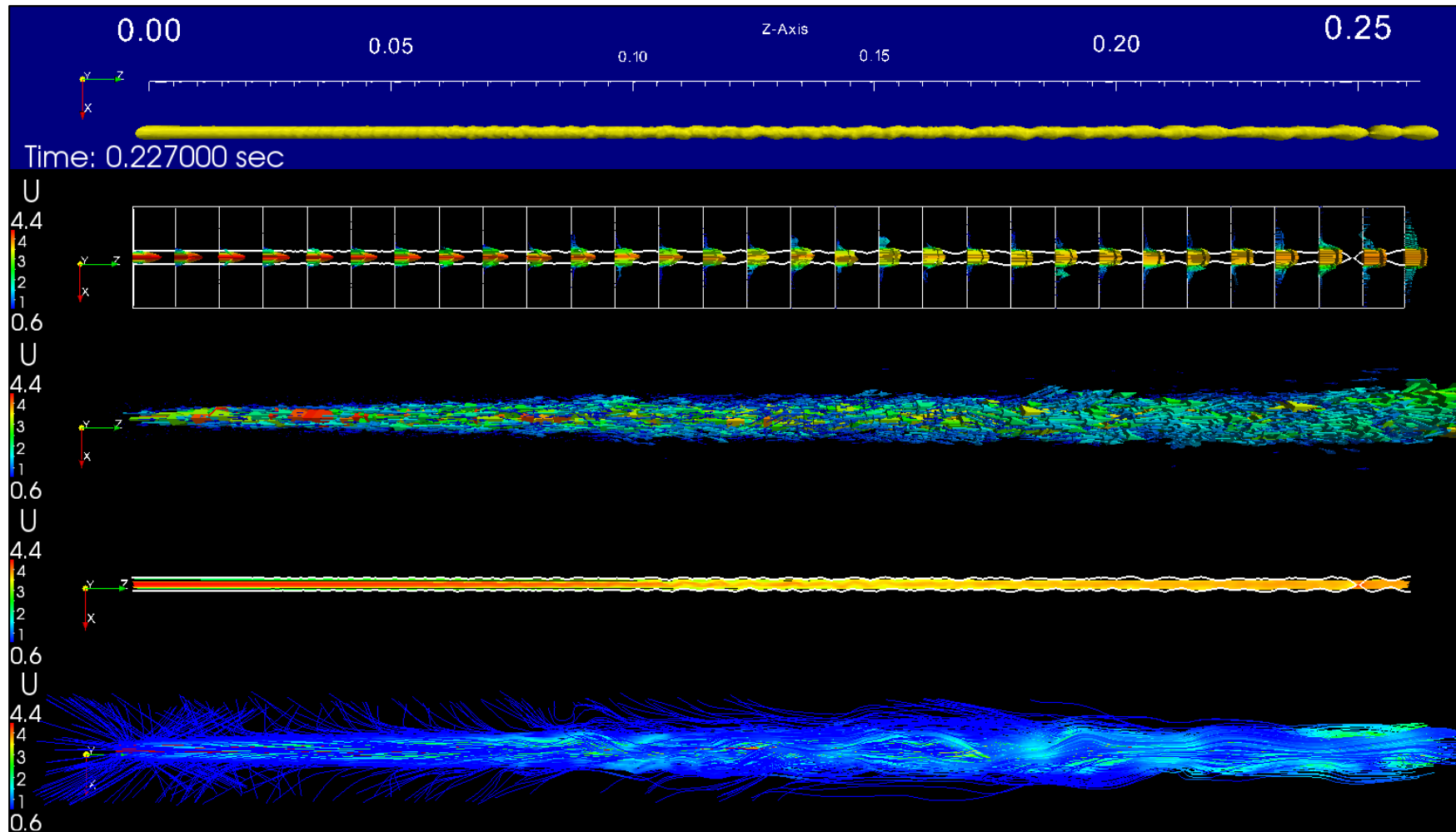


Figure 5.52 Low viscosity laminar liquid jet case results show the liquid column (1st row), domain velocity profile (2nd row), domain velocity field (3rd row), liquid velocity stream lines (4th row) and gas velocity stream lines (5th row)

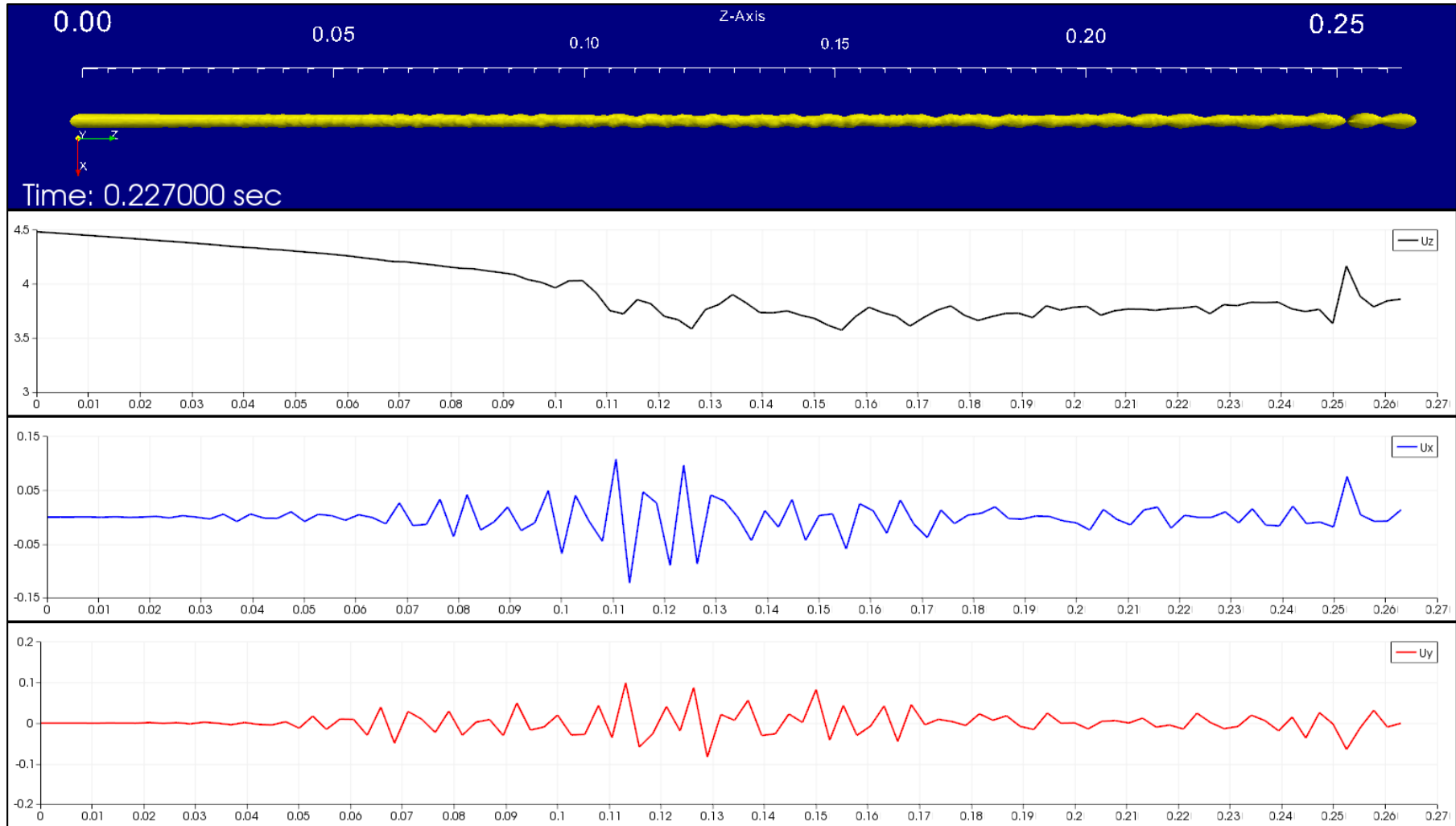


Figure 5.53 Liquid jet core velocity components (U_x U_y and U_z) at time 227 ms of a low viscosity laminar liquid jet case results

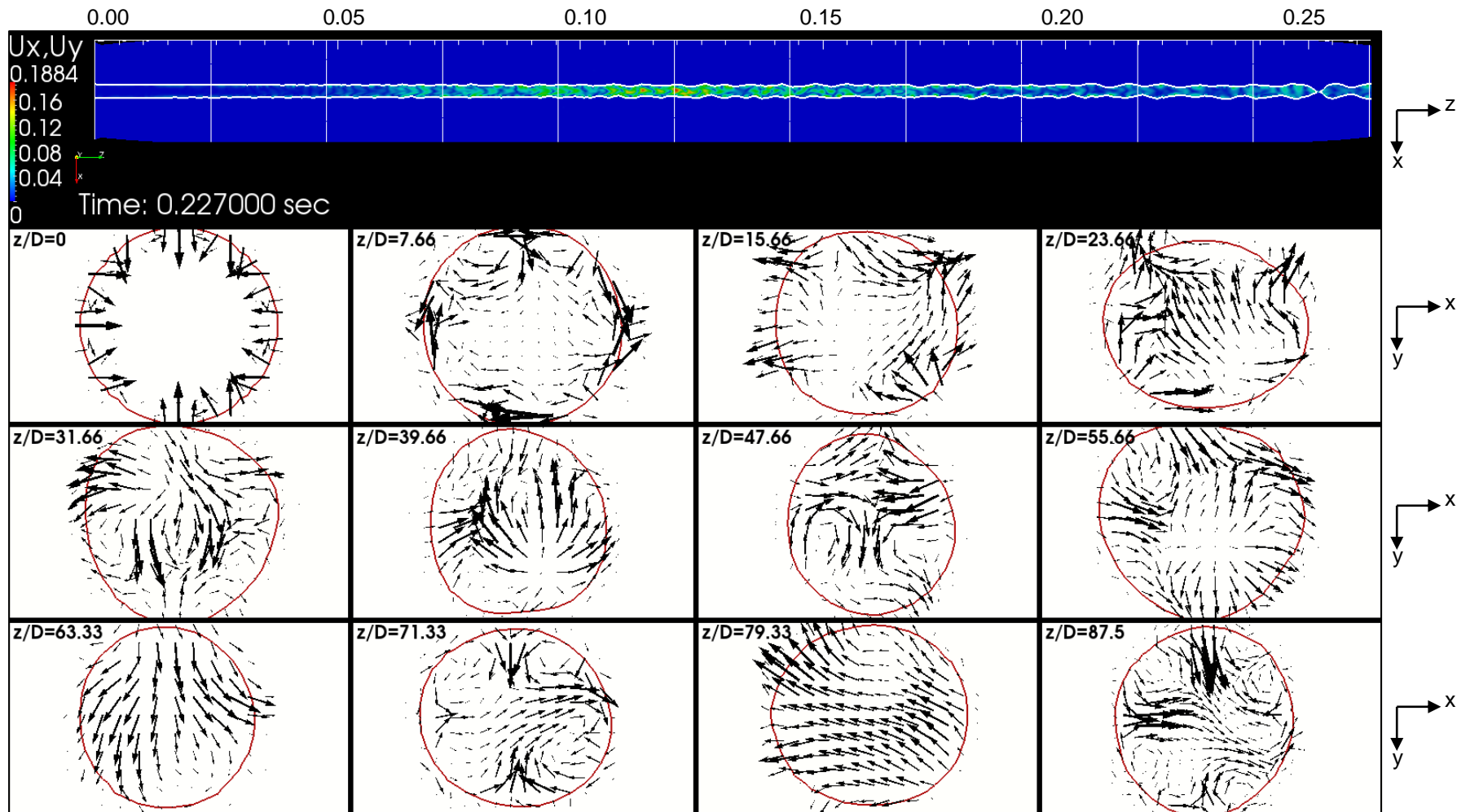


Figure 5.54 Distribution of instantaneous liquid velocity vectors projected onto longitudinal and cross-sectional planes at different axis locations of a low viscosity laminar liquid jet case results

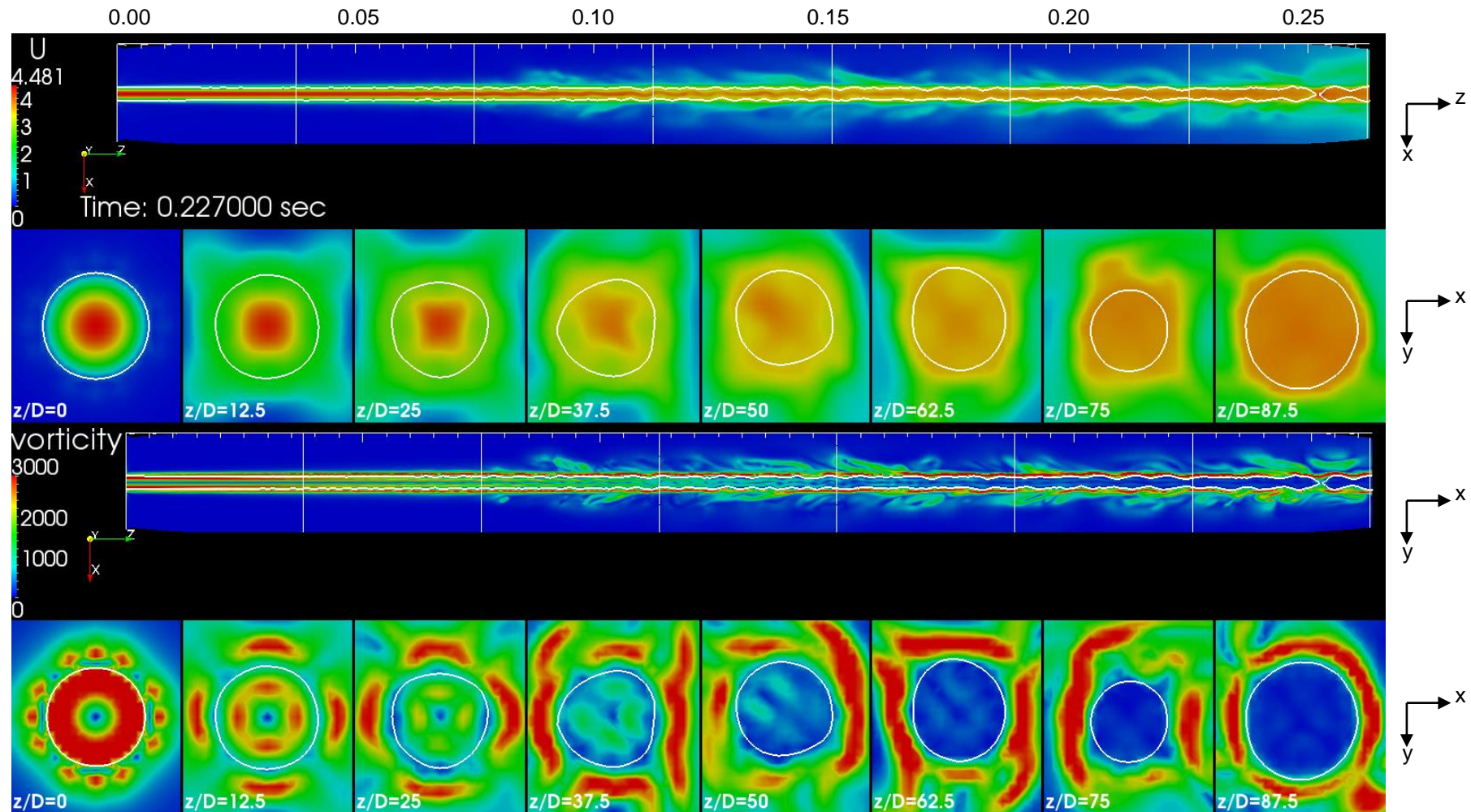


Figure 5.55 Longitudinal and lateral velocity (1st and 2nd rows) and vorticity (3rd and 4th rows) field's distribution for a low viscosity laminar liquid jet case results

5.4 Summary and Conclusions

In this chapter, an investigation has been undertaken to study the principles behind the liquid jet burst and to characterize its phenomena at a high speed laminar jet ($Re=2200$) based on results obtained using OpenFOAM benchmark and sclsVOFFoam interface solver. The effect of turbulent (top hat) and semi-turbulent inflow velocity profile on the high speed jet and burst phenomena was studied and compared in the discussion with the laminar (parabolic) burst jet. The effect of the ambient gas viscosity on the high speed jet and burst phenomena was studied. The effect of low viscous liquid on the laminar burst phenomena was studied. The collected data was post-processed to visualize the important factors that dominated the principle behind the laminar burst jet by using ParaView software.

The observation for each study case can be summarized as below

- For fully developed laminar burst jet case:

From observation, one can summarize that the initiation of the radial motion due to the sudden and sharp relaxation (non-uniform and strong local axial velocity reduction) started at 194 ms and $z/D=40$ (0.12 m) has led to generate strong stream wise vorticity structure inside the liquid core. This strong stream wise vorticity structure disturbed the liquid internally and generated span wise vorticity which could include high shear stresses and/or spinning perpendicular on the jet flow direction. Those two types of vortices disturbed the liquid core from inside and with the assistance of the momentum supplied by the jet, liquid layers exhibited stretching and elongation. Once these instabilities were generated and due to the high liquid jet momentum upstream, liquid layers overlapped, leading to deform the jet surface. This deformation modified with space and time, showing bigger stream wise and span wise vortex structure inside the liquid resulted in bursting the liquid jet column from inside.

When no instabilities generated inside the liquid core, no radial motion, span wise and/or stream wise vortices existed. The span wise vortices as a shear strains were equal in force's magnitude and symmetrical at each point around the liquid core centre line inside the jet. Once strong enough, stream wise vortices were generated (due to the radial motion initiation), they disrupted the force's homogeneity, i.e. shear strain, and the velocity's uniform distribution. Therefore, strong instabilities were generated and modified with time and space due to the interaction between the stream, and span wise vortices eventually overcame the jet surface solidarity and started bursting the jet.

- For turbulent (top hat) inlet velocity profile case:

From investigation of the turbulent (top hat) inflow velocity effect and from the comparison with the laminar (parabolic) burst case, it was concluded that the turbulent case has higher stability, showing no burst or strong jet deformation. No radial movement and/or no vorticity was generated inside the liquid due to no velocity relaxation if compared with the laminar burst jet. If no relaxation, no instabilities were generated as in the turbulent case, no perturbations or disturbances can initiate to grow up ultimately leading to violently deform and burst the jet.

- For semi-turbulent inlet velocity profile case:

From investigation of the semi-turbulent inflow velocity effect and from the comparison with the laminar burst case, it was concluded that the semi-turbulent case was stable and showed no burst or strong jet deformation. No radial movement and or no vorticity were generated inside the liquid despite of the velocity relaxation existing, but were considered relatively lower if compared with the laminar burst jet. If no velocity relaxation or low relaxation effect and no instabilities generated as in the semi-turbulent and turbulent cases, no perturbations or disturbances can initiate to eventually grow up leading to violently deform and burst the jet.

- Laminar burst jet at high and low gas viscosity:

Global turbulence or the aerodynamic movement was suppressed when laminar liquid ejected in high viscous ambient condition if compared with the default case (laminar burst jet in air viscosity). However, locally at the liquid-gas interface, higher gas viscosity resulted in bigger drag (more shear) due to higher friction force, and this assisted the liquid velocity relaxation, therefore the burst jet phenomena occurred quicker by 16 ms. However, liquid jet injected at low viscous gas condition showed lateness in burst jet existence by 59 ms delay if compared with the default burst jet case in air. Although the gas turbulence and aerodynamic movement has been increased tremendously for lower viscous gas, this lagging is attributed to the less shear stress (less friction) at the interface in the lower gas viscosity.

- Laminar jet breakup at low liquid viscosity:

From comparing high and low viscous liquid study cases at $Re=2200$, It can be summarised that parabolic velocity profile relaxation at high laminar speed and high viscous liquid (as in the default burst case) tends to generate strong and different types of vortex structure. This vortex structure was maintained and modified in the higher viscous liquids due to the higher shear stresses and friction (resistance) forces between

the liquid layers. These observations for liquid burst jet disappear for lower viscous liquids, whereas it has less resistance and no strong instabilities initiated inside the liquid as the injection speed is less than the injection speed of the laminar burst jet (default case).

It is concluded that aerodynamic and gas turbulence as presented in different ambient gas viscosity has no influence on the high speed laminar jet burst phenomena. Moreover, changing ambient gas viscosity which was interpreted as increasing or decreasing the friction at the liquid-gas interface has an effect on the processing time of the burst jet phenomena, but not on the existence of the jet burst itself. The main and only reason behind liquid jet burst phenomena is the velocity profile relaxation from fully developed laminar (parabolic) profile to fully turbulent (flat) profile. Through velocity relaxation, friction between liquid layers presented in the shear stresses reduces the relatively high axial velocity. Strong radial velocity initiated inside the liquid core, resulting in generating different types and strong vortex structure inside the liquid core leading to disturb the jet from inside and eventually burst it up. For low viscous liquid and $Re=2200$, the radial velocity generated resultant from the velocity relaxation is lower than the default burst case. No strong and different vortex structure was generated inside the liquid core. The aerodynamic effect and gas turbulence effect is very low as the low viscous liquid jet at $Re=2200$ is in the first wind-induced regime and jet breakup length was attributed to the laminar jet experimental correlations.

From the results obtained, the main conclusions are remarked as listed below:

- OpenFOAM could capture burst phenomena.
- In parabolic (laminar) jet case:
 - The burst is captured.
 - Transition of velocity profile from parabolic to flat.
 - Axial vortices inside liquid jet increases from upstream to downstream.
 - Strong, 3-D vortex structures are generated inside the liquid.
- In turbulent (flat) and semi-turbulent cases:
 - No burst is observed.
 - Very little radial movement was predicted inside liquid.
 - No vortex structure generated inside the liquid.
- In laminar burst jet at high and low ambient gas viscosity cases:
 - The burst phenomenon is observed in both cases.
 - The existence of the high speed laminar jet burst does not seem to be attributed to the influence of gas Reynolds number.

- Increasing the gas viscosity increases the shear stress at the liquid-gas interface, and speeds up the inception of liquid jet burst phenomena, and vice-versa.
- In laminar burst jet condition at less viscous liquid and $Re=2200$:
 - No burst is observed.
 - According to previous empirical correlations for a conventional laminar jet, the jet breaks up in the 'first wind' regime.
 - The velocity profile transitions from parabolic to flat at the location of liquid jet breakup.
 - No significant radial movement is observed within the liquid.
 - No significant vortex structure is generated inside liquid.
- From the results, it has been concluded that:
 - Parabolic (laminar) inlet condition plays an important role in burst formation.
 - Transition of velocity profile from parabolic (velocity relaxation) to flat.
 - Radial movement and strong vortex structure disturbed liquid internally and burst it.
 - High speed laminar liquid jet burst phenomena can be considered as a laminar case.
 - Aerodynamic effect has no role in producing liquid jet burst phenomena.
 - Ambient gas viscosity parameter does not lead to producing liquid jet burst phenomena.
 - For high viscous liquid, velocity profile relaxation at high injection speed has the main role in generating the radial velocity components which result in initiating different and big vortex structure (high instabilities and perturbations) inside the liquid core leading to burst the jet internally in a violent fashion.

Chapter 6 Conclusions and Future Work

6.1 Conclusions

Numerical studies of two multi-phase problems of practical significance were studied, namely: (i) the coalescence of two droplets and (ii) the jet-burst phenomena of a high speed laminar jet, both using an open source free CFD code (OpenFOAM 2.1.1) and sclsVOFFoam (LS+VOF) multiphase solver. For the interaction of two droplets problem, numerical results were obtained for the flow phenomena to investigate the final composite droplet location at different lateral separation, impact speed and liquid properties (viscosity and surface tension). For the high speed laminar jet problem, at $Re_L=2200$, results were obtained for different inflow velocity profile, ambient gas viscosity and reduced liquid viscosity. The results obtained were post-processed using the tool ParaView 3.12.0 which is compatible with the installed version of OpenFOAM.

From the converged results obtained, the main conclusions for each problem are summarised as follows.

6.1.1 Two Droplets Interaction on Substrate

It was found that the composite droplet location relative to the initial condition was controlled by the impacting droplet velocity and liquid properties but showed the same non-trivial final location movement for the different overlap ratios used in this research. Conclusions are summarized as follows:

- Different types of forces (inertia, viscous and surface forces) are embedded in the phenomena of two droplets impact and coalescence conditions. Those forces are considered all important in the deposition of the final composite droplet into equilibrium conditions.
- The left edge retraction under the effect of surface forces was considered the reason for the composite droplet locating to the side of the impact droplet at zero or low inertia conditions ($U=0-0.5$ m/s for the case of $\lambda=0.34$).
- The left edge spreading under the effect of impact speed (inertia) was considered the reason for locating the composite droplet to the opposite side of impact droplet at higher velocity ($U=0.6 - 3$ m/s for the case of $\lambda=0.34$).
- For high value of surface tension, inertial effects are reduced and, the composite droplet is always locates to the impact side. The opposite happens for lower value of surface tension, whereby inertia dominates and the mass centre moves in the opposite direction.

- For a high value of viscosity, inertial influence is reduced, and composite droplet always located to impact side. For the lower value of viscosity, the right and left composite droplet trend always dominated, whereas at high impact speed, inertia dominated and mass centre moved to the opposite direction.
- At zero impact speed and different values of surface tension and viscosity, the threshold line trend of the centre-of-mass relative to the initial centre-of-mass is dominated by the “drawback” phenomena and the surface tension effect. Composite centre-of-mass located left of the initial centre-of-mass dominated the map range of different viscosity and surface tension undertaken in this study for $U=0$ m/s.
- At low impact speed $U=0.2$, inertia influenced the composite centre-of-mass, drawing the sessile (and the composite eventually) to the impact side. Therefore, due to unpinning and surface tension driven force phenomena, composite located right relative of the initial centre-of-mass as presented in the lower threshold line. The effect of drawback at low inertia and high surface tension appeared in the upper threshold of the case $U=0.2$.
- At impact speed $U=0.5$, the composite centre-of-mass located to the left dominated those located to the right relative to the initial centre-of-mass due to the influence of inertia. The threshold line is positioned at higher surface tension values in the viscosity-surface tension map compared with the $U=0.2$ m/s case.
- A gradual increase in impact speed from $U=0.8, 1.0, 1.2$ m/s resulted in the area occupied by the composite centre-of-mass located to the left side dominating the area for those located to the right relative to the initial centre-of-mass. This is due to the effect of inertia as shown on the viscosity-surface tension map. Therefore, the threshold line moves up to higher surface tension values as impact speed increases.
- At any value of viscosity, surface tension is the dominant parameter which determines whether the composite droplet centre-of-mass location moves to the right or to the left relative to the initial centre-of-mass.

6.1.2 Liquid Jet Burst Phenomena

These results agreed reasonably well in magnitude and trends with existing experimental data. In addition, the numerical model provided additional insights that were not obtained experimentally. These results provided insight into the flow characteristics of the laminar burst jet phenomena. It can therefore be concluded that the open source free CFD code (OpenFOAM 2.1.1) and sclsVOFFoam (LS+VOF) multiphase solver is

capable of predicting the flow phenomena for the geometry under consideration. The main findings may be summarized as:

- OpenFOAM is capable of capturing the liquid burst phenomena.
- For the laminar (parabolic) jet case:
 - The liquid burst is captured.
 - The velocity profile transitions downstream from parabolic to flat.
 - Axial vortices inside liquid jet increase from upstream to downstream.
 - Strong, 3D vortex structures are generated inside the liquid.
- For the turbulent (flat) and semi-turbulent cases:
 - No burst is observed.
 - Very little radial movement was predicted inside liquid.
 - No vortex structure was generated inside the liquid.
- For laminar jet burst at high and low ambient gas viscosity cases:
 - The burst phenomenon is observed in both cases.
 - The existence of the high speed laminar jet burst does not seem to be attributed to the influence of gas Reynolds number.
 - Increasing the gas viscosity increases the shear stress at the liquid-gas interface, and speeds up the inception of liquid jet burst phenomena, and vice-versa.
- For the laminar jet burst condition of less viscous liquid with $Re=2200$:
 - No burst is observed.
 - According to previous empirical correlations for a conventional laminar jet, the jet breaks up in the 'first wind' regime.
 - The velocity profile transitions from parabolic to flat at the location of liquid jet breakup.
 - No significant radial movement is observed within the liquid.
 - No significant vortex structure is generated inside liquid.

From the results, it has been concluded that:

- Parabolic (laminar) inlet condition plays an important role in burst formation.
- Transition of velocity profile from parabolic (velocity relaxation) to flat.
- Radial movement and strong vortex structure disturbed the liquid internally induced the burst.

- High speed laminar liquid jet burst phenomena can be considered as a laminar case.
- Aerodynamic effect has no role in producing liquid jet burst phenomena.
- Ambient gas viscosity parameter does not produce liquid jet burst phenomena.
- For high viscous liquid, velocity profile relaxation at a high injection speed has the main role in generating the radial velocity components which result in initiating different and big vortex structure (high instabilities and perturbations) inside the liquid core leading to burst the jet internally in a violent fashion.

6.2 Recommendations for Future Research

6.2.1 Two Droplets Interaction on Substrate

For the two droplets problem, further study should be directed towards investigating the effect of other parameters on the final composite deposition after the impact and coalescence phenomena of two droplets. Such an investigation could consider the contact angle effect of different wettability substrates, heated surface effect on coalescence phenomena and final droplet deposited. For the sake of completion, these aspects are relatively important to broaden the understanding of the impact and coalescence of two droplets on substrate and final composite location at its equilibrium condition.

6.2.2 Liquid Jet Burst Phenomena

The liquid burst phenomena is likely to be an influential process in the topical practical problem of creating of explosive atmospheres from accidental pressurised releases of liquid fuels [8]. Further consideration needs to be given as to how its influence can be accommodated into practical advice when producing engineering guidelines. It remains to be seen whether an open source CFD code such as OpenFOAM can produce reliable predictions for more sophisticated geometries for example modelling complicated nozzle designs, liquid jet with co-flow or counter co-flow air, and modelling fully turbulent jets in the atomization regime.

A drawback of solving this problem numerically is that, due to the large number of equations solved, the large number of nodes and in particular the small time steps required to obtain sufficient convergence and hence accuracy, several weeks (using parallel computing with 48 cores) were required to obtain just one data case study. This could pose a problem in industry when dealing with this or even more sophisticated

geometries. Therefore, an improvement to the solution schemes and/or solver algorithm needs to be given consideration to speed up the solution procedure with respect to an appropriate numerical accuracy for a particular physical case.

Appendix A.1 Multi-phase Solver Verification

A.1.1 Swirling Liquid Jet

Next, OpenFOAM demonstrated its capability to simulate swirling liquid jet problems that are liquid jet ejection with a rotational inlet velocity component. This case was conducted using the *interFoam* (VOF) solver to appraise its potential without (unlike the validation cases in Chapter 3) the ability to compare against other validation data or simulations. The initial condition is given zero for the velocity and the pressure. The geometrical setting is shown schematically in Figure A.1.1. The no-slip boundary condition is used for velocity and Neumann for pressure at all the walls boundaries. Fixed swirl inlet velocity and Neumann boundary condition used for the pressure at the inlet boundary. Fixed atmospheric pressure and Neumann boundary condition used for the velocity at the outlet boundary. Computational and mesh details are presented in Table A.1.1. The physical parameters are presented in Table A.1.2. Snapshots results at several time steps for the swirling jet are presented in Figure A.1.2.

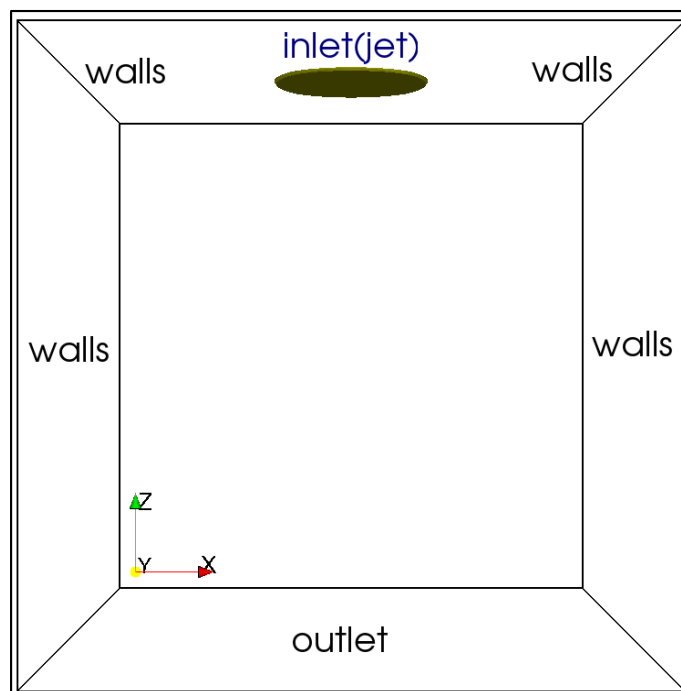


Figure A.1.1 3-D geometrical setting for swirl jet validation case.

Table A.1.1 Geometrical and mesh details of swirling jet case

Geometrical and mesh details	
Computational domain (m)	0.001 × 0.001 × 0.001
Jet diameter (m)	0.00028
Mesh resolution	90 × 90 × 90
Mesh size (m)	1.11 × 10 ⁻⁵

Table A.1.2 Physical parameters conducted for swirl jet case

Medium	Density ρ (kg/m³)	Dynamic viscosity μ (Pa.s)	Surface tension σ (N/m)
Gas (air)	1.226	1.4519 × 10 ⁻⁵	
Liquid (water)	1000	0.001137	0.073

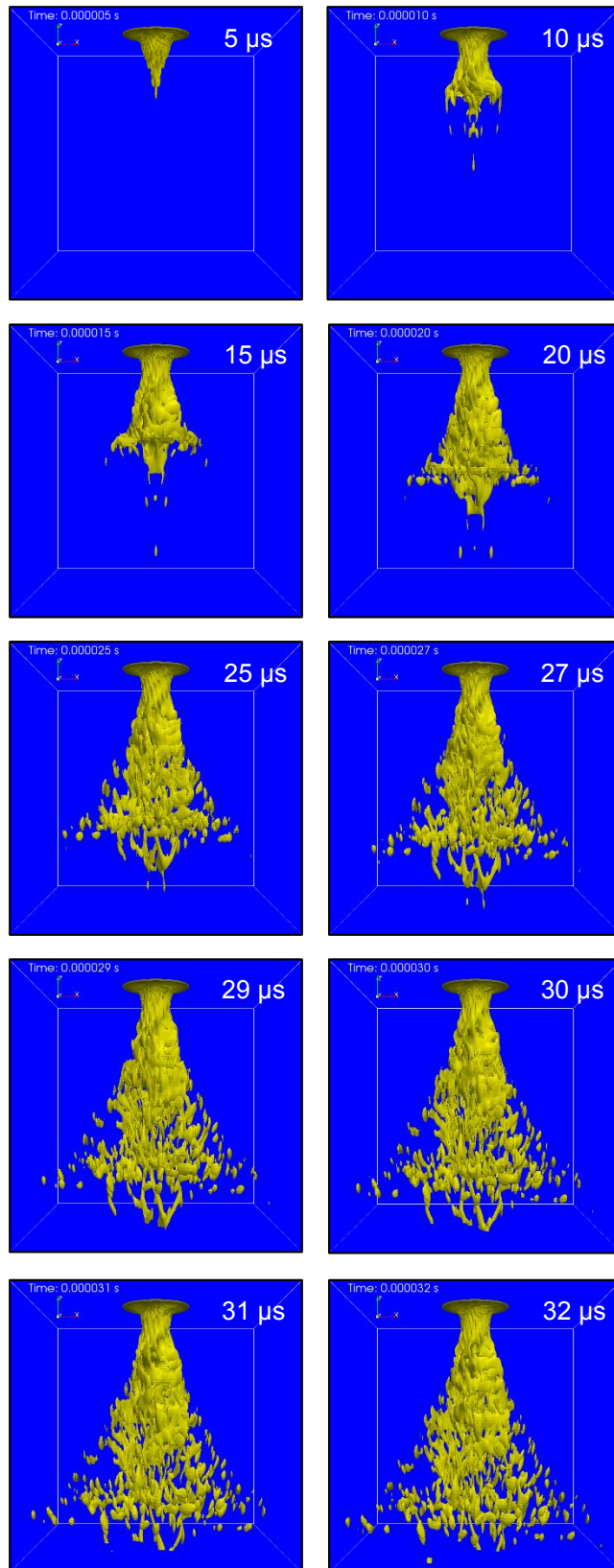


Figure A.1.2 Snapshots of results of 3-D numerical simulation of a swirl jet by OpenFOAM model

A.1.2 Swirl-induced Spray

OpenFOAM was employed to simulate a swirl-induced atomization problem using the same swirl boundary condition used in the previous case (appendix A.1.1), but with different geometrical and physical parameters settings. This case was conducted using *interFoam* (VOF) solver to appraise its potential without being able to directly compare with previous studies. The initial condition is given zero for the velocity and the pressure. The geometrical setting is shown schematically in Figure A.1.3. The no-slip boundary condition is used for velocity and Neumann for pressure at all the walls boundaries. Fixed swirl inlet velocity and Neumann boundary condition used for the pressure at the inlet boundary. Fixed atmospheric pressure and Neumann boundary condition used for the velocity at the outlet boundary. Computational and mesh details are presented in Table A.1.3. The physical parameters for the liquid used (Ethanol) in this simulation are presented in Table A.1.4. Snapshots results at several time steps for the swirl-induced spray are presented in Figure A.1.4. OpenFOAM appeared to be capable of simulating swirling spray to capture the primary atomization process.

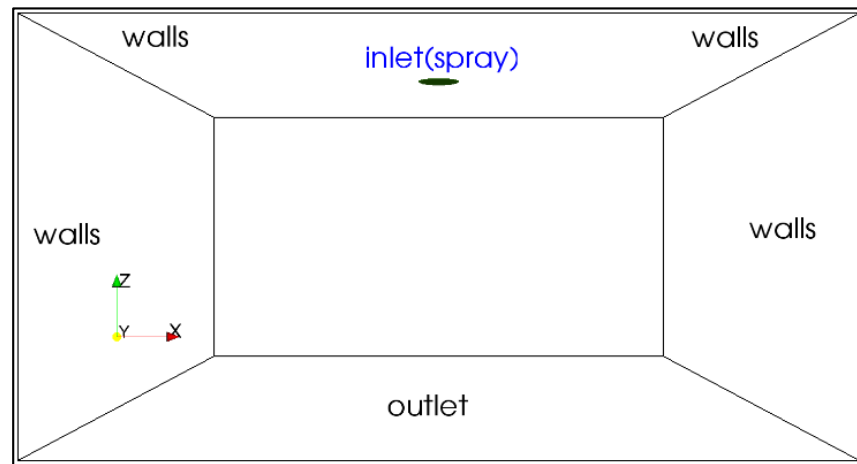


Figure A.1.3 3-D geometrical setting for swirl spray validation case

Table A.1.3 Geometrical and mesh details of swirl spray case

<i>Geometrical and mesh details</i>	
Computational domain (m)	$0.006 \times 0.006 \times 0.004$
Spray diameter (m)	0.0004
Mesh resolution	$420 \times 420 \times 280$
Mesh size (m)	1.42×10^{-5}

Table A.1.4 Physical parameters conducted for swirl spray case

<i>Medium</i>	<i>Density</i> ρ (kg/m ³)	<i>Dynamic viscosity</i> μ (Pa.s)	<i>Surface tension</i> σ (N/m)
Gas (Air)	1.226	1.4519×10^{-5}	
Liquid (Ethanol)	798	0.001083684	0.0221

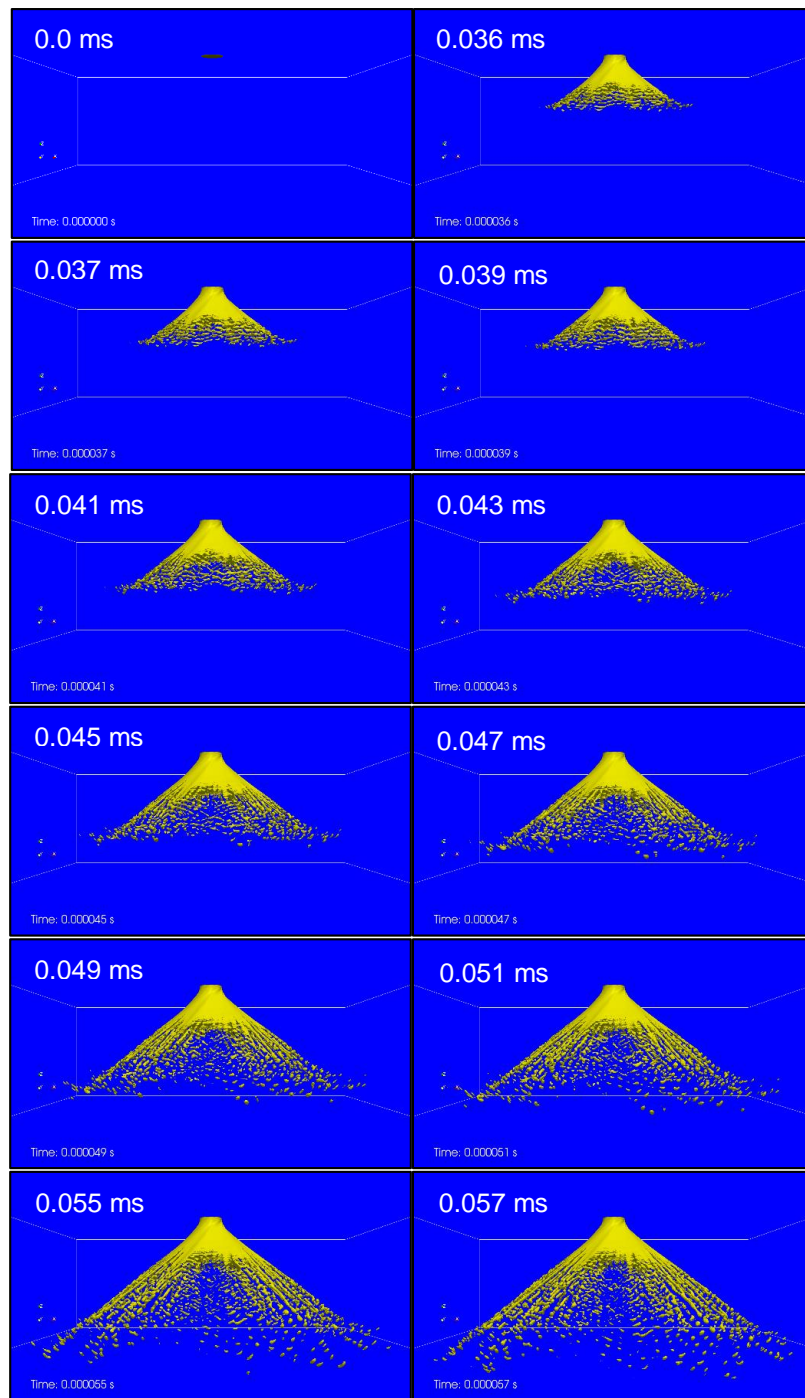


Figure A.1.4 Time-Resolved results of three dimensional numerical simulation of a swirl spray by the OpenFOAM model

Appendix A.2 Numerical Setting Used for Two Droplets Problem

A.2.1 Two Droplets Case Pre-processing

In this section, geometrical mesh setting strategies adopted for case of study in Chapter 4 is illustrated. Furthermore, the software's and any axillary tools assistant to generate the final bench mark to process the physical study cases using OpenFOAM will be thoroughly illustrated.

A.2.1.1 Case Geometry and Mesh

The easiest strategy before pre-processing, is to copy the case directory of the tutorial that uses or matches the physical and mathematical requirements. In our situation, the *damBreak* case was chosen, and renamed:

- twoDroplets (for two droplets case in Chapter 4)
- liquidJet (for liquid jet case in Chapter 5)

These two cases were located on the home directory ready for further action such as re-constructing the physical domain or generating the mesh. OpenFOAM is provided with some tools to generate geometry and meshes, from the simple *blockMesh* to the more complicated *snappyHexMesh*, and contains many tools for importing meshes generated with other software packages [59]. The geometry and mesh for this case were simple, therefore *blockMesh* was sufficient to use for the two droplets project. The geometrical setting utilized to solve Navier-Stokes equations with DNS (laminar model) is presented in Figure A.2.1. Geometrical and mesh details are presented in Table A.2.1.

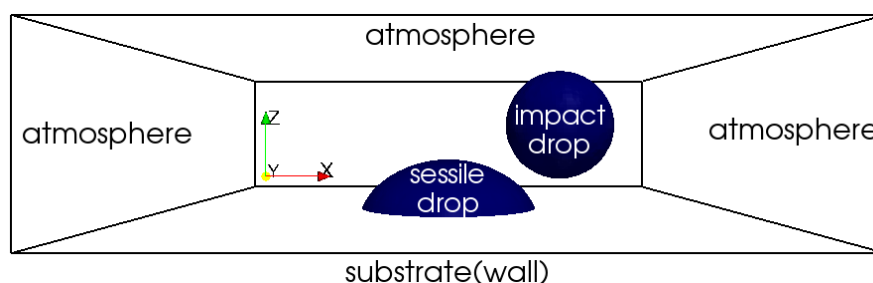


Figure A.2.1 3-D geometrical setting for two droplets validation case

Table A.2.1 Geometrical and mesh details for two droplets case

<i>Geometrical and mesh details</i>	
Computational domain (m)	0.014 × 0.014 × 0.0038
Droplets initial diameter (m)	0.0028
Mesh resolution	166 × 166 × 45
Mesh size (m)	6.44 × 10 ⁻⁵

A.2.1.2 Physical Parameters, Initial and Boundary Conditions Setup

A droplet with velocity (velocity was varied in this study) impacts on a stationary sessile droplet (static contact angle = 63°) at a known centre-to-centre spacing (centre-to-centre spacing was varied in this study). As shown from Figure A.2.1, the boundary faces are a wall (substrate), and atmosphere. Excluding the impact droplet, the initial condition is given zero for the velocity and the pressure. For the substrate (wall), the no-slip ($U=0$) is used, while Neumann boundary condition is used for the velocity to all other boundaries (atmospheric). For the substrate, Neumann boundary condition utilized for pressure, while fixed atmospheric pressure to all other boundaries (atmospheric). The fluid properties are defined in the transportProperties dictionary. The physical parameters (default case [24]) which have been indicated in are presented in Table A.2.2. Different values of physical properties (surface tension and viscosity) have been utilised in this study, representing a wide range of liquid types as discussed in the results and discussion section (Chapter 4).

To generate the initial sessile and impacting droplets inside the domain, the 'setFields' utility was used. An extra dictionary called setFieldsDict to setup initial conditions for droplets was included inside the system directory. setFieldsDict can be copied from another OpenFOAM tutorial like damBreak and adapted to suit the problem considered. When the fields are set using the 'setFields' utility, the cells inside the droplets will be only assigned the value of alpha equal to 1. Two steps were used to generate the two droplets. First, the sessile droplet and associated field were generated (saving the files generated for the sessile and make them the initials for the impact droplet). Second, by using another setFieldDict, the impact droplet was generated and backed up to be merged with sessile by overwriting both droplet fields.

Table A.2.2 Physical parameters conducted for two droplets case. (adapted from [24])

<i>Medium</i>	<i>Density</i> ρ (kg/m ³)	<i>Dynamic viscosity</i> μ (Pa.s)	<i>Surface tension</i> σ (N/m)
Gas (air)	1.25	1.82*10 ⁻⁵	
Liquid (glycerol-water)	1220	0.0858	0.067

A.2.1.3 Time Setup, Data Output Control, Solution and Discretization Schemes for Two Droplets Case

As stated by the OpenFOAM user guide [59], the surface tracking algorithm in *interFoam* is particularly dependent upon the Courant number (stability parameter) compared with other models. The Courant number decreases oscillations, improves accuracy & decreases numerical dispersion if its value is suitably based on mesh size and physical case setup. Courant number helps to find the appropriate time step for any given mesh. In the *controlDict* file, the time adjustments can be applied. It is not efficient to have a fixed time step because the change of the velocity is not easily expected, so *adjustTimeStep* is set to 'yes'. The Courant number is defined as:

$$C_o = \frac{\Delta t |U|}{\Delta x} \quad \text{Equation A.2.1}$$

where Δx is the width of the cell in the velocity direction, Δt is the time step. Courant number increases as a result of a small cell and a high velocity. Initial Δt is set to be 1×10^{-8} for both cases (two droplet in Chapter 4 and liquid jet as in Chapter 5) and adjusted automatically through the calculations. It is recommended that the Courant number is equal to or less than 0.5 at the interface [59]. The extraction time (when the results are written), is controlled and set to initially 0,001 and reduced to 0.0001 for more time details.

A.2.1.4 Parallel Processing Setup

For this Ph.D. study, three desktop computers working with *Linux Ubuntu 12.04* operating system were used with OpenFOAM 2.1.1 to test, validate both study cases and produce results for two droplets study case. Each PC was provided with CPU Intel(R) Core(TM) i7-3820 CPU @ 3.60GHz, 4 cores and 32 Gigabyte memory RAM for two PC and 40 gigabyte memory RAM for the third PC. According to the aforementioned PCs specification, every simulation case could be run on 4 processors for each PC. For some case of two droplets, running the case took a couple of weeks to complete if using a serial using one processor. Through parallelisation using several cores in parallel for each PC, such simulations would only take a couple of days to a week at most, hence providing a consider time saving.

OpenFOAM ships with the OpenMPI library to manage the communications between processors, and run parallel applications with ability to scale up to at least 1000 CPUs [90]. This mechanism of parallel computing is known as domain decomposition

where geometry is splitted up into sub domains, each processor gets its own pieces to work for a solution [59]. To achieve this task, the geometrical domain should be decomposed using a utility called *decomposePar*. This utility asks for another dictionary file called *decomposeParDict* which is located in the system directory. When editing the *decomposeParDict* file, the editor can see the following entries:

- *numberOfSubdomains* – refer to how many portions shall be divided, this number has to equal the number of available nodes on single PC or on HPC cluster.
- *method* - method of decomposition. There are four ways: simple, hierarchical, scotch, and manually. Simple method divide the domain into sub-domain only by direction. Hierarchical decomposition same as simple decomposition, except user can specify the order of decomposition. Scotch decomposition asks no geometric input, user can specify a weighting for the decomposition between processors, through an optional *processorWeights* keyword which can be useful on machines with differing performance between processors. Manual decomposition, user can manually specifies the data location to each node to a particular processor.
- *distributed* - OpenFOAM allow user to distribute data if only local disks are used. *root* - since path of source code may differ between each nodes, the path must be specified [59].

The method strategy used for two droplets problem on each single PC was simple. The simple method controlled by allocating two processors for each direction *x* and *y* as the spreading and contracting occurs at those axes. The *z* direction was left with one processor which gives in total four processors: $2(x\text{-axis}) \times 2(y\text{-axis}) \times 1(z\text{-axis}) = 4$ ($2 \times 2 \times 1=4$)

A.2.2 Two Droplets Case Processing

As for any *UNIX/Linux* executable code, OpenFOAM applications, and its tools can be run using a terminal window. To pre-process and process the two droplets problem, a terminal window was opened and the case directory accessed, thereafter, the two droplets project was run in two stages:

1. Sessile droplet generation.

Generating the sessile droplet was undertaken by running the following commands on the terminal window inside the case directory.

- *blockMesh* (to generate the domain geometry and the mesh).

- `cp 0/alpha1.org 0/alpha1` (the user first needs to do this copy as a backup only for the initial alpha1.org file before running `setFields`).
- `setFields` (executed to set the phase fractions into the domain and as explained before (section A.2.1.2), reads fields from the files and after recalculating, writes them back to the file. Her sessile where generated according to its geometrical and physical details).
- `decomposePar` (splitting the domain into multiple sub-cases folders (4 here because of 4 cores) then the solver runs all cases at once, keeping them in communication. All of this can be done automatically in OpenFOAM).
- `mpirun -np 4 sclsVOFFoam -parallel > log &` (this command starts running on four cores using OpenMPI library).

Functions specified in controlDict were sampled and written to different directories. The execution time for the cases was considerably limited by the case resolution and the physical properties settings. As the cell size decreases, so does the time step, due to the fixed Courant number of maximum 0.5 increased the number of cells will reduce the time step further in addition to the extra computational time to satisfy the governing equations of additional cells. The time considered enough to generate the initial sessile was 5 ms and the sessile considered stable in an equilibrium condition due to the fact that the sessile deposited just in the specified location with a spherical cap geometry as required.

- `reconstructPar` (all the sub-case reconstructed generating single one result for each time of data extracted)

2. Impact droplet generation.

After generating the sessile droplets, the resultant fields already created for the sessile were copied in to the 0 directory after deleting the old files. Then, another `setFields` dictionary file in system directory used to generate the impact droplet with the specified velocity, the case was run according to the following commands:

- `cp 0/alpha1. 0/alpha2` (to maintain sessile field initiated alpha1)
- `cp 0/alpha2. 0/alpha3`
- `setFields` (runs the second `setFields` we kept in system directory to generate the impact droplet)
- `decomposePar`
- `mpirun -np 4 sclsVOFFoam -parallel > log &`
- `reconstructPar` (after processing has finished)

A.2.3 Two Droplets Case Post-processing

After each simulation is completed, the results are written to a folder containing the physical properties of the model at each time step (the frequency of extracting results depends on the case setting). Eventually, after data reconstruction using *reconstructPar* tool, the user can post-process every single extracted data at the specified time by running the command below on terminal:

- *paraFoam*

The user may also post-process a segment of the decomposed domain individually by simply treating the individual processor directory as a case in its own right. For example, if the user starts *paraFoam* as [59].

- *paraFoam -case processor1*

Running *paraFoam*, ParaView software will load the case results with all the parameters calculated already implicitly through simulation or explicitly later from the flow field. ParaView 3.12.0 is an open source program specifically designed to handle large datasets analysis and visualisation that can be used to visualise the results of simulation included with OpenFOAM 2.1.1. Results can be manipulated in similar ways to commercial programs such as Fluent. ParaView was used for all post-processing of simulation results of this Ph.D. thesis, including the production of graphics, animations and for explicit calculation of some parameter (as explained in Chapter 5 for liquid jet problem).

Appendix A.3 Numerical Setting Used for Liquid Jet Problem

A.3.1 Liquid Jet Burst Phenomena Case Pre-processing

In this section, geometrical mesh setting strategies adopted for case of study in Chapter 5 is illustrated. Furthermore, the software's and any axillary tools assistant to generate the final bench mark to process the physical study cases using OpenFOAM will be thoroughly illustrated.

A.3.1.1 Case Geometry and Mesh

The geometrical set up was adopted in the liquid jet burst phenomena presented in Figure A.3.1. Geometrical and mesh details for the computational domain and nozzle orifice for liquid jet study case are presented in Table A.3.1. The reason behind choosing such a large domain aims to reduce any possible effect of the side walls or boundaries on the liquid jet, therefore, special treatment was required to undertake to mesh. The idea was to use uniformly distributed fine mesh in the area where the liquid jet column is solved and around it by size $(3.2D \times 3.2D \times 87.5D)$ [58]. Furthermore, a very course mesh is used in the rest of the domain to reduce any effect of boundaries and computational cost. Although the geometry considered is simple, meshing it to the specific demands was not straightforward by just using *blockMesh*. Despite its ability to grade the mesh to any desired direction, *blockMesh* does not grade the mesh uniformly which is not considered satisfactory for the geometry and mesh development.

Therefore, *snappyHexMesh* (another meshing tool supplied with OpenFOAM [59]) as a more sophisticated tool to control and automate the mesh in any part or region of the physical domain was highly desirable for the case considered. *snappyHexMesh* deforms the mesh (when the mesh refined around the liquid column) already generated by the *blockMesh* tool and increases the mesh number. Hence, the computational cost will be increased severely depending on the level of the mesh refining settings used in the *snappyHexMeshDict* file.

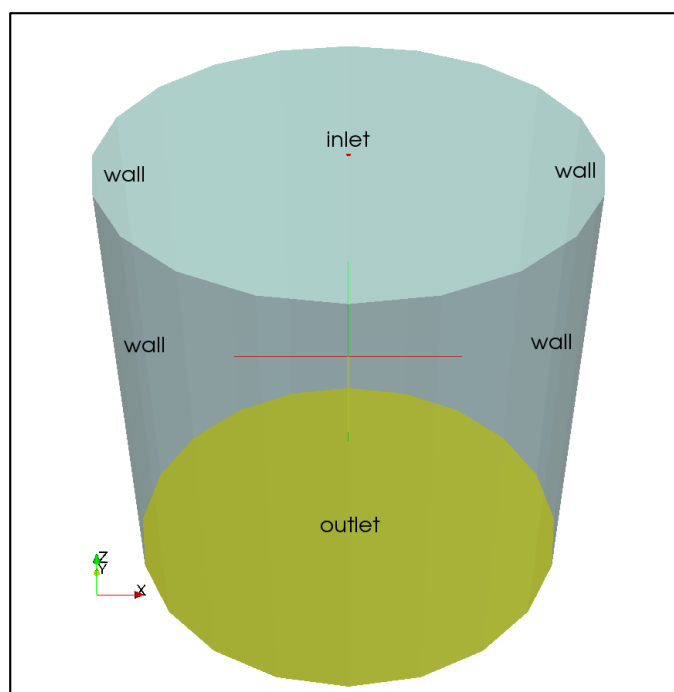


Figure A.3.1 Geometrical domain used for Liquid Jet Case

Table A.3.1 Geometrical and mesh details of laminar jet burst phenomena

	<i>Laminar jet burst phenomena</i> <i>Re=2200, We=28000</i>
Computational domain (m)	0.3 × 0.3 × 0.3
Inlet jet orifice	Diameter(D) = 0.003
Mesh resolution (in the refined region)	51 × 51 × 1600
Mesh size (m)	1.8 × 10 ⁻⁴

The steps used to construct the geometry and meshing for the liquid jet burst phenomena are as follows:

- 1- By editing and adapting the *blockMesh* dictionary, the background domain (cubic shape) was created with the minimum mesh size, to be snapped later to the required resolution. Geometrical dimensions of the cubic shape in *blockMesh* file should fit or be larger than the geometry dimensions to contain all the geometrical detail.
- 2- Construct the geometrical details and name each part as required, which helps to specify the desired boundary conditions for the named parts.
- 3- *swiftSnap* key in Blender (Blender2.66a an open-source 3-D computer graphics and meshing software product [91]) was employed to produce the geometrical (CAD) files in STL format. *swiftSnap* opens the sub-menu to edit all the geometrical details to name each part as specified.

- 4- Press the 'Write' key inside *swiftSnap* sub-menu after step 3, which saves all the geometrical parts named inside *triSurface* directory. This directory is generated automatically in any user-specified location. Eventually this directory should be saved inside the 'constants' case directory and can be chosen to be saved there directly. By pressing the 'write' key, the mesh already generated by *blockMesh* is snapped to the exact constructed geometry. *snappyHexMeshDict* is automatically created and saved alongside the *triSurface* directory. This Dictionary should then end up inside the system case directory, ready for editing later.
- 5- After completing the geometry construction described above, *snappyHexMeshDict* was edited manually and a few of the sub-dictionary sections were added to refine the mesh. Here the cylindrical column was utilised with reasonable resolution to solve liquid jet and around it by specific limit as in literature [58].
- 6- In order to run the meshing tool, its name must be typed in the command line in the case main directory and the meshing will start. In this case, first *blockMesh* generates the background geometry and mesh. Secondly *snappyHexMesh* snaps the mesh to the geometrical domain details and creates the refined regions. The meshing process using *snappyHexMesh* comprises of two steps which will be stored in the main directory as 1 and 2 files respectively. First the refinement is done according to refinement levels set in *snappyHexMesh* dictionary. In the second step cells are snapped in order to get smooth surfaces.
- 7- To check the mesh quality, the *checkMesh* utility is used to check the different meshes for any errors or warning.

On the left side of Figure A.3.2, mesh snapped to the domain geometry is represented. A cut was defined at the centre of the domain to expose the refined mesh in the region of interest, shown on the right side of Figure A.3.2. In the refined region, Cartesian uniform Cartesian mesh is specified, while the remainder shows an adaptive coarse mesh.

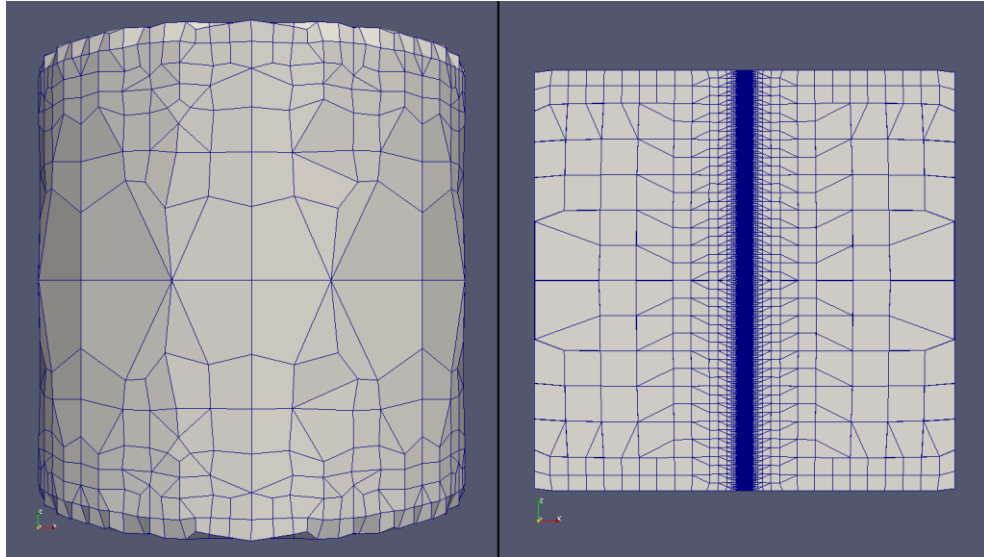


Figure A.3.2 Mesh snapped to the domain geometry in the left side, domain cut at the centre showing mesh strategy in the right side

A.3.1.2 Physical Parameters, Initial and Boundary Conditions Setup

The laminar jet study demands a parabolic velocity profile as in according to Poiseuille law. OpenFOAM by default does not have a boundary condition to impose such a profile. Hence, to implement a 3-D parabolic profile, the *swak4Foam* tool compatible with OpenFOAM version 2.1.1 was compiled [92]. Special velocity boundary condition founded inside the *swak4Foam* utility called *groovyBC* was used to impose the 3-D parabolic velocity profile according to Poiseuille expression. It can be used to set non-uniform boundary conditions without programming (specified as expressions) [93].

The initial condition is given zero for the velocity (U), alpha (α) and the pressure (P). The no-slip ($U=0$) and Neumann boundary condition for pressure are used at all the geometrical boundaries (wall) for the liquid jet problems. Fixed laminar (parabolic $U_{mean}=22.6$ m/s with fixed flow rate at $1.6e-4$ m³/s) for velocity and Neumann for pressure are given for inlet flow boundary condition. Wherever velocity were fixed, Neumann boundary condition (the dynamic pressure is set to *zeroGradient*, i.e. the gradient normal to the faces is zero) enables the pressure to be calculated and adjusted accordingly as the velocity is fixed [94]. For volume fraction (VOF) alpha (α), at the inlet patch alpha is fixed equal to one representing just liquid at the inlet. For the wall patches, Neumann boundary condition was used. Same boundary conditions used for alpha used for psi (Ψ) level set function character (LS) file except using Neumann boundary condition for inlet boundary. The values of the physical parameters [58] utilised in our default case for the liquid jet burst problem is illustrated in Table A.3.2.

Table A.3.2 Physical parameters conducted for liquid jet burst case. (adopted from [58])

<i>Medium</i>	<i>Density</i> ρ (kg/m ³)	<i>Dynamic viscosity</i> μ (Pa.s)	<i>Surface tension</i> σ (N/m)	<i>Re</i>	<i>We</i>	<i>Oh</i>
Gas (air)	1.226	1.4519×10^{-5}				
Liquid (glycerine/water mixture, 79% by weight)	1206	0.0372	0.065	2200	28000	0.076

A.3.1.3 Time Setup, Data Output Control, Solution and Discretization Schemes for Liquid Jet Case

Similarly, the output data control, solution and discretization schemes utilized before for the two droplets also used in this case. However, because of using *swak4Foam* and *groovyBC* for the liquid jet case, extra libraries were added at the end of controlDict in order to call those libraries whenever using that boundary condition. These libraries were not relevant and hence not utilised for the two droplets study case.

A.3.1.4 Parallel Processing Setup Using High Performance Computing (HPC)

For the liquid jet problem in attempts to capture the liquid jet burst phenomena, half of the resolution ($D/\Delta x=12$) used by Pan and Suga [58] was employed. The liquid jet allocated to flow in z-direction, therefore, simple strategy used as: $1(x\text{-axis}) \times 1(y\text{-axis}) \times 4(z\text{-axis}) = 4 (1 \times 1 \times 4)$. The simulation took more than 60 day's execution time on the PC to solve 220 ms physical time. Although the results captured what was considered to be a jet burst, but the results were not fully endorsed as mesh resolution can crucially influence the results.

At this stage, parallelisation with high performance computation (HPC) was required for the liquid jet study case. With support from HPC Wales, the OpenFOAM environment was created on HPC with all the extra utilities needed such as *swake4Foam* and *sclsVOFFoam* solver. HPC Wales (High Performance Computing) service provides a distributed parallel computing facility in support of research activity within the Welsh academic and industrial user community. The service is comprised of a number of distributed HPC clusters, running the Red Hat Linux operating system [95]. HPC Wales comprises a fully integrated and physically distributed HPC environment that provides access to any system from any location within the HPC Wales network. Access to the system is achieved through secure shell (SSH) remote login program [95].

The Cardiff HTC sub-system provided with three clusters and comprises a total of 162 nodes. In the original Cardiff configuration, the Capacity system and HTC system were to share 162 nodes (162 x BX922 dual-processor nodes), each having two processors, six-core Intel Westmere Xeon X5650 2.67 GHz CPUs and 36GB of memory, providing a total of 1994 Intel Xeon cores (with 3 GB of memory/core). More details about Cardiff clusters on HPC may be found in the user guide [95]. After preparing the liquid jet case to be run on HPC, the execution time at different resolution cases was checked, decomposition methods and nodes usage to estimate the time cost of 220 ms physical time. Linear estimation has been evaluated based on 0.1 ms of physical time. Table A.3.3 below shows the estimated execution time cost needed to run 0.1 ms physical time. By using just one node (12 cores) on HPC, Table A.3.3 shows a comparison between the different decomposition methods and strategies utilized at a different mesh resolution.

Although the decomposition method "scotch" was relatively slower than the decomposition method "simple" of the processor's distribution strategy (1 for the x-axis, 1 for the y-axis, and 12 for z-axis) when tested previously on the local desktop. However, from Table A.3.3 it was concluded that the scotch decomposition method was the faster method running on HPC. It was also noticed that the execution cost was reduced dramatically when changing processors distribution strategy from (2 for the x-axis, 2 for the y-axis, and 3 for z-axis) to (1 for the x-axis, 1 for the y-axis, and 12 for z-axis) for the simple method. This means most of the computational load were concentrated on the z-axis (flow direction) rather than x-axis and y-axis and more cores to solve the fluid flow in z-axis was essential to speed up the running.

Based on adopting the scotch decomposition method to run the liquid jet problem on HPC, the execution cost was estimated at 200 ms physical time and three different mesh numbers at different nodes usage as shown in Table A.3.4. Simulating the liquid jet problem with resolution higher than the one we already tested $D/\Delta x$ on our PC was essential. From Table A.3.4, one can see that the $D/\Delta x=18$ test case needed a very long execution time and of course more computational resources. On the other hand, for the $D/\Delta x=16$ test case, the execution time was reasonable and accepted. By considering the small difference in resolution between $D/\Delta x=16$ and $D/\Delta x=18$ (2 cells for jet diameter) and the big difference in execution time and resources, the decision was made to undertake $D/\Delta x=16$ and four nodes (48 cores) using "scotch" as a decomposition method.

Table A.3.3 Execution cost at variant decomposition methods, strategies and resolution for liquid jet burst problem

Case resolution & (total mesh)	Decomposition method & strategy	Execution time cost for 0.1ms physical time
D/ Δx =12 2,379,676	Simple (2-x, 2-y, 3-z)	10324.9 sec (172.08 min, 2.868 hr)
	Simple (1-x, 1-y, 12-z)	1047.81 sec (17.46 min, 0.291 hr)
	scotch (weight distributed equally)	1009.64 sec (16.82 min, 0.28 hr)
D/ Δx =16 3,723,736	Simple (2-x, 2-y, 3-z)	26418.1 sec (440.3 min, 7.338 hr)
	Simple (1-x, 1-y, 12-z)	2576.34 sec (42.939 min, 0.715 hr)
	Scotch (weight distributed equally)	2375.41 sec (39.59 min, 0.659 hr)
D/ Δx =18 5,830,182	Simple (2-x, 2-y, 3-z)	52877.9 sec (881.29 min, 14.68 hr)
	Simple (1-x, 1-y, 12-z)	5923.57 sec (98.72 min, 1.645 hr)
	scotch (weight distributed equally)	5253.98 sec (87.566 min, 1.459 hr)

In order to accelerate the running time on HPC, optimizing cores usages was considered essential. One way to do this was by controlling cores usage on HPC, calling hosts from machines or processors. Each node on HPC has 2 processors, and each processor has 6 cores. On one HPC node, if for instance 8 cores out of 12 were used, 4 cores from each processor, this would accelerate the run time. Acceleration was based on saving (not using for the calculation) 2 cores out of 6 for the communication process, rather than using all cores for calculation and communication at the same time [96]. To call a host (name of any host in particular) from machine file did not work on HPC as such a feature not provided on HPC for parallel processing usage control. The second way attempted is to use the method proposed in [97]. Here HPC used a single node (2 processors, 6 cores for each one) and found that binding the cores in terms of using 8 cores (bind-to-core –bysocket), 4 in each processor was more than 2 times faster than using all 8 cores on one processor(bind-to-core –bycore) and 2 on the other processor. The same strategy was adopted for the current case, using scotch and simple decomposition methods, with outcome results illustrated in Table A.3.5.

Table A.3.4 Time estimation to run Liquid jet on HPC tested at different cores usage using Scotch method for 200 (ms) as estimated from 0.1 (ms) physical time

Case resolution & (total mesh)	1 node (12 cores)	2 node (24cores)	3 node (36 cores)	4 node (48 cores)
D/ Δx =12 2,379,676	2019280 (sec) 33654.666 (min) 560.911 (hr) 23.3712 (days)	1009640 (sec) 16827.333 (min) 280.455 (hr) 11.685 (days)	673093.33 (sec) 11218.222 (min) 186.970 (hr) 7.790 (days)	504820 (sec) 8413.666 (min) 140.227 (hr) 5.842 (days)
D/ Δx =16 3,723,736	4750820 (sec) 79180.33 (min) 1319.6722 (hr) 55 (days)	2375410 (sec) 39590.165 (min) 659.836 (hr) 27.4931 (days)	1583606.6 (sec) 26393.444 (min) 439.890 (hr) 18.32 (days)	1187705 (sec) 19795.083(min) 329.918 (hr) 13.746 (days)
D/ Δx =18 5,830,182	10507960 (sec) 175132.66 (min) 2918.877 (hr) 121.619 (days)	5253980 (sec) 87566.333 (min) 1459.438 (hr) 60.809 (days)	3502653.3 (sec) 58377.555 (min) 972.959 (hr) 40.539 (days)	2626990 (sec) 43783.166(min) 729.7194 (hr) 30.404 (days)

Table A.3.5 Binding control setting on HPC for both ‘Scotch’ and ‘Simple’ decomposition methods for 0.1 (ms) physical time

Type of binding	Decompose method	Cores used	Execution time sec (binding)	Speed up percentage %
No core binding	Scotch	12	1009.64	0 %
bind-to-core (6 by 2)	Scotch	8	1423.22	N/A
bind-to-core –bysocket (4 by 4)	Scotch	8	1092.35	N/A
bind-to-core –bysocket (3 by 3)	Scotch	6	1322.88	N/A
bind-to-core –bysocket (5 by 5)	Scotch	10	1000.11	0.94%
bind-to-core –bysocket (6 by 6)	Scotch	12	952.75	5.63 %
No core binding	simple	12	1052	0 %
bind-to-core –bysocket (4 by 4)	simple	8	1120.67	N/A
bind-to-core –bysocket (5 by 5)	simple	10	1104.65	N/A
bind-to-core –bysocket (6 by 6)	simple	12	1001.04	4.8 %

In contrast to the experience reported in [97], using a lower number of cores within a processor inside a node did not accelerate the current simulation. These binding strategies appear to be worthwhile for heavier (higher resolution) and larger cases and for longer physical run times [97] which is not the case for the problem in hand. However, Keough [97] did report that for some test cases, using full cores binding was faster than without it. This is consistent with the current findings of the current liquid jet case whereas it accelerated by 5.63% and became more efficient than the default (without binding). Based on this test, full cores binding were used to run the liquid jet case in parallel on HPC.

A.3.2 Liquid Jet Burst Phenomena Case Processing

Processing the liquid jet has been done on two steps, whereas during the first step, the mesh was generated according to the following commands:

- *blockMesh*
- *snappyHexMesh -overwrite* (By default generates two time steps of mesh, first for snapping to geometry, the second for refining surfaces. 'overwrite' means to copy the files from the last time folder generated by *snappyHexMesh* back to the original "0" folder).

After generating the mesh, the case is ready to be processed. The case directory was copied to the HPC environment. To run any case on HPC, the user just has to log in to one of the HPC clusters that OpenFOAM identified. For the current case, OpenFOAM with all utilities was identified to HPC, Cardiff clusters. Once the liquid jet case directory has been successfully copied from the PC onto HPC which will be executed on the cluster, a simple script needs to be created which contains the parameters for the scheduler. This job script specifies what computing resources a particular job requires and provides the scheduler with the instructions required to execute the job. The command used to run this script file is:

- *sbatch bench.sh*

Maximum execution time to run any case on HPC was set by default up to 3 days. Liquid jet cases were re-run from the last time the simulation stopped. Results data was copied and checked regularly through the 3 day runs. The reconstruction data procedure was undertaken on the PC after copying from HPC. Post-processing the data just started after enough data had accumulated for each case setup.

A.3.3 Liquid Jet Burst Phenomena Case Post-processing

All the results gained were post-processed using ParaView software similar to the two droplets case. More details about it are explained within the results and discussion sections in Chapter 5.

A.4 Results of Laminar Liquid Jet Burst Phenomena

Presented in the DVD disk attached to this thesis

A.5 Results of Turbulent Jet (top-hat) Inflow Velocity Profile

Presented in the DVD disk attached to this thesis

A.6 Results of Semi-turbulent Inflow Velocity Profile

Presented in the DVD disk attached to this thesis

A.7 Results of Laminar Jet Burst Released at Higher Ambient Gas Viscosity

Presented in the DVD disk attached to this thesis

A.8 Results of Laminar Jet Burst Released at Lower Ambient Gas Viscosity

Presented in the DVD disk attached to this thesis

A.9 Laminar Jet Results at $Re=2200$ and Low Viscous Liquid

Presented in the DVD disk attached to this thesis

References

- [1] K. K.-y. Kuo and R. Acharya, *Fundamentals of turbulent and multi-phase combustion*: John Wiley & Sons, 2012.
- [2] H. Marschall, "Towards the Numerical Simulation of Multi-Scale Two-Phase Flows," Technische Universität München, 2011.
- [3] H. K. V. a. W. Malalasekera., *An introduction to computational fluid dynamics : the finite volume method*, 1995.
- [4] A. B. Kimbrell, "Development and Verification of a Navier-Stokes Solver with Vorticity Confinement Using OpenFOAM," University of Tennessee, 2012.
- [5] J. H. F. M. PeriC, *Computational Methods for Fluid Dynamics*, third, rev. edition ed., 2002.
- [6] N. Ashgriz, *Handbook of atomization and sprays: theory and applications*: Springer Science & Business Media, 2011.
- [7] X. Jiang, G. Siamas, K. Jagus, and T. Karayiannis, "Physical modelling and advanced simulations of gas-liquid two-phase jet flows in atomization and sprays," *Progress in Energy and Combustion Science*, vol. 36, pp. 131-167, 2010.
- [8] P. J. Bowen and L. C. Shirvill, "Combustion hazards posed by the pressurized atomization of high-flashpoint liquids," *Journal of Loss Prevention in the Process Industries*, vol. 7, pp. 233-241, 1994.
- [9] O. Ubbink, "Numerical prediction of two fluid systems with sharp interfaces " Degree of Doctor of Philosophy of the University of London and Diploma of Imperial College, Department of Mechanical Engineering. Imperial College of Science, Technology & Medicine, Imperial College London (University of London), 1997.
- [10] J. A. S. Stanley Osher, "Fronts propagating with curvature dependent speed: algorithms based on Hamilton-Jacobi formulations," *JOURNAL OF COMPUTATIONAL PHYSICS*, vol. 79, pp. 12-49, 1988.
- [11] M. Sussman, P. Smereka, and S. Osher, "A Level Set Approach for Computing Solutions to Incompressible Two-Phase Flow," *Journal of Computational Physics*, vol. 114, pp. 146-159, 1994.
- [12] J. U. Brackbill, D. B. Kothe, and C. Zemach, "A continuum method for modeling surface tension," *J. Comput. Phys.*, vol. 100, pp. 335-354, 1992.
- [13] F. H. Harlow and J. E. Welch, "Numerical Calculation of Time-Dependent Viscous Incompressible Flow of Fluid with Free Surface," *Physics of Fluids*, vol. 8, pp. 2182-2189, 1965.

- [14] M. F. Trujillo, J. Alvarado, E. Gehring, and G. S. Soriano, "Numerical Simulations and Experimental Characterization of Heat Transfer From a Periodic Impingement of Droplets," *Journal of Heat Transfer*, vol. 133, pp. 122201-122201, 2011.
- [15] R. Lobosco, A. Simões, and H. Schulz, *Analysis of two phase flows on stepped spillways*: INTECH Open Access Publisher, 2011.
- [16] S. S. Deshpande, M. F. Trujillo, X. Wu, and G. Chahine, "Computational and experimental characterization of a liquid jet plunging into a quiescent pool at shallow inclination," *International Journal of Heat and Fluid Flow*, vol. 34, pp. 1-14, 4, 2012.
- [17] R. Li, N. Ashgriz, S. Chandra, J. R. Andrews, and S. Drappel, "Coalescence of two droplets impacting a solid surface," *Experiments in Fluids*, vol. 48, pp. 1025-1035, 2009.
- [18] M. Fang, S. Chandra, and C. B. Park, "Experiments on Remelting and Solidification of Molten Metal Droplets Deposited in Vertical Columns," *Journal of Manufacturing Science and Engineering*, vol. 129, pp. 311-318, 2006.
- [19] Y. Zhang, Y. Chen, P. Li, and A. T. Male, "Weld deposition-based rapid prototyping: a preliminary study," *Journal of Materials Processing Technology*, vol. 135, pp. 347-357, 2003.
- [20] H. Sirringhaus, T. Kawase, R. H. Friend, T. Shimoda, M. Inbasekaran, W. Wu, *et al.*, "High-Resolution Inkjet Printing of All-Polymer Transistor Circuits," *Science*, vol. 290, pp. 2123-2126, 2000.
- [21] J. R. Castrejón-Pita, E. S. Betton, K. J. Kubiak, M. C. T. Wilson, and I. M. Hutchings, "The dynamics of the impact and coalescence of droplets on a solid surface," *Biomicrofluidics*, vol. 5, p. 014112, 2011.
- [22] X. Yang, V. H. Chhasatia, J. Shah, and Y. Sun, "Coalescence, evaporation and particle deposition of consecutively printed colloidal drops," *Soft Matter*, vol. 8, pp. 9205-9213, 2012.
- [23] J. W. Boley, C. Shou, P. McCarthy, T. Fisher, and G. T.C.-Chiu, "The Role of Coalescence in Inkjet Printing Functional Films: An Experimental Study," *NIP & Digital Fabrication Conference*, vol. 2013, pp. 508-513, 2013.
- [24] J. R. Castrejón-Pita, K. J. Kubiak, A. A. Castrejón-Pita, M. C. T. Wilson, and I. M. Hutchings, "Mixing and internal dynamics of droplets impacting and coalescing on a solid surface," *Physical Review E*, vol. 88, p. 023023, 2013.
- [25] S. P. Lin, "Regimes of Jet Breakup and Breakup Mechanisms (Physical Aspects)," in *Recent Advances in Spray Combustion: Spray Atomization and Drop Burning Phenomena*, ed: American Institute of Aeronautics and Astronautics, 1996, pp. 109-135.
- [26] M. Birouk and N. Lelic, "LIQUID JET BREAKUP IN QUIESCENT ATMOSPHERE: A REVIEW," *Atomization and Sprays*, vol. 19, pp. 501-528, 2009.

- [27] R. D. B. Reitz, F.V., , "Mechanisms of Breakup of Round Liquid Jets," in *The Encyclopedia of Fluid Mechanics*. vol. Vol. 3, N. Chermisnoff, Ed., ed Houston, Texas, Gulf Publishing, pp. 233-249, 1986.
- [28] D. W. Lee and R. C. Spencer, "Photomicrographic Studies of Fuel Sprays," National Advisory Committee for Aeronautics. Langley Aeronautical Lab.; Langley Field, VA, United States United States, 1934.
- [29] J. W. S. Rayleigh, "On The Instability Of Jets," *Proceedings of The London Mathematical Society*, vol. s1-10, pp. 4--13, 1878.
- [30] P. H. Schweitzer, "Mechanism of Disintegration of Liquid Jets," *Journal of Applied Physics*, vol. 8, pp. 513-521, 1937.
- [31] A. H. Lefebvre, *Atomization and sprays*. New York: Hemisphere, 1989.
- [32] A. Haenlein, S. United, and A. National Advisory Committee for, *Disintegration of a liquid jet*. Washington: [National Advisory Committee for Aeronautics], 1932.
- [33] H. Vahedi Tafreshi and B. Pourdeyhimi, "The effects of nozzle geometry on waterjet breakup at high Reynolds numbers," *Experiments in Fluids*, vol. 35, pp. 364-371, 2003.
- [34] S. P. Lin and R. D. Reitz, "DROP AND SPRAY FORMATION FROM A LIQUID JET," *Annual Review of Fluid Mechanics*, vol. 30, pp. 85-105, 1998.
- [35] N. Tamaki, M. Shimizu, K. Nishida, and H. Hiroyasu, "EFFECTS OF CAVITATION AND INTERNAL FLOW ON ATOMIZATION OF A LIQUID JET," vol. 8, pp. 179-197, 1998.
- [36] N. Tamaki, M. Shimizu, and H. Hiroyasu, "ENHANCEMENT OF THE ATOMIZATION OF A LIQUID JET BY CAVITATION IN A NOZZLE HOLE," vol. 11, p. 14, 2001.
- [37] H. Hiroyasu, "SPRAY BREAKUP MECHANISM FROM THE HOLE-TYPE NOZZLE AND ITS APPLICATIONS," vol. 10, pp. 511-527, 2000.
- [38] R. P. Grant and S. Middleman, "Newtonian jet stability," *AIChE Journal*, vol. 12, pp. 669-678, 1966.
- [39] J. H. Rupe, *On the dynamic characteristics of free-liquid jets and a partial correlation with orifice geometry*. Pasadena, Calif.: Jet Propulsion Laboratory, California Institute of Technology, 1962.
- [40] P.-K. Wu, L.-K. Tseng, and G. M. Faeth, "PRIMARY BREAKUP IN GAS/LIQUID MIXING LAYERS FOR TURBULENT LIQUIDS," vol. 2, pp. 295-317, 1992.
- [41] C. C. Miesse, "Correlation of Experimental Data on the Disintegration of Liquid Jets," *Industrial & Engineering Chemistry*, vol. 47, pp. 1690-1701, 1955.
- [42] W. A. Sirignano and C. Mehring, "Review of theory of distortion and disintegration of liquid streams," *Progress in Energy and Combustion Science*, vol. 26, pp. 609-655, 2000.

- [43] Y. Pan, Suga K., "Simulation of the liquid jet breakup by the level set method," Central R & D Labs., Inc., Nagakute, Aichi, Nagakute, Japan, 2003.
- [44] W. Sander, B. Weigand, K. Jellinghaus, and K. D. Beheng, "Direct Numerical Simulation of Breakup Phenomena in Liquid Jets and of Colliding Raindrops," in *High Performance Computing in Science and Engineering' 05: Transactions of the High Performance Computing Center Stuttgart (HLRS) 2005*, W. E. Nagel, M. Resch, and W. Jäger, Eds., ed Berlin, Heidelberg: Springer Berlin Heidelberg, pp. 129-142, 2006.
- [45] J. Ishimoto, H. Hoshina, T. Tsuchiyama, H. Watanabe, A. Haga, and F. Sato, "Integrated simulation of the atomization process of a liquid jet through a cylindrical nozzle," *Interdisciplinary Information Sciences*, vol. 13, pp. 7-16, 2007.
- [46] R. Lebas, T. Menard, P.-A. Beau, A. Berlemont, and F.-X. Demoulin, "Numerical simulation of primary break-up and atomization: DNS and modelling study," *International Journal of Multiphase Flow*, vol. 35, pp. 247-260, 2009.
- [47] J. Shinjo and A. Umemura, "Simulation of liquid jet primary breakup: Dynamics of ligament and droplet formation," *International Journal of Multiphase Flow*, vol. 36, pp. 513-532, 2010.
- [48] V. Srinivasan, A. J. Salazar, and K. Saito, "Modeling the disintegration of modulated liquid jets using volume-of-fluid (VOF) methodology," *Applied Mathematical Modelling*, vol. 35, pp. 3710-3730, 2011.
- [49] J. Delteil, S. Vincent, A. Erriguible, and P. Subra-Paternault, "Numerical investigations in Rayleigh breakup of round liquid jets with VOF methods," *Computers & Fluids*, vol. 50, pp. 10-23, 2011.
- [50] H. Grosshans, A. Movaghar, L. Cao, M. Oevermann, R. Z. Szász, and L. Fuchs, "Sensitivity of VOF simulations of the liquid jet breakup to physical and numerical parameters," *Computers & Fluids*, vol. 136, pp. 312-323, 2016.
- [51] R. D. Reitz and F. V. Bracco, "Mechanism of atomization of a liquid jet," *Physics of Fluids*, vol. 25, pp. 1730-1742, 1982.
- [52] S. J. Leib and M. E. Goldstein, "The generation of capillary instabilities on a liquid jet," *Journal of Fluid Mechanics*, vol. 168, pp. 479-500, 1986.
- [53] W. Debler and D. Yu, "The Break-Up of Laminar Liquid Jets," *Proceedings of the Royal Society of London A: Mathematical, Physical and Engineering Sciences*, vol. 415, pp. 107-119, 1988.
- [54] E. A. Ibrahim, "Instability of a liquid sheet of parabolic velocity profile," *Physics of Fluids*, vol. 10, pp. 1034-1036, 1998.
- [55] H. B. Squire, "Investigation of the instability of a moving liquid film," *British Journal of Applied Physics*, vol. 4, pp. 167-169, 1953.
- [56] E. A. Ibrahim and S. O. Marshall, "Instability of a liquid jet of parabolic velocity profile," vol. 76, pp. 17-21, 2000.

- [57] S. P. Lin and E. A. Ibrahim, "Instability of a viscous liquid jet surrounded by a viscous gas in a vertical pipe," *Journal of Fluid Mechanics*, vol. 218, pp. 641-658, 1990.
- [58] Y. Pan and K. Suga, "A numerical study on the breakup process of laminar liquid jets into a gas," *Physics of Fluids*, vol. 18, p. 052101, 2006.
- [59] *The Open Source CFD Toolbox User Guide (OpenFOAM, 3rd December 2014)*.
- [60] G. C. J. Morgan, "APPLICATION OF THE INTERFOAM VOF CODE TO COASTAL WAVE/STRUCTURE INTERACTION," Doctor of Philosophy, Department of Architecture and Civil Engineering, University of Bath UK, 2013.
- [61] E. Berberović, N. P. van Hinsberg, S. Jakirlić, I. V. Roisman, and C. Tropea, "Drop impact onto a liquid layer of finite thickness: Dynamics of the cavity evolution," *Physical Review E*, vol. 79, p. 036306, 2009.
- [62] A. Albadawi, D. B. Donoghue, A. J. Robinson, D. B. Murray, and Y. M. C. Delauré, "Influence of surface tension implementation in Volume of Fluid and coupled Volume of Fluid with Level Set methods for bubble growth and detachment," *International Journal of Multiphase Flow*, vol. 53, pp. 11-28, 2013.
- [63] T. Yamamoto, Y. Okano, and S. Dost, "Validation of the S-CLSVOF method with the Density-Scaled Balanced Continuum Surface Force Model in Multiphase Systems Coupled with Thermocapillary Flows," *International Journal for Numerical Methods in Fluids*, 2016.
- [64] W. HG, A new approach to VOF-based interface capturing methods for incompressible and compressible flows, 2008
- [65] S. T. Zalesak, "Fully multidimensional flux-corrected transport algorithms for fluids," *Journal of Computational Physics*, vol. 31, pp. 335-362, 1979.
- [66] H. Rusche, "Computational Fluid Dynamics of Dispersed Two-phase Flows at High Phase Fraction," Doctor of Philosophy, Imperial College of Science, Technology & Medicine and Department of Mechanical Engineering, University of London and Diploma of Imperial College, 2002.
- [67] J. G. Hnat and J. D. Buckmaster, "Spherical cap bubbles and skirt formation," *Physics of Fluids*, vol. 19, pp. 182-194, 1976.
- [68] K. Yokoi, "A practical numerical framework for free surface flows based on CLSVOF method, multi-moment methods and density-scaled CSF model: Numerical simulations of droplet splashing," *Journal of Computational Physics*, vol. 232, pp. 252-271, 2013.
- [69] A. A. Castrejón-Pita, J. R. Castrejón-Pita, and I. M. Hutchings, "Breakup of Liquid Filaments," *Physical Review Letters*, vol. 108, p. 074506, 2012.
- [70] J. Luo, X. Y. Hu, and N. A. Adams, "A conservative sharp interface method for incompressible multiphase flows," *Journal of Computational Physics*, vol. 284, pp. 547-565, 2015.

- [71] P. Tsai, S. Pacheco, C. Pirat, L. Lefferts, and D. Lohse, "Drop Impact upon Micro- and Nanostructured Superhydrophobic Surfaces," *Langmuir*, vol. 25, pp. 12293-12298, 2009.
- [72] R. Li, N. Ashgriz, S. Chandra, J. Andrews, and S. Drappel, "Deposition of Molten Ink Droplets on a Solid Surface," *Journal of Imaging Science and Technology*, vol. 52, pp. 20502-1-20502-10, 2008.
- [73] M. Pasandideh-Fard, Y. M. Qiao, S. Chandra, and J. Mostaghimi, "Capillary effects during droplet impact on a solid surface," *Physics of Fluids*, vol. 8, pp. 650-659, 1996.
- [74] G. Lagubeau, M. A. Fontelos, C. Josserand, A. Maurel, V. Pagneux, and P. Petitjeans, "Spreading dynamics of drop impacts," *Journal of Fluid Mechanics*, vol. 713, pp. 50-60, 2012.
- [75] D. Jang, D. Kim, and J. Moon, "Influence of fluid physical properties on ink-jet printability," *Langmuir*, vol. 25, pp. 2629-2635, 2009.
- [76] D. R. Lide, *CRC handbook of chemistry and physics* vol. 85: CRC press, 2004.
- [77] C. ANDRIEU, D. A. BEYSENS, V. S. NIKOLAYEV, and Y. POMEAU, "Coalescence of sessile drops," *Journal of Fluid Mechanics*, vol. 453, pp. 427-438, 2002.
- [78] W. D. Ristenpart, P. M. McCalla, R. V. Roy, and H. A. Stone, "Coalescence of Spreading Droplets on a Wettable Substrate," *Physical Review Letters*, vol. 97, p. 064501, 2006.
- [79] J. Fukai, Z. Zhao, D. Poulikakos, C. M. Megaridis, and O. Miyatake, "Modeling of the deformation of a liquid droplet impinging upon a flat surface," *Physics of Fluids A*, vol. 5, pp. 2588-2599, 1993.
- [80] K. A. Sallam, Z. Dai, and G. M. Faeth, "Liquid breakup at the surface of turbulent round liquid jets in still gases," *International Journal of Multiphase Flow*, vol. 28, pp. 427-449, 2002.
- [81] C. Dumouchel, "On the experimental investigation on primary atomization of liquid streams," *Experiments in Fluids*, vol. 45, pp. 371-422, 2008.
- [82] M. a. L. Delcayre, M., "Topological feature in the reattachment region of a backward-facing step " presented at the 1 St AFOSR Int. Conf. On DNS and LES, Ruston, Louisiana, USA, 1997.
- [83] D. Degani, A. Seginer, and Y. Levy, "Graphical visualization of vortical flows by means of helicity," *AIAA Journal*, vol. 28, pp. 1347-1352, 1990.
- [84] J. C. R. Hunt and F. Hussain, "A note on velocity, vorticity and helicity of inviscid fluid elements," *Journal of Fluid Mechanics*, vol. 229, pp. 569-587, 1991.
- [85] G. K. Batchelor, *An Introduction to Fluid Dynamics*: Cambridge University Press, 2000.
- [86] F. J. Venneman, "The aerodynamics of an impulsively-started insect wing"An experimental and numerical investigation", Master of Science in Applied

Physics, Faculty of Aerospace Engineering and Applied Sciences, Delft University of Technology, Delft University of Technology, 2009.

- [87] R. M. Ming Jiang, David Thompson, "Detection and visualization of vortices," in *The Visualization Handbook*, 2005.
- [88] B. S. Massey and J. Ward-Smith, *Mechanics of Fluids, Seventh Edition*: Taylor & Francis, 1998.
- [89] W. Sander and B. Weigand, "Direct Numerical Simulation of Primary Breakup Phenomena in Liquid Sheets," in *High Performance Computing in Science and Engineering '06: Transactions of the High Performance Computing Center Stuttgart (HLRS) 2006*, W. E. Nagel, W. Jäger, and M. Resch, Eds., ed Berlin, Heidelberg: Springer Berlin Heidelberg, pp. 223-236, 2007.
- [90] *The open source CFD toolbox*.
- [91] [https://en.wikipedia.org/wiki/Blender_\(software\)](https://en.wikipedia.org/wiki/Blender_(software)). (27/06/2016). *blender*.
- [92] <https://openfoamwiki.net/index.php/Contrib/swak4Foam>. (28/06/2016). *Contrib/swak4Foam*.
- [93] <https://openfoamwiki.net/index.php/Contrib/groovyBC>. (28/06/2016). *Contrib/groovyBC*.
- [94] <http://openfoam.org/release/2-1-0/boundary-conditions-time-dependent/The>. (19th December 2011, 28/06/2016). *OpenFOAM Foundation*. (2011). *BOUNDARIES. ONLINE:*
- [95] <https://portal.hpcwales.co.uk/docs/userguide/index.html>. (2014). *HPC User Guide*.
- [96] <http://www.cfd-online.com/Forums/openfoam-solving/68683-running-openfoam-parallel.html>. (2011, 30/06/2016). *running OpenFoam in parallel*.
- [97] S. Keough, "Optimising the Parallelisation of OpenFOAM Simulations," D. D. S. a. T. O. department of Defenc, Ed., ed. Commonwealth of Australia: Maritime Division DSTO Defence Science and Technology Organisation, 2014.